Chiral Perovskites: Generating and Investigating Chiro-optical Response in Inorganic and Hybrid Perovskite Nanomaterials

by

Zheni Nikolaeva Georgieva

B.A., Franklin & Marshall College, 2016

Submitted to the Graduate Faculty of the

Dietrich School of Arts and Sciences in partial fulfillment

of the requirements for the degree of

Doctor of Philosophy

University of Pittsburgh

2022

UNIVERSITY OF PITTSBURGH

DIETRICH SCHOOL OF ARTS AND SCIENCES

This dissertation was presented

by

Zheni Nikolaeva Georgieva

It was defended on

July 12, 2022

and approved by

Dr. Jill Millstone, Professor, Department of Chemistry

Dr. Geoffrey Hutchison, Associate Professor, Department of Chemistry

Dr. Jung-Kun Lee, Professor, Swanson School of Engineering

Dissertation Advisor: Dr. David Waldeck, Professor, Department of Chemistry

Copyright © by Zheni Nikolaeva Georgieva

2022

Chiral Perovskites: Generating and Investigating Chiro-optical Response in Hybrid and Inorganic Perovskite Nanomaterials

Zheni Nikolaeva Georgieva, Ph.D.

University of Pittsburgh, 2022

The field of chiral nanomaterials, having only emerged over the last two decades, has generated immense interest and research efforts from a multidisciplinary community of physicists, chemists, and biologists. Motivated by the promise of applications in sensing, metamaterials, photovoltaics, quantum computing, and others, chirality has been imparted on many classes of nanomaterials, such as metal and semiconductor quantum dots. Chiral perovskites are one of the most recently established classes of chiral semiconductor nanomaterials. This work is dedicated to the development and examination of chiral imprinting methodologies for perovskite materials with different morphologies and compositions. Firstly, chirality was imprinted onto organic-inorganic perovskite nanoplatelets via a co-capping ligand shell consisting of a chiral and achiral ligand. The study was the first account of direct synthesis of colloidal chiral perovskites. In the second study of this dissertation, the chiral nanoplatelet methodology was expanded to multiple halide and ligand compositions and the relationship between ligand shell composition and chiroptical activity was studied experimentally and computationally as a function of concentration and temperature. It was determined that electronic imprinting on perovskites is highly dependent not only on the number, but also the arrangement and orientation of chiral ligands on the nanoplatelet surface. Next, a second methodology for imparting chirality was established, this time for all-inorganic cesium lead bromide nanocrystals via a post-synthetic ligand modification. The method was shown to produce high degrees of circular dichroism with multiple chiral amine ligands. This discovery was followed by a study of the size-dependence of chirality in cesium lead bromide nanoparticles, where three different size regimes of perovskite nanoparticles were endowed with chirality via post-synthetic ligand exchange and their chiroptical properties were studied as a function of nanoparticle size, as well as ligand shell composition. CD intensity was found to depend strongly on the nanoparticle size with smaller sizes showing higher degrees of chirality. Finally, the magneto-optic properties of 2D hybrid organic-inorganic perovskites were examined and the material was found to change the magnetization of an adjacent ferromagnetic substrate when irradiated with linearly polarized light, demonstrating the existence of interfacial magnetization states *via* the CISS effect in this material.

Table of Contents

List of Tables

List of Figures

List of Equations

Preface

A doctoral degree, while awarded to a single person, is always the result of tremendous team effort. I would like to take this opportunity to express my gratitude for my team of mentors, colleagues, friends, and family, without whom I would not be here today.

First and foremost, I would like to thank my thesis advisor Dr. David Waldeck for his kind leadership and guidance throughout the years. He has been a steadying presence through moments of elation and despair alike. His dedication to science and his students is apparent in every interaction. My colleagues have also been instrumental in my Ph.D. experience, and I would be remiss if I do not thank them for everything they have done for me. Dr. Brian Bloom was first tasked with introducing me to the lab and gets credit for things as trivial as my ability to fill out a waste label and as fundamental as the topic of my dissertation. I'd also like to thank Dr. Supriya Ghosh, a true friend since day one, for bringing a little bit of fun in even the most monotonous days, Caleb Clever for never getting sick of my cat photos and for sharing his own, and Nazifa Tabassum for being my science sister and for saving my life on a couple of occasions.

I am grateful for the support of my family, biological and chosen, throughout my life and especially over the past few years. My husband Robert Hosler deserves an honorary doctorate for his support and sacrifices throughout the past several years. A literal shoulder to cry on, he has continued to love and support me in even my worst moments. I could not have done this without him and the rest of our little family – out cats Joseph and Ebony. I'd also like to thank my mother- and father-in-law who have treated me as their daughter since the very beginning and have provided me with the refuge and sense of family I did not have in the US.

I must express my endless gratitude for the people who made me, literally and figuratively, into the person I am today – my mother Vanya and father Nikolay. The epitome of supportive parents, they allowed me to move to a different continent all by myself at age seventeen, all in pursuit of a better life and education. Our bond never grew weaker despite the distance, and they have been there for me via daily phone calls and messages, have flown across the world to join me in moments of weakness and triumph, and provide me with unprecedented amounts of unconditional love.

My final words of gratitude go out to my grandmother Tanya, who passed away before she could call me Dr. Georgieva but would have been immensely proud to do so. She taught me so much of the integrity, grit, and tenaciousness that it took to obtain this degree. As promised on the day she left us, I dedicate this work to her.

1.0 Introduction

1.1 The CISS Effect

Chiral molecules have been long known for their unique optical properties, however, little was understood about their electron spin properties until the experimental and theoretical discovery of the chiral induced spin selectivity (CISS) effect two decades ago. [1] The CISS effect describes the propensity of chiral molecules and materials to have a preferred spin direction for charge transfer or transport. The two possible spin states (spin up and spin down) of an electron are degenerate in an achiral system unless a magnetic field is applied. In chiral systems, the two spin states can be non-degenerate even in the absence of an external magnetic field. This phenomenon arises from the chiral electrostatic potential that electrons experience in a chiral system; their movement within this potential generates an effective magnetic field which acts on their intrinsic magnetic moment. The two spin directions possess opposite magnetic dipoles and thus the degeneracy between the two spin states is broken. Because the electron transport through chiral systems is thought to occur via tunneling,[2] the difference in tunneling barriers results in one preferred spin direction that is transmitted through the system. When the transport occurs in a system of the opposite chirality, the spin preference is also opposite. The phenomenon is represented graphically for transport through a left- and right-handed helix in Figure 1.1.

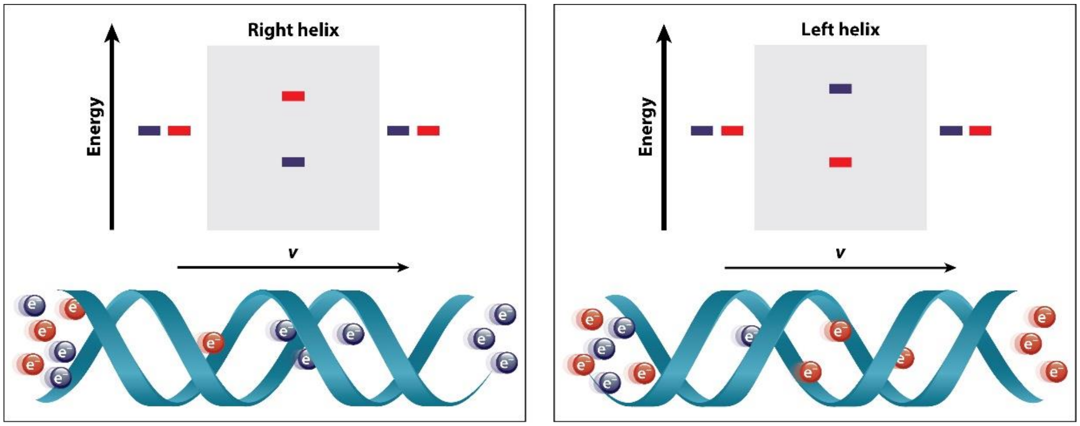

Figure 1.1 The CISS effect illustrated in a schematic form. The red and blue balls represent spin up and spin down, respectively, moving through a left-handed (left) and a right-handed (right) helix. Figure reprinted from Reference 2.

Chirality is an integral part of biological systems, thus the discovery of the CISS effect has led to studies of charge transport through biological molecules and of the role of chirality in living organisms.[3-6] Other fields where CISS has found promising applications include enantioselective synthesis and separations,[7-10] water-splitting reactions,[11, 12] and quantum computing.[2, 13] Recently, chiral inorganic systems have become an important platform for the study for CISS. In 2017 Bloom and Graff described the role of chirality in charge transport between CdSe and CdTe quantum dots, suggesting that a deeper understanding of charge transport through chiral systems offers a new route to the development of next-generation opto-electronic devices.[14] Similar studies have now been published for multiple technologically relevant materials, such as 2D hybrid perovskites ,[15] which rose to prominence as a photovoltaic (PV) converter, reaching 25.7% solar conversion efficiency within a short timeframe.[16]

1.2 Chiral Nanomaterials

The discovery of new chiral systems and platforms has been integral to gaining a better understanding the origin of chirality in inorganic and hybrid materials, studying the CISS effect, and the development of novel technologies. An overview of the field of inorganic and hybrid chiral nanomaterials is presented below, with a specific focus on chiral perovskites, their synthesis and applications, and characterization methods.

1.2.1 Overview of the field

1.2.1.1 Chiral semiconductor nanomaterials

Chiral inorganic and hybrid nanomaterials, having only emerged as a medium over the last two decades, provide an important bridge in the understanding of chirality between small molecules and bulk materials. Pioneering works in the early 2000's developed synthetic methods for noble metal chiral NPs and assemblies, and established some of the first reports of chiral imprinting mechanisms.[17] These works paved the way for the development of the field, establishing important synthetic templates such as chiral NP assemblies[18] and surface-functionalization[19], which remain staples in the synthesis of chiral materials to this day.

Chiral semiconductor nanoparticles were first reported in 2007 by the Gun'ko group in the form of CdS quantum dots capped with D- and L-penicillamine, which exhibited mirror image circular dichroism (CD) spectra with peaks corresponding to the exciton energies of the material.[20] Soon after, the field expanded to include chiral CdSe,[21] CdTe[22], and graphene[23] emerging as alternative chiral semiconductor quantum dots. Several synthetic protocols for generating chiro-optical properties in semiconductor NPs were established, which can be generally split into two categories: i) direct synthesis and ii) post-synthetic modification. Addition of chiral molecules directly into the reaction mixture has led to the formation of chiroptically active CdS, CdSe, and CdTe QDs.[24, 25] Achiral QDs have been treated with post-synthetically to form QDs with individual chirality,[26] as well as to form chiral assemblies.[27] These different synthetic approaches also led to the discovery of a multitude of chiral imprinting mechanisms, which are discussed in the section that follows.

1.2.1.2 Mechanisms of Chiral Imprinting in Semiconductor Nanomaterials

Since the first report of chiral semiconductor QDs, [20] efforts have been made to elucidate the origin of their chiro-optical properties. Despite an increased structural complexity, initial studies of the origin of chirality in semiconductor QDs established similar findings to those in chiral metal NPs, i.e. one of three chirality types: (i) intrinsic chirality arising from chiral dislocations and defects within the QD core,[22, 28] (ii) ligand-induced defects on QD surfaces[29] or interactions between the chiral ligands and achiral QDs,[30] and (iii) assembly into chiral supramolecular structures.[31, 32]

An example of type i chirality was reported for ZnS-coated CdSe QDs and nanorods by the Gun'ko group in 2015. In that study, the as-synthesized nanostructures were found to exist as a mixture of L- and D-nanocrystals which together generate a net zero CD signal. Upon separation via an enantioselective phase transfer procedure, the authors observed measurable CD signals, which they attributed to screw dislocations within the crystal structure of the QDs and nanorods, as examined via HR-TEM. An example of this finding is shown in Figure 1.2.

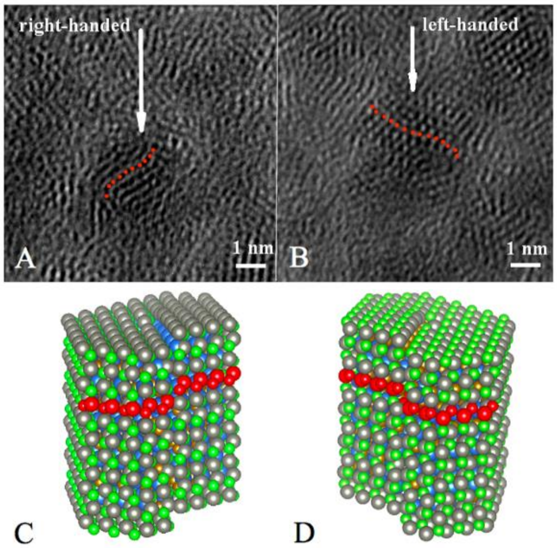

Figure 1.2 TEM images of CdSe/ZnS QDs with right-(A) and left-handed screw dislocations (B). Atomistic models of CdSe/ZnS QDs with right (C) and left (D) screw dislocations. Reprinted with permission from Reference 28.

Type ii chirality is observed when an achiral NP core is capped with a chiral ligand shell and atoms at the NP surface are distorted from ligand-induced strain. Chirality of this category was established computationally in CdS QDs capped with L- and D-penicillamine.[29] Chiral distortion was found only at the surface of the QD and did not penetrate through the QD core, differentiating this system from a type i system. An example of this effect studied experimentally was shown in CdTe QDs, where chiral ligands were replaced with achiral ligands, yet a chiro-optical response was preserved.[22] Optical spectra of QDs capped with L- and D-cysteinemethylester, and then ligand-exchanged to an achiral thiol, are shown in Figure 1.3.

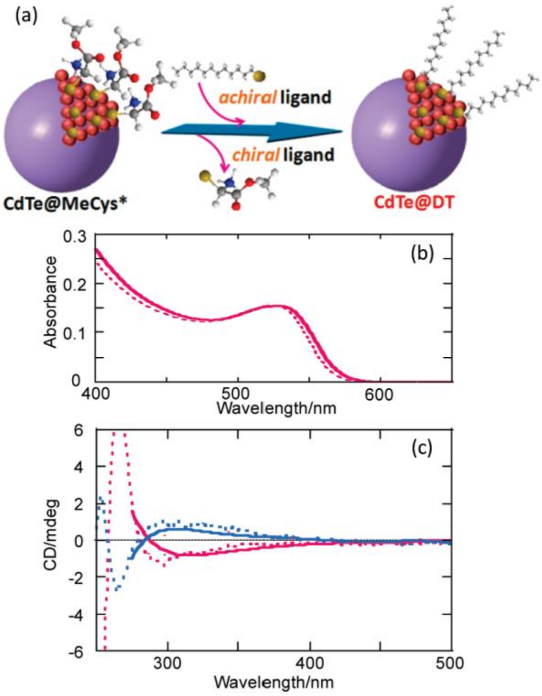

Figure 1.3 Pictorial representation of the ligand exchange experiment on CdTe QDs (a). Absorbance (b) and CD spectra (c) of CdTe QDs with chiral (dotted line) and after exchange with achiral ligands (solid line). Figure reprinted from Reference 22.

Assembling semiconductors into chiral superstructures yields type iii chirality, which can occur spontaneously and be guided by chiral surface ligands,[31] or via a secondary material that acts as a medium for the superstructure formation.[32] Figure 1.4 provides an example from the work of Xu et al. where ZnS-CdSe core-shell QDs were assembled into helical superstructures within a cellulose nanoparticle matrix, yielding a material that emits color-tunable circularly polarized light (CPL).

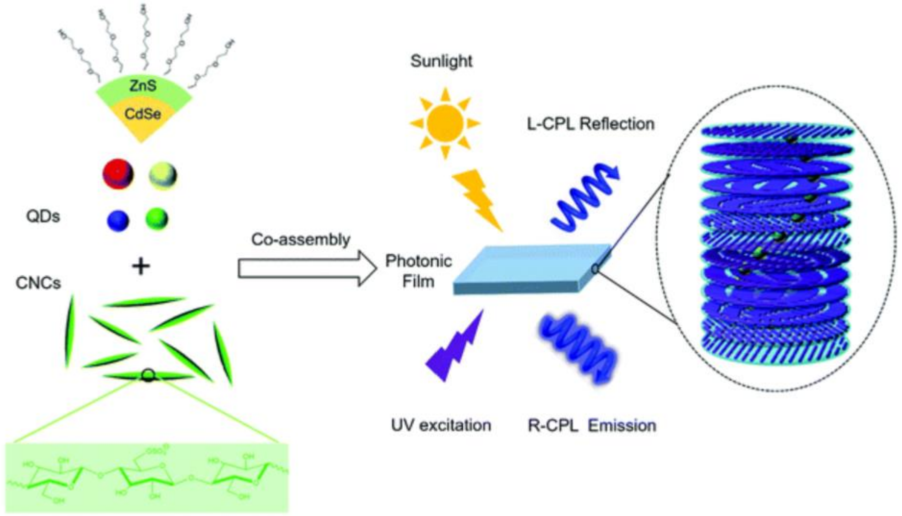

Figure 1.4 Schematic representation of the formation of ZnS/CdSe helical QD assemblies. Figure adapted from Reference 32

While many works identified individual chiral imprinting mechanisms in chiral QDs, later publications suggest that the circular dichroism spectra can originate from multiple imprinting mechanisms present within the same structure.[33, 34] While structural components of NP chirality can often be identified by carefully studying the crystal structure of the material and identifying the presence of a chiral defect or space group, cases of electronic chiral imprinting are less-straightforward to identify. For some electronically imprinted materials, the chiroptical properties can be recreated by generating a derivative line shape, summed over each electronic transition in the absorbance spectrum of the QD.[35] This process suggests that the CD spectra of the material are associated with the interaction of the QD energy levels with those of the chiral ligand.[35, 36]

Despite the significant research efforts on chiral imprinting in semiconductor QDs, a universal model for electronic chiral imprinting still has not been established. The advances in this field have, however, paved the way for the development new classes of chiral nanomaterials, including chiral perovskites, which are the topic of this dissertation.

1.2.2 Chiral Perovskites:

Following the rise in popularity of lead halide perovskites for photovoltaic applications, chiral perovskite materials were developed by several groups. While chiral molecules had been previously incorporated into lead halide perovskites by Billing and Lemmerer,[37] their chiro-optical properties were not explored until 2017 when Ahn and co-workers published the first account of chiral 2D lead iodide perovskite films, which exhibited mirror image circular dichroism.[38] Other perovskite structures followed suit, including colloidal nanocrystals[39] and the Waldeck group's work on chiral perovskite nanoplatelets.[40] Since the publication of these initial accounts, a multitude of different morphologies have appeared in the literature, including chiral perovskite nanowires,[41] nanocrystal superstructures in a chiral gel,[42] and quasi-2D layered structures.[43]

Similar to chiral QDs, chiral perovskites can be prepared via direct synthesis, as well as post-synthetic modification. Chiral ligands have been incorporated into established procedures such as cooling crystallization,[38] ligand-assisted precipitation,[40] and sonochemical synthesis.[44] Strategies for inducing chirality post-synthetically include ligand-exchange procedures,[39, 45] and embedding perovskites into chiral superstructures such as gels[42] and cholesteric stacks.[46] While a wide range of structures and synthetic approaches have been developed, a majority of the chiral perovskite materials reported to date owe their chiro-optical properties to the presence of a chiral amine in the structure, most commonly R- or S-phenylethylamine (R,S-PEA), which is often given a positive charge to bind to the perovskite's negatively-charged surface. Due to the prevalence of arylamines as capping ligands for chiral perovskites, as well as their well-known instability in the presence of water, nearly all reports of chiral perovskites to date are for non-aqueous synthesis and applications. One notable exception is the work of Wang et. al, who prepared 1- and 2-D chiral perovskite single crystals in an acidic aqueous environment.[47]

The quick expansion of the library of chiral perovskite structures has been accompanied by many hypotheses on the topic of their chiral imprinting mechanisms, which are discussed below.

1.2.2.1 Mechanisms of Chiral Imprinting in Perovskites

Understanding the underlying mechanistic principles of perovskite chirality is essential for the design and performance of the material and the devices in which it is used. While chirality is almost always induced via the use of a chiral organic molecule, the underlying mechanism depends strongly on the synthetic approach and the resulting material's morphology. Several mechanisms have been proposed to date for the induction of chirality in perovskites: i) chirality induced within the crystal structure by chiral organic molecules, ii) electronic interactions between chiral ligands and an achiral perovskite structure, iii) surface distortion of the perovskite from interactions with chiral organic ligands, and iv) aggregation of surface ligands in a chiral pattern.

The first perovskite structure to exhibit chiro-optical properties was a 2-dimensional perovskite, consisting of a layered lead iodide framework with chiral spacer cations, either R- or S-methylbenzylamine.[38] The use of chiral spacers imparts chirality onto the whole crystal structure (mechanism i), which is shown schematically in Figure 1.5. The authors found that the resulting chiro-optical features depend on the thickness of the chiral perovskite film, as well as the crystal orientation of the perovskite on the substrate, which can be manipulated by adjusting the concentration of precursors during the spin-coating process.[38]

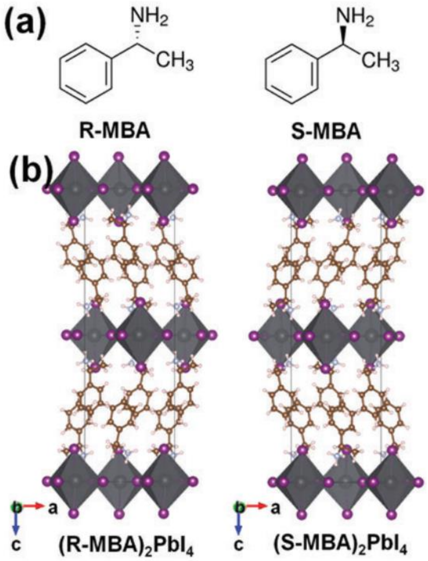

Figure 1.5 Structure of 2D chiral lead iodide perovskites synthesized with R- and S-MBA spacers. Image reproduced from Reference 38.

Type ii chirality was shown in chiral perovskite nanoplatelets directly synthesized with a mixed chiral-achiral ligand shell by the author of this thesis and co-workers.[40] The authors hypothesized that chirality was induced via electronic interactions between the chiral ligand and the perovskite nanoplatelet's electronic states, resulting in the perovskite itself exhibiting chiro-optical properties. Indeed, absorption and CD spectra were both dominated by a known perovskite optical transition.[40] These materials are discussed in detail in Chapter 2.

In an example of type iii chiral imprinting, perovskite chirality was attributed to surface distortion effects in the work of Chen et. al. on cesium lead bromide nanoparticles modified with chiral α-octylamine.[44] The material exhibited circularly polarized photoluminescence and a weak CD signal after the surface modification. While the authors hypothesized that type iii chirality is responsible for the unique optical properties of the material, no experimental or computational evidence was included in the work. [44] Recently, Kim and co-workers contextualized type iii chiral imprinting in perovskites with a computational model, which demonstrated that chiral ligands are capable of causing symmetry-breaking structural distortion in the outermost layers of ligand-exchanged perovskite nanocrystals.[48] A schematic representation of the structural distortion, as well as optical spectra of the experimentally-obtained material are shown in Figure 1.6. The resulting structures do not exhibit chiroptical signatures at energies where perovskite transitions occur,[48] confirming that electronic interactions do not dominate the chiral imprinting mechanism in these structures.

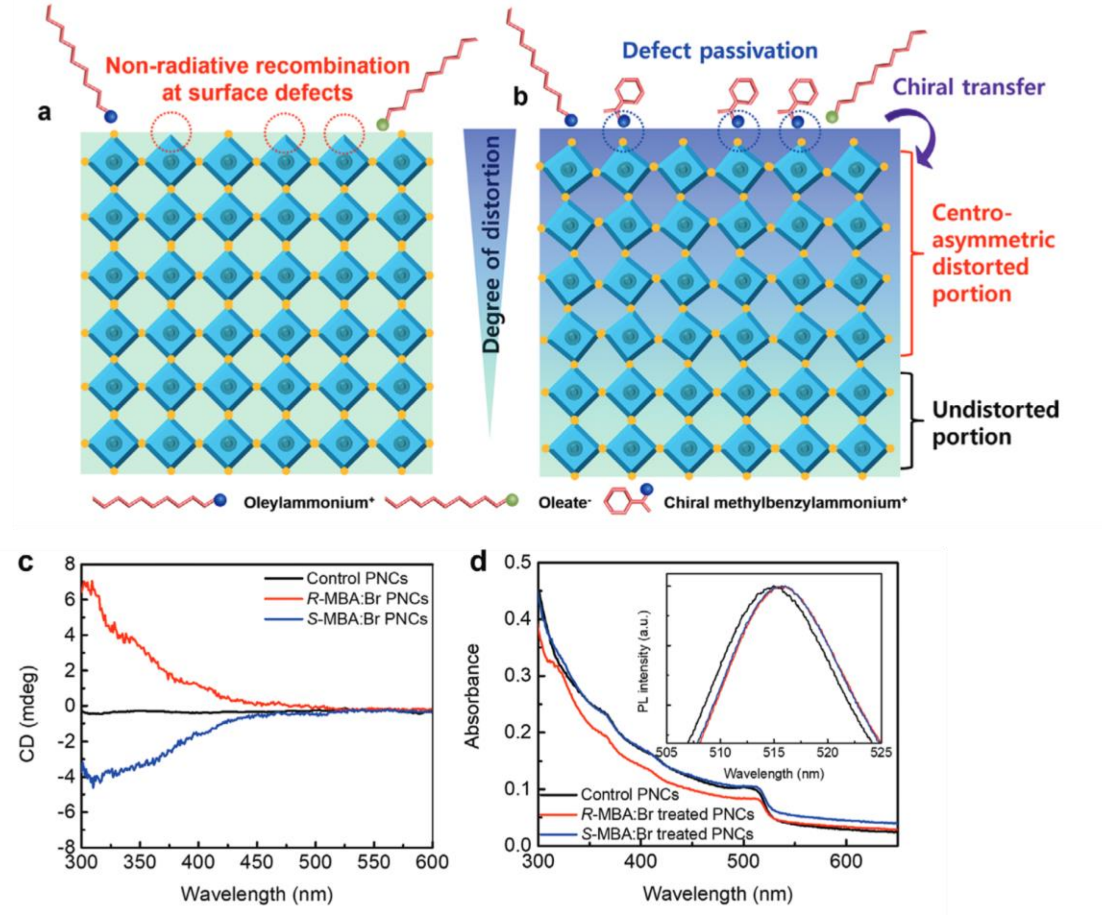

Figure 1.6 Schematic representations of (a) the unperturbed crystal structure of achiral perovskire nanocrystals and (b) distortion of the perovskite latice cause by chiral ligand adsorption. Optical proprties of chiral (red, blue) and achiral (black) perovskite nanocrystals: (c) CD spectra and (d) absorption/emission spectra. Figures reproduced from Reference 48.

While certain structural and optical properties may indicate a specific chiral imprinting mechanism is at play, authors have suggested that a combination of two or more imprinting mechanisms may be present in a single perovskite structure. He et al. reported a ligand exchange procedure to generate chiral colloidal perovskite nanoparticles using enantiomeric 1,2-diaminocyclohexane.[39] The authors suggested a combination of type ii, iii, and iv imprinting mechanisms may be at play, with electronic and surface distortion effects dominating at low chiral ligand concentrations, and asymmetric ligand packing dominating ant high concentrations.[39] Recently, multiple reports have been published that explore the electronic imprinting contributions in layered organic-inorganic perovskites, which were previously reported to only possess structural chirality.[49, 50] By modulating the interactions between chiral aromatic spacers in these structures, the authors were able to demonstrate that the electronic interactions between π-electrons and the perovskite layers play a crucial role in the strength and sign of the material's chiroptical signature.[50] These recent advances highlight the importance of gaining a better understanding of the principles of electronic chiral imprinting, as it may explain anomalous chiroptical behaviors and provide guiding principles for applications of these novel materials.

1.2.2.2 Applications of Chiral Perovskites

Chiral perovskites have been employed in several classes of devices, namely sensors, light-emitting diodes (LEDs), memory devices, piezoelectric devices, and solar cells. [51-53]

Chiral perovskite nanomaterials have been demonstrated to generate circularly polarized photoluminescence (CPPL) by multiple research teams,[46, 47, 54]establishing their promise for applications in CPPL LEDs Traditionally, circularly polarized LEDs require the use of both an electric and a magnetic field. In the work of Kim et. al. circularly polarized light was generated in the absence of a magnetic field and at room temperature by constructing chiral perovskite LEDs based on layered lead iodide perovskites with chiral methylbenzylamine spacers.; the LEDs achieved 2.6% polarized electroluminescence.[55] More recently, Qin and co-workers employed a bromine-functionalized chiral spacer to improve upon this efficiency, demonstrating a layered lead iodide perovskite LED with 11% light polarization.[56] Furthermore, this report found that the polar symmetry of the material allowed it to be used as a piezoelectric harvester and the device's output voltages were studied systematically.[56]

Left and right circularly polarized lights can be used as channels to transmit information. Thus, along with developing circularly polarized light emitters, detectors are needed to facilitate the development of CPPL-based communication. Employing chiral materials in CPPL detectors removes the need for bulky optical elements, which would render the technology simpler and less costly.[53] Chao et. al. first reported the direct detection of CPPL using a chiral hybrid organic-inorganic perovskite composed of lead iodide sheets with chiral methylbenzylamine spacers in 2019.[57] The fabricated device showed competitive performance with existing CPPL detection technology; furthermore, due to the facile fabrication and small dimensions of the chiral perovskite film, the authors were able to incorporate the material into a flexible CPPL detector without jeopardizing device performance.[57] Perovskite CPPL detectors were later shown to surpass the detection capabilities of traditional detectors by Ishii and Miyasaka who employed 1D lead-iodide and naphthylethylamine based perovskites with very high degrees of CD as the photoactive material.[58]

Finally, chiral 2D perovskites were used as the light-harvesting material in a solar cell for the first time by Dayan and co-workers who found that the charge recombination rate is affected by the amount of chiral spacer molecules in the perovskite structure.[59]

1.2.3 Methods of Characterization

Chiral nanomaterials undergo many of the common characterization techniques used in nanoscale synthesis to determine their structure and morphology, as well as optical properties. However, special considerations are taken in some techniques to properly investigate the properties of chiral materials and other techniques are wholly unique to the characterization of chiral materials. Some of these techniques as they relate to chiral perovskites are detailed below.

Light Absorption Techniques

UV-Visible absorption spectroscopy is often the first characterization technique applied to chiroptically active materials, which examines the excitation behavior of the material when exposed to a spectrum of linearly polarized light. While a chiral and achiral material will be indistinguishable in this technique, other important information is gathered, including the energies of the material's band gap and other optically active transitions, which provides a rough landscape of the material's electronic structure. In the field of chiral perovskites quantum-confined structures are frequently employed; their size-dependent optical properties allow for absorbance spectroscopy to be utilized as a facile tool for estimating the size regime of the observed material, i.e. a perovskite which is confined to under 10 nm in any dimension will exhibit narrow blue-shifted absorbance features.[60] Thorough studies of specific combinations between composition and morphology in perovskite nanostructures have even enabled the identification of perovskite nanoplatelet thickness with atomic-layer precision using only linear absorption spectroscopy [60, 61]

Perhaps the most ubiquitous tool for studying chirality is circular dichroism (CD) spectroscopy, which monitors a material's absorption of circularly polarized light, and more specifically the difference between the absorption of left- and right-circularly polarized light. CD is used to quantify the strength of chirality as well as the energies at which chiroptical signal occurs. The shape of CD signatures may also contain information about the type of electronic interactions occurring within the sample, as well as the spatial configuration of the observed chromophores. For a more thorough discussion on CD, see Appendix A.

Light Emission Techniques

Well-known for their emissive properties, perovskites, chiral and achiral alike, are frequently characterized via emission spectroscopy, which measures the radiative decay processes experienced by the material following light-induced excitation. This technique, similarly to absorption spectroscopy, allows for further examination of the material's electronic structure, as well as other characteristics. For example, the emission spectrum is often used to determine the quality of perovskites, as those with high amounts of surface defects will experience a decreased emission efficiency due to an increased number of non-radiative pathways.[48]

Circularly polarized luminescence (CPL) is an emission-based study unique to chiral materials. Just like CD it describes the differential behavior between left and right-circularly polarized light, only in CPL the difference is taken between the left and right circularly polarized light emitted by the material. CPL is most frequently reported as the dissymmetry factor g_{lum}. Like CD, CPL may provide information about the relative spatial orientation of CPL-active coupled chromophores [62]

Electron Microscopy

Transmission electron microscopy (TEM) and scanning electron microscopy (SEM) are commonly used in nanoscience to generate images of the material, determine its morphology and size, and in the case of high resolution (HR) TEM, to examine its crystal lattice. In the field of chiral perovskites TEM and SEM methods are most often employed to determine whether chiral imprinting methods have affected the original perovskite material and to eliminate or confirm the possibility of chiral superstructure formation. In one case, HR-TEM was used to detect chiral disloations within the crystal lattice of CdSe/ZnS[28]; while this method has not yet been used to establish structural chirality in perovskites, it is a powerful characterization tool for chiral nanomaterials.

Crystallographic Techniques

X-ray diffraction (XRD), a common technique for determining the absolute configuration of atoms within a crystal lattice, is used for the identification of different crystalline phases in chiral and achiral perovskites alike. While traditional XRD methods typically do not provide high-enough peak position resolution to measure defect- or strain-induced chirality (for crystals with space groups that are not inherently chiral), additional analysis of XRD spectra, called micro-strain analysis. Micro-strain can be defined as the relative change in the size of a material with respect to its thermodynamic ideal size and can result from minor changes in the lattice caused by structural defects, including dislocations, vacancies, stacking faults, and grain boundaries.[50] Micro-strain manifests in the form of peak broadening so it must be noted that its analysis is only possible when other sources of peak broadening, such as Scherrer broadening (caused by a small grain size) are not a factor. Recently, Ma and co-workers used this technique to elucidate the origin of chirality in hybrid 2D perovskites.[50]

1.3 Dissertation Outline

This dissertation combines the desirable properties of perovskites with those of chiral nanomaterials to expand the library of chiral semiconductor nanomaterials for next-generation opto-electronic devices. The studies presented below provide not only multiple protocols for the preparation of chiral perovskites, but also a look into the mechanistic origins of chiral imprinting and the importance of composition in achieving a high degree of perovskite chirality.

Chapter 2 details the first account of colloidal chiral perovskite nanoplatelets published by our group in 2018. The material is generated via antisolvent crystallization with a co-capping ligand system composed of achiral octylamine and chiral phenylethylammonium ligands. The resulting methyammonium lead bromide nanoplatelets exhibit strong CD signals at the first excitonic transition of the perovskite material; thus, we suggest that the nanoplatelets experience electronic chiral imprinting from the chiral ligand onto the electronic states of the perovskite.

Chapter 3 expands upon the knowledge of chiral perovskite nanoplatelets by introducing additional halide and ligand compositions, as well as a comprehensive study of the role of ligand shell in the imprinting mechanism. Methylammonium lead halide nanoplatelets are synthesized with bromide and chloride as the halide anion, as well as with three different chiral ligands: phenylethylammonium, octylammonium, and naphthylethylammonium. The ratio between chiral and achiral ligands is varied and measured using nuclear magnetic resonance to create a correlation between the composition of the ligand shell and CD intensity. A non-linear relationship is found between the chiral ligand ratio and the CD signal, with high ratios resulting in a plateau of the CD intensity. A chirally-imprinted particle in a box model calculation corroborates the experimental results and suggests that orientational averaging at high chiral ligand ratios causes the plateau formation.

Chapter 4 describes a method for chiral imprinting on highly quantum-confined all-inorganic cesium lead bromide nanoparticles via a post-synthetic ligand modification procedure. Strong CD features are generated with three different chiral ligands and the concentration-dependence, as well as temperature-dependence of the chiroptical properties is recorded. The chiral features are attributed to electronic coupling between the chiral ligand and the nanoparticle.

Chapter 5 examines the size-dependence of chirality in a $CsPbBr_3$ nanoparticle system. Perovskite nanoparticles in three different size-regimes are synthesized and ligand-exchanged with chiral methylphenethylammonium ligands. CD spectra are recorded for all three sizes, however, a significant decrease in CD intensity is observed as nanoparticle size increases. Quantitative NMR studies characterize the nanoparticle ligand shell and find that different relationships exist between chiral ligand coverage and CD intensity in the three different size regimes.

Chapter 6 presents a study on the magneto-optical properties of chiral 2-dimensional hybrid organic-inorganic perovskite (HOIP) films. Magneto-optic Kerr rotation measurements demonstrate that linearly polarized excitation of chiral-HOIPs can change the magnetization of an adjacent ferromagnetic substrate. This discovery demonstrates the existence of interfacial magnetization states *via* the CISS effect in chiral-HOIPs which is beneficial for the future development of quantitative models for CISS.

1.4 References

1. Ray, K.; Ananthavel, S. P.; Waldeck, D. H.; Naaman, R., Asymmetric Scattering of Polarized Electrons by Organized Organic Films of Chiral Molecules. *Science* **1999,** *283* (5403), 814-816.

2. Naaman, R.; Waldeck, D. H., Spintronics and Chirality: Spin Selectivity in Electron Transport Through Chiral Molecules. *Annu. Rev. Phys. Chem.* **2015,** *66* (1), 263-281.

3. Naaman, R.; Fontanesi, C.; Waldeck, D. H., Chirality and its role in the electronic properties of peptides: spin filtering and spin polarization. *Curr. Opin. Electrochem.* **2019,** *14*, 138-142.

4. Beratan, D. N.; Naaman, R.; Waldeck, D. H., Charge and spin transport through nucleic acids. *Curr. Opin. Electrochem.***2017,** *4* (1), 175-181.

5. Naaman, R.; Paltiel, Y.; Waldeck, D. H., Chiral Induced Spin Selectivity and Its Implications for Biological Functions. *Annu. Rev. Biophys.* **2021**.

6. Tassinari, F.; Jayarathna, D. R.; Kantor-Uriel, N.; Davis, K. L.; Varade, V.; Achim, C.; Naaman, R., Chirality Dependent Charge Transfer Rate in Oligopeptides. *Adv. Mater.* **2018,** *30* (21), 1706423.

7. Banerjee-Ghosh, K.; Ben Dor, O.; Tassinari, F.; Capua, E.; Yochelis, S.; Capua, A.; Yang, S.-H.; Parkin Stuart, S. P.; Sarkar, S.; Kronik, L.; Baczewski Lech, T.; Naaman, R.; Paltiel, Y., Separation of enantiomers by their enantiospecific interaction with achiral magnetic substrates. *Science* **2018,** *360* (6395), 1331-1334.

8. Bhowmick, D.; Sang, Y.; Santra, K.; Halbauer, M.; Capua, E.; Paltiel, Y.; Naaman, R.; Tassinari, F., Simultaneous High-Purity Enantiomeric Resolution of Conglomerates Using Magnetic Substrates. *Cryst. Growth Des.* **2021,** *21* (5), 2925-2931.

9. Tassinari, F.; Amsallem, D.; Bloom, B. P.; Lu, Y.; Bedi, A.; Waldeck, D. H.; Gidron, O.; Naaman, R., Spin-Dependent Enantioselective Electropolymerization. *J. Phys. Chem. C* **2020,** *124* (38), 20974-20980.

10. Metzger, T. S.; Mishra, S.; Bloom, B. P.; Goren, N.; Neubauer, A.; Shmul, G.; Wei, J.; Yochelis, S.; Tassinari, F.; Fontanesi, C.; Waldeck, D. H.; Paltiel, Y.; Naaman, R., The Electron Spin as a Chiral Reagent. *Angew. Chem. Int. Ed.* **2020,** *59* (4), 1653-1658.

11. Ghosh, S.; Bloom, B. P.; Lu, Y.; Lamont, D.; Waldeck, D. H., Increasing the Efficiency of Water Splitting through Spin Polarization Using Cobalt Oxide Thin Film Catalysts. *J. Phys. Chem. C* **2020,** *124* (41), 22610-22618.

12. Yutao, S.; Francesco, T.; Kakali, S.; Wenyan, Z.; David, W.; Jonas, F.; Ron, N., Chirality Enhances Oxygen Reduction. *Res. Sq.* **2022**.

13. Aiello, C. D.; Abendroth, J. M.; Abbas, M.; Afanasev, A.; Agarwal, S.; Banerjee, A. S.; Beratan, D. N.; Belling, J. N.; Berche, B.; Botana, A.; Caram, J. R.; Celardo, G. L.; Cuniberti, G.; Garcia-Etxarri, A.; Dianat, A.; Diez-Perez, I.; Guo, Y.; Gutierrez, R.; Herrmann, C.; Hihath, J.; Kale, S.; Kurian, P.; Lai, Y.-C.; Liu, T.; Lopez, A.; Medina, E.; Mujica, V.; Naaman, R.; Noormandipour, M.; Palma, J. L.; Paltiel, Y.; Petuskey, W.; Ribeiro-Silva, J. C.; Saenz, J. J.; Santos, E. J. G.; Solyanik-Gorgone, M.; Sorger, V. J.; Stemer, D. M.; Ugalde, J. M.; Valdes-Curiel, A.; Varela, S.; Waldeck, D. H.; Wasielewski, M. R.; Weiss, P. S.; Zacharias, H.; Wang, Q. H., A Chirality-Based Quantum Leap. *ACS Nano* **2022,** *16* (4), 4989-5035.

14. Bloom, B. P.; Graff, B. M.; Ghosh, S.; Beratan, D. N.; Waldeck, D. H., Chirality Control of Electron Transfer in Quantum Dot Assemblies. *J. Am. Chem. Soc.* **2017,** *139* (26), 9038-9043.

15. Lu, H.; Wang, J.; Xiao, C.; Pan, X.; Chen, X.; Brunecky, R.; Berry, J. J.; Zhu, K.; Beard, M. C.; Vardeny, Z. V., Spin-dependent charge transport through 2D chiral hybrid lead-iodide perovskites. Sci Adv 2019, 5 (12), 1129-1133.

16. NREL.gov, Best Research-Cell Efficiency Chart. https://www.nrel.gov/pv/cell-efficiency.html, 2022.

17. Guerrero-Martínez, A.; Alonso-Gómez, J. L.; Auguié, B.; Cid, M. M.; Liz-Marzán, L. M., From individual to collective chirality in metal nanoparticles. *Nano Today* **2011,** *6* (4), 381-400.

18. Fan, Z.; Govorov, A. O., Plasmonic Circular Dichroism of Chiral Metal Nanoparticle Assemblies. *Nano Lett.* **2010,** *10* (7), 2580-2587.

19. Slocik, J. M.; Govorov, A. O.; Naik, R. R., Plasmonic Circular Dichroism of Peptide-Functionalized Gold Nanoparticles. *Nano Lett.* **2011,** *11* (2), 701-705.

20. Moloney, M. P.; Gun'ko, Y. K.; Kelly, J. M., Chiral highly luminescent CdS quantum dots. *Chem. Commun.* **2007,** (38), 3900-3902.

21. Mukhina, M. V.; Korsakov, I. V.; Maslov, V. G.; Purcell-Milton, F.; Govan, J.; Baranov, A. V.; Fedorov, A. V.; Gun'ko, Y. K., Molecular Recognition of Biomolecules by Chiral CdSe Quantum Dots. *Sci. Rep.* **2016,** *6* (1), 24177.

22. Nakashima, T.; Kobayashi, Y.; Kawai, T., Optical Activity and Chiral Memory of Thiol-Capped CdTe Nanocrystals. *J. Am. Chem. Soc.* **2009,** *131* (30), 10342-10343.

23. Suzuki, N.; Wang, Y.; Elvati, P.; Qu, Z.-B.; Kim, K.; Jiang, S.; Baumeister, E.; Lee, J.; Yeom, B.; Bahng, J. H.; Lee, J.; Violi, A.; Kotov, N. A., Chiral Graphene Quantum Dots. *ACS Nano* **2016,** *10* (2), 1744-1755.

24. Moloney, M. P.; Govan, J.; Loudon, A.; Mukhina, M.; Gun'ko, Y. K., Preparation of chiral quantum dots. *Nat. Protoc.* **2015,** *10* (4), 558-573.

25. Li, Y.; Zhou, Y.; Wang, H.-Y.; Perrett, S.; Zhao, Y.; Tang, Z.; Nie, G., Chirality of Glutathione Surface Coating Affects the Cytotoxicity of Quantum Dots. *Angew. Chem. Int. Ed.* **2011,** *50* (26), 5860-5864.

26. Varga, K.; Tannir, S.; Haynie, B. E.; Leonard, B. M.; Dzyuba, S. V.; Kubelka, J.; Balaz, M., CdSe Quantum Dots Functionalized with Chiral, Thiol-Free Carboxylic Acids: Unraveling Structural Requirements for Ligand-Induced Chirality. *ACS Nano* **2017,** *11* (10), 9846-9853.

27. Govorov, A. O.; Gun'ko, Y. K.; Slocik, J. M.; Gérard, V. A.; Fan, Z.; Naik, R. R., Chiral nanoparticle assemblies: circular dichroism, plasmonic interactions, and exciton effects. *J. Mater. Chem.* **2011,** *21* (42), 16806-16818.

28. Mukhina, M. V.; Maslov, V. G.; Baranov, A. V.; Fedorov, A. V.; Orlova, A. O.; Purcell-Milton, F.; Govan, J.; Gun’ko, Y. K., Intrinsic Chirality of CdSe/ZnS Quantum Dots and Quantum Rods. *Nano Lett.* **2015,** *15* (5), 2844-2851.

29. Elliott, S. D.; Moloney, M. P.; Gun’ko, Y. K., Chiral Shells and Achiral Cores in CdS Quantum Dots. *Nano Lett.* **2008,** *8* (8), 2452-2457.

30. Zhou, R.; Wei, K.-Y.; Zhao, J.-S.; Jiang, Y.-B., Alternative chiral thiols for preparation of chiral CdS quantum dots covered immediately by achiral thiols. *Chem. Commun.* **2011,** *47* (22), 6362-6364.

31. Zhou, Y.; Marson, R. L.; van Anders, G.; Zhu, J.; Ma, G.; Ercius, P.; Sun, K.; Yeom, B.; Glotzer, S. C.; Kotov, N. A., Biomimetic Hierarchical Assembly of Helical Supraparticles from Chiral Nanoparticles. *ACS Nano* **2016,** *10* (3), 3248-3256.

32. Xu, M.; Ma, C.; Zhou, J.; Liu, Y.; Wu, X.; Luo, S.; Li, W.; Yu, H.; Wang, Y.; Chen, Z., Assembling semiconductor quantum dots in hierarchical photonic cellulose nanocrystal films: circularly polarized luminescent nanomaterials as optical coding labels. *J. Mater. Chem. C* **2019,** *7* (44), 13794-13802.

33. Gao, X.; Zhang, X.; Deng, K.; Han, B.; Zhao, L.; Wu, M.; Shi, L.; Lv, J.; Tang, Z., Excitonic Circular Dichroism of Chiral Quantum Rods. *J. Am. Chem. Soc.* **2017,** *139* (25), 8734-8739.

34. Kuznetsova, V.; Gromova, Y.; Martinez-Carmona, M.; Purcell-Milton, F.; Ushakova, E.; Cherevkov, S.; Maslov, V.; Gun’ko, Y. K., Ligand-induced chirality and optical activity in semiconductor nanocrystals: theory and applications. *Nanophotonics* **2021,** *10* (2), 797-824.

35. Ben-Moshe, A.; Teitelboim, A.; Oron, D.; Markovich, G., Probing the Interaction of Quantum Dots with Chiral Capping Molecules Using Circular Dichroism Spectroscopy. *Nano Lett.* **2016,** *16* (12), 7467-7473.

36. Tohgha, U.; Deol, K. K.; Porter, A. G.; Bartko, S. G.; Choi, J. K.; Leonard, B. M.; Varga, K.; Kubelka, J.; Muller, G.; Balaz, M., Ligand Induced Circular Dichroism and

Circularly Polarized Luminescence in CdSe Quantum Dots. *ACS Nano* **2013,** *7* (12), 11094-11102.

37. Billing, D. G.; Lemmerer, A., Synthesis and crystal structures of inorganic–organic hybrids incorporating an aromatic amine with a chiral functional group. *Cryst. Eng. Comm.* **2006,** *8* (9), 686-695.

38. Ahn, J.; Lee, E.; Tan, J.; Yang, W.; Kim, B.; Moon, J., A new class of chiral semiconductors: chiral-organic-molecule-incorporating organic–inorganic hybrid perovskites. *Mater. Horizons* **2017,** *4* (5), 851-856.

39. He, T.; Li, J.; Li, X.; Ren, C.; Luo, Y.; Zhao, F.; Chen, R.; Lin, X.; Zhang, J., Spectroscopic studies of chiral perovskite nanocrystals. *Appl. Phys. Lett.* **2017,** *111* (15), 151102.

40. Georgieva, Z. N.; Bloom, B. P.; Ghosh, S.; Waldeck, D. H., Imprinting Chirality onto the Electronic States of Colloidal Perovskite Nanoplatelets. *Adv. Mater.* **2018,** *30* (23), 1800097.

41. Yuan, C.; Li, X.; Semin, S.; Feng, Y.; Rasing, T.; Xu, J., Chiral Lead Halide Perovskite Nanowires for Second-Order Nonlinear Optics. *Nano Lett.* **2018,** *18* (9), 5411-5417.

42. Shi, Y.; Duan, P.; Huo, S.; Li, Y.; Liu, M., Endowing Perovskite Nanocrystals with Circularly Polarized Luminescence. *Adv. Mater.* **2018,** *30* (12), 1705011.

43. Long, G.; Jiang, C.; Sabatini, R.; Yang, Z.; Wei, M.; Quan, L. N.; Liang, Q.; Rasmita, A.; Askerka, M.; Walters, G.; Gong, X.; Xing, J.; Wen, X.; Quintero-Bermudez, R.; Yuan, H.; Xing, G.; Wang, X. R.; Song, D.; Voznyy, O.; Zhang, M.; Hoogland, S.; Gao, W.; Xiong, Q.; Sargent, E. H., Spin control in reduced-dimensional chiral perovskites. *Nat. Photonics* **2018,** *12* (9), 528-533.

44. Chen, W.; Zhang, S.; Zhou, M.; Zhao, T.; Qin, X.; Liu, X.; Liu, M.; Duan, P., Two-Photon Absorption-Based Upconverted Circularly Polarized Luminescence Generated in Chiral Perovskite Nanocrystals. *J. Phys. Chem. Lett.* **2019,** *10* (12), 3290-3295.

45. Debnath, G. H.; Georgieva, Z. N.; Bloom, B. P.; Tan, S.; Waldeck, D. H., Using post-synthetic ligand modification to imprint chirality onto the electronic states of cesium lead bromide (CsPbBr3) perovskite nanoparticles. *Nanoscale* **2021,** *13* (36), 15248-15256.

46. Wang, C.-T.; Chen, K.; Xu, P.; Yeung, F.; Kwok, H.-S.; Li, G., Fully Chiral Light Emission from CsPbX3 Perovskite Nanocrystals Enabled by Cholesteric Superstructure Stacks. *Adv. Funct. Mater.* **2019,** *29* (35), 1903155.

47. Wang, J.; Fang, C.; Ma, J.; Wang, S.; Jin, L.; Li, W.; Li, D., Aqueous Synthesis of Low-Dimensional Lead Halide Perovskites for Room-Temperature Circularly Polarized Light Emission and Detection. *ACS Nano* **2019,** *13* (8), 9473-9481.

48. Kim, Y.-H.; Song, R.; Hao, J.; Zhai, Y.; Yan, L.; Moot, T.; Palmstrom, A. F.; Brunecky, R.; You, W.; Berry, J. J.; Blackburn, J. L.; Beard, M. C.; Blum, V.; Luther, J. M., The Structural Origin of Chiroptical Properties in Perovskite Nanocrystals with Chiral Organic Ligands. *Adv. Funct. Mater.* **2022,** *32* (25), 2200454.

49. Zhang, Y.; Sun, M.; Zhou, N.; Huang, B.; Zhou, H., Electronic Tunability and Mobility Anisotropy of Quasi-2D Perovskite Single Crystals with Varied Spacer Cations. *J. Phys. Chem. Lett.* **2020,** *11* (18), 7610-7616.

50. Ma, S.; Jung, Y.-K.; Ahn, J.; Kyhm, J.; Tan, J.; Lee, H.; Jang, G.; Lee, C. U.; Walsh, A.; Moon, J., Elucidating the origin of chiroptical activity in chiral 2D perovskites through nano-confined growth. *Nat. Commun.* **2022,** *13* (1), 3259.

51. Dang, Y.; Liu, X.; Cao, B.; Tao, X., Chiral halide perovskite crystals for optoelectronic applications. *Matter* **2021,** *4* (3), 794-820.

52. Dong, Y.; Zhang, Y.; Li, X.; Feng, Y.; Zhang, H.; Xu, J., Chiral Perovskites: Promising Materials toward Next-Generation Optoelectronics. *Small* **2019,** *0* (0), 1902237.

53. Long, G.; Sabatini, R.; Saidaminov, M. I.; Lakhwani, G.; Rasmita, A.; Liu, X.; Sargent, E. H.; Gao, W., Chiral-perovskite optoelectronics. *Nat. Rev. Mater.* **2020,** *5* (6), 423-439.

54. Seo, I. C.; Lim, Y.; An, S.-C.; Woo, B. H.; Kim, S.; Son, J. G.; Yoo, S.; Park, Q. H.; Kim, J. Y.; Jun, Y. C., Circularly Polarized Emission from Organic–Inorganic Hybrid Perovskites via Chiral Fano Resonances. *ACS Nano* **2021,** *15* (8), 13781-13793.

55. Kim, Y.-H.; Zhai, Y.; Lu, H.; Pan, X.; Xiao, C.; Gaulding, E. A.; Harvey Steven, P.; Berry Joseph, J.; Vardeny Zeev, V.; Luther Joseph, M.; Beard Matthew, C., Chiral-induced spin selectivity enables a room-temperature spin light-emitting diode. *Science* **2021,** *371* (6534), 1129-1133.

56. Qin, Y.; Gao, F.-F.; Qian, S.; Guo, T.-M.; Gong, Y.-J.; Li, Z.-G.; Su, G.-D.; Gao, Y.; Li, W.; Jiang, C.; Lu, P.; Bu, X.-H., Multifunctional Chiral 2D Lead Halide Perovskites with Circularly Polarized Photoluminescence and Piezoelectric Energy Harvesting Properties. *ACS Nano* **2022,** *16* (2), 3221-3230.

57. Chen, C.; Gao, L.; Gao, W.; Ge, C.; Du, X.; Li, Z.; Yang, Y.; Niu, G.; Tang, J., Circularly polarized light detection using chiral hybrid perovskite. *Nat. Commun.* **2019,** *10* (1), 1927.

58. Ishii, A.; Miyasaka, T., Direct detection of circular polarized light in helical 1D perovskite-based photodiode. *Sci. Adv.* *6* (46), eabd3274.

59. Shpatz Dayan, A.; Wierzbowska, M.; Etgar, L., Ruddlesden–Popper 2D Chiral Perovskite-Based Solar Cells. *Small Structures* **2022,** *n/a* (n/a), 2200051.

60. Kim, Y.-H.; Wolf, C.; Kim, Y.-T.; Cho, H.; Kwon, W.; Do, S.; Sadhanala, A.; Park, C. G.; Rhee, S.-W.; Im, S. H.; Friend, R. H.; Lee, T.-W., Highly Efficient Light-Emitting

Diodes of Colloidal Metal–Halide Perovskite Nanocrystals beyond Quantum Size. *ACS Nano* **2017,** *11* (7), 6586-6593.

61. Tyagi, P.; Arveson, S. M.; Tisdale, W. A., Colloidal Organohalide Perovskite Nanoplatelets Exhibiting Quantum Confinement. *J. Phys. Chem. Lett.* **2015,** *6* (10), 1911-1916.

62. Kumar, J.; Nakashima, T.; Kawai, T., Circularly Polarized Luminescence in Chiral Molecules and Supramolecular Assemblies. *J. Phys. Chem. Lett.* **2015,** *6* (17), 3445-3452.

2.0 Imprinting Chirality onto the Electronic States of Colloidal Perovskite Nanoplatelets

This work was published as Georgieva, Z. N.; Bloom, B. P.; Ghosh, S.; Waldeck, D. H., Imprinting Chirality onto the Electronic States of Colloidal Perovskite Nanoplatelets. Advanced Materials 2018, 30 (23), 1800097. The author of the thesis performed the nanoplatelet synthesis, experimental design, and all optical and crystallographic characterization, and participated in the writing of the manuscript.

This work reports on the direct synthesis of chiroptical organic-inorganic perovskite nanoplatelets that are passivated by R- or S-phenylethylammonium (PEA) ligands. The circular dichroism spectra can be divided into two components: 1) a region associated with a charge transfer transition between the ligand and the nanoplatelet, 300-350 nm, and 2) a region corresponding to the excitonic absorption maximum of the perovskite, 400-450 nm. The temperature and concentration dependent circular dichroism spectra indicate that the chiro-optical response arises from chiral imprinting by the ligand on the electronic states of the quantum confined perovskite rather than chiral ligand-induced stereoselective aggregation.

2.1 Introduction

We report on the synthesis and characterization of chiral quantum-confined colloidal perovskite nanoplatelets (NPs). Perovskite semiconductors offer extraordinary promise for next generation opto-electronic materials because of their desirable characteristics of color tunability (through halide composition and quantum confinement effects),[1, 2] long carrier lifetime and diffusion lengths,[3, 4] and high electron/hole mobility;[5, 6] recent applications include light emitting diodes,[7, 8] lasers,[9, 10] and photovoltaics.[11, 12] In addition to spin-mediated transport processes[13-15] and chiral memory applications,[16, 17] which arise from the chiral induced spin selectivity effect (CISS),[18, 19] chiro-optical semiconductor nanomaterials are particularly interesting for stereoselective synthesis[20] and as circularly polarized light sources.[21] Recent work on $CH_3NH_3PbBr_3$ perovskite materials shows strong spin-orbit coupling of the electronic states,[22] suggesting that chiral perovskites might display interesting spin polarization properties.

The mechanism for generating chirality in inorganic semiconductors is typically associated with (i) near surface enantiomeric distortions of the crystal lattice, (ii) electronic coupling between a chiral ligand and an otherwise achiral semiconductor, (iii) assembly into a chiral secondary structure, and (iv) the formation of chiral surface defects.[23-25] To date, we are only aware of two published reports for the synthesis of chiral organic-inorganic perovskite materials. Ahn *et al.* synthesized (S- or R-phenylethylamine)$_2$PbI$_4$ powders that could be dissolved in DMF and then used to form thin films of a perovskite material upon crystallization.[26] Their circular dichroism (CD) spectra showed optical activity in the perovskite film's excitonic transitions and it was attributed to the formation of a chiral crystalline structure that forms between twisted perovskite unit cells within the layered films (mechanism iii). In another report, He *et al.* synthesized oleylamine capped CsPb(I/Br)$_3$ perovskites and used post-synthetic modification (namely heating in the presence of chiral 1,2-diaminocyclohexane) to produce a colloidal perovskite solution (mechanism iv).[27] Their CD spectra showed optical activity of a ligand-perovskite charge transfer band, but did not display any chiroptical features at the absorption maximum of the perovskite exciton band (~560 nm). Herein we report a procedure for the direct synthesis of chiral quantum-confined colloidal perovskite NPs, in which a chiral ligand shell imprints its chirality onto the excitonic transitions of the NP (mechanism ii).

2.2 Results and Discussion

Chiral perovskite nanoplatelets (NPs) were synthesized using a combination of chiral (S- or R-phenylethylammonium, S-PEA or R-PEA) and achiral octylamine (OA) ligands. The procedure is derived from that reported previously by Tisdale and co-workers for achiral methylammonium lead bromide nanoplatelets.[1, 2]

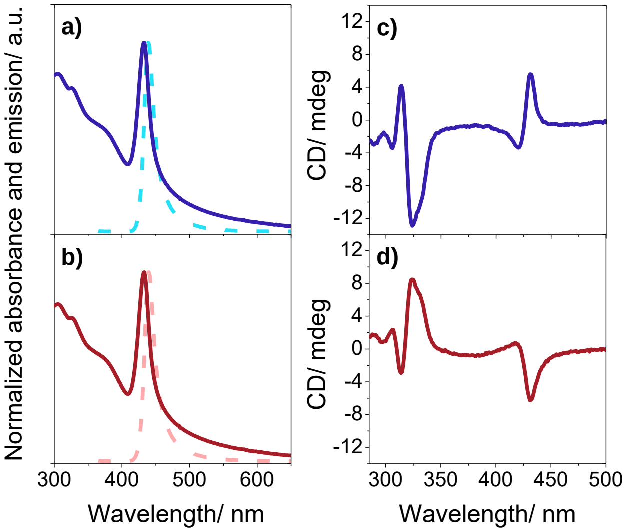

Figure 2.1 Panels a) and b) show absorption (solid line) and emission (dashed line) spectra of S-PEA (a, blue) and R-PEA (b, red) perovskite nanoplatelet (NP) in toluene solutions. Panels c) and d) show circular dichroism spectra of the S-PEA (c, blue) and R-PEA (d, red) NP toluene solutions.

Figure 2.1a and 1b show the absorption and emission spectra for the NPs synthesized with S-PEA (blue) and R-PEA (red) respectively. The sharp absorption peak at 432 nm is consistent with a quantum confined NP of a single unit cell thickness.[1, 2] The extended tail in the absorption spectra, and the asymmetry in the emission spectra, indicate that perovskites of different thicknesses are likely present (absorbance at 450 nm indicates 1.5 unit cells), however the dominant material is a single unit cell thick nanoplatelet. Those spectra are indistinguishable from the absorbance and emission of achiral octylamine passivated perovskite nanoplatelets (see Figure B.1).

The circular dichroism (CD) spectra of the NP solutions are shown in Figure 1c and 1d. The perovskite NPs synthesized with the two enantiomers of the ligand display mirror image CD spectra that consist of two regions of interest: 300-350 nm and 400-450 nm. Neither the phenylethylamine nor the phenylethylammonium bromide exhibit chiroptical features at wavelengths longer than 280 nm (see Figure B.2). The signal generated from 300-350 nm is attributed to the excitation of a charge transfer band between the chiral ligand and the NP surface. Comparable chiroptical features are present in ligand solutions of S- or R-PEA with lead bromide in the absence of NPs (see Figure B.3), and a similar phenomenon was previously found for chiral ligands coordinated to CdSe and CdTe nanoparticles.[14, 25] The bisignate peak between 400 nm and 450 nm overlaps with the maximum of the perovskite NPs' exciton absorption (see Figure 2.1a and 2.1b) and indicates that the ligand imprints its chirality onto the NP's electronic structure. The bisignate peak associated with the charge transfer band exhibits positive to negative Cotton effects with increasing wavelength for S-PEA NPs, whereas the bisignate peak at the absorbance maximum exhibits negative to positive Cotton effects with increasing wavelength. This phenomenon is associated with an enantiomeric difference between the chiral ligand and its packing geometry, further substantiating the claim that the chirality originates cooperatively from electronic coupling between the chiral ligand shell and the perovskite nanoplatelet. Cotton effects from higher energy excitonic transitions of the perovskite should occur at lower wavelengths, however, they are most likely masked by the presence of the intense charge transfer band.

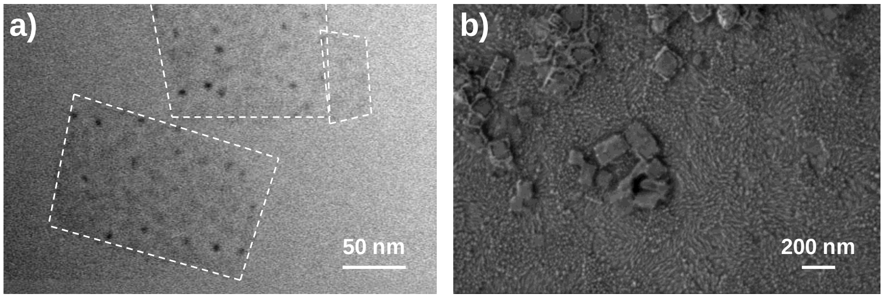

Figure 2.2 TEM (a) and SEM (b) images of the perovskite nanoplatelets (NPs) are shown. The NPs in the TEM are outlined in white to highlight their shape. The small quasiparticles (5-7 nm) in the TEM are attributed to metallic lead and PbBr2.

Figure 2.2 shows representative TEM (a) and SEM (b) images of the chiral perovskite NPs. Panel (a) shows a TEM image of three nanoplatelets, outlined in white to highlight their shape. The small quasiparticle features found on the nanoplatelets in the image are consistent with previous reports[1, 28, 29] and originate from the degradation of the perovskite into $PbBr_2$ and metallic Pb. The TEM suggests that the edges of the nanoplatelets are more prone to degradation and a ring like structure can be seen around some of the nanoplatelets in the SEM. Exposure of the nanoplatelets to the electron beam accelerates the degradation of the perovskite, making it difficult to isolate images without the quasiparticles.[28] Energy dispersive spectroscopy of the NPs showed a Pb:Br ratio of 1:1.6, similar to that reported by Sichert *et al.* (see Figure B.4).[29]

Figure 2.3a shows powder X-ray diffraction patterns of chiral NPs (red and blue) and achiral bulk perovskite crystals (black). The observed peak positions are consistent with previous reports on methylammonium lead bromide nanoparticles, nanoplatelets, and bulk perovskites.[1, 28, 30] The S- and R-NPs exhibit identical diffraction patterns and show good agreement with the bulk peak positions, indicating that the chiral NPs have a crystal lattice consistent with that of a perovskite. Note that the X-ray diffraction patterns on chiral perovskite materials synthesized by Ahn et al. were also not sensitive to the chirality.[26]

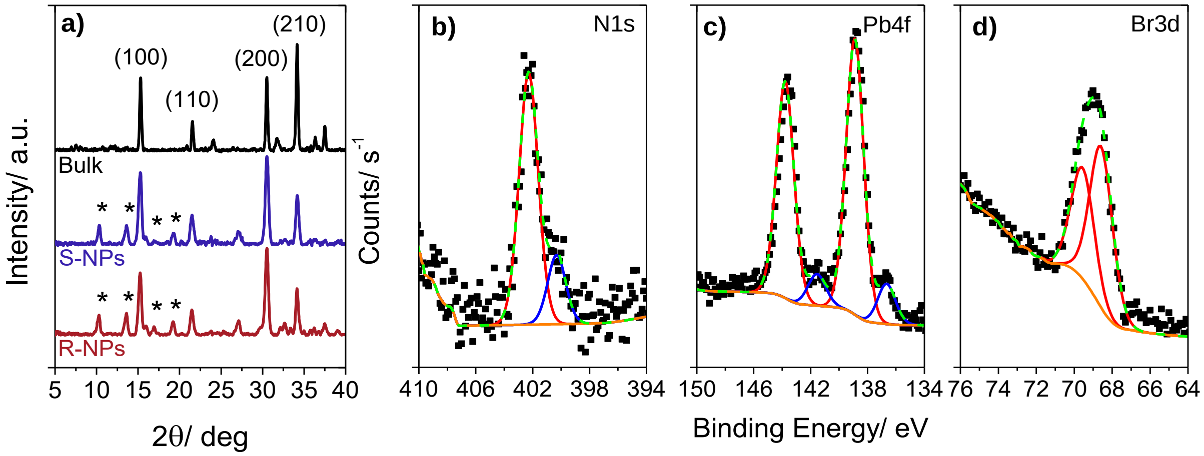

Figure 2.3 Panel a) shows powder X-ray diffraction patterns for bulk perovskites (black), S-PEA nanoplatelets (blue), and R-PEA nanoplatelets (red). The numbers in parentheses specify crystal facets and the asterisks indicate a periodicity associated with stacking of nanoplatelets in the powder sample. Panels b)-d) show N1s, Pb4f, and Br3d X-ray photoelectron spectra of the perovskite nanoplatelets (black). The data were fit using a weighted Gaussian-Lorentzian form (red, blue) and a Shirley background (orange). The envelope is plotted as a dashed green line.

Additional peaks, marked with asterisks in figure 2.3a, occur at intervals of 3.3° 2θ (equivalent to a spacing of 2.6 nm) and are attributed to reflections from stacked NPs in the powder.[2] A one unit cell thick perovskite nanoplatelet has a reported thickness of ~1.2 nm.[1] The remaining 1.4 nm are attributed to a combination of OA and PEA ligands; the approximate lengths for two interacting ligands are ~1.3 nm and ~1.65 nm for PEA-PEA and OA-PEA respectively.

Figure 2.3b-2.3d show x-ray photoelectron spectra of the chiral perovskite NPs. The nitrogen 1s spectrum was fit to two peaks, and the envelope is plotted as a dashed green line. The red peak at 402.3 eV is characteristic of nitrogen in a perovskite material,[31] and the blue peak at

400.3 eV is consistent with unbound amine ligands.[32] The Pb and Br spectra each exhibit a prominent doublet (red), in agreement with previous studies of perovskites: the Pb $4f_{7/2}$ and Pb $4f_{5/2}$ doublet is at 138.9 and 143.8 eV, and the Br $3d_{5/2}$ and Br $3d_{3/2}$ doublet is at 68.6 eV and 69.5 eV.[7, 33] The additional lead doublet at 136.7 and 141.7 eV (blue) is consistent with the binding energy for metallic Pb[34] and validate the assignment of the quasiparticles in the TEM to metallic Pb. The atomic percent ratio from eighteen different regions of a chiral perovskite NP sample was calculated and an average stoichiometry of $N_{4.4}Pb_2Br_{8.4}$ was found (the standard deviation for N and Br was approximately 0.3). A NP with a single unit cell has a stoichiometry of $N_3Pb_2Br_7$, suggesting that an additional equal proportion of N and Br (1.4 / perovskite) is present in the sample. This excess may originate from decomposed nanoplatelets, as suggested by the metallic Pb doublet discussed above, and / or contributions from nanoplatelets with a different thickness.

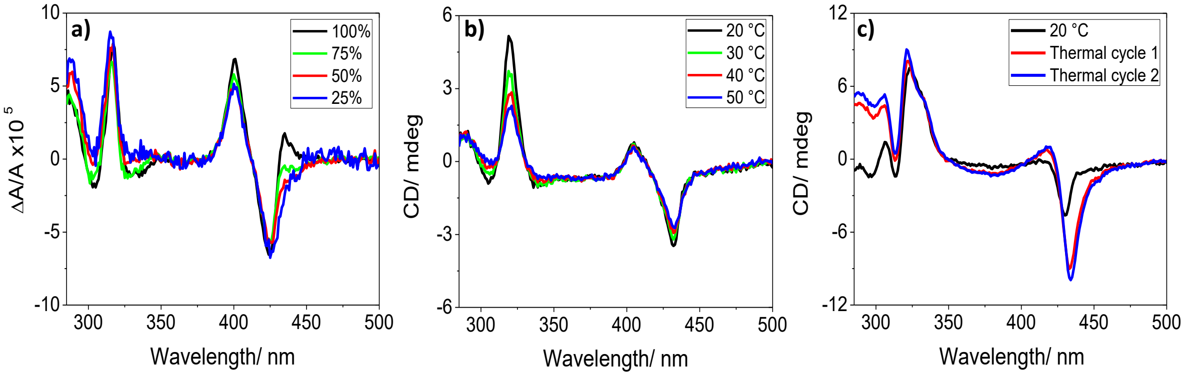

Figure 2.4 Panel a) shows concentration dependent CD spectra of R-PEA nanoplatelets in toluene; the spectra are scaled by the solution optical density at 432 nm. Panel b) shows temperature dependent CD spectra of R-PEA perovskite nanoplatelets with excess ligand present in the solution. The temperature was varied from 20 °C to 50 °C. Panel c) shows CD spectra for solutions of R-PEA NPs with no excess ligand added, at 20 °C before heat treatment (black), after one heating cycle (red), and after two heating cycles (blue) from 20 °C to 50 °C and back to 20 °C.

In an effort to elucidate the origin of the perovskite chirality, the dependence of the CD signal on the concentration and temperature of the NP solutions was investigated. If the chiroptical features manifest from the formation of chiral NP aggregates, then decreasing the NP concentration should decrease aggregation and result in a less intense CD signal per NP. Figure 2.4a shows CD spectra that are scaled by the total absorbance of four diluted aliquots from the same NP solution. Dilution of the R-PEA capped perovskite solution with added free R-PEA does not significantly change the CD spectra or the transition strength per NP over the range shown in Figure 2.4a. The circular dichroism of a perovskite NP film was also studied (see Figure B.5). The perovskite solution was drop casted onto a glass substrate to simulate the effects of aggregation and the CD was compared to the same perovskite NP but in solution. The film and solution samples had identical optical densities; however, the perovskite film exhibited a much weaker CD signal. Additional scatter was also present in the NP film that occurs to the red of the bisignate peak occurring at the absorption maximum (similar to the experiments by Ahn *et al.* for thin chiral perovskite films).[26] These results suggest that aggregation does not promote chirality of our materials and instead the chirality is consistent with a model for chiral ligand imprinting onto the electronic structure of individual perovskite NPs. Temperature dependent CD spectra of R-PEA NPs further corroborate this interpretation. As the temperature is changed from 20 °C to 50 °C, in the presence of excess R-PEA, the CD intensity in the exciton region of 400-450 nm shows a modest change, whereas a substantial decrease occurs in the CD signal at 300-350 nm as the temperature increases (Figure 2.4b). The decrease of the charge transfer band's absorbance likely originates from a decrease in chiral ligand surface coverage. In a recent study on the binding equilibrium of ammonium ligands on $CsPbBr_3$ perovskites, Roo et al. reported that the dissociation rate of the ammonium ligand, k_{off}, is facile.[35] This interpretation is supported by temperature studies in which no excess ligand is added to the solution and larger changes in the CD signal strength are found (see Figure B.6). Despite the decrease in ligand coverage, inferred from the decrease in intensity of the charge transfer band at 300-350 nm (Figure 2.4b), the chiroptical features at the exciton absorption maximum largely persist. We postulate that this weaker change reflects the cooperative nature of the chiral imprinting and is sensitive to features of the ligand layer's packing on the NP, as well as ligand coverage.

In the absence of excess R-PEA ligands in solution, increasing the temperature from 20 °C to 50 °C causes a decrease of the NPs' CD signal intensity (Figure B.4), but upon cooling back to 20 °C the CD intensity of the exciton transition becomes larger than it was prior to heating (see Figure 2.4c). A third heating cycle causes only a modest change; however, the effect saturates. Previous studies demonstrated that the crystal structure of perovskites changes from a tetragonal to a cubic lattice upon mild heating;[36, 37] however, X-ray diffraction data for the NPs are the same before heating and after heating and cooling (see Figure B.7), indicating that any structural phase change is reversible. It is reasonable that the thermal cycling anneals the ligand packing, which enhances the chiral imprinting and increases the circular dichroism strength.[23] This explanation is corroborated by thermal treatment studies on nanoparticles which show that ligand rearrangement increases the photoluminescence intensity.[38] When excess ligand is present in solution, one observes a less drastic change in the exciton's CD strength, presumably because the ligand surface coverage remains high and limits the annealing. Note that differences in the CD line shape and intensity in the charge transfer band between Figure 2.1c and Figure 2.4a and 2.4b are thought to be associated with different ligand configurations and coverage on the NP surface when excess ligand is present. Other variability in the CD signal shape and intensity at the absorbance maximum of the NPs likely arise from different unit cell thickness distributions between batches of NPs.

2.3 Summary

Chiral colloidal quantum-confined perovskite nanoplatelets were synthesized using S- or R-phenylethylamine as the capping ligand. The circular dichroism spectra indicate the formation of a charge transfer band between the ligand and the perovskite and a feature involving the perovskite's exciton, which is attributed to the electronic coupling between the ligands and the quantum confined axis of the nanoplatelets. This work demonstrates a new strategy for generating chiroptical perovskite materials.

2.4 Experimental Methods

2.4.1 Synthesis of Precursor Salts

S and R-phenylethylammonium bromide salts were synthesized following a similar procedure for arylammonium salts published previously.[39] Briefly, S-(-)-phenylethylamine or R-(+)-phenylethylamine (2.5 mL) was mixed with 15.0 mL of ethanol in a round-bottom flask and stirred in an ice water bath until the temperature reached 0 °*C*. Hydrobromic acid (3.40 mL, 48% in water) was added slowly into the flask, and the reaction was stirred for two hours. The solvents were evaporated using a rotary evaporator at 80 °C until the solution turned into a viscous tan-colored liquid. The liquid was collected and cooled to initiate crystallization. The crystals were washed with cold diethyl ether and purified by recrystallization from chlorobenzene, then stored under vacuum overnight. Proton NMR on a solution of the S- and R-phenylethylammonium bromide in deuterated chloroform confirmed the synthesis of the desired product (See Figure B.7).

2.4.2 Synthesis of Chiral NPs

Precursor solutions were prepared by dissolving lead bromide (0.04 mmol), methylammonium bromide (0.02 mmol), S- or R-PEA bromide (0.18 mmol) and octylamine (0.032 mmol) in 2 mL of anhydrous dimethylformamide. A small amount of precursor solution (20 μL) was dispersed into 10 mL of toluene while stirring on a vortex mixer. An immediate color change indicated the formation of perovskite nanoplatelets. The platelets were centrifuged into a pellet and then dissolved in toluene for further analysis.

2.4.3 Optical Spectroscopy

The spectral data were collected in a 1-cm quartz cuvette, which was pretreated with dimethyldichlorosilane in order to prevent adsorption of the perovskite onto the walls of the cuvette. Silanization solution I (5% dimethyldichlorosilane in heptane, Sigma-Aldrich) was placed in a cuvette for 20-30 minutes and then removed. The cuvette was dried in a fume hood overnight and then rinsed multiple times with toluene. This procedure was repeated periodically as needed.

Absorption spectroscopy was performed using a Model 8453 Agilent Spectrometer, and steady-state emission spectra were measured on a Horiba Jobin-Yvon Fluoromax 3 fluorescence spectrophotometer. Circular dichroism (CD) spectra were measured using an Olis DSM 17 CD spectrometer with an integration time of 3 s and a bandwidth of 1 nm. The optical density of the NP solution was approximately 1 a.u. and the spectra were background subtracted with a toluene blank.

2.4.4 X-Ray Photoelectron Spectroscopy

Samples were prepared for X-ray photoelectron spectroscopy (XPS) by drop casting the colloidal perovskite suspension onto a clean ITO substrate and letting it dry in a desiccator for 12 hours. XPS spectra were collected using an ESCALAB 250XI instrument at a base pressure of 10^{-9} mbar. Each spectrum was averaged over 20 scans to minimize noise and the binding energy was referenced to adventitious carbon (284.8 eV). The data were processed with a Shirley background and the peaks were fit using a Gaussian – Lorentzian shape. The Pb ($4f_{7/2}$ and $4f_{5/2}$) and Br ($3d_{5/2}$ and $3d_{3/2}$) doublet peaks were constrained according to their appropriate spin-orbit coupling intensity ratios.

2.4.5 Powder X-ray Diffraction

Powder X-ray diffraction patterns were collected using a Bruker X8 Prospector Ultra diffractometer equipped with an Apex II CCD detector and a Cu Kα X-ray source (λ = 1.54178 Å). Data analysis was conducted with the Apex II software package; EVA program from the Bruker Powder Analysis Software package was used for further processing. The perovskite NP sample was prepared through centrifugation of the colloidal sample to form a pellet. The pellet was then dried into a powder using a flow of argon gas and packed into a capillary tube for data acquisition.

2.4.6 Scanning and Tunneling Electron Microscopy

Scanning electron microscopy images were collected with a ZEISS Sigma 500 VP SEM with a secondary electron in-beam detector. The accelerating voltage was 1 kV and the working distance was 6.2 mm. Transmission electron microscopy images were collected using a Hitachi 9500 ETEM at 300 kV. The samples were prepared with ultrathin carbon film on a lacey carbon support film, 400 mesh copper grids. Elemental analysis was done using the QUANTAX ESPIRIT EDS package.

2.5 References

1. Tyagi, P.; Arveson, S. M.; Tisdale, W. A., Colloidal Organohalide Perovskite Nanoplatelets Exhibiting Quantum Confinement. *J. Phys. Chem. Lett.* **2015,** *6* (10), 1911-1916.

2. Weidman, M. C.; Seitz, M.; Stranks, S. D.; Tisdale, W. A., Highly Tunable Colloidal Perovskite Nanoplatelets through Variable Cation, Metal, and Halide Composition. *ACS Nano* **2016,** *10* (8), 7830-7839.

3. deQuilettes, D. W.; Koch, S.; Burke, S.; Paranji, R. K.; Shropshire, A. J.; Ziffer, M. E.; Ginger, D. S., Photoluminescence Lifetimes Exceeding 8 μs and Quantum Yields Exceeding 30% in Hybrid Perovskite Thin Films by Ligand Passivation. *ACS Energy Lett.* **2016,** *1* (2), 438-444.

4. Xing, G.; Mathews, N.; Sun, S.; Lim, S. S.; Lam, Y. M.; Grätzel, M.; Mhaisalkar, S.; Sum, T. C., Long-Range Balanced Electron- and Hole-Transport Lengths in Organic-Inorganic $CH_3NH_3PbI_3$. *Science* **2013,** *342* (6156), 344.

5. Dong, Q.; Fang, Y.; Shao, Y.; Mulligan, P.; Qiu, J.; Cao, L.; Huang, J., Electron-hole diffusion lengths >175 μm in solution-grown $CH_3NH_3PbI_3$ single crystals. *Science* **2015,** *347* (6225), 967-970.

6. Yang, S.; Fu, W.; Zhang, Z.; Chen, H.; Li, C.-Z., Recent advances in perovskite solar cells: efficiency, stability and lead-free perovskite. *J. Mater. Chem. A* **2017,** *5* (23), 11462-11482.

7. Palma, A. L.; Cinà, L.; Busby, Y.; Marsella, A.; Agresti, A.; Pescetelli, S.; Pireaux, J.-J.; Di Carlo, A., Mesoscopic Perovskite Light-Emitting Diodes. *ACS Appl. Mater. Interfaces* **2016,** *8* (40), 26989-26997.

8. Kim, Y.-H.; Wolf, C.; Kim, Y.-T.; Cho, H.; Kwon, W.; Do, S.; Sadhanala, A.; Park, C. G.; Rhee, S.-W.; Im, S. H.; Friend, R. H.; Lee, T.-W., Highly Efficient Light-Emitting Diodes of Colloidal Metal–Halide Perovskite Nanocrystals beyond Quantum Size. *ACS Nano* **2017,** *11* (7), 6586-6593.

9. Zhu, H.; Fu, Y.; Meng, F.; Wu, X.; Gong, Z.; Ding, Q.; Gustafsson, M. V.; Trinh, M. T.; Jin, S.; Zhu, X. Y., Lead halide perovskite nanowire lasers with low lasing thresholds and high quality factors. *Nat. Mater.* **2015,** *14* (6), 636-642.

10. Liu, P.; He, X.; Ren, J.; Liao, Q.; Yao, J.; Fu, H., Organic–Inorganic Hybrid Perovskite Nanowire Laser Arrays. *ACS Nano* **2017,** *11* (6), 5766-5773.

11. Yang Woon, S.; Park, B.-W.; Jung Eui, H.; Jeon Nam, J.; Kim Young, C.; Lee Dong, U.; Shin Seong, S.; Seo, J.; Kim Eun, K.; Noh Jun, H.; Seok Sang, I., Iodide management in formamidinium-lead-halide–based perovskite layers for efficient solar cells. *Science* **2017,** *356* (6345), 1376-1379.

12. Shin Seong, S.; Yeom Eun, J.; Yang Woon, S.; Hur, S.; Kim Min, G.; Im, J.; Seo, J.; Noh Jun, H.; Seok Sang, I., Colloidally prepared La-doped BaSnO3 electrodes for efficient, photostable perovskite solar cells. *Science* **2017,** *356* (6334), 167-171.

13. Bloom, B. P.; Graff, B. M.; Ghosh, S.; Beratan, D. N.; Waldeck, D. H., Chirality Control of Electron Transfer in Quantum Dot Assemblies. *J. Am. Chem. Soc.* **2017,** *139* (26), 9038-9043.

14. Bloom, B. P.; Kiran, V.; Varade, V.; Naaman, R.; Waldeck, D. H., Spin Selective Charge Transport through Cysteine Capped CdSe Quantum Dots. *Nano Lett.* **2016,** *16* (7), 4583-4589.

15. Michaeli, K.; Varade, V.; Naaman, R.; Waldeck, D. H., A new approach towards spintronics–spintronics with no magnets. *J. Phys. Condens. Matter* **2017,** *29* (10), 103002.

16. Ben Dor, O.; Yochelis, S.; Radko, A.; Vankayala, K.; Capua, E.; Capua, A.; Yang, S.-H.; Baczewski, L. T.; Parkin, S. S. P.; Naaman, R.; Paltiel, Y., Magnetization switching in ferromagnets by adsorbed chiral molecules without current or external magnetic field. *Nat. Commun.* **2017,** *8* (1), 14567.

17. Koplovitz, G.; Primc, D.; Ben Dor, O.; Yochelis, S.; Rotem, D.; Porath, D.; Paltiel, Y., Magnetic Nanoplatelet-Based Spin Memory Device Operating at Ambient Temperatures. *Adv. Mater.* **2017,** *29* (17), 1606748.

18. Naaman, R.; Waldeck, D. H., Chiral-Induced Spin Selectivity Effect. *J. Phys. Chem. Lett.* **2012,** *3* (16), 2178-2187.

19. Naaman, R.; Waldeck, D. H., Spintronics and Chirality: Spin Selectivity in Electron Transport Through Chiral Molecules. *Annu. Rev. Phys. Chem.* **2015,** *66* (1), 263-281.

20. Shah, E.; Soni, H. P., Inducing chirality on ZnS nanoparticles for asymmetric aldol condensation reactions. *RSC Advances* **2013,** *3* (38), 17453-17461.

21. Tohgha, U.; Deol, K. K.; Porter, A. G.; Bartko, S. G.; Choi, J. K.; Leonard, B. M.; Varga, K.; Kubelka, J.; Muller, G.; Balaz, M., Ligand Induced Circular Dichroism and Circularly Polarized Luminescence in CdSe Quantum Dots. *ACS Nano* **2013,** *7* (12), 11094-11102.

22. Niesner, D.; Wilhelm, M.; Levchuk, I.; Osvet, A.; Shrestha, S.; Batentschuk, M.; Brabec, C.; Fauster, T., Giant Rashba Splitting in $CH_3NH_3PbBr_3$ Organic-Inorganic Perovskite. *Phys. Rev. Lett.* **2016,** *117* (12), 126401.

23. Choi, J. K.; Haynie, B. E.; Tohgha, U.; Pap, L.; Elliott, K. W.; Leonard, B. M.; Dzyuba, S. V.; Varga, K.; Kubelka, J.; Balaz, M., Chirality Inversion of CdSe and CdS Quantum Dots without Changing the Stereochemistry of the Capping Ligand. *ACS Nano* **2016,** *10* (3), 3809-3815.

24. Goldsmith, M.-R.; George, C. B.; Zuber, G.; Naaman, R.; Waldeck, D. H.; Wipf, P.; Beratan, D. N., The chiroptical signature of achiral metal clusters induced by dissymmetric adsorbates. *PCCP* **2006,** *8* (1), 63-67.

25. Milton, F. P.; Govan, J.; Mukhina, M. V.; Gun'ko, Y. K., The chiral nano-world: chiroptically active quantum nanostructures. *Nanoscale Horiz.* **2016,** *1* (1), 14-26.

26. Ahn, J.; Lee, E.; Tan, J.; Yang, W.; Kim, B.; Moon, J., A new class of chiral semiconductors: chiral-organic-molecule-incorporating organic–inorganic hybrid perovskites. *Mater. Horizons* **2017,** *4* (5), 851-856.

27. He, T.; Li, J.; Li, X.; Ren, C.; Luo, Y.; Zhao, F.; Chen, R.; Lin, X.; Zhang, J., Spectroscopic studies of chiral perovskite nanocrystals. *Appl. Phys. Lett.* **2017,** *111* (15), 151102.

28. Dou, L.; Wong Andrew, B.; Yu, Y.; Lai, M.; Kornienko, N.; Eaton Samuel, W.; Fu, A.; Bischak Connor, G.; Ma, J.; Ding, T.; Ginsberg Naomi, S.; Wang, L.-W.; Alivisatos, A. P.; Yang, P., Atomically thin two-dimensional organic-inorganic hybrid perovskites. *Science* **2015,** *349* (6255), 1518-1521.

29. Sichert, J. A.; Tong, Y.; Mutz, N.; Vollmer, M.; Fischer, S.; Milowska, K. Z.; García Cortadella, R.; Nickel, B.; Cardenas-Daw, C.; Stolarczyk, J. K.; Urban, A. S.; Feldmann, J., Quantum Size Effect in Organometal Halide Perovskite Nanoplatelets. *Nano Lett.* **2015,** *15* (10), 6521-6527.

30. Huang, H.; Zhao, F.; Liu, L.; Zhang, F.; Wu, X.-g.; Shi, L.; Zou, B.; Pei, Q.; Zhong, H., Emulsion Synthesis of Size-Tunable $CH_3NH_3PbBr_3$ Quantum Dots: An Alternative

Route toward Efficient Light-Emitting Diodes. *ACS Appl. Mater. Interfaces* **2015,** *7* (51), 28128-28133.

31. Ito, S.; Mizuta, G.; Kanaya, S.; Kanda, H.; Nishina, T.; Nakashima, S.; Fujisawa, H.; Shimizu, M.; Haruyama, Y.; Nishino, H., Light stability tests of CH3NH3PbI3 perovskite solar cells using porous carbon counter electrodes. *PCCP* **2016,** *18* (39), 27102-27108.

32. Graf, N.; Yegen, E.; Gross, T.; Lippitz, A.; Weigel, W.; Krakert, S.; Terfort, A.; Unger, W. E. S., XPS and NEXAFS studies of aliphatic and aromatic amine species on functionalized surfaces. *Surf. Sci.* **2009,** *603* (18), 2849-2860.

33. Kim, T. G.; Seo, S. W.; Kwon, H.; Hahn, J.; Kim, J. W., Influence of halide precursor type and its composition on the electronic properties of vacuum deposited perovskite films. *PCCP* **2015,** *17* (37), 24342-24348.

34. Ng, T.-W.; Chan, C.-Y.; Lo, M.-F.; Guan, Z. Q.; Lee, C.-S., Formation chemistry of perovskites with mixed iodide/chloride content and the implications on charge transport properties. *J. Mater. Chem. A* **2015,** *3* (17), 9081-9085.

35. De Roo, J.; Ibáñez, M.; Geiregat, P.; Nedelcu, G.; Walravens, W.; Maes, J.; Martins, J. C.; Van Driessche, I.; Kovalenko, M. V.; Hens, Z., Highly Dynamic Ligand Binding and Light Absorption Coefficient of Cesium Lead Bromide Perovskite Nanocrystals. *ACS Nano* **2016,** *10* (2), 2071-2081.

36. Baikie, T.; Fang, Y.; Kadro, J. M.; Schreyer, M.; Wei, F.; Mhaisalkar, S. G.; Graetzel, M.; White, T. J., Synthesis and crystal chemistry of the hybrid perovskite (CH3NH3)PbI3 for solid-state sensitised solar cell applications. *J. Mater. Chem. A* **2013,** *1* (18), 5628-5641.

37. Milot, R. L.; Eperon, G. E.; Snaith, H. J.; Johnston, M. B.; Herz, L. M., Temperature-Dependent Charge-Carrier Dynamics in $CH_3NH_3PbI_3$ Perovskite Thin Films. *Adv. Funct. Mater.* **2015,** *25* (39), 6218-6227.

38. Kim, J. I.; Kim, J.; Lee, J.; Jung, D.-R.; Kim, H.; Choi, H.; Lee, S.; Byun, S.; Kang, S.; Park, B., Photoluminescence enhancement in CdS quantum dots by thermal annealing. *Nanoscale Res. Lett.* **2012,** *7* (1), 482.

39. Zhu, R.; Liu, H.; Shen, L.; Sun, D.; Li, X., Modifying CH3NH3PbBr3 nanocrystals with arylamines. *J. Phys. Chem. Solids* **2017,** *103*, 164-169.

3.0 Ligand Coverage and Exciton Delocalization Control Chiral Imprinting in Perovskite Nanoplatelets

Chiral perovskites have generated significant recent interest, yet little is known about how their chiro-optical properties arise. In this study, chiral methylammonium lead halide perovskite nanoplatelets (NPLs) with varied halide and ligand compositions are prepared using direct synthetic methods. Circular dichroism (CD) and ^{1}H-NMR studies find a non-linear relationship between the chiroptical properties and the ratio of chiral phenylethylammonium (PEA) to achiral octylamine (OA) ligands on the NPL surface. We use density functional theory (DFT) computations and a chiral imprinted particle-in-a-box model to rationalize the experimentally observed trend and find that the perovskite and the saturation point of the induced chirality depends on the size of the perovskite exciton relative to the size of the ligands. Temperature-dependent CD and ^{1}H-NMR studies, combined with DFT analysis, show that the CD intensity and sign both depend strongly on the structure and orientation of the ligands. This work reveals the complex nature of chiral imprinting in perovskite nanostructures and establishes a simple model for ligand-induced chiral imprinting to help guide the further development and understanding of chiral materials.

3.1 Introduction

Hybrid perovskite materials show tremendous promise for next generation opto-electronic and energy capture/conversion materials because of their color tunability,[1, 2] long carrier lifetimes and diffusion lengths,[3-6] and large electron/hole mobilities.[4, 7] These factors indicate a promising future for photovoltaic applications of perovskites, with a current efficiency record of 25.5% for a single-junction cell,[8] as well as for other applications including LEDs,[9, 10] lasing,[11-13] and sensing.[14, 15] Recently, chirality has been introduced into perovskite nanostructures,[16-26] further expanding their potential applications as circularly polarized emitters[23, 27, 28] and sensors.[19, 29] While methods for generating chiral perovskite have been reported,[16, 17, 21, 22, 24, 26, 30] little is known about the underlying mechanisms of chiral imprinting and the features which give rise to large g-factors. Control over the intensity of chiroptical features is essential, as CD intensity has been shown to be a good predictor of certain electronic properties of chiral materials.[31]

Chiral imprinting is defined as the transfer of chirality from a chiral adsorbate to an achiral partner, resulting in the emergence of chiroptical signals from the previously achiral object. Signatures of chiral imprinting on optical rotatory dispersion (ORD) and circular dichroism (CD) spectra have even appeared in studies of chiral species dissolved in achiral solvents. For example, chiral imprinting was predicted and found to induce ORD and CD originating from the solvent when (S)-methyloxirane was dissolved in benzene[32] and chiral imprinting was predicted for nanoparticles as well.[33] Indeed, the CD and ORD signatures of small molecules can change qualitatively as the chiral species self-assemble.[34] It was also shown that the ORD signals of chiral species in solution can change sign as a result of chiral imprinting by the solvent.[32, 35] Theoretical models have been used to assess the physical origins of chiral imprinting at nanoparticle surfaces, and computational tools enable dissection of the molecular origins for experimentally observed chiroptical signatures. [34-37]

Since the seminal work by Gun’ko and coworkers on the synthesis of chiral CdS nanoparticles in 2007,[38] considerable effort has focused on understanding the origins of chiroptical properties in semiconductor nanoparticles (NPs). One of three mechanisms is typically invoked: (i) intrinsically chiral materials may arise from a stereogenic unit or a chiral crystal structure (e.g., symmetry group of the crystal space group),[39, 40] (ii) ligands may induce chiral surface features[41, 42] derived from ligand-NPs interactions,[33, 43] and (iii) chiral supramolecular structures may be formed through self-assembly or within a chiral matrix.[44] The size, shape, composition, and ligand structure of a NP can contribute to the observed chiroptical signature.[45, 46] In most cases, the chiroptical features in a CD spectrum can be approximated by computing the derivative of a Gaussian line shape for each exciton transition of the nanoparticle's absorbance spectrum, and this characteristic CD spectrum is associated with the interaction between the NP electronic states and those of the ligand.[47, 48] These interactions were later framed within the context of a non-degenerate coupled oscillator model[45] and may explain many of the remarkable properties of chiral NPs. For example, NPs with the same ligand shell, but different crystal structures, show CD signals with the opposite signs,[48, 49] NPs coated with ligands of the same handedness and similar chemical structure showing inverted NP CD spectra,[42, 50] and asymmetric changes in CD intensities are produced as a function of ligand coverage.[51] As well as enhancing our understanding of chiral imprinting, extensive studies of chiral semiconductor NPs have created a foundation which motivates the exploration of new chiral nanomaterials, namely chiral perovskites.

Chiral molecules were first incorporated into hybrid organic-inorganic perovskites in 2006 by Billing and Lemmerer,[16] however, studies of the chiroptical properties of perovskites did not begin until 2017 with the studies of Ahn and co-workers.[17] Their work reported the synthesis of layered lead iodide perovskite thin films with chiral organic cations as spacers, which generated structural chirality within the perovskite crystal lattice and resulted in mirror image circular dichroism spectra from cations of opposite handedness.[17] Following these initial studies, other chiral imprinting methods for perovskite materials were reported, including the use of chiral ligands to synthesize materials with a non-centrosymmetric space group,[18-22] sol-gel techniques using chiral gelators,[23] and nanoparticle-ligand electronic interactions.[24-26] While recent studies suggest that a combination of structural and electronic interactions are responsible for the generation of chiroptical signatures,[52] identifying the mechanisms of chirality transfer in perovskite materials is an open challenge. Our study aims to further advance the understanding of how chiroptical properties for colloidal nanomaterials arise from surface passivation with chiral adsorbates.

In this study, imprinting of chirality onto the electronic states of methylammonium lead halide perovskite nanoplatelets (NPLs) is realized by encapsulating the NPLs with a mixed layer of achiral and chiral ammonium ligands. A nonlinear relationship was found between the fraction of chiral vs achiral ligands and the CD signal. That is, the intensity of the CD signal from the lowest energy exciton transition saturates as the fraction of chiral ligand grows. We use a charge perturbed particle-in-a-box model to describe the electronic chiral imprinting and to explain the observed saturation of the experimental CD intensity as a function of the chiral-to-achiral adsorbate ratio. Chiral ligands can imprint chirality onto nanomaterials through electrostatic or structural perturbation. In our analysis, we assume that the perovskite atomic positions are unperturbed by adsorption. In this approximation, the proposed mechanism for electronic imprinting depends on the size of the NPL exciton and the density of the chiral ligands, as well as their orientation on the NPL surface.

3.2 Results and Discussion

Methylammonium lead halide (X=Br or Cl) perovskite NPLs with a thickness of $n = 2$, where n is the number of lead halide layers in the structure, were synthesized using previously reported procedures.[24] The ligand shell comprises a mixture of achiral octylamine (OA) and chiral ligands, either S-/R-phenylethylammonium (S- or R-PEA), S/R-naphthylethylammonium (S- or R-NEA), or S/R-2-octylammonium (S- or R-OA). The structures are represented in Figure 3.1.

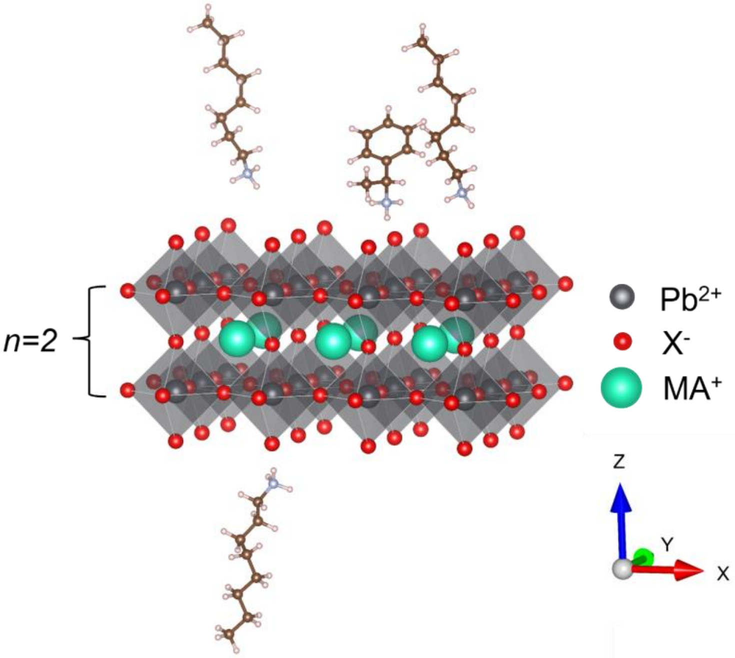

Figure 3.1 Schematic representation of the methylammonium lead halide perovskite NPLs structure with chiral S-PEA ligands and achiral OA ligands. X^- denotes Cl^- or Br^- anions, shown in red. The gray spheres denote the position of Pb^{2+} anions and methylammonium cations are shown as teal spheres. The lead halide octahedra are shown in gray.

The NPLs are ~1.2 nm thick (containing one full unit cell) and have lateral dimensions of 10's to 100's of nanometers, as found in earlier studies on bromide NPLs.[1] The NPL thickness is controlled by the concentration of OA ligands in the precursor mixture, and the thickness is monitored using UV-visible absorption spectroscopy. Strong quantum confinement of the exciton along the z-axis (see Figure 3.1) reveals the NPL thickness.[1]

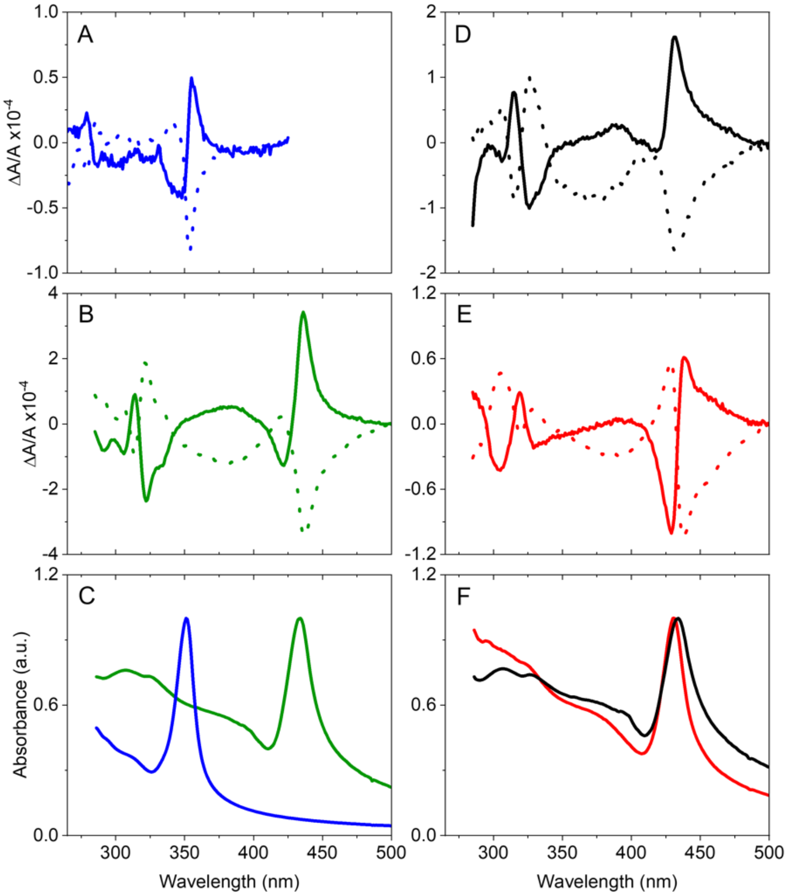

Figure 3.2 Optical properties of NPLs. Circular dichroism (A, B, D, E) and absorption (C, F) spectra for NPLs with different halide and ligand compositions. Panels A-C show circular dichroism (A, B) and absorbance (C) spectra of methylammonium lead chloride (blue) and bromide (green) NPLs coated with PEA ligands. Panels D-F show circular dichroism (D, E) and absorbance (F) spectra of methylammonium lead bromide NPLs capped with chiral OA (black) and NEA ligands (red). The solid lines in the circular dichroism spectra denote S- chirality and the dotted lines denote R- chirality. The spectra in panel A were collected on quartz slides to avoid solvent interference; all other spectra were collected in toluene solutions.

Figure 3.2 shows experimental absorption and CD spectra of hybrid organic-inorganic NPLs with the structure $CH_3NH_3Pb_2X_7$ (X=Cl, Br). Panels A (X=Cl) and B (X=Br) show CD spectra for NPLs with S- or R-PEA ligands. Figure 3.2C shows the corresponding absorbance spectra for the X=Cl and X=Br NPLs. Figure C.1 shows absorption and CD spectra for NPLs prepared with a mixture of chloride and bromide, which allows additional tunability of the chiro-optical features. The systematic shift of the exciton transition as a function of the relative amounts of the halides in the perovskite from 433 nm for bromide to 351 nm for chloride is consistent with the findings of previous studies[1] and demonstrates that this optical transition arises from the perovskite rather than from the ligand. The CD spectra for each of the different types of nanoplatelets indicate that the lowest energy transition exhibits a bisignate line shape (composed of positive and negative lobes centered at a particular energy). The CD transitions occur at the frequency of the lowest energy NPL electronic transition. Moreover, the signs of the CD transitions are determined by the enantiomeric form of the PEA used during synthesis, the CD transition change sign as the R- and S- adsorbates are interchanged.

DFT calculations of bulk $MAPbX_3$ shown in Figure C.2 indicate that the conduction band minimum (CBM) comprises mainly Pb *p* atomic orbitals and that the valence band maximum (VBM) comprises mainly Pb *s* and halide *p* orbitals, consistent with earlier studies.[53, 54] The perovskite electronic structure produces a direct bandgap and strong optical transitions.[53, 54] The energy separation between the two lowest-energy optical transitions in the absorbance spectra for Br NPLs (Figure 3.2C) is consistent with the computed absorption coefficients of the model perovskite NPL in vacuum (see Figure C.3). For the Br NPLs, our computed absorption coefficients show a lowest energy absorption at 534 nm, which is a longer wavelength than is measured for the NPLs. This difference may arise from solvent effects that are neglected, or from errors introduced by the DFT functional.

CD spectra simulated with a cluster model for a single R- or S- PEA adsorbate are shown in Figure C.4, and they exhibit CD spectra with mirror image symmetry and a bisignate line shape. This shape is characteristic of coupled chromophore CD transitions, as a single chromophore (i.e., the chiral ligand alone) does not show bisignate CD features.[55] A second feature is observed in the experimental CD spectra at a higher energy (~320 nm) and it has a weaker intensity than the 433 nm transition (Figure 3.2A,B). TD-DFT analysis finds that the oscillator strength of the first exciton transition is ~10 times larger than the higher-energy transition oscillator strength, and so the corresponding transition dipole moment is larger, while the magnitudes of magnetic dipole moments are similar for the first exciton transition and higher-energy transitions. Because the CD signal is proportional to the inner product of the electric and magnetic dipole transition moments, the high energy transitions which have smaller magnitudes of the electric transition dipole moments also have smaller CD rotational strengths.

Figures 3.2D-F show spectra for the $CH_3NH_3Pb_2Br_7$ NPLs in which the chiral component of the ligand shell is changed, namely, S- or R-OA (panel D) and S- or R-NEA (panel E) instead of the S- or R-PEA shown in panel (B). The absorption spectra in Panel 2F show similar lowest exciton energies for both ligands and indicate that the band gap of the NPL is not affected by the chiral ligand's structure. As with the PEA coated nanoplatelets, the lowest energy bisignate transitions for the bromide nanoplatelets occur at the same wavelength as their lowest energy exciton transitions (Figure 3.2F), 430 nm for OA and 432 nm for NEA. While the energy of the bisignate features do not change substantially with ligand type, the areas of the chiral exciton's two bisignate features change with the ligand; R- and S-OA produce bisignate lobes that differ the most in area, and the R- and S- NEA ligands produce the most similar areas of the two lobes. The change in CD lineshape can be correlated with ligand properties, including i) steric bulk, (which may influence the ligand packing on the nanoplatelet surface), ii) ligand polarizability, and iii) the low-energy electronic transition of the ligand, which may influence the electronic coupling between the nanoplatelet and the ligand.

Temperature-dependent CD and ^{1}H-NMR studies were performed on the chiral perovskite NPLs to determine how the dissociation of chiral ligands from the NPL influences the chiral imprinting. Figure 3.3A-C show CD and ^{1}H-NMR spectra, collected for the same chiral NPL samples, at temperatures ranging from 20 to 80°C. Significant changes in the CD spectra for X = Br NPLs arise upon heating. The CD intensity at 20°C is 10 times larger than at 80°C, and the sign of the exciton's bisignate peak flips at 50°C; this inversion persists up to 80 °C. Upon cooling the sample back to 20°C, the CD intensity and bisignate shapes return nearly to those found initially. Similar behavior, including the change in intensity and sign inversion, was also observed for X = Cl NPLs (Figure C.5). Previous studies examining temperature-dependent CD signals for chiral perovskites did not report a sign inversion, however these studies were performed within a smaller temperature range, and in the presence of excess ligand in the solution, which can significantly affect the ligand coverage on the NPL.[24]

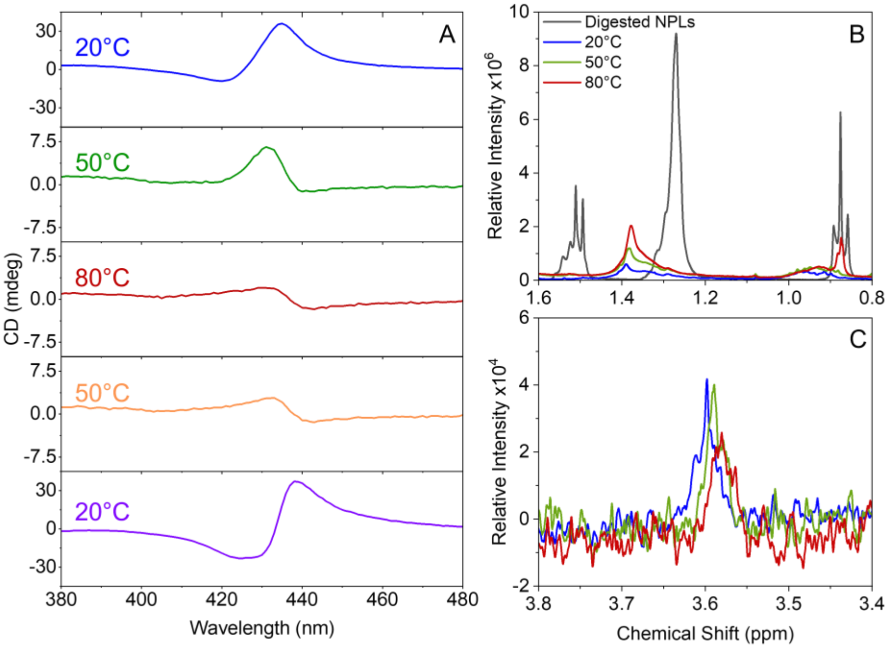

Figure 3.3 Temperature dependence on ligand coverage and CD spectra. Panel A shows CD spectra at the first exciton transition as a function of temperature. The plots from top to bottom show the process of heating a sample of S-PEA-NPLs to 80°C and then cooling it back down to 20°C. Panel (B) and (C) show ^{1}H-NMR peaks associated with OA and S-PEA ligands, respectively, from a NPL sample dissolved in toluene-d8 at 20 (blue) 50 (green) and 80°C (red). A ^{1}H-NMR spectrum of digested S-PEA-NPLs in DMSO-d6 is shown in black in panel B.

To explore the temperature-induced changes in the NPL ligand shell, variable temperature ^{1}H-NMR experiments were conducted in deuterated toluene (Figure 3.3B, C). The NPLs are intact in these studies, and most of the ligands (OA and PEA) are expected to remain anchored to the NPL surface.[56, 57] As such, the proton signals arising from the ligands manifest in the spectra as weak and broadened peaks (blue, green, and red traces). For comparison, spectra of NPLs digested in DMSO-d_6 (black), in which the NPL structure is destroyed and the ligands are free in solution exhibit sharp, narrow peaks. Figure 3B shows NMR resonances attributed to OA protons, namely those on the terminal -CH_3 group observed at 0.9 ppm and the 14 protons on the alkyl chain at 1.4

ppm. As the temperature increases, the peak intensities grow for both OA resonances, suggesting that OA ligands detach from the NPL surface upon heating. This structural hypothesis is further supported by the appearance of a new peak at 0.9 ppm with sharp features at 80°C. This new feature corresponds to a similar feature that is found in the digested NPL samples. In contrast, PEA proton resonances that arise from the protons adjacent to the ammonium group (see Figure 3.3B) are relatively unchanged with temperature. Thus, we postulate that the diminished CD signal strength and sign inversion at higher temperatures arises from orientational changes of the PEA ligands rather than from any significant detachment of PEA species from the surface.

The temperature dependent NMR data suggest that the NPL ligand shell is less dense at elevated temperatures, caused by a shift in the equilibrium between free and NPL-anchored OA molecules. Although the absorptivity of the samples does not change significantly, the CD spectra show considerable weakening in their strength at elevated temperatures (see Figure C.6). The difference in temperature-dependent behavior between the achiral and chiral ligands suggests that OA desorbs from the surface upon heating, whereas PEA remains anchored, which is consistent with the charge difference at their binding moieties. Earlier theoretical studies indicated that cationic organic ammonium adsorbates, such as PEA, form ionic bonds to the perovskite surface with a binding energy of ~1 eV,[56, 57] while OA binds only half as strongly at 0.5 eV.[58] The strong binding affinity of the PEA cations, as compared to OA molecules, suggests that PEA ligands are less likely to detach from the surface at elevated temperatures. The decrease in neighboring adsorbed molecules may allow the PEA ligands to take on geometries where the aromatic ring becomes more nearly cofacial with respect to the NPL surface. Indeed, temperature-dependent reorientation of nanoparticle ligand shells is reported in the literature, and it is understood to strongly influence a material's optical properties.[59, 60]

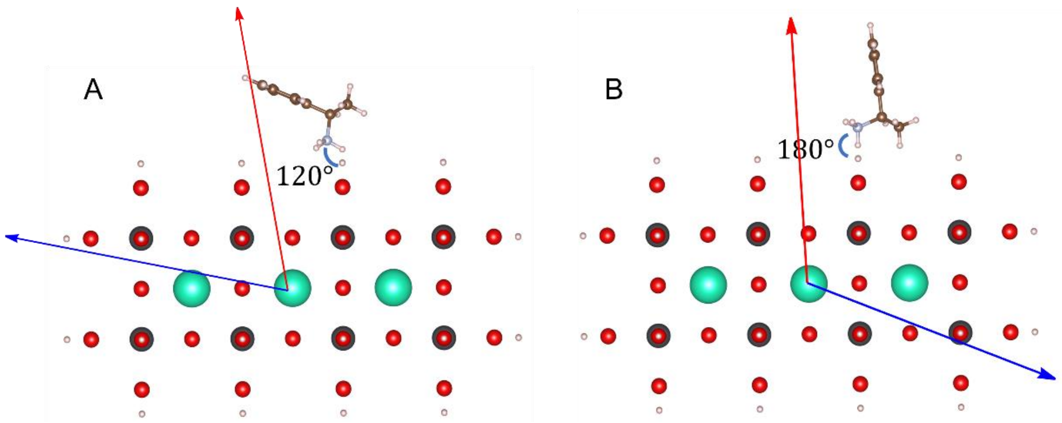

Figure 3.4 Ligand orientation effect on CD signatures. Panel A and B show unit vectors of electric transition dipole moments (red) and magnetic transition dipole moments (blue) for a $CsPbBr_3$ cluster with one R-PEA ligand at the band edge transition. Side view of the $CsPbBr_3$ cluster, angle between H-Br and H-N is 120° (A) and 180°(B).

TD-DFT calculations were performed to explore how ligand reorientation may give rise to an inversion of the CD response. The effect of phenyl ring geometry on the CD response of the chiral NPL system was modeled by varying the angles between a perovskite cluster and a chiral PEA ligand. Ligands with a 120° orientation yielded a computed rotatory strength of - $10x10^{-40}$ cgs, while a 180° orientation gave $+11.8x10^{-40}$ cgs, suggesting that ligand orientation can influence not only the strength of the chiro-optical transition, but its sign as well. Figures 3.4A and 3.4B illustrate how the rotatory strength can invert with different chiral ligand orientations, i.e., the transition electric dipole and transition magnetic dipole moments rotate, causing their dot products have opposite signs. Thus, the imprinted CD signal of the perovskite is strongly sensitive to the orientation of chiral ligands on the surface. These computational findings are consistent with the observed experimental behavior of the NPLs, further suggesting that changes in ligand orientation, triggered by differences in the ligand shell composition, may result in sign inversions of the CD signal.

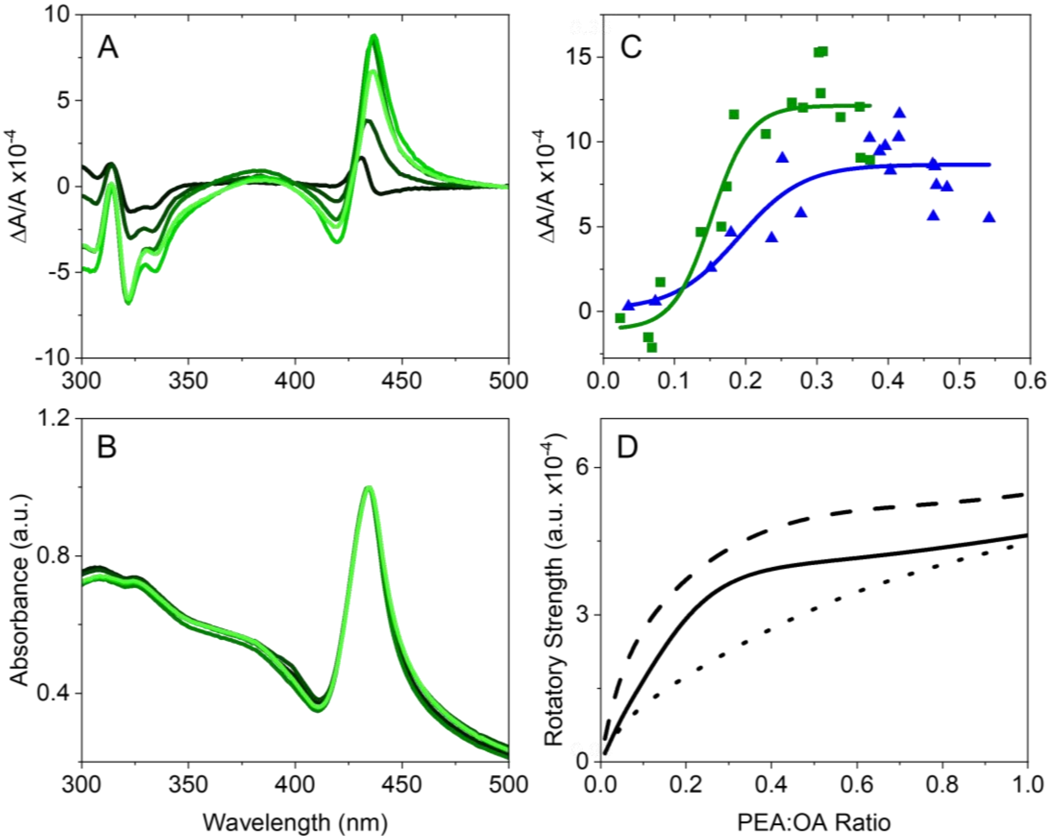

Figure 3.5 Coverage dependence of chiroptical properties. Panel A shows CD spectra and panel B shows absorbance spectra for toluene solutions of X=Br NPLs synthesized with S-PEA:OA ratios between 0.05 (dark green) and 0.35 (light green). Panel C shows the CD at the first exciton transition as a function of PEA:OA ligand ratio for X=Br (green) and X=Cl (blue) NPLs fit by a Boltzmann function to guide the eye. Panel D shows computational results for the dependence of rotatory strength on the PEA:OA ratio and exciton edge length (dot - 1.8 nm, dash - 2.4 nm, and solid - 3.0 nm).

The dependence of NPL chiroptical properties on the surface concentration of chiral ligands was studied by synthesizing NPLs with varied S-PEA:OA ratios, ranging from 1:1 to 7:1, then collecting CD and ^{1}H-NMR spectra for each sample. The CD intensity was determined by subtracting the trough value (bisignate minimum) from the peak value (bisignate maximum) at the exciton; these values are reported in the unitless quantity ΔA/A (see Figure 3.5A). To determine the PEA:OA ligand ratio on the surface of the perovskites, the NPLs were purified to remove excess ligand, then digested in DMSO-d_6 and studied via proton NMR. Representative data and peak assignments are shown in Figure C.7. The surface ligand ratios were calculated using equation 1,

$$Molar\ ratio = \frac{\left[\frac{I_{PEA}}{nH_{PEA}}\right]}{\left[\frac{I_{OA}}{nH_{OA}}\right]} \qquad \textbf{Equation 3.1}$$

where I_{PEA} and I_{OA} are the integrated peak areas of the PEA and OA resonances, and nH_{PEA} and nH_{OA} are the number of protons associated with each peak. Representative CD and normalized absorbance spectra of S-PEA-capped X=Br NPL samples synthesized with different PEA:OA ratios are shown in Figures 3.5A and 3.5B. Ratios of PEA:OA as measured by ^{1}H-NMR are indicated with a color map; low ratios (as low as 0.05 PEA:OA) are shown in dark green, and high ratios (up to 0.35 PEA:OA) in light green. The upper limit for the PEA:OA ratios was chosen to prevent changes in the NPL thickness distribution triggered by large amounts of PEA, which manifest as a red-shift of the exciton and absorbance peak broadening (see Figure C.8); the X=Cl NPLs show a greater tolerance for high chiral ligand concentrations, allowing for larger amounts of PEA to be used in the synthesis before changes in the sample composition are observed. The NPLs' linear absorption properties remain constant within the selected PEA:OA range, based on their normalized absorbance spectra (Figure 3.5B). The CD intensity (Figure 5A) increases with an increase in PEA:OA ratio, except for a slight observed decrease for samples with ratios approaching 0.35. Samples with the lowest accessible PEA:OA ratios (Figure 3.5A, dark green) can exhibit a CD signal inversion at the exciton energy, with the bisignate trough appearing at higher wavelengths than the peak. CD inversion was not found for X=Cl NPLs in the accessible PEA:OA range.

CD intensities are shown as a function of molar ratio data for X=Br and X=Cl NPLs in Figure 3.5C. Both the chloride and bromide NPLs show a similar relationship between CD intensity and PEA:OA ratio, with three distinct regions: small slope. (0-0.1 PEA:OA), large slope (0.1-0.25 PEA:OA for Br and 0.1-0.3 PEA:OA for Cl), and a plateau region (above 0.3). These data indicate that the strength of chiral imprinting manifesting in the CD intensity, while proportional to the PEA:OA ratio, is not directly proportional to the fraction of chiral ligands in the shell. That is, a linear dependence of the CD intensity on the ratio of chiral ligands is not observed. A non-linear relationship between chiral ligand concentration and CD intensity was previously reported for cysteine-capped CdSe/CdS QDs and attributed to a change in the cysteine binding motif at different ligand concentrations.[51] Unlike cysteine, PEA has only one moiety available to bind to the NPL surface; thus, we posit that the non-linear nature of the CD-PEA:OA relationship arises from the averaging of the CD signal that is produced from NPLs with different PEA configurations.

A chirally imprinted particle-in-a-box model[33] was used to probe the spectroscopic signatures of chiral imprinting on nanoparticles from a theoretical perspective (see details in Appendix C). Here, we calculated the dependence of rotatory strengths on the PEA:OA ratio using a similar model, and the results are plotted in Figure 3.5D for three different exciton sizes which are approximated by the number of unit cells over which the excitons can delocalize. Specifically, grid sizes of 3 x 3, 4 x 4, and 5 x 5 unit cells (corresponding to 1.8, 2.4, and 3.0 nm lengths) in the x, y plane of the NPL are considered. The experimentally measured exciton size varies from 2 to 7.1 nm,[61, 62] which are somewhat larger than the exciton sizes considered in these simulations. The absolute value of the rotatory strength for the 1.8 nm exciton, see dotted line of Figure 5D, increases rapidly for small PEA:OA ratios; the rotatory strength is 1x10^{-4} atomic units (a.u.) when PEA:OA = 0.1. At higher PEA:OA ratios, the rotatory strength increases steadily and reaches 4.5x10^{-4} a.u. for PEA:OA = 1. The 4 x 4 and 5 x 5 cases show a similar shape as a function of PEA:OA ratio. For the 4 x 4 exciton (2.4 nm, dashed line), the rotatory strength variation has a large slope at low PEA:OA ratios and then reaches a plateau when PEA:OA > 0.4. The maximum rotatory strength of the 4 x 4 exciton is 5.4x10^{-4} a.u. at PEA:OA = 1. The rotatory strength of the 5 x 5 (3.0 nm, solid line) exciton increases more slowly than the 4 x 4 exciton at low PEA:OA ratios. As the PEA:OA ratio increases, the rotatory strength reaches a plateau with a rotatory strength of 4.6x10^{-4} a.u. The slope of the rotatory strength vs. PEA:OA plot decreases for all three exciton sizes, with the two larger exciton sizes showing the largest slope decrease (Figure C.9). The rotatory strength reaches a plateau at ratios greater than 0.5 for the 2.4 and 3.0 nm excitons.

While a difference in the position of the plateau region of rotatory strength is observed in Figure 3.5D, all three exciton sizes produce similar computed rotatory strength magnitudes, suggesting that the size of the exciton does not dictate the magnitude of the rotatory strength of the chiral imprint. Larger excitons can be perturbed by more PEA at fixed PEA:OA ratios, but the exciton wavefunction is more delocalized. Therefore, the magnitude of the rotatory strength is similar for the three exciton sizes. The two larger excitons (2.4 nm and 3 nm) show a clear saturation of rotatory strength as the PEA:OA ratio approaches 1, while that for the 1.8 nm exciton is less clear. When the exciton size is small (i.e., comparable to the size of the chiral ligand), the asymmetric charges associated with the stereogenic center are similar in size to the wavefunction of the confined exciton. The induced rotatory strengths are large (compared to that from a large size exciton) and are strongly dependent on the placement of chiral ligand asymmetric charges.

Therefore, the rotatory strengths produced by placing chiral ligands symmetrically with respect to the exciton wavefunction inversion center, cannot be canceled. In contrast, for large excitons, the induced rotatory strengths are relatively weak and less dependent on the chiral ligand position with respective the exciton wavefunction inversion center. Therefore, the asymmetric environment created by ligand placement is more likely to be averaged out as the size of the stereogenic center of chiral ligand is small compared to the spatial extend of the wave function, and the rotatory strength quickly reaches a plateau at the high PEA:OA ratio, which is consistent with the computed rotatory strength for large exciton sizes (2.4 and 3 nm).

3.3 Summary

Chirally imprinted perovskite nanoplatelets were synthesized with different halide and ligand compositions. The effect of the ligand shell's composition on the chiroptical signatures were investigated using experimental and theoretical methods. We establish a relationship between the CD spectra and the surface ligand's orientation, as well as on the density of the chiral ligands on the NPL. A nonlinear dependence was found between the fraction of the chiral ligands and the measured CD intensity, suggesting that chiral imprinting saturates at high chiral ligand concentrations. Computational studies indicate that the point of saturation is determined by averaging of ligand configurations on the NPL surface and the CD intensity is dictated by the perovskite exciton's spatial extent in the NPL plane, as the number of possible ligand binding orientations increases with exciton size. This study advances our understanding of chiral imprinting in perovskite nanostructures and establishes a model to describe ligand-induced chirality that can be applied to other ligand-capped NPL and NP systems. An expanded understanding of the underlying mechanisms for chiral imprinting should contribute to the continued development of novel chiral nanomaterials and their applications.

3.4 References

1. Weidman, M. C.; Seitz, M.; Stranks, S. D.; Tisdale, W. A., Highly Tunable Colloidal Perovskite Nanoplatelets through Variable Cation, Metal, and Halide Composition. *ACS Nano* **2016,** *10* (8), 7830-7839.

2. Tyagi, P.; Arveson, S. M.; Tisdale, W. A., Colloidal Organohalide Perovskite Nanoplatelets Exhibiting Quantum Confinement. *J. Phys. Chem. Lett.* **2015,** *6* (10), 1911-1916.

3. deQuilettes, D. W.; Koch, S.; Burke, S.; Paranji, R. K.; Shropshire, A. J.; Ziffer, M. E.; Ginger, D. S., Photoluminescence Lifetimes Exceeding 8 μs and Quantum Yields Exceeding 30% in Hybrid Perovskite Thin Films by Ligand Passivation. *ACS Energ. Lett.* **2016,** *1* (2), 438-444.

4. Dong, Q.; Fang, Y.; Shao, Y.; Mulligan, P.; Qiu, J.; Cao, L.; Huang, J., Electron-hole diffusion lengths >175 μm in solution-grown $CH_3NH_3PbI_3$ single crystals. *Science* **2015,** *347* (6225), 967-970.

5. Stranks, S. D.; Eperon, G. E.; Grancini, G.; Menelaou, C.; Alcocer, M. J. P.; Leijtens, T.; Herz, L. M.; Petrozza, A.; Snaith, H. J., Electron-Hole Diffusion Lengths Exceeding 1 Micrometer in an Organometal Trihalide Perovskite Absorber. *Science* **2013,** *342* (6156), 341.

6. Xing, G.; Mathews, N.; Sun, S.; Lim, S. S.; Lam, Y. M.; Grätzel, M.; Mhaisalkar, S.; Sum, T. C., Long-Range Balanced Electron- and Hole-Transport Lengths in Organic-Inorganic $CH_3NH_3PbI_3$. *Science* **2013,** *342* (6156), 344.

7. Yang, S.; Fu, W.; Zhang, Z.; Chen, H.; Li, C.-Z., Recent advances in perovskite solar cells: efficiency, stability and lead-free perovskite. *J. Mater. Chem. A* **2017,** *5* (23), 11462-11482.

8. NREL.gov, Best Research-Cell Efficiency Chart. https://www.nrel.gov/pv/cell-efficiency.html, 2022.

9. Ochsenbein, S. T.; Krieg, F.; Shynkarenko, Y.; Rainò, G.; Kovalenko, M. V., Engineering Color-Stable Blue Light-Emitting Diodes with Lead Halide Perovskite Nanocrystals. *ACS Appl. Mater. Interfaces* **2019,** *11* (24), 21655-21660.

10. Lin, K.; Xing, J.; Quan, L. N.; de Arquer, F. P. G.; Gong, X.; Lu, J.; Xie, L.; Zhao, W.; Zhang, D.; Yan, C.; Li, W.; Liu, X.; Lu, Y.; Kirman, J.; Sargent, E. H.; Xiong, Q.; Wei, Z., Perovskite light-emitting diodes with external quantum efficiency exceeding 20 per cent. *Nature* **2018,** *562* (7726), 245-248.

11. Zhou, H.; Yuan, S.; Wang, X.; Xu, T.; Wang, X.; Li, H.; Zheng, W.; Fan, P.; Li, Y.; Sun, L.; Pan, A., Vapor Growth and Tunable Lasing of Band Gap Engineered Cesium Lead Halide Perovskite Micro/Nanorods with Triangular Cross Section. *ACS Nano* **2017,** *11* (2), 1189-1195.

12. Shi, Z.-F.; Sun, X.-G.; Wu, D.; Xu, T.-T.; Tian, Y.-T.; Zhang, Y.-T.; Li, X.-J.; Du, G.-T., Near-infrared random lasing realized in a perovskite CH3NH3PbI3 thin film. *J. Mater. Chem. C* **2016,** *4* (36), 8373-8379.

13. Tang, B.; Dong, H.; Sun, L.; Zheng, W.; Wang, Q.; Sun, F.; Jiang, X.; Pan, A.; Zhang, L., Single-Mode Lasers Based on Cesium Lead Halide Perovskite Submicron Spheres. *ACS Nano* **2017,** *11* (11), 10681-10688.

14. George K, J.; Halali, V. V.; C. G, S.; Suvina, V.; Sakar, M.; Balakrishna, R. G., Perovskite nanomaterials as optical and electrochemical sensors. *Inorg. Chem. Front.* **2020,** *7* (14), 2702-2725.

15. Ai, B.; Fan, Z.; Wong, Z. J., Plasmonic–perovskite solar cells, light emitters, and sensors. *Microsyst. Nanoeng.* **2022,** *8* (1), 5.

16. Billing, D. G.; Lemmerer, A., Synthesis and crystal structures of inorganic–organic hybrids incorporating an aromatic amine with a chiral functional group. *Cryst. Eng. Comm.* **2006,** *8* (9), 686-695.

17. Ahn, J.; Lee, E.; Tan, J.; Yang, W.; Kim, B.; Moon, J., A new class of chiral semiconductors: chiral-organic-molecule-incorporating organic–inorganic hybrid perovskites. *Mater. Horiz.* **2017,** *4* (5), 851-856.

18. Peng, Y.; Yao, Y.; Li, L.; Liu, X.; Zhang, X.; Wu, Z.; Wang, S.; Ji, C.; Zhang, W.; Luo, J., Exploration of Chiral Organic–Inorganic Hybrid Semiconducting Lead Halides. *Chem. Asian J.* **2019,** *14* (13), 2273-2277.

19. Chen, C.; Gao, L.; Gao, W.; Ge, C.; Du, X.; Li, Z.; Yang, Y.; Niu, G.; Tang, J., Circularly polarized light detection using chiral hybrid perovskite. *Nat. Commun.* **2019,** *10* (1), 1927.

20. Peng, Y.; Yao, Y.; Li, L.; Wu, Z.; Wang, S.; Luo, J., White-light emission in a chiral one-dimensional organic–inorganic hybrid perovskite. *J. Mater. Chem. C* **2018,** *6* (22), 6033-6037.

21. Yuan, C.; Li, X.; Semin, S.; Feng, Y.; Rasing, T.; Xu, J., Chiral Lead Halide Perovskite Nanowires for Second-Order Nonlinear Optics. *Nano Lett.* **2018,** *18* (9), 5411-5417.

22. Ma, J.; Fang, C.; Chen, C.; Jin, L.; Wang, J.; Wang, S.; Tang, J.; Li, D., Chiral 2D Perovskites with a High Degree of Circularly Polarized Photoluminescence. *ACS Nano* **2019,** *13* (3), 3659-3665.

23. Shi, Y.; Duan, P.; Huo, S.; Li, Y.; Liu, M., Endowing Perovskite Nanocrystals with Circularly Polarized Luminescence. *Adv. Mater.* **2018,** *30* (12), 1705011.

24. Georgieva, Z. N.; Bloom, B. P.; Ghosh, S.; Waldeck, D. H., Imprinting Chirality onto the Electronic States of Colloidal Perovskite Nanoplatelets. *Adv. Mater.* **2018,** *30* (23), 1800097.

25. Long, G.; Jiang, C.; Sabatini, R.; Yang, Z.; Wei, M.; Quan, L. N.; Liang, Q.; Rasmita, A.; Askerka, M.; Walters, G.; Gong, X.; Xing, J.; Wen, X.; Quintero-Bermudez, R.; Yuan, H.; Xing, G.; Wang, X. R.; Song, D.; Voznyy, O.; Zhang, M.; Hoogland, S.; Gao, W.; Xiong, Q.; Sargent, E. H., Spin control in reduced-dimensional chiral perovskites. *Nat. Photonics* **2018,** *12* (9), 528-533.

26. Chen, W.; Zhang, S.; Zhou, M.; Zhao, T.; Qin, X.; Liu, X.; Liu, M.; Duan, P., Two-Photon Absorption-Based Upconverted Circularly Polarized Luminescence Generated in Chiral Perovskite Nanocrystals. *J. Phys. Chem. Lett.* **2019,** *10* (12), 3290-3295.

27. Kim, Y.-H.; Zhai, Y.; Gaulding, E. A.; Habisreutinger, S. N.; Moot, T.; Rosales, B. A.; Lu, H.; Hazarika, A.; Brunecky, R.; Wheeler, L. M.; Berry, J. J.; Beard, M. C.; Luther, J. M., Strategies to Achieve High Circularly Polarized Luminescence from Colloidal Organic–Inorganic Hybrid Perovskite Nanocrystals. *ACS Nano* **2020,** *14* (7), 8816-8825.

28. Seo, I. C.; Lim, Y.; An, S.-C.; Woo, B. H.; Kim, S.; Son, J. G.; Yoo, S.; Park, Q. H.; Kim, J. Y.; Jun, Y. C., Circularly Polarized Emission from Organic–Inorganic Hybrid Perovskites via Chiral Fano Resonances. *ACS Nano* **2021,** *15* (8), 13781-13793.

29. Zhao, Y.; Li, X.; Feng, J.; Zhao, J.; Guo, Y.; Yuan, M.; Chen, G.; Gao, H.; Jiang, L.; Wu, Y., Chiral 1D perovskite microwire arrays for circularly polarized light detection. *Giant* **2022,** *9*, 100086.

30. Debnath, G. H.; Georgieva, Z. N.; Bloom, B. P.; Tan, S.; Waldeck, D. H., Using post-synthetic ligand modification to imprint chirality onto the electronic states of cesium lead bromide (CsPbBr3) perovskite nanoparticles. *Nanoscale* **2021,** *13* (36), 15248-15256.

31. Bloom, B. P.; Graff, B. M.; Ghosh, S.; Beratan, D. N.; Waldeck, D. H., Chirality Control of Electron Transfer in Quantum Dot Assemblies. *J. Am. Chem. Soc.* **2017,** *139* (26), 9038-9043.

32. Mukhopadhyay, P.; Zuber, G.; Wipf, P.; Beratan, D. N., Contribution of a Solute's Chiral Solvent Imprint to Optical Rotation. *Angew. Chem. Int. Ed.* **2007,** *46* (34), 6450-6452.

33. Goldsmith, M.-R.; George, C. B.; Zuber, G.; Naaman, R.; Waldeck, D. H.; Wipf, P.; Beratan, D. N., The chiroptical signature of achiral metal clusters induced by dissymmetric adsorbates. *PCCP* **2006,** *8* (1), 63-67.

34. Goldsmith, M.-R.; Jayasuriya, N.; Beratan, D. N.; Wipf, P., Optical Rotation of Noncovalent Aggregates. *J. Am. Chem. Soc.* **2003,** *125* (51), 15696-15697.

35. Mukhopadhyay, P.; Wipf, P.; Beratan, D. N., Optical Signatures of Molecular Dissymmetry: Combining Theory with Experiments To Address Stereochemical Puzzles. *Acc. Chem. Res.* **2009,** *42* (6), 809-819.

36. de Wergifosse, M.; Grimme, S., A Unified Strategy for the Chemically Intuitive Interpretation of Molecular Optical Response Properties. *J. Chem. Theory Comput.* **2020,** *16* (12), 7709-7720.

37. Kondru Rama, K.; Wipf, P.; Beratan David, N., Atomic Contributions to the Optical Rotation Angle as a Quantitative Probe of Molecular Chirality. *Science* **1998,** *282* (5397), 2247-2250.

38. Moloney, M. P.; Gun'ko, Y. K.; Kelly, J. M., Chiral highly luminescent CdS quantum dots. *Chem. Commun.* **2007,** (38), 3900-3902.

39. Mukhina, M. V.; Maslov, V. G.; Baranov, A. V.; Fedorov, A. V.; Orlova, A. O.; Purcell-Milton, F.; Govan, J.; Gun'ko, Y. K., Intrinsic Chirality of CdSe/ZnS Quantum Dots and Quantum Rods. *Nano Lett.* **2015,** *15* (5), 2844-2851.

40. Nakashima, T.; Kobayashi, Y.; Kawai, T., Optical Activity and Chiral Memory of Thiol-Capped CdTe Nanocrystals. *J. Am. Chem. Soc.* **2009,** *131* (30), 10342-10343.

41. Elliott, S. D.; Moloney, M. P.; Gun'ko, Y. K., Chiral Shells and Achiral Cores in CdS Quantum Dots. *Nano Lett.* **2008,** *8* (8), 2452-2457.

42. Choi, J. K.; Haynie, B. E.; Tohgha, U.; Pap, L.; Elliott, K. W.; Leonard, B. M.; Dzyuba, S. V.; Varga, K.; Kubelka, J.; Balaz, M., Chirality Inversion of CdSe and CdS Quantum Dots without Changing the Stereochemistry of the Capping Ligand. *ACS Nano* **2016,** *10* (3), 3809-3815.

43. Zhou, R.; Wei, K.-Y.; Zhao, J.-S.; Jiang, Y.-B., Alternative chiral thiols for preparation of chiral CdS quantum dots covered immediately by achiral thiols. *Chem. Commun.* **2011,** *47* (22), 6362-6364.

44. Zhou, Y.; Marson, R. L.; van Anders, G.; Zhu, J.; Ma, G.; Ercius, P.; Sun, K.; Yeom, B.; Glotzer, S. C.; Kotov, N. A., Biomimetic Hierarchical Assembly of Helical Supraparticles from Chiral Nanoparticles. *ACS Nano* **2016,** *10* (3), 3248-3256.

45. Gao, X.; Zhang, X.; Deng, K.; Han, B.; Zhao, L.; Wu, M.; Shi, L.; Lv, J.; Tang, Z., Excitonic Circular Dichroism of Chiral Quantum Rods. *J. Am. Chem. Soc.* **2017,** *139* (25), 8734-8739.

46. Kuznetsova, V.; Gromova, Y.; Martinez-Carmona, M.; Purcell-Milton, F.; Ushakova, E.; Cherevkov, S.; Maslov, V.; Gun'ko, Y. K., Ligand-induced chirality and optical

activity in semiconductor nanocrystals: theory and applications. *Nanophotonics* **2021,** *10* (2), 797-824.

47. Ben-Moshe, A.; Teitelboim, A.; Oron, D.; Markovich, G., Probing the Interaction of Quantum Dots with Chiral Capping Molecules Using Circular Dichroism Spectroscopy. *Nano Lett.* **2016,** *16* (12), 7467-7473.

48. Tohgha, U.; Deol, K. K.; Porter, A. G.; Bartko, S. G.; Choi, J. K.; Leonard, B. M.; Varga, K.; Kubelka, J.; Muller, G.; Balaz, M., Ligand Induced Circular Dichroism and Circularly Polarized Luminescence in CdSe Quantum Dots. *ACS Nano* **2013,** *7* (12), 11094-11102.

49. Gao, X.; Zhang, X.; Zhao, L.; Huang, P.; Han, B.; Lv, J.; Qiu, X.; Wei, S.-H.; Tang, Z., Distinct Excitonic Circular Dichroism between Wurtzite and Zincblende CdSe Nanoplatelets. *Nano Lett.* **2018,** *18* (11), 6665-6671.

50. Varga, K.; Tannir, S.; Haynie, B. E.; Leonard, B. M.; Dzyuba, S. V.; Kubelka, J.; Balaz, M., CdSe Quantum Dots Functionalized with Chiral, Thiol-Free Carboxylic Acids: Unraveling Structural Requirements for Ligand-Induced Chirality. *ACS Nano* **2017,** *11* (10), 9846-9853.

51. Kuznetsova, V. A.; Mates-Torres, E.; Prochukhan, N.; Marcastel, M.; Purcell-Milton, F.; O’Brien, J.; Visheratina, A. K.; Martinez-Carmona, M.; Gromova, Y.; Garcia-Melchor, M.; Gun’ko, Y. K., Effect of Chiral Ligand Concentration and Binding Mode on Chiroptical Activity of CdSe/CdS Quantum Dots. *ACS Nano* **2019,** *13* (11), 13560-13572.

52. Yan, L.; Jana, M. K.; Sercel, P. C.; Mitzi, D. B.; You, W., Alkyl–Aryl Cation Mixing in Chiral 2D Perovskites. *J. Am. Chem. Soc.* **2021,** *143* (43), 18114-18120.

53. Ompong, D.; Inkoom, G.; Singh, J., Effective mass of heavy, light, and spin split-off band electron and hole g-factor in cubic perovskite materials. *J. Appl. Phys.* **2020,** *128* (23), 235109.

54. Tan, M.; Wang, S.; Rao, F.; Yang, S.; Wang, F., Pressures Tuning the Band Gap of Organic–Inorganic Trihalide Perovskites ($MAPbBr_3$): A First-Principles Study. *J. Electron. Mater.* **2018,** *47* (12), 7204-7211.

55. Rodger, A., Norden, B., *Circular Dichroism and Linear Dichroism*. Oxford University Press: New York, 1997.

56. Hassan, Y.; Park, J. H.; Crawford, M. L.; Sadhanala, A.; Lee, J.; Sadighian, J. C.; Mosconi, E.; Shivanna, R.; Radicchi, E.; Jeong, M.; Yang, C.; Choi, H.; Park, S. H.; Song, M. H.; De Angelis, F.; Wong, C. Y.; Friend, R. H.; Lee, B. R.; Snaith, H. J., Ligand-engineered bandgap stability in mixed-halide perovskite LEDs. *Nature* **2021,** *591* (7848), 72-77.

57. Stelmakh, A.; Aebli, M.; Baumketner, A.; Kovalenko, M. V., On the Mechanism of Alkylammonium Ligands Binding to the Surface of $CsPbBr_3$ Nanocrystals. *Chem. Mater.* **2021,** *33* (15), 5962-5973.

58. Quarta, D.; Imran, M.; Capodilupo, A.-L.; Petralanda, U.; van Beek, B.; De Angelis, F.; Manna, L.; Infante, I.; De Trizio, L.; Giansante, C., Stable Ligand Coordination at the Surface of Colloidal CsPbBr3 Nanocrystals. *J. Phys. Chem. Lett.* **2019,** *10* (13), 3715-3726.

59. Balan, A. D.; Olshansky, J. H.; Horowitz, Y.; Han, H.-L.; O'Brien, E. A.; Tang, L.; Somorjai, G. A.; Alivisatos, A. P., Unsaturated Ligands Seed an Order to Disorder Transition in Mixed Ligand Shells of CdSe/CdS Quantum Dots. *ACS Nano* **2019,** *13* (12), 13784-13796.

60. Widmer-Cooper, A.; Geissler, P. L., Ligand-Mediated Interactions between Nanoscale Surfaces Depend Sensitively and Nonlinearly on Temperature, Facet Dimensions, and Ligand Coverage. *ACS Nano* **2016,** *10* (2), 1877-1887.

61. Baranowski, M.; Galkowski, K.; Surrente, A.; Urban, J.; Kłopotowski, Ł.; Maćkowski, S.; Maude, D. K.; Ben Aich, R.; Boujdaria, K.; Chamarro, M.; Testelin, C.; Nayak, P. K.; Dollmann, M.; Snaith, H. J.; Nicholas, R. J.; Plochocka, P., Giant Fine Structure Splitting of the Bright Exciton in a Bulk MAPbBr3 Single Crystal. *Nano Lett.* **2019,** *19* (10), 7054-7061.

62. Droseros, N.; Longo, G.; Brauer, J. C.; Sessolo, M.; Bolink, H. J.; Banerji, N., Origin of the Enhanced Photoluminescence Quantum Yield in MAPbBr3 Perovskite with Reduced Crystal Size. *ACS Energy Lett.* **2018,** *3* (6), 1458-1466.

4.0 Using Post-Synthetic Ligand Modification to Imprint Chirality onto the Electronic States of Cesium Lead Bromide ($CsPbBr_3$) Perovskite Nanoparticles

This work was published as Debnath G. H., Georgieva, Z. N.; Bloom, B. P.; Tan, S.; Waldeck, D. H., Using Post-Synthetic Ligand Modification to Imprint Chirality onto the Electronic States of Cesium Lead Bromide. Nanoscale 2021, 13, 15248. The author of the thesis contributed to synthesis, experimental design, NMR studies, and participated in the writing of the manuscript.

This study presents a post-synthetic ligand modification strategy for the generation of chiroptically active, blue emitting $CsPbBr_3$ nanoparticles (NPs); an expansion to the library of 3D chiral perovskite nanomaterials. Addition of [R- and S-] 1-phenylethylamine, 1-(1-naphthyl)ethylamine, or 2-aminooctane to the synthesized $CsPbBr_3$ NPs is shown to induce Cotton effects in the NP first exciton transition, suggestive of a successful electronic coupling between the chiral ligands and the NPs. The availability of these chiral $CsPbBr_3$ NPs thrusts them into the forefront of perovskite nanomaterials for examining the implications of the chiral induced spin selectivity (CISS) effect and other applications in spintronics.

4.1 Introduction

Synthetic strategies to generate metal halide perovskite semiconductor nanomaterials have grown exponentially over the past six years,[1] largely driven by their promising optoelectronic properties which include emission tunability over the entire visible spectral region (through modulation in halide composition and quantum confinement effects);[2, 3] high defect tolerance;[4] near unity fluorescence quantum yields (in cases);[5] low exciton binding energy, and high charge carrier mobility.[6] These properties have brought them to the forefront of applications in lasers,[7] light emitting diodes (LEDs),[8, 9] and photovoltaics, among others.[10] Of particular interest here are the recent developments in chiral perovskites and their general implications for the chiral induced spin selectivity (CISS) effect[11-15] which have led to demonstrations of spin polarized charge transport,[16-18] spin dependent photovoltaic and photogalvanic responses in optoelectronic devices,[19] and as sources for generating circularly polarized light.[20] In 2006 Billing and coworkers[21] introduced the possibility of incorporating chiral molecules in 1D or 2D hybrid organic-inorganic perovskites but it was not until 2017 when reports on the synthesis of chiroptically active hybrid organic-inorganic 2D metal halide perovskite thin films, pioneered by Moon and coworkers,[22] became available. The chiroptical activity was proposed to stem from chiral crystalline structures arising from twisted perovskite unit cells.[22] In 2018 we reported the synthesis of colloidal methylammonium lead bromide nanoplatelets[23] (NPLs) that exhibit both quantum confinement effects and chiroptical activity. The origin of the chiroptical activity was attributed to the electronic coupling of the chiral ligand shell and the NPLs. In comparison to the significant number of reports on chiral films and nanoplatelets, reports on 3D chiral perovskite nanomaterials are much less common. Duan and coworkers[24] reported the direct synthesis of chiral α-octylamine modified cesium lead bromide ($CsPbBr_3$) nanoparticles (NPs) that display circular dichroism and circularly polarized luminescence; they attributed the chiro-optical properties to asymmetric distortions of the surface perovskite lattice induced by the chiral α-octylamine. A number of recent reviews are available and provide a more comprehensive introduction to the development and applications of chiral perovskites.[25-28]

An alternate strategy to the commonly deployed direct synthetic route for synthesizing chiral perovskites is post-synthetic modification of achiral perovskite NPs. The first report on such post-synthetic ligand exchange discussed the generation R and S-1,2-diaminocyclohexane (DACH) capped $CsPb(I/Br)_3$ NPs from their achiral counterparts;[29] however, the chiroptical response was centered around the ligand-perovskite charge transfer band with no signatures evident near the perovskite excitonic absorption maximum. Later, Liu and coworkers[30] co-assembled achiral cesium lead halide ($CsPbX_3$, X = Cl, Br, I) NPs with chiral lipid gelators to demonstrate circularly polarized luminescence from $CsPbX_3$ NPs. A report by Luther and coworkers[31] discusses the role of mixed achiral (oleylamine) and chiral (R-2-octylamine) ligands during synthesis followed by a post-synthetic ligand treatment by R/S-methylbenzyl ammonium bromide to produce circularly polarized luminescence from formamidium lead bromide ($FAPbBr_3$) NPs. Scheme 1 shows a post-synthetic ligand modification strategy that leads to the generation of chiral $CsPbBr_3$ NPs, starting from their achiral counterparts. This work demonstrates (i) a synthetic procedure to generate ultra-small, strongly quantum confined $CsPbBr_3$ NPs and (ii) a room temperature post-synthetic ligand modification strategy that imprints chirality onto the electronic states of $CsPbBr_3$ NPs and generates robust CD signatures centered on the NP excitonic transition - using chiral ligands like R- and S-1-phenylethylamine (R- and S-PEA), R- and S-2-aminooctane (R- and S-OcAm) and R- and S-1-(1-naphthyl)ethylamine (R- and S-NEA).

The CD signal intensity (in mdeg) and dissymmetry factors (in $\Delta A/A$) reported in this study is among the highest when compared to the available literature on chiral perovskite NPs synthesized via ligand exchange.[29-31] While the ligand exchange strategy presented here follows the spirit of those used for typical II-VI semiconductors nanomaterials,[32] the intrinsically labile perovskite framework and the dynamic surface ligand composition present a different set of synthetic challenges for obtaining chiral $CsPbBr_3$ NPs that can sustain their chiroptical responses over time. Additionally, the post-synthetic approach is unique in that it allows one to monitor the chiral imprinting on the perovskite NPs before and after ligand addition, without having to account for the unwanted introduction of synthetic heterogeneity[33] which can play a role in modulating chiroptical responses[34]. Also, as shown in Scheme 1 unique chiral perovskite NPs can be generated from a large batch of achiral NPs by simply changing the identity of the chiral ligand during ligand exchange without having to depend on individual separate syntheses, thereby saving time and effort; a challenge one faces when using a direct synthetic strategy to generate chiral perovskite NPs with different ligand identity.

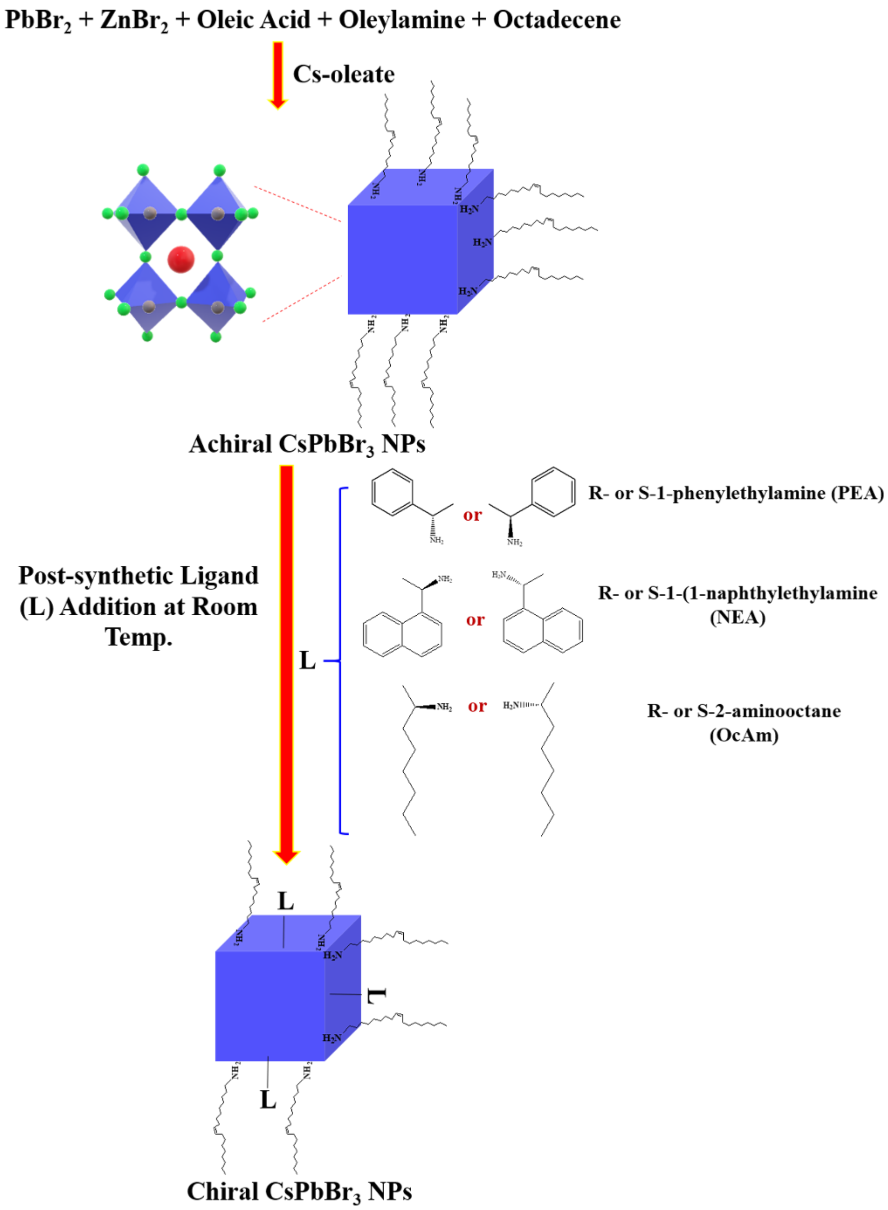

Figure 4.1 Representation of the room temperature post-synthetic ligand modification leading to the generation of chiral $CsPbBr_3$ NPs from their achiral counterparts is shown.

4.2 Results and Discussion

$CsPbBr_3$ NPs were synthesized using previously published methods with modifications; see experimental section for details. Figure 1a shows the UV-visible absorption spectrum, and Figure 1b shows the emission spectrum of the synthesized $CsPbBr_3$ NPs (blue solid line) with absorption and emission maxima at 428 nm and 434 nm, respectively. Note that the currently available reports of blue emitting $CsPbBr_3$ nanomaterials in the literature emit significantly to the red of 434 nm, in the 450-465 nm.[35-37] The high degree of quantum confinement for the NPs, and subsequent blue shift of the emission, reported here was achieved by having excess [Br^-] during the synthesis; a technique known to induce size focusing of $CsPbBr_3$ NPs (see experimental section for more details). Additional confirmation of this observation comes from electron microscopy studies (*vide infra*). A larger quantum confinement is believed also to provide larger electronic coupling between chiral ligands and the confined carriers' wavefunctions as reported by Markovich and coworkers for the size dependent chiroptical activity in chiral CdSe and CdS quantum dots.[38] The post-synthetic addition of R-PEA (black dashed line) and S-PEA (red solid line) to the $CsPbBr_3$ NPs modestly shifts the absorption (430 nm) and emission (436 nm) maxima to lower energies accompanied by the attenuation of higher excitonic transitions; see Figure 4.1. These observations, along with a gradual red shift in the absorption maximum of $CsPbBr_3$ NPs as a function R- and S-PEA concentration is shown in Figure E.1 and its implications on the NP dimension is discussed later. The inherent defect tolerance of the perovskites[39] prevents any significant emission line broadening, which contrasts with the defect mediated broad emission bands that are often encountered while synthesizing chiral cadmium chalcogenide NPs.[40] The relative quantum yield of the $CsPbBr_3$ and R-/S-PEA-$CsPbBr_3$ NPs are 45% and 42% respectively; similar to reports by others for $CsPbBr_3$ NPs.[41] The lowering in the quantum yield for the R- and

S-PEA-$CsPbBr_3$ NPs can be correlated to the reorganization of surface capping ligands and the introduction of associated non-radiative decay channels.[42] The changes in the average lifetime <τ> from 5.85 ± 0.23 ns for the $CsPbBr_3$ NPs[41] to 3.0 ± 0.3 ns for the R-/S-PEA-$CsPbBr_3$ NPs further support this explanation (See Figure E.2 and Table E.1).

The retention of the emission line shape and the quantum yield of the R- and S-PEA-$CsPbBr_3$ NPs is an important outcome because a stable emission signature for chiral perovskite NPs is a prerequisite to gauge their efficiency as circularly polarized luminophores.[24, 30] The spectroscopic and chiroptical properties of chiral 3D confined perovskite QDs and 2D NPLs have undergone significant evaluation.[25, 43] When compared to the chiral perovskite QDs, the design criteria of chiral NPLs must be studied further to overcome their stability issues. For example, a recent report by Tisdale and coworkers on n = 2 MAPbBr NPLs (absorption maximum = 434 nm; emission maximum = 437 nm; quantum yields = 3.5% to 6.8%), discusses their propensity to undergo degradation and further transformation into n = 3 or n = 4 structures on exposure to UV light.[43] This is reflected by a significant decrease in the intensity and broadening of their emission spectra (with emergence of new peaks centered at 455 and 474 nm).[44] A fundamental understanding of the efficiency of chiral imprinting/CD signatures in these assemblies of perovskite nanomaterials will require the establishment of detailed understanding of the effect of ligand identity[45], crystal structure,[34] and ligand concentration[46, 47] on the chiral imprinting for perovskite QDs and NPL building blocks.

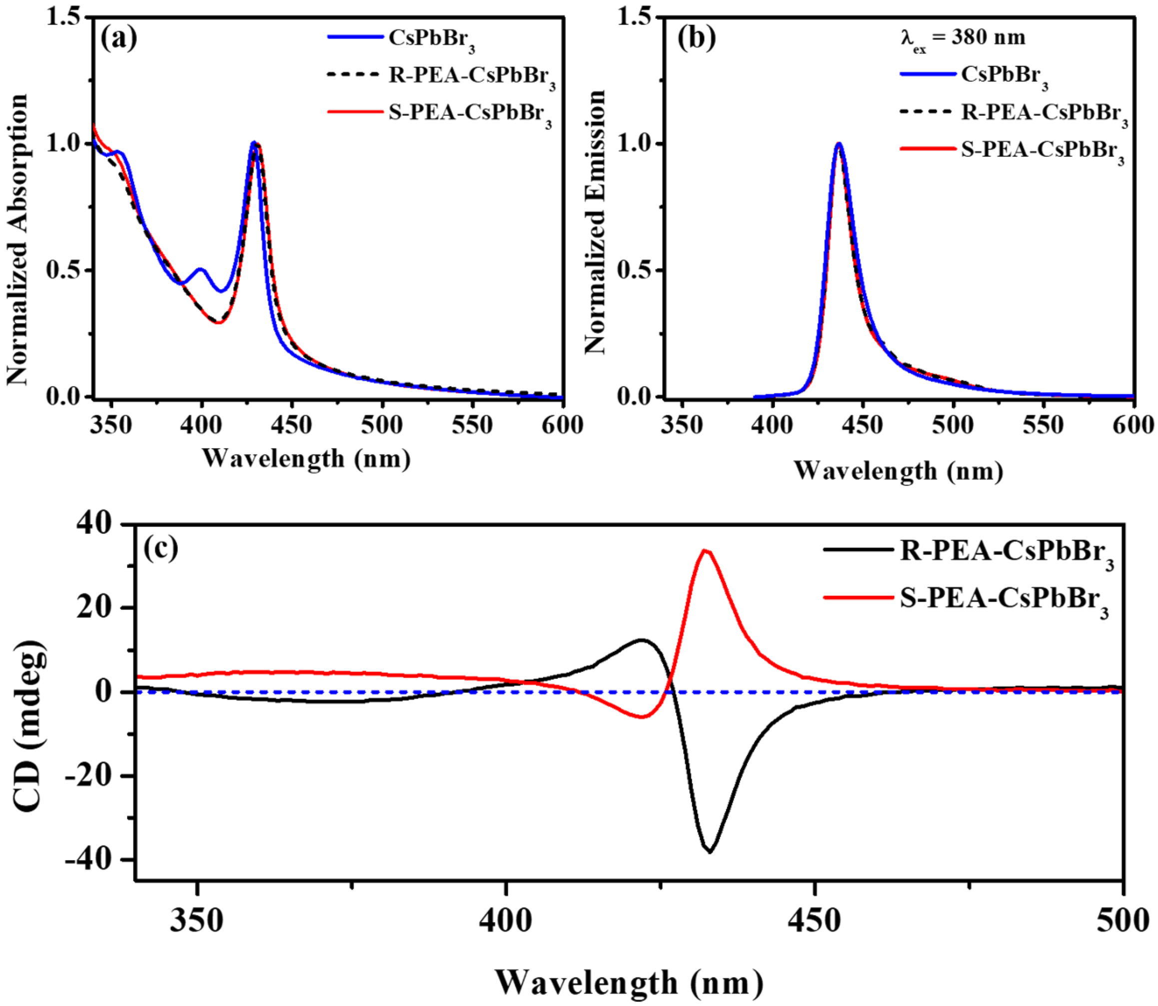

Figure 4.2 (a) Normalized absorption, (b) emission and (c) circular dichroism spectra of the $CsPbBr_3$, R- and S-PEA-$CsPbBr_3$ NPs in toluene are shown. The PEA concentration in the NP dispersion was maintained at 10mM for spectra in panels a-b and at 20 mM for panel c.

Circular dichroism (CD) spectra of the R-(black) and S-PEA-$CsPbBr_3$ NPs (red) in Figure 4.2c show mirror image profiles with R-PEA-$CsPbBr_3$ NPs displaying positive to negative Cotton effects and S-PEA-$CsPbBr_3$ NPs negative to positive Cotton effects near the absorption maximum, with increasing wavelength. The R- and S-PEA ligands, not on the surface of the NPs, display CD signals at wavelengths below 280 nm (see Figure E.3). The strong overlap between the R- and S-PEA-$CsPbBr_3$ NP first excitonic transition with the bisignate CD spectral features (circa 400-460 nm) demonstrates the successful chiral imprinting of the R- and S-PEA onto the $CsPbBr_3$ NP electronic structure.[23]

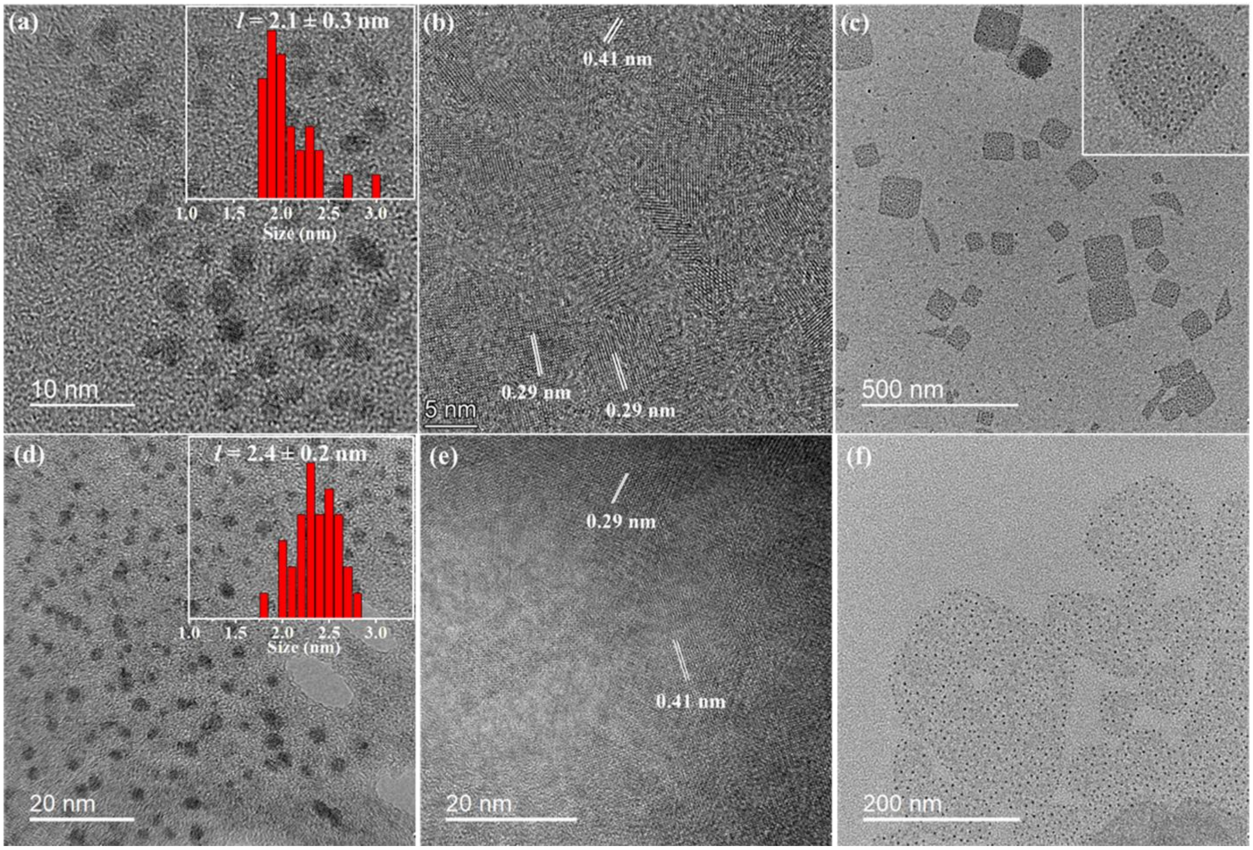

Figure 4.3 (a-c) TEM images of $CsPbBr_3$ NPs and their size distribution along with high resolution (HR) images and superstructured assemblies are shown. TEM, size distribution, HRTEM and superstructured images of PEA-$CsPbBr_3$ NPs are shown in panels (d-f, [PEA] = 10 mM in NP dispersion).

The transmission electron microscopy (TEM) images of the $CsPbBr_3$ NPs are shown in Figure 4.3 (a-c). The $CsPbBr_3$ NPs have quasi-cubic shapes with an average particle size of 2.1 ± 0.3 nm (panel a). This narrow particle size distribution is attributed to size focusing during synthesis; which was realized by maintaining a Br/Pb precursor ratio of ~20:1 and a growth time of three minutes at 85 °C (for details see experimental section). The lowest accessible $CsPbBr_3$ NP dimension reported (using an excess [Br^-]) stands at 3.7 nm with an excitonic absorption maximum centered around 455-460 nm.[48] Note that the absence of excess [Br^-] at the mentioned synthetic conditions is known to produce non-emissive Cs_4PbBr_6 NPs.[48]

The high resolution TEM image (Figure 4.3b) of the $CsPbBr_3$ NPs shows lattice spacings of 0.29 and 0.41 nm which is consistent with the (220) and (020) planes of the orthorhombic $CsPbBr_3$.[49] Additional confirmation of this claim manifests in the powder XRD patterns of the $CsPbBr_3$ NPs (see Figure E.4) with distinct peaks at $2\theta = 13.2^o$, 15.2^o, 21.6^o, 30.7^o and 34.5^o corresponding to the (101), (110), (020), (220) and (130) planes of orthorhombic $CsPbBr_3$ crystal structure (PDF: 01-072-7929).[41, 49] The $CsPbBr_3$ NPs can also assemble into cube-like superstructures with domains spanning tens to hundreds of nanometers in length, see Figure 4.3c and is consistent with reports by Son and coworkers.[48]

The red shift in the first excitonic transition of $CsPbBr_3$ NPs upon ligand modification to R- and S-PEA-$CsPbBr_3$ NPs (see Figures 4.2 and E.1) coincides with an increase in NP size. The TEM images indicate that the average size of the NPs increase from 2.1 ± 0.3 nm for the achiral $CsPbBr_3$ (Figure 4.3 a-c) to 2.4 ± 0.2 nm (Figure 4.3 d-f) with 10 mM PEA in the NP dispersion. The increase in NP size as a function of PEA concentration likely arises during the PEA induced restructuring of the oleylamine/oleic acid ligand shell. The subsequent destabilization of the ligand shell in the $CsPbBr_3$ NPs and the intrinsically labile perovskite framework allows the ~ 2 nm NPs to coalesce and is argued to attenuate the higher excitonic absorption transitions (see Figure 1). Changes in capping ligand concentration and solvent polarity have been shown to greatly affect the $CsPbX_3$ NP morphology leading to a wide gamut of shapes in the form of large cubes, wires, and rods through the oriented attachment of initially formed cubic seeds.[36] The identical d-spacings of 0.29 and 0.41 nm for the PEA-$CsPbBr_3$ NPs along with their assembly into superstructures, much like the achiral $CsPbBr_3$ NPs, indicate the retention of the orthorhombic crystal phases.

X-ray photoelectron spectroscopy was used to further compare the $CsPbBr_3$ and R-PEA-$CsPbBr_3$ NPs. Figure E.5 shows that the Cs 3d, Pb 4f, and Br 3d spectra do not change upon ligand modification and are in agreement with other reported values.[50, 51] Differences arise in the N1s and C1s spectra however.

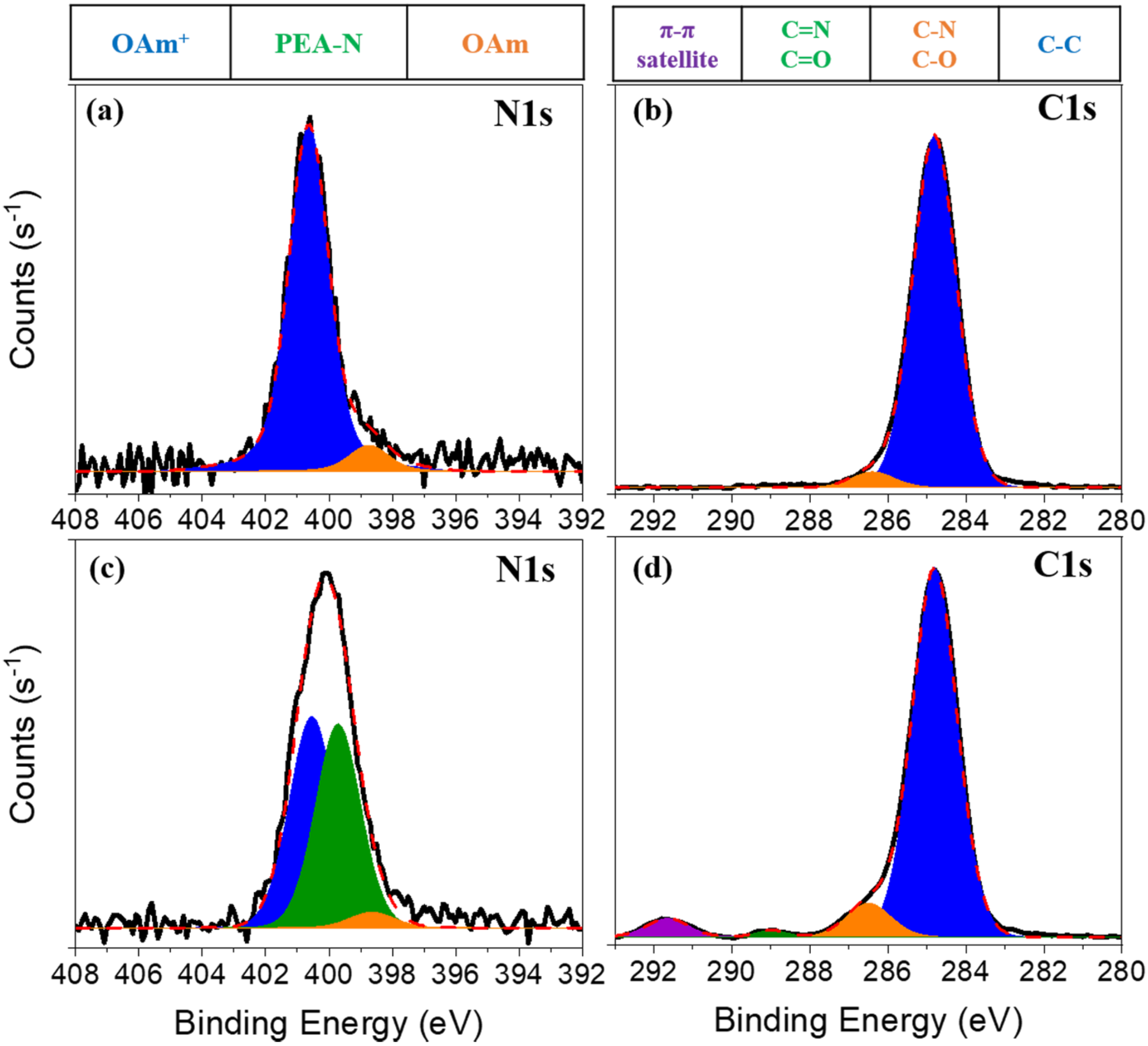

Figure 4.4 N1s and C1s X-ray photoelectron spectra of the $CsPbBr_3$ NPs (a,b) along with those of the R-PEA-$CsPbBr_3$ NPs (c, d) are shown.

The N1s spectrum (black) for the $CsPbBr_3$ NPs (Figure 4.4a) is fit to a sum of two peaks centered at 398.7 eV (orange) and 400.6 eV (blue) and correspond to oleylammonium (OAm^+) and oleylamine (OAm) respectively.[52] The full-width-at-half-maximum (FWHM) of the envelope marked by a red dashed line was found to be 1.7 eV. In contrast, the envelope for the N1s spectrum for the R-PEA-$CsPbBr_3$ NPs (Figure 4.4c) shows a distinct broadening with an increase in FWHM to 2.2 eV. The spectrum was fit to a sum of three peaks at 398.7 eV (orange), 399.8 eV (green) and 400.6 eV (blue) and the emergence of the new peak at 399.8 eV is attributed to contributions from the nitrogen on the PEA ligand.

The C1s spectrum (black) for the $CsPbBr_3$ NPs (Figure 4.4b) is fit to a sum of two peaks at 286.4 eV (blue) and 284.8 eV (orange) which originate from the C–C and C–N/C–O components of OAm/OA respectively.[53] The C1s spectrum of the R-PEA-$CsPbBr_3$ NPs (Figure 4.4d) shows two additional peaks, barring the C–C and C–N/C–O components, at 289 eV (green) and 291.7 eV (purple) and they are attributed to C=N/C=O and π–π satellite components[53] of the PEAs, respectively. These observations further corroborate the presence of the PEA ligands without detrimental changes to the integrity of the $CsPbBr_3$ NPs. Additional XPS spectra of the R-NEA-$CsPbBr_3$ NPs and R-OcAm-$CsPbBr_3$ NPs are shown in Fig E.6-7 and exhibit a similar behavior to that described for the PEAs.

To further confirm the presence of the chiral ligands on the surface of the NPs ^1H NMR spectroscopy was performed on purified $CsPbBr_3$, R- and S-PEA-$CsPbBr_3$ NPs; see Figures S8 and S9. Because ligand binding to the NP surface is known to induce signal broadening and attenuation, dissolution of the $CsPbBr_3$ NPs in DMSO-d6 was performed.[54] NMR spectral analysis of the solutions generated from the $CsPbBr_3$ dissolution showed resonances [assignment] corresponding to CH_3[6], CH_2 [3], H_2C–HC= [4 and 5 respectively], NH_2 [α], α-CH_2 [1 for oleic acid, β for oleylamine], β-CH_2 [2]. These resonances overlap with the ^1H NMR of oleic acid (OA, pink) and oleylamine (OAm, red) and confirm the presence of the ligands in the $CsPbBr_3$ NPs; in agreement with the literature reports.[55, 56] For the R-PEA-$CsPbBr_3$ in DMSO-d6 (blue), additional phenyl [Z], methylene [Y], and methyl [X] resonances are present and further validate that the ligand shell comprises both PEA and OA/OAm.[23, 31] Proof of principle experiments illustrating the attenuation of bound ligands is shown in Figure E.10 where NMR spectra of the purified R-PEA-$CsPbBr_3$ NPs in toluene-d8 show attenuated Z, Y, and X resonances, compared to the dissolution of the same material in DMSO-d6. The weak signal intensity of the PEA resonances in toluene-d8 indicates that the ^1H NMR in the DMSO-d6 solution does not arise from the unbound/unpurified ligands. Additional NMR spectra R- and S-NEA-$CsPbBr_3$ NPs and their corresponding ligands are presented in Figure E.11. These experiments further illustrate the success of the ligand modification strategy.

The progression of the CD response in R- and S-PEA-$CsPbBr_3$ NPs as a function of ligand concentration is presented in Figure 4.5 (a, b, d). The spectra are presented as $\Delta A/A$, the difference in absorptivity normalized to the absorbance at 430 nm.[23] The general trend is similar for both R- and S-PEA and they show a gradual increase in $\Delta A/A$ as a function of PEA concentration that is used in the ligand modification. We anticipate a saturation in the available ligand binding sites on the NP surface to dictate the observed trend. The increase in $\Delta A/A$ is accompanied by a gradual red shift in the CD minima (maxima) for the R-PEA-$CsPbBr_3$ (S-PEA-$CsPbBr_3$) NPs and results from an increase in the NP size as evident by the TEM results. A similar observation has been noted by Gun'ko and coworkers on D-/L-cysteine (Cys) capped CdSe/CdS NPs, which shows the evolution of CD intensity with Cys concentration.[47]

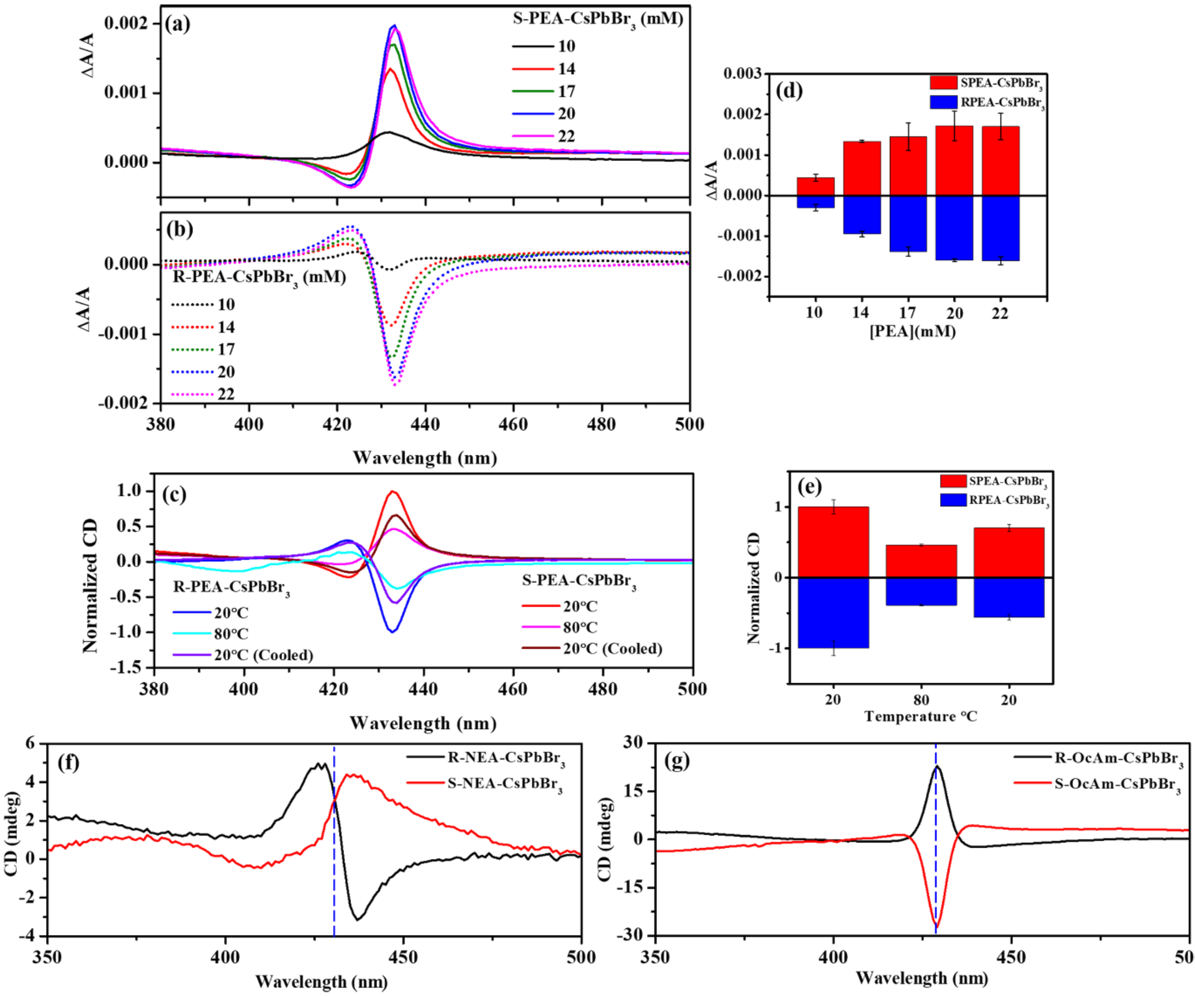

Figure 4.5 (a,b,d) Shows the concentration dependent evolution of CD strengths in R- and S-PEA $CsPbBr_3$ NPs represented in values of ΔA/A. (c, e) Shows the effect of thermal cycling on the CD intensities of R-and S-PEA-$CsPbBr_3$ NPs ([PEA] = 20 mM in NP dispersion). (f,g) Shows the CD spectra of R- and S-NEA-$CsPbBr_3$ NPs ([NEA = 30 mM in NP dispersion) and R- and S-OcAm-$CsPbBr_3$ NPs ([OcAm] = 11 mM in NP dispersion) highlighting the generality of the post-synthetic ligand modification. The peak position of the first exciton in each case is marked with a blue dashed line. The NPs were dispersed in toluene.

The effect of thermal cycling on the CD intensities was also evaluated for R- and S-PEA-$CsPbBr_3$ NPs; see Figure 4.5 (c, e). For both enantiomers, a reduction in CD intensity from the initial value is observed as the temperature is increased from 20 °C to 80 °C; the CD intensity is reduced to 39% for R- and 46% for S-PEA-$CsPBr_3$ NPs. Cycling the temperature back to 20°C led to a partial, but incomplete, recovery of the CD intensity to ~70% of the original value; see Figure 4.5e. Ligand binding in $CsPbBr_3$ NPs has been shown to be a highly dynamic process with the existence of a fast exchange between the free and bound forms.[55] A temperature mediated shift in the PEA adsorption-desorption equilibrium, with an increase in temperature generating a greater population of unbound/loosely bound ligands is the most plausible explanation for the observed temperature dependence.

To demonstrate the effectiveness and generality of the post-synthetic ligand modification strategy, the study was extended to include chiral 2-aminooctane (R- and S-OcAm) and 1-(1-naphthyl)ethylamine (R-and S-NEA) modified $CsPbBr_3$ NPs; see Figure 4.5(f-g). Similar to the case for R- and S-PEA-$CsPbBr_3$ NPs, both the R- and S-OcAm-$CsPbBr_3$ NPs and R- and S-NEA-$CsPbBr_3$ NPs show near-mirror image CD signals in the region of the NP absorption maximum, thereby indicating the successful imprinting of chirality. The CD spectra of the R- and S-OcAm and R- and S-NEA ligands in solution, i.e., without the NPs are shown in Figures E.12 and E.13, respectively. The absorption spectra of the R- and S-NEA-$CsPbBr_3$ NPs and R- and S-OcAm-$CsPbBr_3$ NPs are shown in Figure E.14 and are consistent with the perovskite excitonic absorption feature seen for R- and S-PEA-$CsPbBr_3$ NPs. The dissymmetry factors for the R and S- PEA-$CsPbBr_3$ NPs (Figure 4.5) and R- and S-OcAm-$CsPbBr_3$ NPs (see Fig E.15) are an order of magnitude higher than the ones reported for chiral 2-octylamine capped $CsPbBr_3$ NPs (with an excitonic absorption maximum at 508 nm and an average particle size of 20 nm)[24] and highlights the importance of a strongly quantum confined system which provides a larger electronic coupling between chiral ligands and the confined carriers' wavefunctions, thereby affecting CD strengths. Finally, the evolution of the CD signals in chiral $CsPbBr_3$ NPs as a function of time is evaluated. R- and S-OcAm-$CsPbBr_3$ NPs were chosen particularly because of their similarity to oleylamine, which forms an integral part of the ligand shell for the achiral $CsPbBr_3$ NPs. The progression of the CD response as a function of ligand incubation time is shown in Figure E.15 for R- and S-OcAm-$CsPbBr_3$ NPs. Although the CD signals decrease with time following the degradation of the NPs, as evidenced from the decrease in their absorption spectra (see Fig E.16), there is an observable CD response even after 168 hour of ligand incubation.

4.3 Summary

This study demonstrates a post-synthetic ligand modification strategy for synthesizing chiral 3D $CsPbBr_3$ NPs. Highly quantum confined $CsPbBr_3$ NPs were synthesized by tuning the Br/Pb ratio during synthesis and the post-synthetic addition of R- and S-PEA to the $CsPbBr_3$ NP solution was used to induce chiroptical activity. The chiroptical activity is argued to originate from the electronic coupling of the ligands to the quantum confined $CsPbBr_3$ NPs. When compared to the achiral $CsPbBr_3$ NPs, TEM revealed a modest increase in NP size upon increasing PEA concentration. A concentration dependent evolution of CD signals was also observed. Thermal cycling was also shown to modulate the CD strengths in the R- and S-PEA-$CsPbBr_3$ NPs and was attributed to the temperature dependent binding strength of the chiral ligands. The post-synthetic strategy was then extended to generate chiral R- and S-OcAm-$CsPbBr_3$ NPs and R- and S-NEA-$CsPbBr_3$ NPs. The methods presented in this work further develop strategies for creating 3D chiral perovskites which may enable new opportunities for their application in spintronics and optoelectronics.

4.4 Experimental Details

4.4.1 Materials

Cesium carbonate (Cs_2CO_3, 99.9% trace metals basis), lead (II) bromide ($PbBr_2$, 99.999% trace metals basis), zinc (II) bromide ($ZnBr_2$, 99.999% trace metals basis), oleic acid (OA, technical grade, 90%), oleylamine (OAm, technical grade, 70%), octadecene (ODE, 90%), R(+)-1-phenylethylamine (R-PEA, ≥99%), S(-)-1-phenylethylamine (S-PEA, ≥99%), R(+)-1-(1-naphthyl)ethylamine (R-NEA, ≥99%), S(-)-1-(1-naphthyl)ethylamine (S-NEA, ≥99%) and coumarin 153 (C153, 98%) were purchased from Sigma Aldrich. R-(-)-2-aminooctane (99+%) and S-(+)-2-aminooctane (99+%) were purchased from Alfa Aesar. Dimethyl sulfoxide (DMSO)-d6 was purchased from Cambridge Isotope Laboratories Inc. Toluene-d8 was purchased from Acros Organics. Toluene, acetone and tert-butanol were purchased from Fisher. All chemicals were used without further purification.

4.4.2 Synthesis of $CsPbBr_3$ NPs

$CsPbBr_3$ NPs were synthesized according to the reports by Son and coworkers with modifications.[48] For a typical synthesis 0.2 g Cs_2CO_3, 0.68 ml OA and 10 ml ODE were loaded onto a 50 ml three neck round bottomed (RB) flask and flushed with argon for 1 hour at 120 ℃. The reaction was then sealed in an argon atmosphere and the temperature was raised to 140 ℃ for the complete dissolution of Cs_2CO_3 to form Cs-oleate. The reaction temperature was then maintained at 120 ℃ to prevent precipitation of Cs-oleate.

In another 50 ml three neck RB flask 80 mg $PbBr_2$, 600 mg $ZnBr_2$, 2 ml OA, 2 ml OAm and 5 ml ODE were flushed with argon for 45 minutes at 120 °C after which the reaction was sealed in the argon atmosphere and heated at 120 °C for an additional 45 minutes. The temperature was then decreased to 85 °C and after equilibration, 0.8 ml Cs-oleate was rapidly injected. The reaction was quenched after 180 seconds by cooling the flask in an ice bath.

Next, 2 ml of the crude mixture was dispersed in 5 ml of toluene and then centrifuged at 6500 rpm for 15 minutes to remove any unreacted precursors. The supernatant was collected, left unagitated for a few hours and then concentrated further by bubbling in argon and centrifuged at 11000 rpm at 4 °C for 30 minutes to collect the purified nanoparticles. A few drops of acetone or tert-butanol was sometimes added to facilitate complete precipitation.

4.4.3 Post-synthetic Ligand Modification

$CsPbBr_3$ NPs dispersed in toluene were prepared with an optical density (O.D.) ≈ 1.0 at the first excitonic transition (428-430 nm). To the dispersions, R- or S-PEA was added so that the final concentration of the R- or S-PEA in solution ranged from 10-22 mM and incubated overnight at room temperature before further characterization. A similar approach was used for the modification of $CsPbBr_3$ NPs by R- or S-OcAm and R- or S-NEA.

4.4.4 UV-Visible Absorption and Emission Spectroscopy

UV-Visible absorption spectra were collected on an Agilent 8453 spectrometer. Steady-state emission spectra were collected using a Horiba Jobin Yvon Fluoromax 3 fluorescence spectrometer with an integration time of 1 sec and a spectral resolution of 2 nm. The relative emission quantum yields of the samples (Φ_x) were calculated with respect to coumarin 153 (C153) dissolved in methanol ($\Phi_r = 0.42$)[57] using equation 4.1.

$$\frac{\Phi_x}{\Phi_r} = \frac{A_r\ (\lambda_r)\ I_{ex}\ (\lambda_r)\ \eta_x^2 \int_0^\infty I_{em,x}\ (\overline{\upsilon})\ d\overline{\upsilon}}{A_x\ (\lambda_x)\ I_{ex}\ (\lambda_x)\ \eta_r^2 \int_0^\infty I_{em,r}\ (\overline{\upsilon})\ d\overline{\upsilon}} \qquad \textbf{Equation 4.1}$$

where the subscripts x and r stand for sample and reference respectively, A is the absorbance at excitation wavelength (λ), I_{ex} is the intensity of the excitation light at the same wavelength, η is the refractive index (η = 1.496 for toluene and 1.327 for methanol) and $I_{em}(\overline{\upsilon})$ is the emission intensity as a function of wavenumber ($\overline{\upsilon}$). The experiments were performed at room temperature.

4.4.5 Time-resolved Luminescence Spectroscopy

The time-resolved emission decay profiles of the $CsPbBr_3$ and R- and S-PEA-$CsPbBr_3$ NPs were collected using the time-correlated single photon counting (TCSPC) method with a PicoHarp 300 TCSPC module (PicoQuant GmbH). The samples were excited using a picosecond diode laser at 378 nm (PiL037SM) with a repetition rate of 1MHz and the emission was collected at the magic angle. The full-width-at-half-maxima (FWHM) of the instrument response function (IRF) was ≤ 96 ps. The decays were fitted using an iterative reconvolution method with the fluorescence analysis software (FAST) from Edinburgh Instruments.

4.4.6 Circular Dichroism Spectroscopy

CD spectra were collected with an OLIS DSM 17 CD spectrometer. NP dispersions in toluene with an O.D. ≈ 1.0 at the first excitonic transition were typically used for measurements along with an integration time of 3 sec and a spectral resolution of 1 nm. The spectra are reported in units of mdeg (degrees of ellipticity) and ΔA/A (difference in absorptivity normalized to absorption). The reported spectra are background subtracted with an achiral $CsPbBr_3$ NP acting as a blank. All spectra were acquired at 20 ℃. For temperature dependent CD experiments, the samples were cycled from 20 to 80 ℃.

4.4.7 Transmission Electron Microscope Imaging

The TEM images were acquired using a JEOL JEM-2100F and a Thermo Fisher Scientific Titan Themis 200 aberration corrected TEM operated at an acceleration potential of 200 kV. The samples were prepared by drop-casting a 10 µl NP dispersion in toluene onto a Cu TEM grid with ultra-thin carbon supporting film and dried in air.

4.4.8 Powder X-Ray Diffraction

Powder XRD patterns were collected from a Bruker D8 Discover XRD instrument equipped with a PSD (LYNXEYE) detector operated with an X-ray generator voltage and current of 40 kV and 40 mA respectively along with a Cu Kα source (λ = 1.54187 Å). Concentrated NP dispersions were drop-cast on a clean glass substrate and then dried before acquiring the spectra at room temperature. Data analysis was performed on the EVA and HighScore XRD analysis software.

4.4.9 X-Ray Photoelectron Spectroscopy

XPS spectra were collected using a Thermo Fisher Scientific ESCALAB 250 Xi. Samples were prepared by drop-casting a concentrated NP dispersion in toluene on clean glass substrates and dried. Each spectrum was referenced to adventitious carbon (C 1s 284.8 eV).

4.4.10 Nuclear Magnetic Resonance Spectroscopy

^{1}H NMR spectra were obtained using a Bruker Advance 400 MHz spectrometer. The spectra were calibrated to the residual solvent peak (DMSO-d6, 2.50 ppm). To prepare NP samples for NMR, purified suspensions of NPs in toluene were centrifuged into a pellet, then dried under Ar flow and stored in a vacuum desiccator. DMSO-d6 (~1 g) was added to the dried NPs and mixed until complete digestion occurred, as indicated by the formation of a clear solution.

4.5 References

1. Shamsi, J.; Urban, A. S.; Imran, M.; De Trizio, L.; Manna, L., Metal Halide Perovskite Nanocrystals: Synthesis, Post-Synthesis Modifications, and Their Optical Properties. *Chem. Rev.* **2019,** *119* (5), 3296-3348.

2. Protesescu, L.; Yakunin, S.; Bodnarchuk, M. I.; Krieg, F.; Caputo, R.; Hendon, C. H.; Yang, R. X.; Walsh, A.; Kovalenko, M. V., Nanocrystals of Cesium Lead Halide Perovskites (CsPbX3, X = Cl, Br, and I): Novel Optoelectronic Materials Showing Bright Emission with Wide Color Gamut. *Nano Lett.* **2015,** *15* (6), 3692-3696.

3. Akkerman, Q. A.; D'Innocenzo, V.; Accornero, S.; Scarpellini, A.; Petrozza, A.; Prato, M.; Manna, L., Tuning the Optical Properties of Cesium Lead Halide Perovskite Nanocrystals by Anion Exchange Reactions. *J. Am. Chem. Soc.* **2015,** *137* (32), 10276-10281.

4. Huang, H.; Bodnarchuk, M. I.; Kershaw, S. V.; Kovalenko, M. V.; Rogach, A. L., Lead Halide Perovskite Nanocrystals in the Research Spotlight: Stability and Defect Tolerance. *ACS Energy Lett.* **2017,** *2* (9), 2071-2083.

5. Di Stasio, F.; Christodoulou, S.; Huo, N.; Konstantatos, G., Near-Unity Photoluminescence Quantum Yield in $CsPbBr_3$ Nanocrystal Solid-State Films via Postsynthesis Treatment with Lead Bromide. *Chem. Mater.* **2017,** *29* (18), 7663-7667.

6. Herz, L. M., Charge-Carrier Dynamics in Organic-Inorganic Metal Halide Perovskites. *Annu. Rev. Phys. Chem.* **2016,** *67* (1), 65-89.

7. Dong, H.; Zhang, C.; Liu, X.; Yao, J.; Zhao, Y. S., Materials chemistry and engineering in metal halide perovskite lasers. *Chem. Soc. Rev.* **2020,** *49* (3), 951-982.

8. Van Le, Q.; Jang, H. W.; Kim, S. Y., Recent Advances toward High-Efficiency Halide Perovskite Light-Emitting Diodes: Review and Perspective. *Small Methods* **2018,** *2* (10), 1700419.

9. Kim, Y.-H.; Kim, S.; Kakekhani, A.; Park, J.; Park, J.; Lee, Y.-H.; Xu, H.; Nagane, S.; Wexler, R. B.; Kim, D.-H.; Jo, S. H.; Martínez-Sarti, L.; Tan, P.; Sadhanala, A.; Park, G.-S.; Kim, Y.-W.; Hu, B.; Bolink, H. J.; Yoo, S.; Friend, R. H.; Rappe, A. M.; Lee, T.-W., Comprehensive defect suppression in perovskite nanocrystals for high-efficiency light-emitting diodes. *Nat. Photonics* **2021,** *15* (2), 148-155.

10. Jena, A. K.; Kulkarni, A.; Miyasaka, T., Halide Perovskite Photovoltaics: Background, Status, and Future Prospects. *Chem. Rev.* **2019,** *119* (5), 3036-3103.

11. Naaman, R.; Waldeck, D. H., Chiral-Induced Spin Selectivity Effect. *J. Phys. Chem. Lett.* **2012,** *3* (16), 2178-2187.

12. Naaman, R.; Waldeck, D. H., Spintronics and Chirality: Spin Selectivity in Electron Transport Through Chiral Molecules. *Annu. Rev. Phys. Chem.* **2015,** *66* (1), 263-281.

13. Bloom, B. P.; Lu, Y.; Metzger, T.; Yochelis, S.; Paltiel, Y.; Fontanesi, C.; Mishra, S.; Tassinari, F.; Naaman, R.; Waldeck, D. H., Asymmetric reactions induced by electron spin polarization. *PCCP* **2020,** *22* (38), 21570-21582.

14. Naaman, R.; Paltiel, Y.; Waldeck, D. H., Chiral Molecules and the Spin Selectivity Effect. *J. Phys. Chem. Lett.* **2020,** *11* (9), 3660-3666.

15. Naaman, R.; Paltiel, Y.; Waldeck, D. H., Chiral Induced Spin Selectivity Gives a New Twist on Spin-Control in Chemistry. *Acc. Chem. Res.* **2020,** *53* (11), 2659-2667.

16. Lu, H.; Xiao, C.; Song, R.; Li, T.; Maughan, A. E.; Levin, A.; Brunecky, R.; Berry, J. J.; Mitzi, D. B.; Blum, V.; Beard, M. C., Highly Distorted Chiral Two-Dimensional Tin Iodide Perovskites for Spin Polarized Charge Transport. *J. Am. Chem. Soc.* **2020,** *142* (30), 13030-13040.

17. Lu, H.; Wang, J.; Xiao, C.; Pan, X.; Chen, X.; Brunecky, R.; Berry, J. J.; Zhu, K.; Beard, M. C.; Vardeny, Z. V., Spin-dependent charge transport through 2D chiral hybrid lead-iodide perovskites. *Sci Adv* **2019,** *5* (12), eaay0571-eaay0571.

18. Huang, Z.; Bloom, B. P.; Ni, X.; Georgieva, Z. N.; Marciesky, M.; Vetter, E.; Liu, F.; Waldeck, D. H.; Sun, D., Magneto-Optical Detection of Photoinduced Magnetism via Chirality-Induced Spin Selectivity in 2D Chiral Hybrid Organic–Inorganic Perovskites. *ACS Nano* **2020,** *14* (8), 10370-10375.

19. Wang, J.; Lu, H.; Pan, X.; Xu, J.; Liu, H.; Liu, X.; Khanal, D. R.; Toney, M. F.; Beard, M. C.; Vardeny, Z. V., Spin-Dependent Photovoltaic and Photogalvanic Responses of Optoelectronic Devices Based on Chiral Two-Dimensional Hybrid Organic–Inorganic Perovskites. *ACS Nano* **2021,** *15* (1), 588-595.

20. Kim, Y.-H.; Zhai, Y.; Lu, H.; Pan, X.; Xiao, C.; Gaulding, E. A.; Harvey, S. P.; Berry, J. J.; Vardeny, Z. V.; Luther, J. M.; Beard, M. C., Chiral-induced spin selectivity enables a room-temperature spin light-emitting diode. *Science* **2021,** *371* (6534), 1129.

21. Billing, D. G.; Lemmerer, A., Synthesis and crystal structures of inorganic–organic hybrids incorporating an aromatic amine with a chiral functional group. *Cryst. Eng. Comm.* **2006,** *8* (9), 686-695.

22. Ahn, J.; Lee, E.; Tan, J.; Yang, W.; Kim, B.; Moon, J., A new class of chiral semiconductors: chiral-organic-molecule-incorporating organic–inorganic hybrid perovskites. *Mater. Horiz.* **2017,** *4* (5), 851-856.

23. Georgieva, Z. N.; Bloom, B. P.; Ghosh, S.; Waldeck, D. H., Imprinting Chirality onto the Electronic States of Colloidal Perovskite Nanoplatelets. *Adv. Mater.* **2018,** *30* (23), 1800097.

24. Chen, W.; Zhang, S.; Zhou, M.; Zhao, T.; Qin, X.; Liu, X.; Liu, M.; Duan, P., Two-Photon Absorption-Based Upconverted Circularly Polarized Luminescence Generated in Chiral Perovskite Nanocrystals. *J. Phys. Chem. Lett.* **2019,** *10* (12), 3290-3295.

25. Dong, Y.; Zhang, Y.; Li, X.; Feng, Y.; Zhang, H.; Xu, J., Chiral Perovskites: Promising Materials toward Next-Generation Optoelectronics. *Small* **2019,** *15* (39), 1902237.

26. Dang, Y.; Liu, X.; Cao, B.; Tao, X., Chiral halide perovskite crystals for optoelectronic applications. *Matter* **2021,** *4* (3), 794-820.

27. Long, G.; Sabatini, R.; Saidaminov, M. I.; Lakhwani, G.; Rasmita, A.; Liu, X.; Sargent, E. H.; Gao, W., Chiral-perovskite optoelectronics. *Nat. Rev. Mater.* **2020,** *5* (6), 423-439.

28. Xiao, L.; An, T.; Wang, L.; Xu, X.; Sun, H., Novel properties and applications of chiral inorganic nanostructures. *Nano Today* **2020,** *30*, 100824.

29. He, T.; Li, J.; Li, X.; Ren, C.; Luo, Y.; Zhao, F.; Chen, R.; Lin, X.; Zhang, J., Spectroscopic studies of chiral perovskite nanocrystals. *Appl. Phys. Lett.* **2017,** *111* (15), 151102.

30. Shi, Y.; Duan, P.; Huo, S.; Li, Y.; Liu, M., Endowing Perovskite Nanocrystals with Circularly Polarized Luminescence. *Adv. Mater.* **2018,** *30* (12), 1705011.

31. Kim, Y.-H.; Zhai, Y.; Gaulding, E. A.; Habisreutinger, S. N.; Moot, T.; Rosales, B. A.; Lu, H.; Hazarika, A.; Brunecky, R.; Wheeler, L. M.; Berry, J. J.; Beard, M. C.; Luther, J. M., Strategies to Achieve High Circularly Polarized Luminescence from Colloidal Organic–Inorganic Hybrid Perovskite Nanocrystals. *ACS Nano* **2020,** *14* (7), 8816-8825.

32. Tohgha, U.; Varga, K.; Balaz, M., Achiral CdSe quantum dots exhibit optical activity in the visible region upon post-synthetic ligand exchange with D- or L-cysteine. *Chem. Commun.* **2013,** *49* (18), 1844-1846.

33. Kim, B. H.; Heo, J.; Kim, S.; Reboul, C. F.; Chun, H.; Kang, D.; Bae, H.; Hyun, H.; Lim, J.; Lee, H.; Han, B.; Hyeon, T.; Alivisatos, A. P.; Ercius, P.; Elmlund, H.; Park, J., Critical differences in 3D atomic structure of individual ligand-protected nanocrystals in solution. *Science* **2020,** *368* (6486), 60.

34. Gao, X.; Zhang, X.; Zhao, L.; Huang, P.; Han, B.; Lv, J.; Qiu, X.; Wei, S.-H.; Tang, Z., Distinct Excitonic Circular Dichroism between Wurtzite and Zincblende CdSe Nanoplatelets. *Nano Lett.* **2018,** *18* (11), 6665-6671.

35. Bi, C.; Yao, Z.; Sun, X.; Wei, X.; Wang, J.; Tian, J., Perovskite Quantum Dots with Ultralow Trap Density by Acid Etching-Driven Ligand Exchange for High Luminance and Stable Pure-Blue Light-Emitting Diodes. *Adv. Mater.*, 2006722.

36. Seth, S.; Samanta, A., A Facile Methodology for Engineering the Morphology of CsPbX3 Perovskite Nanocrystals under Ambient Condition. *Sci. Rep.* **2016,** *6* (1), 37693.

37. Shamsi, J.; Kubicki, D.; Anaya, M.; Liu, Y.; Ji, K.; Frohna, K.; Grey, C. P.; Friend, R. H.; Stranks, S. D., Stable Hexylphosphonate-Capped Blue-Emitting Quantum-Confined CsPbBr3 Nanoplatelets. *ACS Energy Lett.* **2020,** *5* (6), 1900-1907.

38. Ben Moshe, A.; Szwarcman, D.; Markovich, G., Size Dependence of Chiroptical Activity in Colloidal Quantum Dots. *ACS Nano* **2011,** *5* (11), 9034-9043.

39. Huang, H.; Bodnarchuk, M. I.; Kershaw, S. V.; Kovalenko, M. V.; Rogach, A. L., Lead Halide Perovskite Nanocrystals in the Research Spotlight: Stability and Defect Tolerance. *ACS Energy Lett.* **2017,** *2* (9), 2071-2083.

40. Moloney, M. P.; Gun'ko, Y. K.; Kelly, J. M., Chiral highly luminescent CdS quantum dots. *Chem. Commun.* **2007,** (38), 3900-3902.

41. Almeida, G.; Goldoni, L.; Akkerman, Q.; Dang, Z.; Khan, A. H.; Marras, S.; Moreels, I.; Manna, L., Role of Acid–Base Equilibria in the Size, Shape, and Phase Control of Cesium Lead Bromide Nanocrystals. *ACS Nano* **2018,** *12* (2), 1704-1711.

42. Lakowicz, J. R., *Principles of Fluorescence Spectroscopy*. Third ed.

43. Ma, S.; Ahn, J.; Moon, J., Chiral Perovskites for Next-Generation Photonics: From Chirality Transfer to Chiroptical Activity. *Adv. Mater.* **2021**, 2005760.

44. Ha, S. K.; Mauck, C. M.; Tisdale, W. A., Toward Stable Deep-Blue Luminescent Colloidal Lead Halide Perovskite Nanoplatelets: Systematic Photostability Investigation. *Chem. Mater.* **2019,** *31* (7), 2486-2496.

45. Tohgha, U.; Deol, K. K.; Porter, A. G.; Bartko, S. G.; Choi, J. K.; Leonard, B. M.; Varga, K.; Kubelka, J.; Muller, G.; Balaz, M., Ligand Induced Circular Dichroism and Circularly Polarized Luminescence in CdSe Quantum Dots. *ACS Nano* **2013,** *7* (12), 11094-11102.

46. Cheng, J.; Hao, J.; Liu, H.; Li, J.; Li, J.; Zhu, X.; Lin, X.; Wang, K.; He, T., Optically Active CdSe-Dot/CdS-Rod Nanocrystals with Induced Chirality and Circularly Polarized Luminescence. *ACS Nano* **2018,** *12* (6), 5341-5350.

47. Kuznetsova, V. A.; Mates-Torres, E.; Prochukhan, N.; Marcastel, M.; Purcell-Milton, F.; O'Brien, J.; Visheratina, A. K.; Martinez-Carmona, M.; Gromova, Y.; Garcia-Melchor, M.; Gun'ko, Y. K., Effect of Chiral Ligand Concentration and Binding Mode on Chiroptical Activity of CdSe/CdS Quantum Dots. *ACS Nano* **2019,** *13* (11), 13560-13572.

48. Dong, Y.; Qiao, T.; Kim, D.; Parobek, D.; Rossi, D.; Son, D. H., Precise Control of Quantum Confinement in Cesium Lead Halide Perovskite Quantum Dots via Thermodynamic Equilibrium. *Nano Lett.* **2018,** *18* (6), 3716-3722.

49. Kostopoulou, A.; Sygletou, M.; Brintakis, K.; Lappas, A.; Stratakis, E., Low-temperature benchtop-synthesis of all-inorganic perovskite nanowires. *Nanoscale* **2017,** *9* (46), 18202-18207.

50. Rathore, E.; Maji, K.; Rao, D.; Saha, B.; Biswas, K., Charge Transfer in the Heterostructure of CsPbBr3 Nanocrystals with Nitrogen-Doped Carbon Dots. *J. Phys. Chem. Lett.* **2020,** *11* (19), 8002-8007.

51. Wang, Y.; Ren, Y.; Zhang, S.; Wu, J.; Song, J.; Li, X.; Xu, J.; Sow, C. H.; Zeng, H.; Sun, H., Switching excitonic recombination and carrier trapping in cesium lead halide perovskites by air. *Commun. Phys.* **2018,** *1* (1), 96.

52. Shahriar, S.; Castaneda, V.; Martinez, M.; Mishra, A. K.; Akter, T.; Schutt, K.; Boscoboinik, J. A.; Hodges, D., Oxidation states in perovskite layers formed using various deposition techniques. *Journal Renew. Sustain. Energy* **2019,** *11* (5), 053504.

53. Chen, P.; Bai, Y.; Wang, S.; Lyu, M.; Yun, J.-H.; Wang, L., In Situ Growth of 2D Perovskite Capping Layer for Stable and Efficient Perovskite Solar Cells. *Adv. Funct. Mater.* **2018,** *28* (17), 1706923.

54. Hens, Z.; Martins, J. C., A Solution NMR Toolbox for Characterizing the Surface Chemistry of Colloidal Nanocrystals. *Chem. Mater.* **2013,** *25* (8), 1211-1221.

55. De Roo, J.; Ibáñez, M.; Geiregat, P.; Nedelcu, G.; Walravens, W.; Maes, J.; Martins, J. C.; Van Driessche, I.; Kovalenko, M. V.; Hens, Z., Highly Dynamic Ligand Binding and Light Absorption Coefficient of Cesium Lead Bromide Perovskite Nanocrystals. *ACS Nano* **2016,** *10* (2), 2071-2081.

56. Udayabhaskararao, T.; Houben, L.; Cohen, H.; Menahem, M.; Pinkas, I.; Avram, L.; Wolf, T.; Teitelboim, A.; Leskes, M.; Yaffe, O.; Oron, D.; Kazes, M., A Mechanistic Study of Phase Transformation in Perovskite Nanocrystals Driven by Ligand Passivation. *Chem. Mater.* **2018,** *30* (1), 84-93.

57. Lewis, J. E.; Maroncelli, M., On the (uninteresting) Dependence of the Absorption and Emission Transition Moments of Coumarin 153 on Solvent. *Chem. Phys. Lett.* **1998,** *282*, 197-203.

5.0 Size-Dependent Chiro-Optical Properties of $CsPbBr_3$ Nanoparticles

5.1 Introduction

Chiral perovskites have generated significant interest since their chiro-optical properties were first reported,[1] with recent publications showing promising applications in circularly polarized light emission[2-5] and detection,[6-8] memory devices,[9] piezoelectric devices,[10] and solar cells.[11] A robust library of available compositions and morphologies has enabled this broad range of applications, however, the further improvement of these devices depends strongly on our understanding of the structure-property relationships within chiral perovskites.

Recent studies have attempted to elucidate the mechanisms through which perovskites gain chiro-optical properties, with authors reporting either structural distortion caused by chiral ligands[12] or electronic coupling between chiral components and the perovskite[13, 14] as the possible mechanisms. Other works have focused on maximizing the magnitude of chiro optical properties such as circular dichroism (CD) and circularly polarized photoluminescence (CPPL) in an effort to optimize synthetic procedures for future applications. Lin and co-workers achieved enhanced CD and CPPL in 2D chiral perovskites by manipulating the d-spacing and halogen-halogen interactions within the material.[15] Kim and colleagues employed mixed ligand shells to optimize the luminescence dissymmetry factor of colloidal formamidinium lead bromide NPs.[16] Others have explored the effects of perovskite composition on CD strength,[17] as well as the concentration of chiral ligands in post-synthetic ligand modification procedures.[14, 18] However, the role of NP size in perovskite chiral imprinting remains largely unexplored.

Many of the guiding principles for chiral imprinting used in generating chiro-optically active perovskites originated in the field of chiral quantum dots (QDs). Structure-property relationships in chiral QDs have been thoroughly explored, including the relationship between QD size and chiro-optical properties. For example, size effects for chiral CdSe QDs were examined by Ben-Moshe and colleagues who found an exponential decrease in CD intensity as a function of size.[19] Quantum-confinement effects in chiral CdTe QDs were studied and analysis of the CD shape and intensity were used to elucidate the mechanism of chiral imprinting.[20] In another study, CD and photoluminescence intensities were studied as a function of shell thickness in core-shell CdSe/CdS QDs. [21] CD was found to be inversely proportional to the shell thickness, while photoluminescence magnitudes increased with thicker shells.[21] These fundamental studies provided crucial knowledge and strategies for the design of QD-based devices.

In this work, the size-dependent chiro-optical properties of colloidal $CsPbBr_3$ NPs were examined. NPs in three different size regimes were synthesized and their native oleic acid (OA) and oleylamine (OAm) ligands were exchanged for chiral S-(-)-β-methyphenethylammonim (S-MPEA) or R-(+)-β-methyphenethylammonium (R-MPEA) ligands. A strong correlation was established between NP size and CD intensity, with a considerable decrease in intensity observed as the NP size increase. The chiral ligand coverage was measured using quantitative ^1H-NMR and the relationship between ligand coverage and the resulting CD was also found to depend strongly on the NP size. These studies establish previously unexplored structure-property relationships for chiral perovskite NPs; it is hoped that the findings of this work can guide the further development and improvement of chiral perovskite-based devices and technologies.

5.2 Results and Discussion

Cesium lead bromide NPs of three different quantum-confined sizes were synthesized using previously published hot injection procedures.[18, 22, 23] The NPs were then ligand-exchanged with solutions of R-MPEABr or S-MPEABr; experimental details are outlined in Section 5.4.

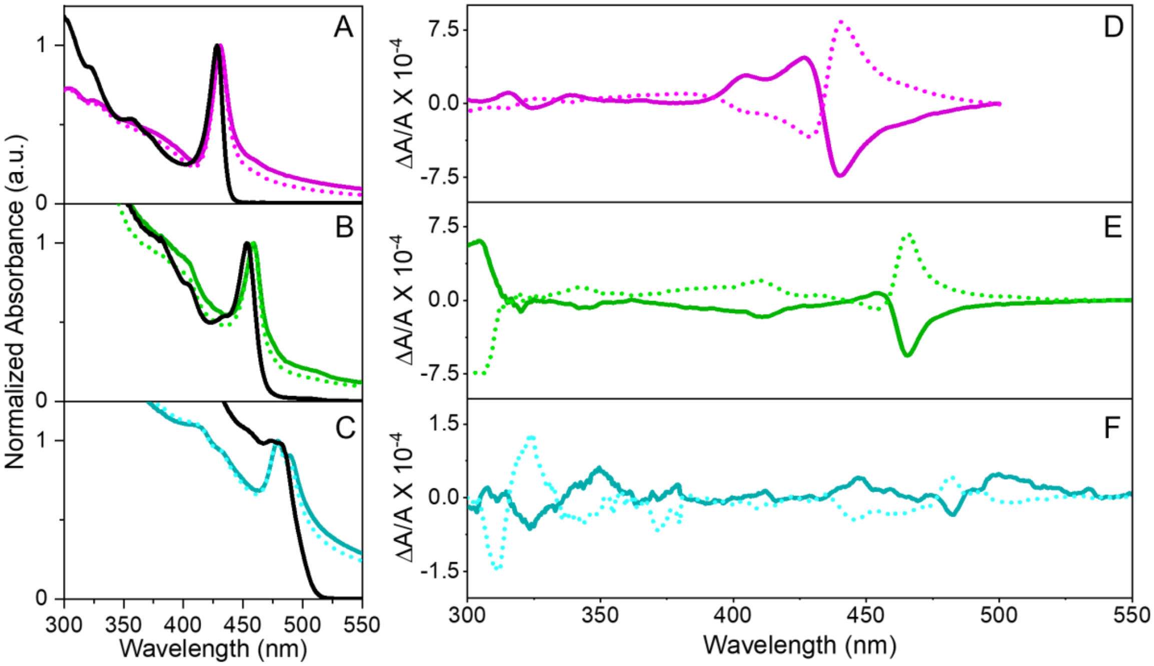

Figure 5.1 Absorbance (A-C) and CD spectra (D-F) of $CsPbBr_3$ NPs dispersed in toluene. NPs in the 2, 4, and 6-nm size regmes are shown in pink, green, and blue, respectively. Black curves in the absorbance spectra signify achiral NPs; chiral NPs are shown with colored lines (R-solid, S-dotted).

Representative optical spectra of perovskite NPs are shown in Figure 5.1. The NPs exhibit size-dependent bandgap shifts typical of structures in the quantum-confined regime with absorbance maxima at 428 nm for the small (~2nm) NPs, 453 nm for the medium (~4 nm) NPs, and 482 nm for the large (~6 nm) achiral NPs (Figure 5.1A, B, C, black spectra). A red-shift is observed upon ligand exchange for all NP sizes with larger sizes exhibiting a greater change in wavelength. Similar shifts have previously been reported in the literature and are associated with

NP growth during the ligand exchange.[18] While the optical spectra suggest a change in the NP size after ligand exchange, their crystal phase remains unaltered, with all size-regimes exhibiting an orthorhombic crystal lattice before and after ligand exchange, as shown in Figures F.1-3. Along with peaks originating from orthorhombic $CsPbBr_3$, The XRD patterns for the chiral medium and large NPs exhibit reflections from rhombohedral Cs_4PbBr_6. Evidence of Cs4PbBr$_6$ was also found in the UV-Vis spectra (Figure F.4A, B), which contain peaks at 315nm for the R and S-MPEABr coated NPs, corresponding to the absorbance maximum of Cs_4PbBr_6 nanostructures.[24] This byproduct does not affect the chiro-optical properties of the NPs and has previously been shown to occur as a result of NP decomposition within the sample.[24]

Circular dichroism (CD) spectra of the chiral NPs are shown in Figures 5.1D-F. Mirror image signatures are observed for S- and R-chiral NPs of all three sizes with prominent bisignate (consisting of a positive and negative lobe) features occurring at the energy of the first NP exciton and weaker features in the near-UV region. A bisignate CD shape has been associated with the electronic coupling between a chiral and an achiral chromophore, in this case the chiral ligand and the achiral NP, resulting in a coupled oscillator interaction.[25] CD intensities in these representative spectra appear to weaken overall as the NP size increases, with UV features gaining prominence in the medium and large size regimes. Average values from a larger data set are shown and analyzed *vide infra*.

Transmission electron microscopy (TEM) images were collected to estimate the exact size of the small NPs (Figure F.5); however, ongoing stability issues prevented accurate TEM size measurements for the medium and large NPs. To circumvent this issue, literature data for the 2-6 nm size range were analyzed as a tool to estimate the average NP edge length from the sample's absorbance maximum. Data adapted from published reports for $CsPbBr_3$ NPs synthesized via the hot injection method,[26-31] as well as the calculated NP sizes in this work, are shown in Figure 5.2.

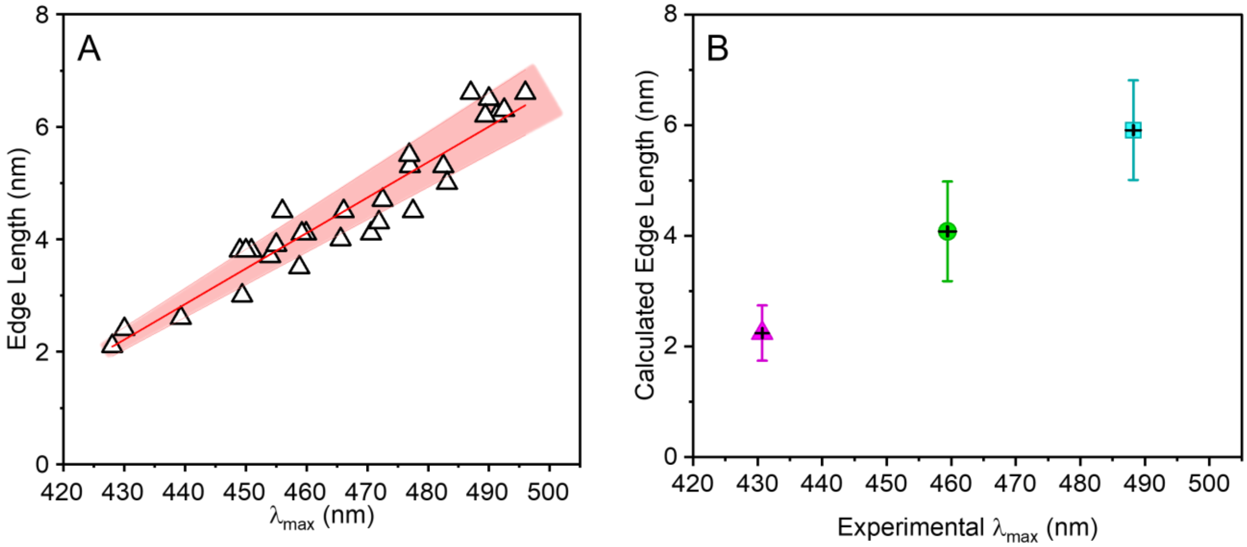

Figure 5.2 (A) Literature values for $CsPbBr_3$ NP size and absorbance maxima from References 5-10, shown with a linear fit. The red area signifies the 95% confidence interval of the fit. (B) Average NP sizes derived from experimental absorbance data for chiral NPs in the 2 nm (pink, N=9), 4 nm (green, N=8) and 6 nm (blue, N=9) size regimes and the linear fit equation from panel B.

A linear fit was generated for the data in Figure 5.2A, yielding equation 5.1, with an adjusted R^2 value of 0.8998.

$$Edge\ Length = -25.2093 + 0.06369\lambda_{max}$$ **Equation 5.1**

Experimentally derived λ_{max} values were then used to calculate the average edge length of NPs in each sample. Achiral NPs exhibit average sizes of 2.05 nm, 3.1 nm, and 5.6 nm for the three size regimes, as shown in Figure F.6. After ligand exchange, the average NP sizes increase, with average values for the three size regimes as follows: 2.2 nm, 4.2 nm, and 5.9 nm (Figure 5.2B). NPs in the 4-nm size regime experience the most significant size increase. While NP growth has been previously reported to be a consequence of ligand-exchange processes for $CsPbBr_3$ NPs,[18] the size-increase may be amplified by the inherent instability of the as-synthesized NPs in this size regime.[22]

Quantitative proton NMR experiments were performed to study the composition of the NP ligand shell. Purified and dried NP pellets were weighed and subsequently dissolved in DMSO-d6. All observed resonance peaks were attributed to known reagents, as is shown in Figure F.6. Oleic acid and oleylamine resonances, which are nearly indistinguishable due to their structural similarities, appear in the sub-2 ppm region. Solvent peaks originating from residual toluene and DMSO-d6 are seen at 2.3 and 2.5 ppm respectively; water, a common contaminant, appears in most samples at 3.3 ppm. MPEABr resonances are observed at 1.2, 3.0 and 7-8 ppm, although only the 3.0 ppm resonance can be used for quantitative studies due to overlap of the other peaks with the achiral ligand and toluene peaks. Ferrocene was used as an internal standard and concentrations of achiral and chiral ligands were calculated using Equation 5.2:

$$\frac{I_{Analyte}}{I_{Standard}} = \frac{H_{Analyte}C_{Analyte}}{H_{Standard}C_{Standard}}$$ **Equation 5.2**

where I_{Analyte} is the peak integral for the analyte and I_{Standard} is the peak integral for the ferrocene resonance at 4.0 ppm, H is the number of protons comprising the peak, and C is the concentration in mol/L. Because of the overlap in oleic acid and oleylamine resonances, we solve for the sum of their concentrations and report it as the total concentration of achiral ligands. The total NP surface area in each sample was calculated using the mass of NPs measured during the q-NMR experiment and literature values for the unit cell mass and volume (See Appendix F).[6] Data from the ligand coverage studies are shown in Figure 5.3A.

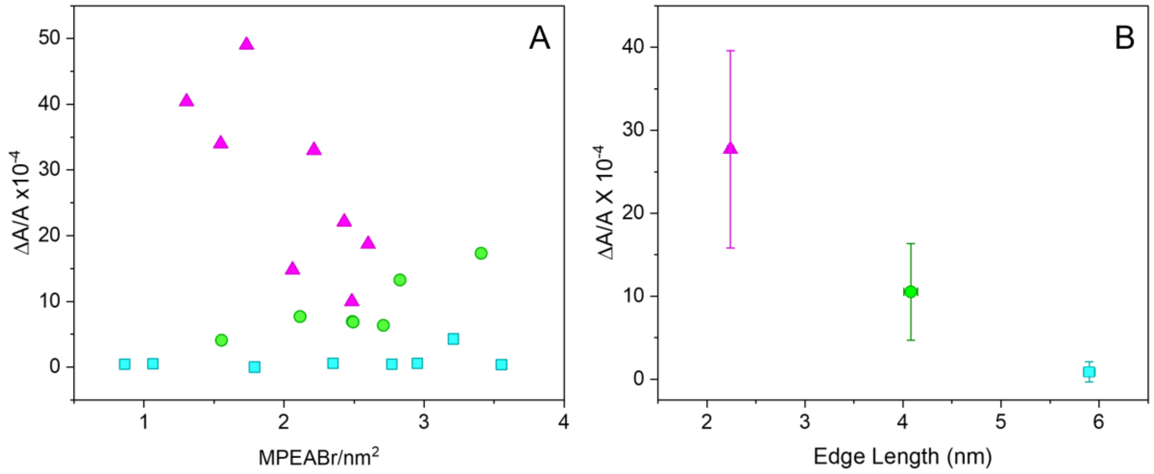

Figure 5.3 (A) CD intensity as a function of chiral ligand coverage for NPs in the 2 nm (magenta), 4 nm (green), and 6 nm (aqua) size regimes. (B) Average CD intensity as a function of NP edge length, as estimated in Figure 5.2.

The significance of chiral ligand coverage was found to be strongly affected by the size of the NP, as is shown in Figure 5.3A. NPs in the 2nm size regime exhibit the steepest slope, with a nearly five-fold change in CD intensity within the studied MPEABr/nm^2 range. As the NP size increases, the intensity of CD features becomes less dependent on MPEABr coverage, with NPs in the 4 nm size regime showing a diminished slope, and 6 nm NPs exhibiting nearly static CD intensity values over the accessible ligand coverage range. Interestingly, NPs in the 2 nm regime exhibit an inverse proportionality with respect to the ligand coverage, with lower amounts of MPEABr on the NP surface yielding higher CD signals. Previous work, discussed in Chapter 3 (Figures 3.5), suggested that chiral perovskite nanoplatelets reach a CD strength saturation point, followed by a decline in CD intensity as the fraction of chiral ligand on the surface increases, which was attributed to orientational averaging of chiral ligands on the nanoparticle surface. Furthermore, $CsPbBr_3$ NPs treated with increasing amounts of chiral ligands also exhibited an increase in CD intensity, followed by a saturation point and a subsequent decrease in CD intensity.[14] Thus, the datasets in Figure 5.3A may represent chiral NPs in different regions of the CD-ligand coverage dependence established in Chapter 3, with the larger sizes situated before the CD saturation point, and the smallest size beyond the saturation point.

Figure 5.3B displays the average CD intensities observed for each of the three size regimes in this study as a function of the NP edge length. The reported average CD intensities exhibit large error values, which decrease with NP size. The degree of error correlates well with the observed ligand coverage dependence of CD, i.e. small NPs whose CD signal is strongly affected by the number of chiral ligands per nm^2 exhibit the most error, while large NPs, which show no correlation between chiral ligand coverage and CD, have the least error. This, the error in this measurement can be attributed primarily to the variation in chiral ligand coverage between samples. NPs were found to exhibit lower average CD intensities with an increase in edge length; a thirty-fold decrease in intensity was observed between the 2 and the 6 nm size regime. This finding highlights the importance of the NP surface in chiral imprinting, as the surface-to-volume ratio decreases as the edge length increases. Ligand-induced chirality in perovskites has been attributed to electronic interactions between ligand and NP,[32] as well as structural distortion of the NP surface,[33] both of which are expected to depend strongly on the availability of surface sites. Another factor, which may contribute to the observed CD magnitude, is the energy overlap between ligand and NP electronic states. As NPs become larger and thus more energetically separated from the ligand, the effects of electronic chiral imprinting are expected to diminish.

5.3 Summary

Colloidal $CsPbBr_3$ NPs with sizes ranging between 2 and 6 nm were synthesized and ligand exchanged with chiral S- and R-MPEA to study the effect of size on chiral imprinting. Chiral imprinting strength (as measured by CD intensity) was seen to decrease dramatically between the smallest and the largest NPs, with the intermediate size exhibiting CD strength that fits within the trend. Thus, we posit that NP size plays a major role in determining the chiral imprinting strength in $CsPbBr_3$ NPs. Chiral ligand coverage was also measured for the three different NP size. CD strength was directly proportional to the chiral ligand coverage for medium sized particles, and inversely proportional for small NPs, while the largest NPs showed no obvious correlation. This interesting observation emphasizes the need for a deeper understanding of the factors which contribute to perovskite chirality. While preliminary in nature, this work may serve as a foundation to establishing a model for size-dependent chiral imprinting in perovskite NPs and guide the development of chiral perovskite-based devices.

5.4 Experimental Methods

5.4.1 Materials

Cesium carbonate (Cs_2CO_3 99.9% trace metals basis), lead (II) bromide ($PbBr_2$, 99.999% trace metals basis), zinc (II) bromide ($ZnBr_2$, 99.999% trace metals basis), oleic acid (OA, technical grade, 90%), oleylamine (OAm, technical grade, 70%), octadecene (ODE, 90%), ethyl acetate, and hydrobromic acid (HBr, 48%) were purchased from Sigma Aldrich. S-(-)-β-methyphenethylamine (S-MPEA, >98.0%) and R-(+)-β-methyphenethylamine (R-MPEA, >98.0%), were purchased from TCI. Dimethyl sulfoxide (DMSO)-d6 was purchased from Cambridge Isotope Laboratories Inc. Ferrocene (99%), toluene and tert-butanol were purchased from Thermo Fisher Scientific.

5.4.2 Synthesis of Precursor Salts

Bromide salts of R- and S-MPEA were synthesized by mixing equimolar amounts of the desired chiral amine and HBr in 15 mL of absolute ethanol. The reaction was stirred in an ice bath for 2 hours, then the solvent was removed via rotary evaporation until crystals were formed. The crystals were collected, recrystallized with chlorobenzene, and then vacuum filtered and washed several times with toluene. The product was dried in a vacuum desiccator for several hours before storage.

5.4.3 Synthesis of $CsPbBr_3$ NPs

For all syntheses, 0.2 g Cs_2CO_3, 0.7 mL OA and 10 mL ODE were added to a 50-mL three neck round bottom flask and flushed with argon for 1 hour at 120 ℃. The reaction was then sealed in an Ar atmosphere and the temperature was raised to 140 ℃ until the complete dissolution of Cs_2CO_3 and the formation of Cs-oleate. The reaction temperature was then maintained at 120 ℃ to prevent precipitation.

To obtain NPs in the 2 nm size regime, 160 mg $PbBr_2$, 1.20 g $ZnBr_2$, 4 mL OA, 4 mL OAm and 10 mL ODE were flushed with argon for 1 h at 130 ℃ after which the reaction was sealed in the Ar atmosphere and heated at 130 ℃ for an additional 45 minutes. The temperature was then decreased to 85 °C and after equilibration, 1.2 mL Cs-oleate was rapidly injected. The reaction was quenched after 180 seconds by cooling the flask in an ice bath.

To obtain NPs in the 4 nm size regime 138 mg $PbBr_2$ and 10 mL ODE were combined in a round bottom flask and flushed with argon for 1 h at 120 °C after which the reaction was sealed in the Ar atmosphere. OA and OAm were added to the reaction in a 2:1 ratio to a total volume of 1.8 mL and the reaction mixture was heated at 140 °C for an additional 45 minutes until complete dissolution of the $PbBr_2$. The temperature was then decreased to 90 °C and after equilibration, 1.6 mL Cs-oleate was rapidly injected. The reaction was quenched after 20 seconds by cooling the flask in an ice bath.

To obtain NPs in the 6 nm size regime 140 mg $PbBr_2$ and 10 mL ODE were combined in a round bottom flask and flushed with argon for 1 h at 120 °C after which the reaction was sealed in the Ar atmosphere. OA and OAm were injected into the flask in a 1:1 ratio to a total volume of 2.0 mL and the reaction mixture was heated at 140 °C for an additional 45 minutes until complete dissolution of the $PbBr_2$. While maintaining the reaction temperature at 140 °C, 1.6 mL Cs-oleate was rapidly injected. The reaction was quenched after 10-15 seconds by cooling the flask in an ice bath.

5.4.4 Purification of achiral NPs and Ligand Exchange

For 2 nm NPs 2 ml of the as-synthesized mixture was dispersed in 5 ml of toluene and then centrifuged at 6500 rpm for 15 minutes at room temperature to remove any unreacted precursors. The supernatant was collected and stored overnight to allow for NP ripening. The ripened NP mixture was then centrifuged at 11000 rpm for an hour at -3°C. The precipitate was resuspended in toluene and diluted to an absorbance intensity of 2 a.u. at λ_{max}. R- or S-MPEABr was added to the NPs as a solution in tert-butanol to reach a total chiral ligand concentration of 1.85 mM. The NP-ligand mixture was allowed to rest for 2h, then centrifuged at 6000 rpm for 15 minutes at 10℃. The precipitate was collected for measurements.

For 4 nm NPs the as-synthesized mixture was centrifuged at 10000 rpm for 15 minutes at 15℃. The supernatant was collected, and ethyl acetate was added in a 3:1 ration by volume, then centrifuged at 10000 rpm for 20 minutes at 10℃. The precipitate was resuspended in toluene and diluted to an absorbance intensity of 2 a.u. at λ_{max}. R- or S-MPEABr was added to the NPs as a solution in tert-butanol to reach a total chiral ligand concentration of 0.46 mM. The NP-ligand mixture was allowed to rest for 1h, then centrifuged at 11000 rpm for 30 minutes at -5℃. The precipitate was collected for measurements.

For 6 nm NPs the as-synthesized mixture was centrifuged at 7000 rpm for 25 minutes at room temperature. The precipitate was resuspended in toluene and diluted to an absorbance intensity of 2 a.u. at λ_{max}. R- or S-MPEABr was added to the NPs as a solution in tert-butanol to reach a total chiral ligand concentration of 1.85 mM. The NP-ligand mixture was allowed to rest overnight (~18 hours), then centrifuged at 11000 rpm for 20 minutes at room temperature. The precipitate was collected for measurements.

5.4.5 Characterization of NPs

UV-Visible absorption spectra were collected on an Agilent 8453 spectrometer. Cirular Dichroism spectra were collected on a Jasco J-810 spectropolarimeter with an scan speed of 100 nm/min and up to 15 averaged scans for each spectrum.

TEM images were acquired using a JEOL JEM-2100F and a Thermo Fisher Scientific Titan Themis 200 aberration corrected TEM operated at an acceleration potential of 200 kV. The samples were prepared by drop-casting a 10 µl NP dispersion in toluene onto a Cu TEM grid with ultra-thin carbon supporting film and dried in air.

Powder X-Ray Diffraction patterns were collected on a Bruker D8 Discover XRD instrument equipped with a PSD (LYNXEYE) detector operated with an X-ray generator voltage and current of 40 kV and 40 mA respectively along with a Cu Kα source (λ = 1.54187 Å). Concentrated NP dispersions were drop-cast on a clean glass substrate and then dried before acquiring the spectra at room temperature. Data analysis was performed on the EVA and HighScore XRD analysis software.

^{1}H NMR spectra were obtained using a Bruker Advance 400 MHz spectrometer. The spectra were calibrated to the residual solvent peak (DMSO-d6, 2.50 ppm). To prepare NP samples for NMR, purified suspensions of NPs in toluene were centrifuged into a pellet, then dried under Ar flow and stored in a vacuum desiccator. DMSO-d6 (~1 g) was added to the dried NPs and mixed until complete digestion occurred, as indicated by the formation of a clear solution. A standard solution was prepared by dissolving ferrocene in DMSO-d6 in a volumetric flask and a known amount was added to the NMR sample.

5.4.6 Calculating Ligand Coverage

Concentrations of chiral and achiral ligands were obtained via ^{1}H-NMR measurements as described in the main text. The mass of the NP pellet for each NMR sample was recorded and the total mass of ligands, as estimated from NMR measurements was subtracted to yield the mass of $CsPbBr_3$ only. Calculated values for the orthorhombic $CsPbBr_3$ unit cell mass and volume, as well as the measured edge length of NPs in the sample, were used to convert the NP mass to total number of NPs and total surface area. The total number of chiral ligands (derived from NMR measurements) was then divided by the total surface are of the dissolved NPs.

5.5 References

1. Ahn, J.; Lee, E.; Tan, J.; Yang, W.; Kim, B.; Moon, J., A new class of chiral semiconductors: chiral-organic-molecule-incorporating organic–inorganic hybrid perovskites. *Mater. Horiz.* **2017,** *4* (5), 851-856.

2. Wang, C.-T.; Chen, K.; Xu, P.; Yeung, F.; Kwok, H.-S.; Li, G., Fully Chiral Light Emission from CsPbX3 Perovskite Nanocrystals Enabled by Cholesteric Superstructure Stacks. *Adv. Funct. Mater.* **2019,** *29* (35), 1903155.

3. Wang, J.; Fang, C.; Ma, J.; Wang, S.; Jin, L.; Li, W.; Li, D., Aqueous Synthesis of Low-Dimensional Lead Halide Perovskites for Room-Temperature Circularly Polarized Light Emission and Detection. *ACS Nano* **2019,** *13* (8), 9473-9481.

4. Kim, Y.-H.; Zhai, Y.; Lu, H.; Pan, X.; Xiao, C.; Gaulding, E. A.; Harvey Steven, P.; Berry Joseph, J.; Vardeny Zeev, V.; Luther Joseph, M.; Beard Matthew, C., Chiral-induced spin selectivity enables a room-temperature spin light-emitting diode. *Science* **2021,** *371* (6534), 1129-1133.

5. Seo, I. C.; Lim, Y.; An, S.-C.; Woo, B. H.; Kim, S.; Son, J. G.; Yoo, S.; Park, Q. H.; Kim, J. Y.; Jun, Y. C., Circularly Polarized Emission from Organic–Inorganic Hybrid Perovskites via Chiral Fano Resonances. *ACS Nano* **2021,** *15* (8), 13781-13793.

6. Chen, C.; Gao, L.; Gao, W.; Ge, C.; Du, X.; Li, Z.; Yang, Y.; Niu, G.; Tang, J., Circularly polarized light detection using chiral hybrid perovskite. *Nat. Commun.* **2019,** *10* (1), 1927.

7. Ishii, A.; Miyasaka, T., Direct detection of circular polarized light in helical 1D perovskite-based photodiode. *Sci Adv 6* (46), eabd3274.

8. Long, G.; Sabatini, R.; Saidaminov, M. I.; Lakhwani, G.; Rasmita, A.; Liu, X.; Sargent, E. H.; Gao, W., Chiral-perovskite optoelectronics. *Nat. Rev. Mater.* **2020,** *5* (6), 423-439.

9. Dang, Y.; Liu, X.; Cao, B.; Tao, X., Chiral halide perovskite crystals for optoelectronic applications. *Matter* **2021,** *4* (3), 794-820.

10. Qin, Y.; Gao, F.-F.; Qian, S.; Guo, T.-M.; Gong, Y.-J.; Li, Z.-G.; Su, G.-D.; Gao, Y.; Li, W.; Jiang, C.; Lu, P.; Bu, X.-H., Multifunctional Chiral 2D Lead Halide Perovskites

with Circularly Polarized Photoluminescence and Piezoelectric Energy Harvesting Properties. *ACS Nano* **2022,** *16* (2), 3221-3230.

11. Shpatz Dayan, A.; Wierzbowska, M.; Etgar, L., Ruddlesden–Popper 2D Chiral Perovskite-Based Solar Cells. *Small Structures* **2022,** *n/a* (n/a), 2200051.

12. Kim, Y.-H.; Song, R.; Hao, J.; Zhai, Y.; Yan, L.; Moot, T.; Palmstrom, A. F.; Brunecky, R.; You, W.; Berry, J. J.; Blackburn, J. L.; Beard, M. C.; Blum, V.; Luther, J. M., The Structural Origin of Chiroptical Properties in Perovskite Nanocrystals with Chiral Organic Ligands. *Adv. Funct. Mater.* **2022,** *32* (25), 2200454.

13. Ma, S.; Jung, Y.-K.; Ahn, J.; Kyhm, J.; Tan, J.; Lee, H.; Jang, G.; Lee, C. U.; Walsh, A.; Moon, J., Elucidating the origin of chiroptical activity in chiral 2D perovskites through nano-confined growth. *Nat. Commun.* **2022,** *13* (1), 3259.

14. Jiang, S.; Song, Y.; Kang, H.; Li, B.; Yang, K.; Xing, G.; Yu, Y.; Li, S.; Zhao, P.; Zhang, T., Ligand Exchange Strategy to Achieve Chiral Perovskite Nanocrystals with a High Photoluminescence Quantum Yield and Regulation of the Chiroptical Property. *ACS Appl. Mater. Interfaces* **2022,** *14* (2), 3385-3394.

15. Lin, J.-T.; Chen, D.-G.; Yang, L.-S.; Lin, T.-C.; Liu, Y.-H.; Chao, Y.-C.; Chou, P.-T.; Chiu, C.-W., Tuning the Circular Dichroism and Circular Polarized Luminescence Intensities of Chiral 2D Hybrid Organic–Inorganic Perovskites through Halogenation of the Organic Ions. *Angew. Chem. Int. Ed.* **2021,** *60* (39), 21434-21440.

16. Kim, Y.-H.; Zhai, Y.; Gaulding, E. A.; Habisreutinger, S. N.; Moot, T.; Rosales, B. A.; Lu, H.; Hazarika, A.; Brunecky, R.; Wheeler, L. M.; Berry, J. J.; Beard, M. C.; Luther, J. M., Strategies to Achieve High Circularly Polarized Luminescence from Colloidal Organic–Inorganic Hybrid Perovskite Nanocrystals. *ACS Nano* **2020,** *14* (7), 8816-8825.

17. Ahn, J.; Ma, S.; Kim, J.-Y.; Kyhm, J.; Yang, W.; Lim, J. A.; Kotov, N. A.; Moon, J., Chiral 2D Organic Inorganic Hybrid Perovskite with Circular Dichroism Tunable Over Wide Wavelength Range. *J. Am. Chem. Soc.* **2020,** *142* (9), 4206-4212.

18. Debnath, G. H.; Georgieva, Z. N.; Bloom, B. P.; Tan, S.; Waldeck, D. H., Using post-synthetic ligand modification to imprint chirality onto the electronic states of cesium lead bromide (CsPbBr3) perovskite nanoparticles. *Nanoscale* **2021,** *13* (36), 15248-15256.

19. Ben Moshe, A.; Szwarcman, D.; Markovich, G., Size Dependence of Chiroptical Activity in Colloidal Quantum Dots. *ACS Nano* **2011,** *5* (11), 9034-9043.

20. Zhou, Y.; Zhu, Z.; Huang, W.; Liu, W.; Wu, S.; Liu, X.; Gao, Y.; Zhang, W.; Tang, Z., Optical Coupling Between Chiral Biomolecules and Semiconductor Nanoparticles: Size-Dependent Circular Dichroism Absorption. *Angew. Chem. Int. Ed.* **2011,** *50* (48), 11456-11459.

21. Purcell-Milton, F.; Visheratina, A. K.; Kuznetsova, V. A.; Ryan, A.; Orlova, A. O.; Gun'ko, Y. K., Impact of Shell Thickness on Photoluminescence and Optical Activity in Chiral CdSe/CdS Core/Shell Quantum Dots. *ACS Nano* **2017,** *11* (9), 9207-9214.

22. Bi, C.; Yao, Z.; Sun, X.; Wei, X.; Wang, J.; Tian, J., Perovskite Quantum Dots with Ultralow Trap Density by Acid Etching-Driven Ligand Exchange for High Luminance and Stable Pure-Blue Light-Emitting Diodes. *Adv. Mater.* **2021,** *33* (15), 2006722.

23. Debnath, G. H.; Bloom, B. P.; Tan, S.; Waldeck, D. H., Room temperature doping of Ln3+ in perovskite nanoparticles: a halide exchange mediated cation exchange approach. *Nanoscale* **2022,** *14* (16), 6037-6051.

24. Li, Y.; Huang, H.; Xiong, Y.; Kershaw, S. V.; Rogach, A. L., Reversible transformation between CsPbBr3 and Cs4PbBr6 nanocrystals. *Cryst. Eng. Comm.* **2018,** *20* (34), 4900-4904.

25. Rodger, A., Norden, B., *Circular Dichroism and Linear Dichroism*. Oxford University Press: New York, 1997.

26. Dong, Y.; Qiao, T.; Kim, D.; Parobek, D.; Rossi, D.; Son, D. H., Precise Control of Quantum Confinement in Cesium Lead Halide Perovskite Quantum Dots via Thermodynamic Equilibrium. *Nano Lett.* **2018,** *18* (6), 3716-3722.

27. Cheng, O. H.-C.; Qiao, T.; Sheldon, M.; Son, D. H., Size- and temperature-dependent photoluminescence spectra of strongly confined CsPbBr3 quantum dots. *Nanoscale* **2020,** *12* (24), 13113-13118.

28. Brennan, M. C.; Herr, J. E.; Nguyen-Beck, T. S.; Zinna, J.; Draguta, S.; Rouvimov, S.; Parkhill, J.; Kuno, M., Origin of the Size-Dependent Stokes Shift in CsPbBr3 Perovskite Nanocrystals. *J. Am. Chem. Soc.* **2017,** *139* (35), 12201-12208.

29. Brennan, M. C.; Forde, A.; Zhukovskyi, M.; Baublis, A. J.; Morozov, Y. V.; Zhang, S.; Zhang, Z.; Kilin, D. S.; Kuno, M., Universal Size-Dependent Stokes Shifts in Lead Halide Perovskite Nanocrystals. *J. Phys. Chem. Lett.* **2020,** *11* (13), 4937-4944.

30. Protesescu, L.; Yakunin, S.; Bodnarchuk, M. I.; Krieg, F.; Caputo, R.; Hendon, C. H.; Yang, R. X.; Walsh, A.; Kovalenko, M. V., Nanocrystals of Cesium Lead Halide Perovskites (CsPbX3, X = Cl, Br, and I): Novel Optoelectronic Materials Showing Bright Emission with Wide Color Gamut. *Nano Lett.* **2015,** *15* (6), 3692-3696.

31. Li, Y.; Lai, R.; Luo, X.; Liu, X.; Ding, T.; Lu, X.; Wu, K., On the absence of a phonon bottleneck in strongly confined CsPbBr3 perovskite nanocrystals. *Chem. Sci.* **2019,** *10* (23), 5983-5989.

32. Georgieva, Z. N.; Bloom, B. P.; Ghosh, S.; Waldeck, D. H., Imprinting Chirality onto the Electronic States of Colloidal Perovskite Nanoplatelets. *Adv. Mater.* **2018,** *30* (23), 1800097.

33. He, T.; Li, J.; Li, X.; Ren, C.; Luo, Y.; Zhao, F.; Chen, R.; Lin, X.; Zhang, J., Spectroscopic studies of chiral perovskite nanocrystals. *Appl. Phys. Lett.* **2017,** *111* (15), 151102.

6.0 Magneto-Optical Detection of Photoinduced Magnetism via Chirality Induced Spin Selectivity in 2D Chiral Hybrid Organic-Inorganic Perovskites

This work was published as Hunag, Z., Bloom, B. P.; Ni, X.; Georgieva, Z. N.; Marciesky, M.; Vetter, E.; Liu, F.; Waldeck, D. H.; Sun, D., Magneto-Optical Detection of Photoinduced Magnetism via Chirality Induced Spin Selectivity in 2D Chiral Hybrid Organic-Inorganic Perovskites. ACS Nano 2020, 14, 8, 1037 and is adapted here with permission from the publisher. Copyright 2020 American Chemical Society. The author of the thesis synthesized the chiral material, established experimental parameters for sample preparation, and participated in the preparation of the manuscript.

The recent convergence of chiral molecules with metal halide perovskite frameworks gives rise to an interesting family of chiral systems: two-dimensional, chiral hybrid organic-inorganic perovskites (2D-chiral-HOIPs). While possessing photovoltaic properties of traditional HOIPs, this class of materials is endowed with chirality through its organic ligands in which the degeneracy of the electron spin in charge transport is broken, *i.e.*, the Chirality-Induced Spin Selectivity (CISS) effect manifests, making it a promising platform to bridge opto-spintronic studies and the CISS effect. In this work 2D-chiral-HOIP/NiFe heterostructures are studied by means of the magneto-optical Kerr effect using a Sagnac interferometer. Upon illumination of the HOIPs, the Kerr signal at the chiral-HOIP / NiFe interface changes and a linear dependence of the response on the magnetic field is observed. The sign of the slope was found to depend on the chirality of the HOIPs. The results demonstrate the utility of chiral-HOIP materials for chiral opto-spintronic applications.

6.1 Introduction

The growing field of spintronics research holds promise for a wide array of applications in information technology and quantum computation.[1, 2] The central focus of the spintronics field is the generation, manipulation, and detection of spin-encoded information. For example in a spin valve, one of the most important inventions in the spintronics field, spin current is generated through the spin-selective transport of magnetized ferromagnetic electrodes.[3] Recently, the chiral induced spin selectivity (CISS) effect[4-6] has been used to demonstrate device strategies that manipulate the electron spin quantum number for spintronic applications.[7-10] Spin selective transport has been observed for a variety of proteins, chiral molecules and their assemblies, oligopeptides, double stranded DNA, and inorganic semiconductors. Additionally, studies have shown that the electronic coupling between chiral molecules and ferromagnetic interfaces manifest 'spinterface' effects[11] - similar to those found in traditional achiral organic-ferromagnetic interfaces: induced magnetization[12-14] and manipulation of spin-to-charge conversion[15] - but they display a dependence on the enantiomeric form of the molecule.

This work examines the opto-spintronic response of chiral two-dimensional hybrid organic-inorganic perovskite (chiral-2D-HOIP) films in relation to the CISS effect. Previous studies have shown the promise of achiral 2D-HOIPs for opto-spintronic applications owing to their large tunable spin-orbit couplings and spin dependent optical selection rules.[16, 17] The recent advances for imparting chirality onto perovskite nanostructures[18-22] gives rise to a class of materials that possesses chiro-optical activity, as well as the photovoltaic properties traditionally present in HOIPs. Furthermore, magnetic conductive probe atomic force microscopy and magnetoresistance measurements show that 2D-chiral-HOIP films exhibit spin filtering capabilities consistent with the predicted CISS effect.[23]

Here, the magnetic field effects of 2D-chiral-HOIPs interfaced with NiFe contacts are studied using the magneto-optic Kerr effect (MOKE). This technique was chosen because of its proven sensitivity to small amounts of spin accumulation.[24, 25] Figure 6.1 outlines the general scheme of the experiment. A 405 nm laser photoexcites the 2D-chiral-HOIP, and a Sagnac interferometer is used to probe the change in out-of-plane magnetization using a 1550 nm laser beam that is incident on the sample's surface along its normal direction. As a result of the 2D-chiral-HOIP's optoelectronic response and the CISS effect, a spin-polarized photocurrent should manifest and introduce an effective net magnetization to the top NiFe layer at the interface (Figure 6.1). This all-optical excitation and measurement scheme demonstrates an alternative approach for studying the CISS effect which is not prone to artifacts from charging and shorting that can occur in electrical transport measurements.

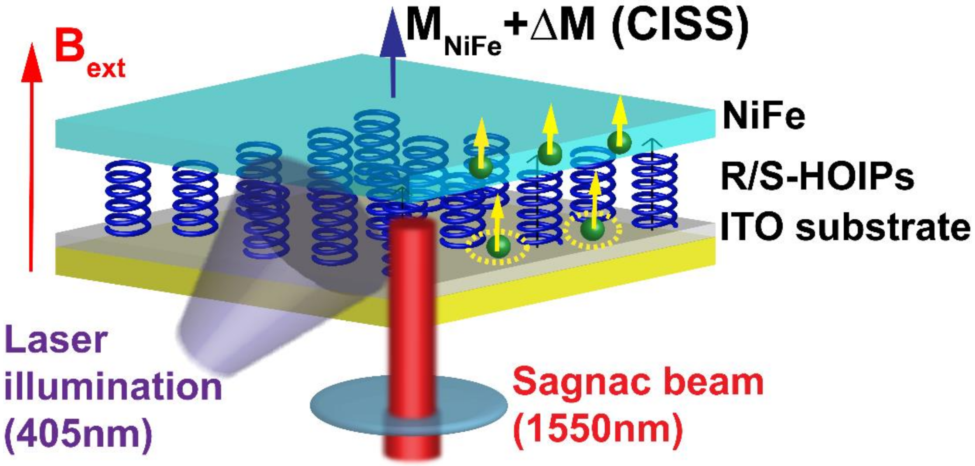

Figure 6.1 A sketch of a generalized scheme describing the Sagnac MOKE experiment for the light-driven CISS-induced interfacial magnetization at the interface of *R*/*S*-chiral-HOIP and NiFe substrate. The HOIP is illuminated by a 405 nm laser through the ITO substrate. The resulting extra out-of-plane magnetization ($\Delta\mathbf{M}(\mathbf{CISS})$) at the 2D-chiral-HOIP/NiFe interface is measured by Sagnac MOKE approach. The blue springs represent the HOIPs and the green dots represent the spin-polarized photogenerated carriers (yellow arrows) under the illumination.

6.2 Results and Discussion

The synthesis of 2D-chiral-HOIPs was performed following previously published protocols[26] and then spin-coated onto pre-cleaned Indium Tin Oxide (ITO) substrates. The chiral perovskite comprises 1-phenylethylamonium lead iodide ($(C_8H_{11}N)_2PbI_4$). The scheme in Figure 6.2a depicts the layered structure of the HOIP and illustrates how the chiral *S*- or *R*-phenylethylamine (*S*/*R*-PEA) ligands separate the lead halide octahedral layers. Figure 6.2b shows representative circular dichroism spectra of the HOIPs using *S*- (green, *S*-HOIP) *R*-phenylethylamine (purple, *R*-HOIP) films, which exhibit an approximate mirror image symmetry. After the R/S-HOIP film formation, 15 nm of ferromagnetic NiFe was evaporated using e-beam deposition on top of the chiral-HOIP layer (see Methods).

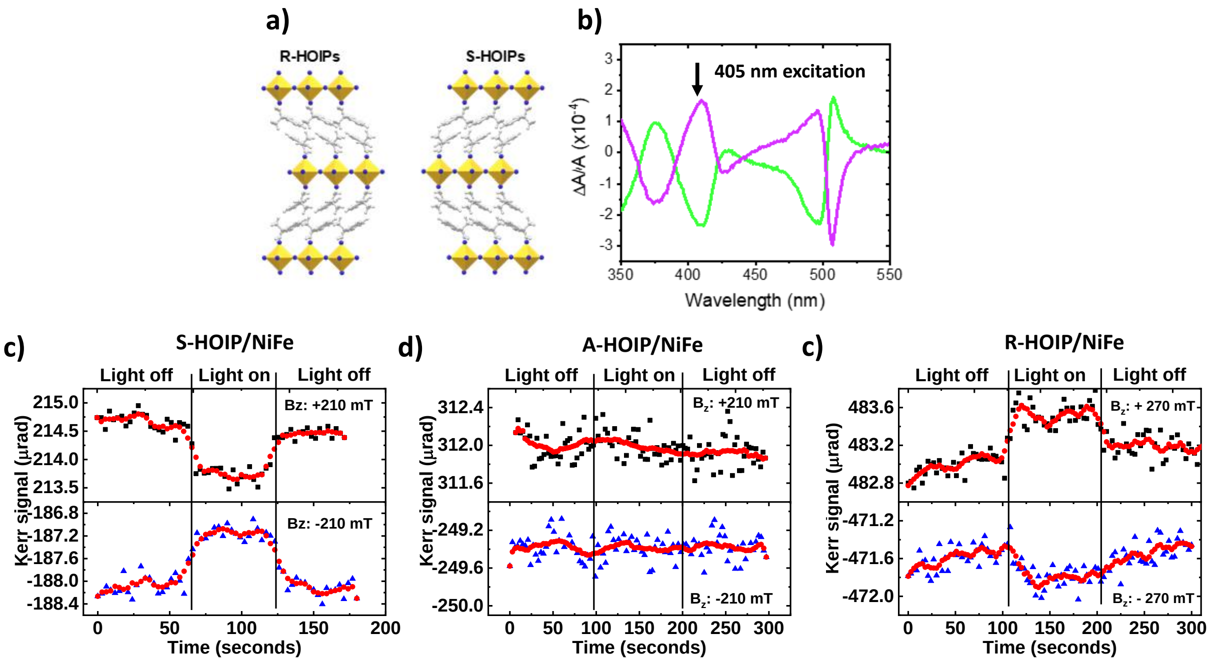

Figure 6.2 Panel a) shows a cartoon illustrating the chiral structure of the *S*- (left) and *R*-HOIPs (right). Panel b) shows the measured CD spectra for *S*-HOIP (green) and *R*-HOIP (purple) thin films. Panels c)-e) show the change in Kerr signal upon photoexcitation for samples with *S*-HOIP/NiFe, A-HOIP/NiFe, and *R*-HOIP/NiFe under positive

(top, black) and negative (bottom, blue) out-of-plane external magnetic field, respectively. The red line is an adjacent average smoothing of the data.

The prepared sample was placed in an electromagnet and the magnetic field was applied along the out-of-plane direction (Fig. G.1). The sample area was illuminated through the transparent ITO substrate by 405 nm light from a diode laser. The sample was illuminated at a low laser intensity ($\leq$ 0.6 mW) to suppress laser-induced heating. The Kerr signal was collected by the Sagnac probing beam (1550nm) through the backside of the sample and overlapping with the 405 nm illumination area at the HOIP/NiFe interface. Because the chiral-HOIP layer has no absorbance at 1550 nm, this experimental design enables direct measurement of the magnetic response at the chiral-HOIP/NiFe interface without perturbing the system. It is anticipated that the out-of-plane net magnetization response stemming from the CISS effect coincides with the polar MOKE configuration, which has the highest Kerr sensitivity (Fig. G.1). The laser power of the probing Sagnac beam was kept < 20 μW to prevent potential laser-induced heating.[22, 24] Changes in the Kerr response under the laser illumination were recorded as a function of time. Comparison of the response under 405 nm illumination to the response in the dark was used to separate the photoresponse from the total magnetization of the NiFe film and the background drift.

Panels (c), (d), and (e) of Figure 6.2 show the time evolution of the Kerr angle and how it changes under 405 nm illumination for different external magnetic field directions and for three different sample types: S-HOIPs/NiFe (Fig 6.2c), A-HOIPs/NiFe (Fig 6.2d), and R-HOIP/NiFe (Fig 6.2e). The data reveal that the photoinduced Kerr response is sensitive to both the chirality of the HOIPs and the external magnetic field. At B_z = +210 mT, the S- HOIPs (Fig. 6.2c, top) exhibit a decrease in Kerr signal upon photoexcitation on the order of a microradian ($\Delta\theta_{Kerr} \approx -0.8\, \mu rad$), whereas the R-HOIP/NiFe (Fig. 6.2e, top) display an increase in Kerr signal upon photoexcitation. When the external magnetic field is reversed, an opposite change of Kerr signal is observed in both samples. In contrast to the chiral-HOIP/NiFe samples, the same experiment has been performed on achiral-HOIP/NiFe samples, using 2-phenylethylamine ligands (A-HOIPs). The achiral sample does not exhibit any significant change in Kerr signal upon photoexcitation (Fig. 6.2d). These data suggest that photoexcitation generates a magnetization at the NiFe surface (*i.e.*, the extra Kerr signal) which adds to the magnetization of the NiFe film and that the sign of the spin-polarization depends on the chirality of the chiral-HOIPs, thus implying that the photocurrent generated in the chiral films must be spin-polarized.

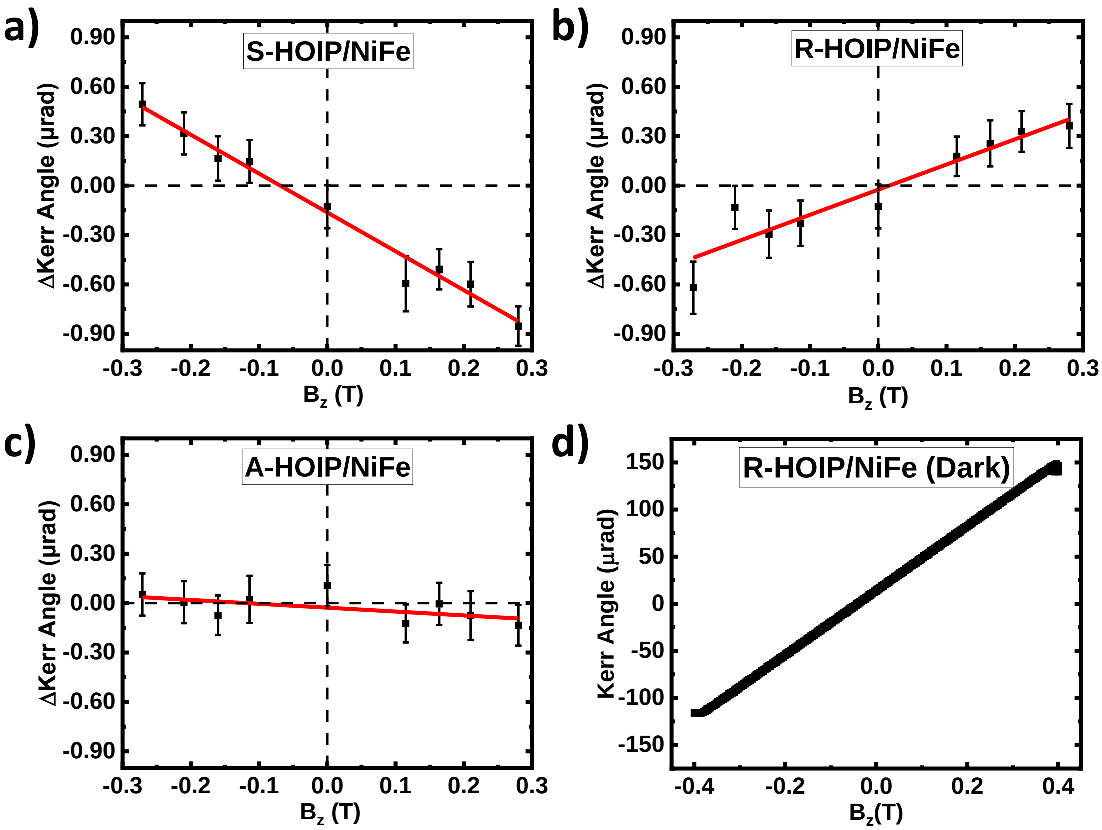

Figure 6.3 The photoinduced change in the Kerr angle (black, squares) is plotted as a function of external magnetic field. Panels a), b), and c) correspond to *S*-HOIP/NiFe, A-HOIP/NiFe, and *R*-HOIP/NiFe, respectively. The red line is a linear fit to the data. The Kerr signals have been averaged by four cycles of the illumination to improve the signal-to-noise. (d) Out-of-plane overall M-H loop for the *R*-HOIP/NiFe sample measured by Sagnac MOKE without the illumination. Note that a 1.0 μrad change in the Kerr angle corresponds to ~3mT.

Figure 6.3a, 6.3b, and 6.3c show the magnetic field dependence of the photoinduced Kerr signal for *S*-HOIP/NiFe, A-HOIP/NiFe, and *R*-HOIP/NiFe samples, respectively. The change in Kerr angle exhibits a linear dependence on the external magnetic field, showing no saturation up to 0.3 T. The *S*-HOIP/NiFe (Fig. 6.3a) gives a slope of -2.36 μrad/T with an error of ±0.11 μrad. The *R*-HOIP/NiFe (Fig. 6.3c) shows a slope of +1.53 μrad/T with an error of ±0.20 μrad/T. The fitting errors here are mainly determined by the Sagnac sensitivity and sample stability under the light illumination as shown in Fig. 6.2. The A-HOIP/NiFe gives a best fit slope of -0.23 μrad/T which is roughly within the error of ±0.13 μrad/T, indicating no significant response over this magnetic field range. Thus, the photogenerated magnetic response changes significantly with the external magnetic field for the chiral samples and has opposite signs for the two enantiomers (*R*-HOIP and *S*-HOIP), Conversely, the A-HOIP does not display a significant photoresponse or applied field dependence.

By scaling the MOKE signal $\Delta\theta_{Kerr}$ for the *R*-HOIP/NiFe in the dark to its known magnetization, it is possible to estimate the size of the photogenerated magnetization from the photogenerated change in $\Delta\theta_{Kerr}$. The Kerr signal of the *R*-HOIP/NiFe sample in the dark is $\sim 150\ \mu rad$ (see Fig. 3d), whereas the photoinduced $\Delta\theta_{Kerr}$ is $\sim 1\ \mu rad$, so that the effective photogenerated magnetization, ΔM, is about 0.7% of the total observed magnetization. This comparison indicates that an effective out-of-plane magnetic field of ~ ±2 mT acts on the NiFe layer. Note, while it is believed that ΔM is rooted in spin polarization mediated effects, the percent change in magnetic field does necessitate a similar magnitude of spin polarization. The magnitude of the photoinduced effective field is orders of magnitude lower than that estimated from photoemission measurements at DNA/Au interfaces (up to tens of Tesla[23]), but it is consistent with recent observations of the NiFe/chiral-molecule interface using the anomalous Hall effect.[13]

Elucidating the origins of these differences requires further study, however it could arise from limited photogenerated carriers under the low light intensity (< 0.6 mW) and differences in spin relaxation rates for the two types of experiments, among others.

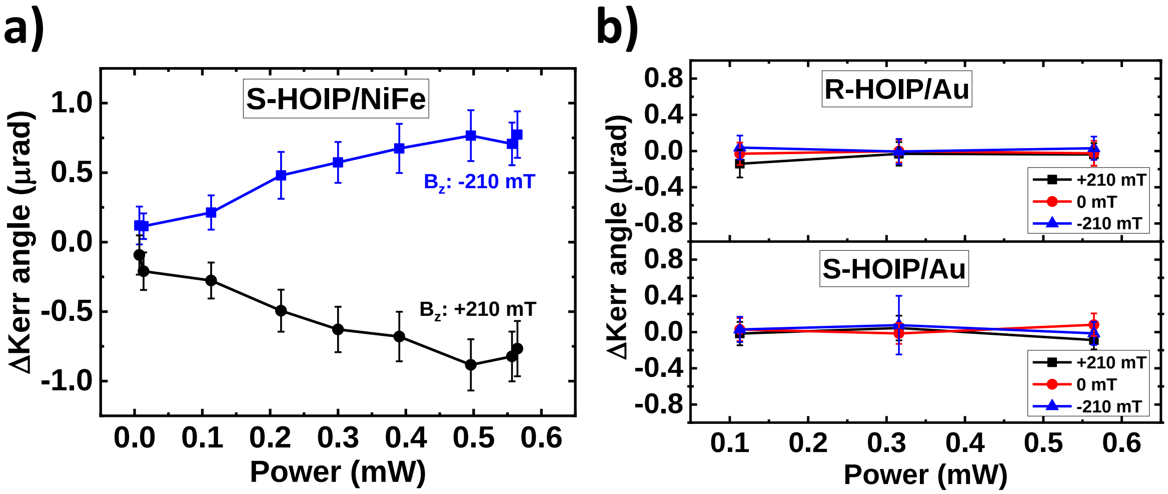

Figure 6.4 Excitation power dependence studies of the ΔKerr angle. Panel a) shows the power dependence for S-HOIP/NiFe under +210 mT (Black, circles) and -210 mT (blue, squares) external magnetic field. Panel b) shows experiments of architectures in which the NiFe layer is replaced by gold for both R- (top) and S-HOIP/Au (bottom) with +210 mT (blue), 0 mT (red), and -210 mT (black) external magnetic fields.

The influence of the incident excitation (405 nm) power on the magnitude of the Kerr signal was measured and is shown in Fig. 6.4. Figure 6.4a shows the change in Kerr angle for samples fabricated with *S*-HOIPs under a positive (blue, circles) and negative (black, squares) magnetic field, respectively. The $\Delta\theta_{Kerr}$ signal in the *S*- HOIP/NiFe sample decreases (increases) when the illumination intensity increases at positive (negative) magnetic fields, until it saturates at ~0.6 mW. An increase in photon flux generates a larger change in the Kerr angle, presumably arising from more photocurrent density in the HOIP film, and hence results in more exchange current with the ferromagnetic substrate that increases the net magnetization. The saturation at the low light intensity implies an interfacial effect instead of a bulk photocurrent in the thick chiral-HOIPs film

(~300nm) which is consistent with the spin diffusion length of the generated spin-polarized carriers is limited to within 5 nm at room temperature.[27, 28]

To further validate that the exchange current between the adjacent ferromagnetic NiFe layer and spin-polarized photocarriers in the chiral-HOIPs gives rise to the extra Kerr signals, control architectures were studied in which the NiFe layer was replaced with Au (Figure 6.4b). The data shown in Fig. 6.4b for *R*-HOIP/Au (top) and *S*-HOIP/Au (bottom), at applied magnetic fields of +210 mT, (black), 0 mT (red), and -210 mT (blue), show no discernable change in Kerr signal upon photoexcitation. To eliminate the possibility of magnetic fields generated by sample heating or direct photoexcitation effects of the ferromagnetic substrate, control experiments were performed in which NiFe was deposited directly onto an ITO substrate; architectures without the presence of chiral-HOIPs. These data are presented in Figure G.2-G.3 and show that no substantial change in Kerr angle occurs for these samples. As a further control experiment, the chiral-HOIP/NiFe assemblies were also studied under 808 nm illumination (Figure G.4), for which the perovskite absorbance is negligible, and in this case no Kerr response was observed. Thus, the laser heating-related reduction of the bulk magnetization in the NiFe can be excluded, as can the change of the Verdet constant of the chiral-HOIPs.[29] Therefore, the photoinduced Kerr response of the chiral-HOIP/NiFe assemblies require both the chiral-HOIP and the ferromagnetic layer; namely, the spin-polarized photogenerated carriers in the chiral-HOIP film are needed to 'activate' the interfacial magnetization of the adjacent ferromagnet.

We propose that the observed changes in the photoinduced Kerr signal manifest from contributions of two correlated phenomena: (i) a spin-filtering of the photogenerated carriers *via* the CISS effect and (ii) a hybridization/magnetic proximity effect at the 'spinterface' formed between the chiral-HOIP and the ferromagnetic layer. DFT calculations have been performed to study the possible magnetic proximity effect between the NiFe substrate and the chiral-HOIPs (see Fig.G.6-G.8). To simplify the calculation, only the 'active' component, *i.e.*, the chiral molecules which align perpendicularly as those in the HOIP crystal structure, but without adding the PbI_6 inorganic framework, were considered. The configurations of *R*-PEA/NiFe and *S*-PEA/NiFe with the chiral centers of *R*(*S*)-PEA facing the NiFe substrate (lattice constant of 4.997 Å) are shown in Fig. G.6(b) and (c), respectively. The calculated density of states (DOS) of NiFe, *R*-PEA/NiFe, and *S*-PEA/NiFe [Fig. G.6(d) to (e)], indicate that there is not a significant change of the spin-polarization degree in the DOS in Ni or Fe atoms after the addition of the chiral molecules. The molecular chirality alone is unlikely to cause a change of magnetization of the NiFe substrate directly because of the relatively poor coupling. Therefore, we hypothesize that the inorganic perovskite framework, hybridized with its frontier molecular orbitals and imprinted with the chiral molecules, must be responsible for the observed photoinduced magnetism *via* the CISS effect. It is possible that the CISS effect in chiral-HOIPs not only generates spin-polarized current, but also forms 'local' magnetic states which may be coupled or mediated by polarons or delocalized carriers that are formed in the metal−halogen framework under photoexcitation.[30, 31]

A strong inter- or intra-layer coupling may result in an effective net magnetization even at room temperature, which changes as a function of external magnetic field as shown in Fig. 6.5. We anticipate that the generation of carriers/polarons are crucial in determining the amplitude of the CISS effect, exchange couplings, and resulting interfacial magnetization, which requires further studies to understand sufficiently.

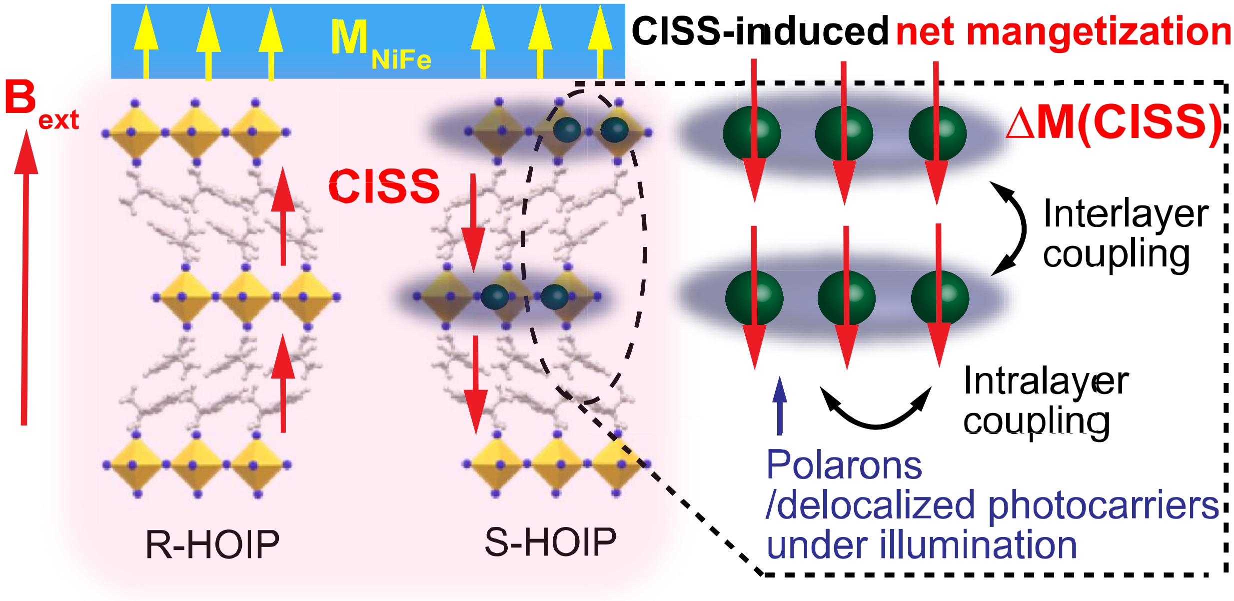

Figure 6.5 Schematic illustration of the proposed photoinduced magnetism at the NiFe/chiral-HOIP interface. The generation of a net magnetization mediated by spin-dependent polarons/photocarriers *via* the CISS effect is formed in the chiral-HMH structure next to the NiFe layer under the illumination.

6.3 Summary

This work demonstrates the rich characteristics of chiral-HOIPs for bridging opto-spintronic applications with the CISS effect, *i.e.* chiral opto-spintronics. Magneto-optic Kerr rotation measurements prove that linearly polarized excitation of chiral-HOIPs can change the magnetization of an adjacent ferromagnetic substrate. Demonstration of the existence of interfacial magnetization states *via* the CISS effect in chiral-HOIPs may aid in developing quantitative models for CISS by relaxing the large spin orbit coupling condition required for the proposed CISS effect. This will shed light on CISS-related behaviors observed in other chiral systems. Moreover, the Sagnac MOKE technique provides a means to directly probe the net magnetization at the molecular level and allows for ‘benchtop’ precise magnetic measurements without large scale facilities.

6.4 Experimental Methods

6.4.1 Chiral Perovskite Material Synthesis

Chiral 2D-HOIPs were synthesized following previously published protocols.[26] Briefly, 200 mg of PbO was dissolved in 6.0 mL of 57% HI solution and 200μL of either *R*-, or *S*-phenylethylamine was added to the solution. The combination resulted in a precipitate which was dissolved by heating in a silicone oil bath at 100°C. The reaction was then slowly cooled to room temperature, causing crystallization. The crystallites were collected and washed three times with toluene using a Buchner funnel and then dried in a desiccator for two days before use. For the preparation of achiral 2D-HOIPs an equimolar amount of 2-phenylethylamine was used in place of the *R*- or *S*-phenylethylamine.

6.4.2 Sample Preparation and Sagnac MOKE Measurement

The fabrication of all devices for MOKE measurements was performed using a nitrogen filled glove box. A 25% by mass solution of the HOIP crystallites was dissolved in DMF and ~0.15μL/mm^2 of solution was drop cast onto a freshly cleaned ITO substrate. The substrate was then spun at 5000 rpm for 30 seconds and then baked at 100 °C for 8 min. E-beam evaporation was then used to deposit 15 nm of either NiFe or Au onto the substrate at a rate of 0.2Å/s, followed by a careful encapsulation to prevent the thin film from degrading during the measurement. The prepared sample was placed in an electromagnet (GMW Associates). The Kerr signal was measured in a Faraday configuration (*i.e.*, Polar MOKE configuration) at room temperature. The spot size for the overlapped laser illumination and Sagnac beam is 1mm and 0.5 mm, respectively. 405 nm is chosen because of the maximum circular dichroism response in *R*- and *S*-HOIP thin films at this wavelength, as shown in Fig. 6.2 b). The Kerr signals have been averaged by four cycles of the illumination to improve the signal-to-noise.

6.4.3 DFT Calculations

The first-principles calculations were performed using the Vienna ab initio Simulation Package (VASP) based on the projected augmented wave approach within the framework of density functional theory.[32, 33] The generalized gradient approximation (GGA) in the Perdew, Burke, and Ernzerhof (PBE) form was used for the exchange-correlation functional.[34, 35] All the self-consistent calculations were performed with a plane-wave cutoff of 500 eV on a 11×11×1 Monkhorst-Pack k-point mesh. A vacuum layer with a thickness of larger than 15 Å was adopted to ensure the decoupling between the neighboring slabs under the periodic boundary condition. All the structures were fully relaxed until the atomic force was less than 0.01 eV/Å. The molecular properties of *R*(*S*)-PEA were carried out using Gaussian16 with B3LYP functional and 3-21G basis set.[36]

6.5 References

1. Wolf, S. A.; Awschalom, D. D.; Buhrman, R. A.; Daughton, J. M.; von Molnár, S.; Roukes, M. L.; Chtchelkanova, A. Y.; Treger, D. M., Spintronics: A Spin-Based Electronics Vision for the Future. *Science* **2001,** *294* (5546), 1488.

2. Wolf, S. A.; Chtchelkanova, A. Y.; Treger, D. M., Spintronics—A retrospective and perspective. *IBM J. Res. Dev.* **2006,** *50* (1), 101-110.

3. Bader, S. D.; Parkin, S. S. P., Spintronics. *Annu. Rev. Condens. Matter Phys.* **2010,** *1* (1), 71-88.

4. Naaman, R.; Paltiel, Y.; Waldeck, D. H., Chiral molecules and the electron spin. *Nat. Rev. Chem.* **2019,** *3* (4), 250-260.

5. Naaman, R.; Waldeck, D. H., Chiral-Induced Spin Selectivity Effect. *J. Phys. Chem. Lett.* **2012,** *3* (16), 2178-2187.

6. Naaman, R.; Waldeck, D. H., Spintronics and Chirality: Spin Selectivity in Electron Transport Through Chiral Molecules. *Annu. Rev. Phys. Chem.* **2015,** *66* (1), 263-281.

7. Dor, O. B.; Yochelis, S.; Mathew, S. P.; Naaman, R.; Paltiel, Y., A chiral-based magnetic memory device without a permanent magnet. *Nat. Commun.* **2013,** *4* (1), 2256.

8. Koplovitz, G.; Primc, D.; Ben Dor, O.; Yochelis, S.; Rotem, D.; Porath, D.; Paltiel, Y., Magnetic Nanoplatelet-Based Spin Memory Device Operating at Ambient Temperatures. *Adv. Mater.* **2017,** *29* (17), 1606748.

9. Michaeli, K.; Varade, V.; Naaman, R.; Waldeck, D. H., A new approach towards spintronics–spintronics with no magnets. *J. Phys.: Condens. Matter* **2017,** *29* (10), 103002.

10. Al-Bustami, H.; Koplovitz, G.; Primc, D.; Yochelis, S.; Capua, E.; Porath, D.; Naaman, R.; Paltiel, Y., Single Nanoparticle Magnetic Spin Memristor. *Small* **2018,** *14* (30), 1801249.

11. Sanvito, S., The rise of spinterface science. *Nat. Phys.* **2010,** *6* (8), 562-564.

12. Ben Dor, O.; Morali, N.; Yochelis, S.; Baczewski, L. T.; Paltiel, Y., Local Light-Induced Magnetization Using Nanodots and Chiral Molecules. *Nano Lett.* **2014,** *14* (11), 6042-6049.

13. Ben Dor, O.; Yochelis, S.; Radko, A.; Vankayala, K.; Capua, E.; Capua, A.; Yang, S.-H.; Baczewski, L. T.; Parkin, S. S. P.; Naaman, R.; Paltiel, Y., Magnetization switching in ferromagnets by adsorbed chiral molecules without current or external magnetic field. *Nat. Commun.* **2017,** *8* (1), 14567.

14. Koplovitz, G.; Leitus, G.; Ghosh, S.; Bloom, B. P.; Yochelis, S.; Rotem, D.; Vischio, F.; Striccoli, M.; Fanizza, E.; Naaman, R.; Waldeck, D. H.; Porath, D.; Paltiel, Y., Single Domain 10 nm Ferromagnetism Imprinted on Superparamagnetic Nanoparticles Using Chiral Molecules. *Small* **2019,** *15* (1), 1804557.

15. Ghosh, S.; Mishra, S.; Avigad, E.; Bloom, B. P.; Baczewski, L. T.; Yochelis, S.; Paltiel, Y.; Naaman, R.; Waldeck, D. H., Effect of Chiral Molecules on the Electron's Spin Wavefunction at Interfaces. *J. Phys. Chem. Lett.* **2020,** *11* (4), 1550-1557.

16. Odenthal, P.; Talmadge, W.; Gundlach, N.; Wang, R.; Zhang, C.; Sun, D.; Yu, Z.-G.; Valy Vardeny, Z.; Li, Y. S., Spin-polarized exciton quantum beating in hybrid organic–inorganic perovskites. *Nat. Phys.* **2017,** *13* (9), 894-899.

17. Zhang, C.; Sun, D.; Sheng, C. X.; Zhai, Y. X.; Mielczarek, K.; Zakhidov, A.; Vardeny, Z. V., Magnetic field effects in hybrid perovskite devices. *Nat. Phys.* **2015,** *11* (5), 427-434.

18. Dong, Y.; Zhang, Y.; Li, X.; Feng, Y.; Zhang, H.; Xu, J., Chiral Perovskites: Promising Materials toward Next-Generation Optoelectronics. *Small* **2019,** *0* (0), 1902237.

19. Georgieva, Z. N.; Bloom, B. P.; Ghosh, S.; Waldeck, D. H., Imprinting Chirality onto the Electronic States of Colloidal Perovskite Nanoplatelets. *Adv. Mater.* **2018,** *30* (23), 1800097.

20. Long, G.; Jiang, C.; Sabatini, R.; Yang, Z.; Wei, M.; Quan, L. N.; Liang, Q.; Rasmita, A.; Askerka, M.; Walters, G.; Gong, X.; Xing, J.; Wen, X.; Quintero-Bermudez, R.; Yuan, H.; Xing, G.; Wang, X. R.; Song, D.; Voznyy, O.; Zhang, M.; Hoogland, S.; Gao, W.; Xiong, Q.; Sargent, E. H., Spin control in reduced-dimensional chiral perovskites. *Nat. Photonics* **2018,** *12* (9), 528-533.

21. Xiao, L.; An, T.; Wang, L.; Xu, X.; Sun, H., Novel properties and applications of chiral inorganic nanostructures. *Nano Today* **2020,** *30*, 100824.

22. Long, G.; Zhou, Y.; Zhang, M.; Sabatini, R.; Rasmita, A.; Huang, L.; Lakhwani, G.; Gao, W., Theoretical Prediction of Chiral 3D Hybrid Organic–Inorganic Perovskites. *Adv. Mater.* **2019,** *31* (17), 1807628.

23. Lu, H.; Wang, J.; Xiao, C.; Pan, X.; Chen, X.; Brunecky, R.; Berry, J. J.; Zhu, K.; Beard, M. C.; Vardeny, Z. V., Spin-dependent charge transport through 2D chiral hybrid lead-iodide perovskites. *Sci Adv* **2019,** *5* (12), eaay0571-eaay0571.

24. Liu, H.; McLaughlin, R.; Sun, D.; Vardeny, Z. V., Long-range transverse spin Seebeck effect in permalloy stripes using Sagnac interferometer microscopy. *J. Phys. D: Appl. Phys.* **2018,** *51* (13), 134003.

25. McLaughlin, R.; Sun, D.; Zhang, C.; Groesbeck, M.; Vardeny, Z. V., Optical detection of transverse spin-Seebeck effect in permalloy film using Sagnac interferometer microscopy. *Phys. Rev. B* **2017,** *95* (18), 180401.

26. Ahn, J.; Lee, E.; Tan, J.; Yang, W.; Kim, B.; Moon, J., A new class of chiral semiconductors: chiral-organic-molecule-incorporating organic–inorganic hybrid perovskites. *Mater. Horiz.* **2017,** *4* (5), 851-856.

27. Sun, D.; Zhang, C.; Kavand, M.; van Schooten, K. J.; Malissa, H.; Groesbeck, M.; McLaughlin, R.; Boehme, C.; Valy Vardeny, Z. Spintronics of Organometal Trihalide Perovskites **2016**, p. arXiv:1608.00993.

28. Sun, D.; Zhang, C.; Kavand, M.; Wang, J.; Malissa, H.; Liu, H.; Popli, H.; Singh, J.; Vardeny, S. R.; Zhang, W.; Boehme, C.; Vardeny, Z. V., Surface-enhanced spin current to charge current conversion efficiency in CH3NH3PbBr3-based devices. *J. Chem. Phys.* **2019,** *151* (17), 174709.

29. Yu, Z. G., Effective-mass model and magneto-optical properties in hybrid perovskites. *Sci. Rep.* **2016,** *6* (1), 28576.

30. Thouin, F.; Valverde-Chávez, D. A.; Quarti, C.; Cortecchia, D.; Bargigia, I.; Beljonne, D.; Petrozza, A.; Silva, C.; Srimath Kandada, A. R., Phonon coherences reveal the polaronic character of excitons in two-dimensional lead halide perovskites. *Nat. Mater.* **2019,** *18* (4), 349-356.

31. Yin, J.; Li, H.; Cortecchia, D.; Soci, C.; Brédas, J.-L., Excitonic and Polaronic Properties of 2D Hybrid Organic–Inorganic Perovskites. *ACS Energy Lett.* **2017,** *2* (2), 417-423.

32. Kresse, G.; Hafner, J., Ab initio molecular dynamics for liquid metals. *Phys. Rev. B* **1993,** *47* (1), 558-561.

33. Kresse, G.; Furthmüller, J., Efficient iterative schemes for ab initio total-energy calculations using a plane-wave basis set. *Phys. Rev. B* **1996,** *54* (16), 11169-11186.

34. Perdew, J. P.; Burke, K.; Ernzerhof, M., Generalized Gradient Approximation Made Simple. *Phys. Rev. Lett.* **1996,** *77* (18), 3865-3868.

35. Perdew, J. P.; Burke, K.; Ernzerhof, M., Generalized Gradient Approximation Made Simple *Phys. Rev. Lett.* **1997,** *78* (7), 1396-1396.

36. Frisch, M. J.; Trucks, G. W.; Schlegel, H. B.; Scuseria, G. E.; Robb, M. A.; Cheeseman, J. R.; Scalmani, G.; Barone, V.; Petersson, G. A.; Nakatsuji, H.; Li, X.; Caricato, M.; Marenich, A. V.; Bloino, J.; Janesko, B. G.; Gomperts, R.; Mennucci, B.; Hratchian, H. P.; Ortiz, J. V.; Izmaylov, A. F.; Sonnenberg, J. L.; Williams; Ding, F.; Lipparini, F.; Egidi, F.; Goings, J.; Peng, B.; Petrone, A.; Henderson, T.; Ranasinghe, D.; Zakrzewski, V. G.; Gao, J.; Rega, N.; Zheng, G.; Liang, W.; Hada, M.; Ehara, M.; Toyota, K.; Fukuda, R.; Hasegawa, J.; Ishida, M.; Nakajima, T.; Honda, Y.; Kitao, O.; Nakai, H.; Vreven, T.; Throssell, K.; Montgomery Jr., J. A.; Peralta, J. E.; Ogliaro, F.; Bearpark, M. J.; Heyd, J. J.; Brothers, E. N.; Kudin, K. N.; Staroverov, V. N.; Keith, T. A.; Kobayashi, R.; Normand, J.; Raghavachari, K.; Rendell, A. P.; Burant, J. C.; Iyengar, S. S.; Tomasi, J.; Cossi, M.; Millam, J. M.; Klene, M.; Adamo, C.; Cammi, R.;

Ochterski, J. W.; Martin, R. L.; Morokuma, K.; Farkas, O.; Foresman, J. B.; Fox, D. J. *Gaussian 16 Rev. C.01*, Wallingford, CT, **2016**.

7.0 Concluding Remarks

This dissertation has focused on the development of new methodologies for preparing chiral perovskite nanomaterials, as well as on gaining a better understanding of their properties and the origin of their chirality. The works detailed in the chapters above have contributed significantly to a field in its infancy, where the employment of chiral perovskites in new technologies and devices is wholly contingent upon the establishment of a robust library of compositions and morphologies, as well as the establishment of structure-property relationships.

Chapter 2 detailed the first ever report of chiral perovskite NPLs generated via direct synthesis in the presence of achiral octylamine and chiral phenylethylammonium ligands. These methylammonium lead bromide nanoplatelets exhibited strong CD signals, which were energetically aligned with the first excitonic transition of the perovskite itself. Based on this finding, we posited that the chiral response results from electronic imprinting from the chiral ligand onto the electronic structure of the that the perovskite NPL. The method reported in Chapter 2 was also used to generate chiral NPLs with tunable CD features by altering the material's band gap through its halide composition.

Chapter 3 built on our understanding of chirality in perovskite NPLs through a comprehensive study of the role of ligand shell in the imprinting mechanism. Methylammonium lead halide nanoplatelets were synthesized with bromide and chloride anions, as well as with three different chiral molecules embedded in the ligand shell. Nuclear magnetic resonance was used to measure the ratio between chiral and achiral ligands on the NPL surface to establish a correlation between the composition of the ligand shell and CD intensity. We found a non-linear relationship between the chiral ligand ratio and the CD signal, with a plateau of the CD intensity occurring at high chiral:achiral ratios. These experimental results were corroborated by a chirally-imprinted particle in a box model calculation which suggested that orientational averaging at high chiral ligand ratios caused the CD plateau.

Another method for chiral imprinting was presented in Chapter 4, this time on highly quantum-confined all-inorganic cesium lead bromide nanoparticles. Strong CD features were generated via a post-synthetic ligand modification procedure with three different chiral ligands. Concentration-dependence and temperature-dependence studies of the chiroptical properties were performed and found that the imprinting was robust but its intensity was influenced by these experimental conditions. Electronic coupling between the chiral ligand and the nanoparticle was suggested as the mechanism for chiral imprinting.

Chapter 5 examines the size-dependence of chiroptical properties in $CsPbBr_3$ nanoparticles. Three size-regimes of nanoparticles ligand-exchanged with chiral methylphenethylammonium ligands were studied via CD spectroscopy and quantitative proton NMR. CD intensities decreased significantly as nanoparticles approached the limit of the quantum-confined regime. It was found that the relationship between chiral ligand coverage and CD intensity varies with nanoparticle size, i.e. smaller regimes exhibiting an opposite dependence on the amount of chiral ligand, and larger sizes showing no dependence at all.

The magneto-optical properties of 2D chiral organic-inorganic perovskite films were examined in Chapter 4. Linearly polarized excitation of the perovskite material was found via magneto-optic Kerr rotation measurements to change the magnetization of an adjacent ferromagnetic substrate. This behavior suggests that the CISS effect generates interfacial magnetization states in chiral 2D perovskites

The work in this dissertation focused on electronic chiral imprinting of colloidal platelet- and cube-shaped perovskite nanoparticles. While the chapters above have laid a foundation for generating and studying chiral perovskites, much about their properties remains unexplored and challenges with material stability await a solution. For example, studies of chiral imprinting mechanisms in perovskites have examined one mechanism at a time, however, the presence of multiple mechanisms of chiral imprinting within a single structure remains unexplored and its effects are unknown. Another challenge ahead of perovskites is their susceptibility to degradation due to moisture and UV light exposure. Advancements in stability have been achieved in the field of achiral perovskites but have yet to be incorporated into the current strategies for creating chiral perovskites. Finally, opportunities for applications of chiral perovskites, such as employing chiral perovskites in a solar cell, require further development. It is hoped that the contributions of this thesis will aid in the future growth and development of this new field.

Appendix A

Appendix A.1 Circular Dichroism: Theoretical Background

Circular dichroism, or CD, is most simply defined as the difference in absorption of left and right circularly polarized light. A difference in light-matter interactions between left and right circularly polarized light is a property solely exhibited by chiral materials; thus, the presence of a CD signal signifies that the observed material possesses some form of chirality, making CD spectroscopy an essential tool in the discovery of new chiral materials. Circular dichroism is defined as the difference in Equation A.1:

$$CD = A^l - A^r$$ **Equation A.1**

where A^l and A^r are the absorptions of left and right circularly polarized light. The resulting quantity is typically reported as an ellipticity θ with units of millidegrees (mdeg) or a differential absorption (ΔA). The two quantities are related according to Equation A.2:

$$\theta = 32980 \times \Delta A$$ **Equation A.2**

Any CD quantity can be corrected for the sample concentration, resulting in the common use of units such as molar ellipticity or the unitless quantity ΔA/A. Another common quantity reported to reflect the strength of chirality is the g-factor or dissymmetry factor, which is equivalent to ΔA/A as long as the linear absorbance and CD spectra are collected from the same sample.

Every optical transition within a molecule or material possesses an electric and a magnetic dipole moment. While in linear absorption spectroscopy only the linear translation of charge is important (i.e. the electric transition dipole), both dipoles determine the strength of the resulting CD signal, as described in Equation A.3 for a single chromophore:

$$R_{ij} = \mu_{ij} m_{ij} \cos(\mu, m) \qquad \textbf{Equation A.3}$$

where R_{ij} is the rotatory strength of a CD transition (another description of its strength) from state i to state j, μ_{ij} is the magnitude of the electric dipole moment vector, m_{ij} is the magnitude of the magnetic dipole moment vector, and $\cos(\mu, m)$ is the cosine of the angle between the two vectors. CD signatures of chiroptically active species are called Cotton effects and for an isolated chromophore they typically appear with shapes similar to those observed in absorbance spectra although they possess a positive or negative sign depending on the handedness of the molecule studied. As the complexity of chiral systems increases, so does the observed CD.

Appendix A.2 Davydov Splitting

When two chromophores experience coupling within a sample, a splitting of the Cotton effects occurs resulting in a bisignate peak, i.e. a peak consisting of a positive and a negative lobe cenrered around a wavelength λ_0. Studies of CD and absolute configurations of coupled chromophore systems have allowed researchers to establish relationships between the shape of a CD signatures and the spatial configuration of the originating chromophores.[1] For example, the energy difference between the two lobes of a bisignate peak, dubbed the Davydov splitting, contains information about the distance and angle between the coupled species. The Davydov splitting, equal to two times V_{12}, which is the potential for the interaction between electric dipoles 1 and 2, can be approximated with a Coulomb dipole-dipole term, shown in Equation A.4:

$$2V_{12} = 2\frac{\mu_1\mu_2}{r_{12}^3}[\overrightarrow{e_1}\cdot\overrightarrow{e_2} - 3(\overrightarrow{e_1}\cdot\overrightarrow{e_{12}})(\overrightarrow{e_2}\cdot\overrightarrow{e_{12}})] \qquad \textbf{Equation A.4}$$

where μ_1 and μ_2 are the intensities of the two transition dipoles, r_{12} is the distance between them, and the e terms signify the corresponding unit vectors. The interaction that produces the Davydov splitting, as well as a representative spectrum are shown schematically in Figure A.1.

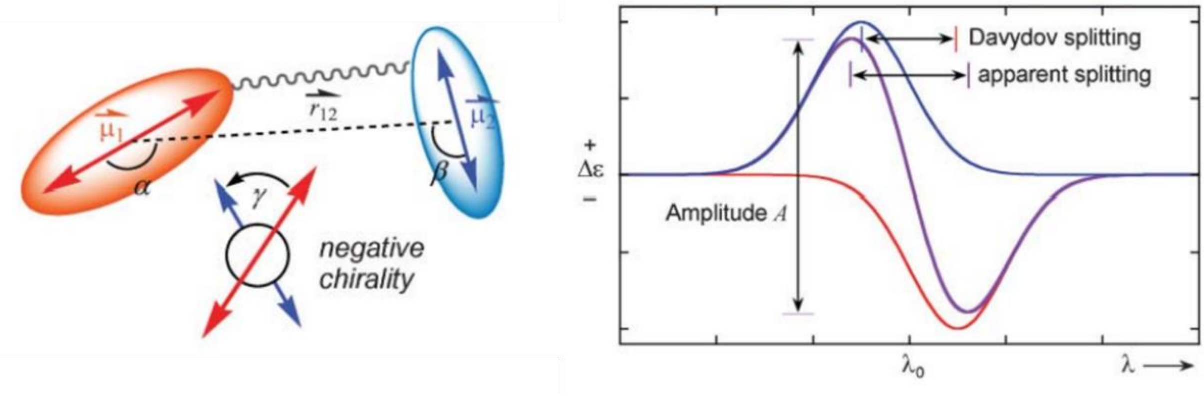

Figure A.1 Schematic of two excitonically coupled chromophores (left) and the resulting CD signature (right). Figure reproduced from reference 1.

Appendix A.3 References

1. Berova, N.; Bari, L. D.; Pescitelli, G., Application of electronic circular dichroism in configurational and conformational analysis of organic compounds. *Chem. Soc. Rev.* **2007,** *36* (6), 914-931.

Appendix B

Appendix B.1 Materials

Lead (II) Bromide (99.999%), methylammonium bromide (98%), N,N-dimethylformamide (anhydrous, 99.8%), toluene (anhydrous, 99.8%), and hydrobromic acid (48% in water) were purchased from Sigma Aldrich. S-(-)-1-Phenylethylamine and R-(+)-1-Phenylethylamine (99+%) were purchased from Alfa Aesar. Ethanol (200 proof, anhydrous) was purchased from Decon Laboratories. Diethyl ether (99.5%, extra dry) was purchased from Acros Organics.

Appendix B.2 Supporting Data

Figure B.1 shows absorbance and emission spectra for toluene solutions of achiral perovskite NPs capped with octylammonium ligands. The absorbance maximum occurs at the same wavelength as S- and R-PEA-capped chiral NPs (432 nm, Figure 2.1.) A slight difference in the Stokes shift between chiral and achiral NPs occurs (7 nm vs 5 nm respectively) in the emission spectra and falls within the error of the instrument.

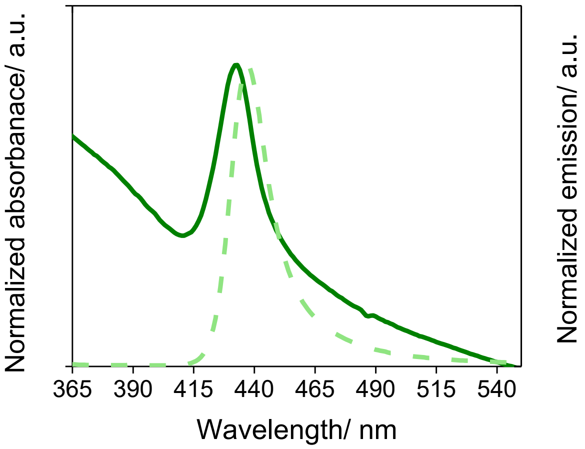

Figure B.2 Absorbance (solid line) and emission (dashed line) spectra of toluene solutions of achiral perovskite NPs capped with octylamine ligands.

Figure B.2 shows absorbance and circular dichroism spectra for solutions of R- and S-phenylethylamine and R- and S- phenylethylammonium bromide. The absorbance spectra in panels a) and b) show a broad feature (225-275 nm) which is attributed to the vibronic transitions of the benzene ring in the ligand structure. The same feature is seen in the circular dichroism spectra of S- and R-phenylethylamine and S- and R-phenylethylammonium bromide (panels c and d), indicating that the chirality persists upon transformation.

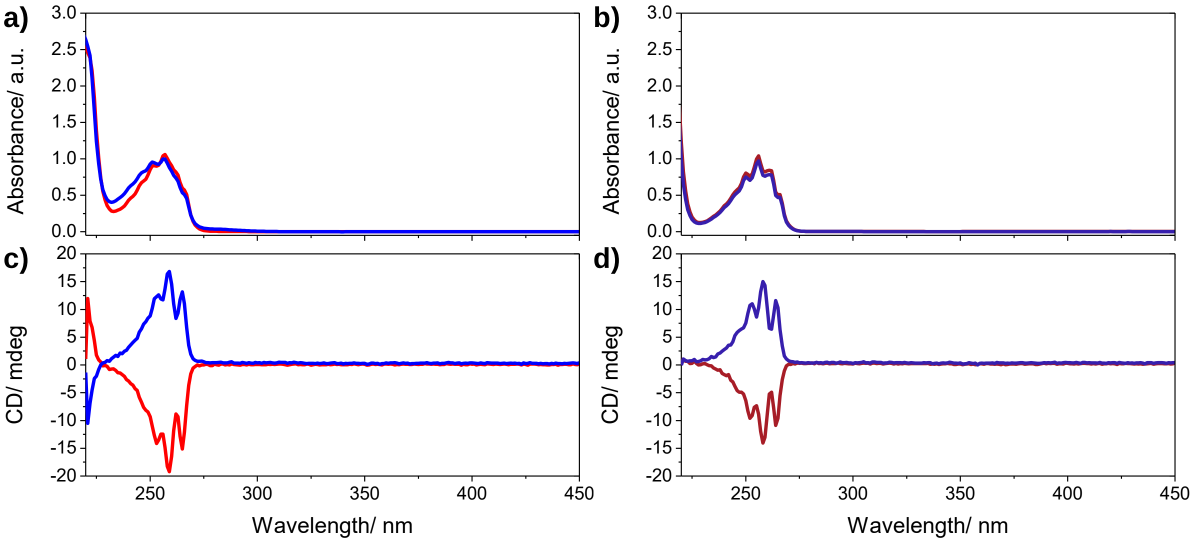

Figure B.3 Absorbance (a, b) and circular dichroism (c, d) spectra for solutions of S- phenylethylamine (blue), R-phenylethylamine (red), S-phenylethylammonium bromide (dark blue), and R-phenylethylammonium bromide (dark red).

A chiroptical feature in the 300-350 nm region of the CD spectra of chiral NP solutions (shown in the main text, Figure 2.4a) was attributed to a charge transfer band between the NP surface and the ligand. Figure B.3 shows absorption and circular dichroism spectra of a charge transfer band that occurs in the same spectral region for a lead bromide and R-phenylethylammonium bromide complex in solution. R-phenylethylammonium bromide and lead bromide solutions alone (Panels b and d) do not exhibit any chiroptical activity; upon mixing of the two solutions, a chiroptical feature around 300nm appears (panel c), and the spectra for S- (black) and R- (red) complexes exhibit mirror image circular dichroism.

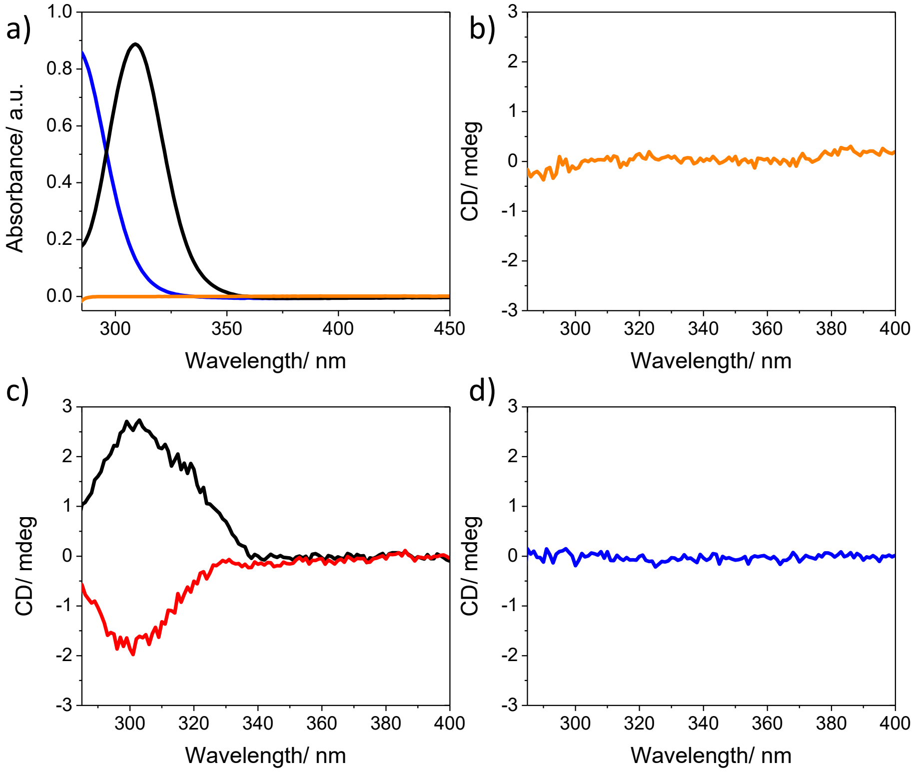

Figure B.4 Panel a) shows absorption spectra of DMF/toluene solutions of lead bromide (blue), R-PEA ligands (orange), and the charge transfer band formed upon mixing the two solutions (black). Panels b) and d) show CD spectra of R-PEA and lead bromide in DMF/toluene respectively. Panel c) shows CD spectra of the charge transfer bands that form upon mixing lead bromide and S-PEA (black) or R-PEA (red) solutions.

Figure B.4 shows the energy dispersive spectrum of chiral NPs, which showed a Pb:Br ratio of 1:1.6. Additional peaks appear from the Cu grid used in the experiment and environmental C.

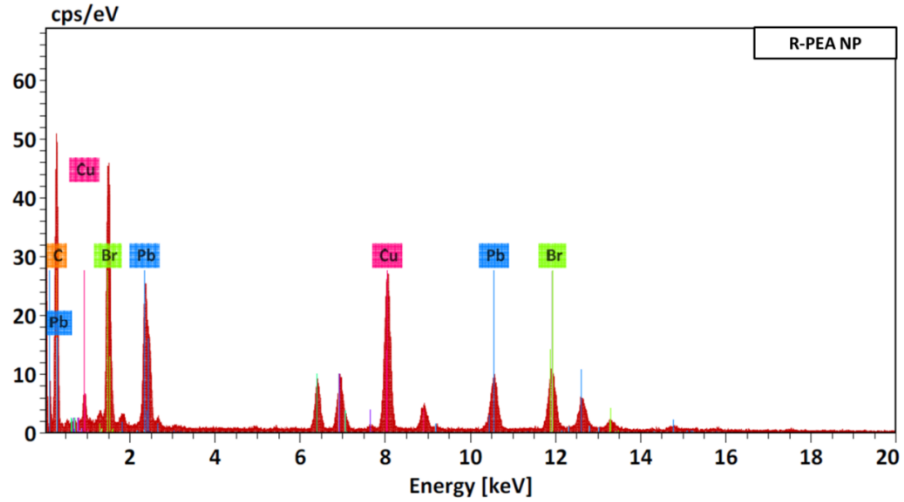

Figure B.5 Energy dispersive spectroscopy spectrum of R-PEA NPs. The computed Pb to Br ratio is 1.6. The additional peaks in the elemental analysis are attributed to the TEM grid.

Figure B.5 shows absorbance and CD spectra of a chiral perovskite NP solution sample in toluene (black), and a chiral perovskite film prepared from that solution. The film exhibits a substantial decrease in CD intensity, Panel b), and additional scatter to the red of the bisignante peak at the absorption maximum is also present when the data are scaled with respect to one another, Panel C). These results illustrate that aggregation inhibits the CD intensity of the perovskite NPs and that chiral induced aggregation is not the acting mechanism.

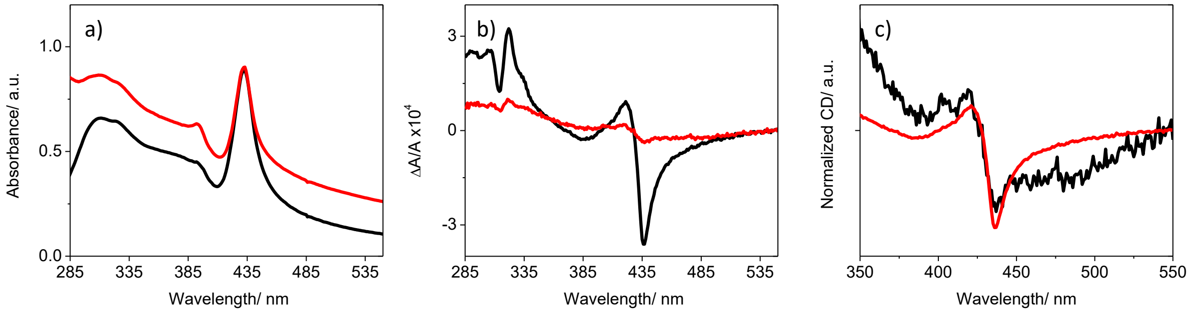

Figure B.6 Panel a) absorbance spectra of a toluene solution of chiral perovskite NPs (black) and a film prepared from that solution by dropcasting onto a clean glass substrate (red). Panel b) CD spectra of a toluene solution of chiral perovskite NPs (black) and a film prepared from the same solution (red). Panel c) normalized spectra of the chiral perovskite NPs solution (black) and film (red) illustrating the additional scatter present in the film.

The CD intensity of R-PEA NP solutions in toluene decreases significantly when the solutions are heated to 50 °C and excess ligand is not present. This can be seen in Figure B.6, where spectra of the stepwise heating of the solutions are shown. The CD intensity is not significantly affected when the temperature is incresed from 20 °C to 30 °C (black and green), then decreases drastically at 40 °C and 50 °C (red and blue). Upon cooling back to 20 °C, the intensity of the chiroptical features from the NP solution increase at the exciton absorption maximum of the NPs (432 nm), as shown in Figure 2.4c of the main text.

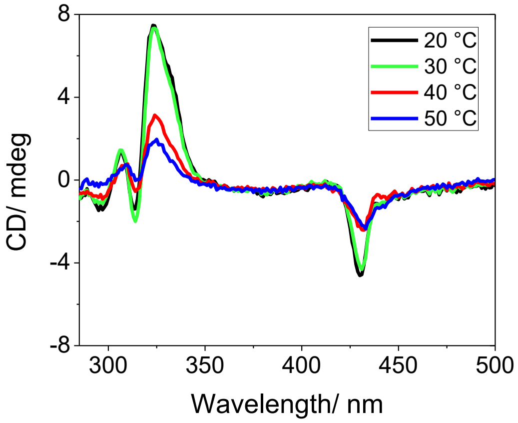

Figure B.7 The figure shows temperature dependent CD spectra of R-PEA perovskite nanoplatelets in which no excess ligand is added to the solution. The temperature was varied from 20 °C to 50 °C.

Figure B.7 shows that the x-ray diffraction patterns of perovskite NPs is the same before (black) and after (red) heating a sample that has been allowed to cool back to room temperature, further substantiating that the increase in CD intensity is not related to a structural change of the perovskite.

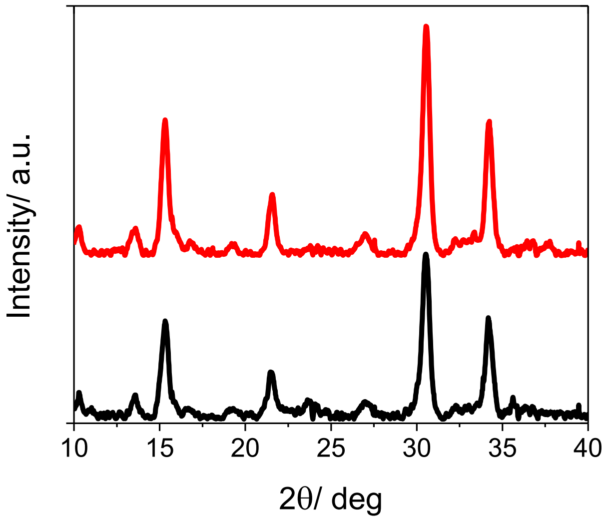

Figure B.8 Powder X-ray diffraction patterns of R-PEA NPs heated to 50 °C, then cooled to room temperature (red) and R-PEA NPs handled at room temperature without heating (black).

Figure B.8 shows ^{1}H NMR spectra of R-phenylethylammonium bromide (a) and S-phenylethylammonium bromide (b) salts synthesized from R-phenylethylamine (c) and S-phenylethylamine (d). The chemical shift of the "Y" proton supports the reaction conversion of phenylethylamine to phenylethylammonium bromide.

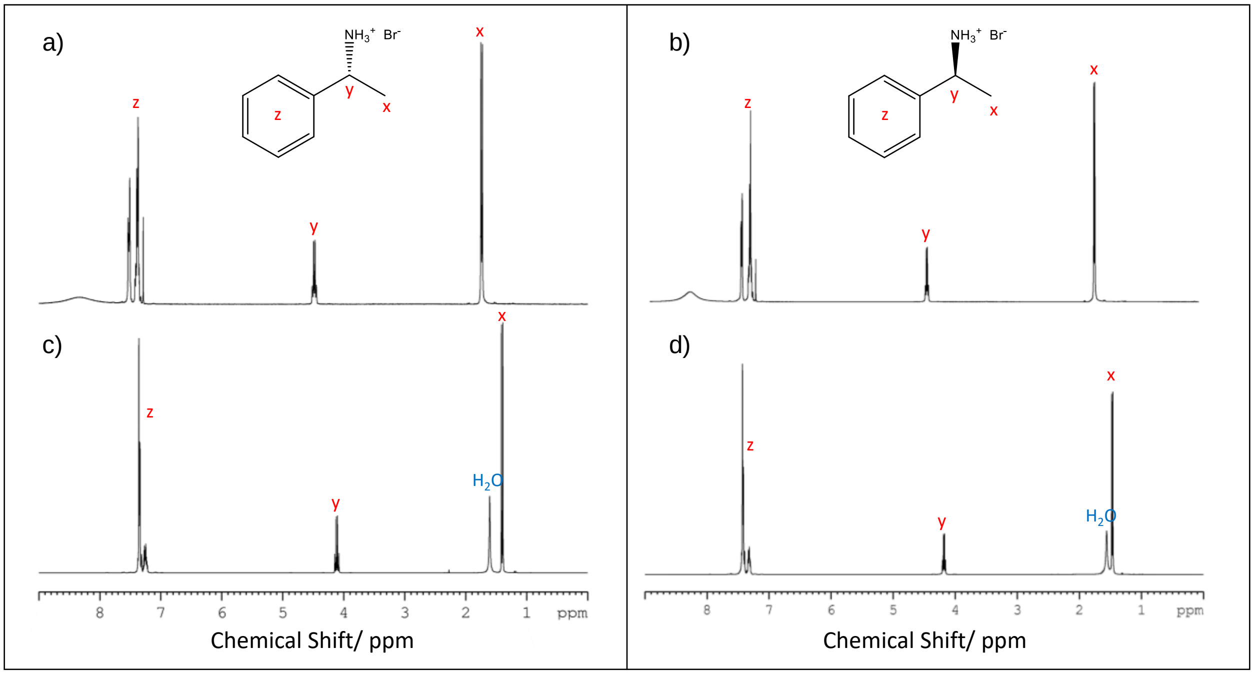

Figure B.9 ^{1}H NMR spectra of, R-phenylethylammonium bromide (a), S-phenylethylammonium bromide (b), R-phenylethylamine (c), and S-phenylethylamine (d).

Appendix C

Appendix C.1 Materials and Methods

Appendix C.1.1 Materials

Toluene anhydrous 99.8%, N,N-Dimethylformamide anhydrous 99.8%, Lead (II) Bromide 99.999%, Lead (II) Chloride 99.999%, Methylammonium Bromide >99%, and Methylamine Hydrochloride >98%, (*R*)-(+)-α-Methylbenzylamine 99%+, (*S*)-(-)-α-Methylbenzylamine 99%+, (*R*)-(+)-1-(1-Naphthyl)ethylamine 99%+, (*S*)-(-)-1-(1-Naphthyl)ethylamine 99%+ were purchased from Sigma-Aldrich. S-(+)-2-aminooctane 99%+ and R-(-)-2-aminooctane 99%+ were purchased from Thermo Scientific.

Appendix C.1.2 Experimental Procedures

Synthesis of precursor salts

Chiral phenylethylammonium halide salts were synthesized by mixing equimolar amounts of the desired chiral amine and HBr or HCl in 15 mL of absolute ethanol. The reaction was stirred in an ice bath for 2 hours, then the solvent was removed via rotary evaporation until crystals were formed. The crystals were collected, recrystallized with chlorobenzene, and then vacuum filtered and washed several times with toluene. The product was kept in a desiccator overnight, then transferred into an Ar glove box.

NPL synthesis

NPL synthesis was performed in an Ar glove box at room temperature. Solutions of each precursor were prepared in anhydrous DMF. The concentrations were chosen to reflect the desired ratio of reagents in the overall synthesis, for example 0.08M $PbCl_2$, 0.04M MACl, 0.36M S- or R-PEACl (octylamine was used as a neat liquid). Equal volumes of PbX_2 and MAX solutions were added into a glass vial and mixed well. Octylamine was added in an equimolar amount to the PbX_2 added into the precursor mixture. The amount of PEAX solution in the precursor mixture was varied for the ligand concentrations studies, with PEA:OA molar ratios ranging from 1.6:1 to 6.75:1. For a single batch, 20 µL of the precursor mixture were injected into 10 mL of anhydrous toluene while agitating with a vortex stirrer for 30 seconds. The NPLs were purified *via* centrifugation and resuspended in fresh anhydrous toluene to an optical density of approximately one.

Spectral measurements

The spectral data were collected in a 1-cm quartz cuvette, which was pretreated with dimethyldichlorosilane in order to prevent adsorption of the perovskites onto the walls of the cuvette. To study optical transitions occurring beyond the spectral window of toluene, NPL suspensions in toluene were drop-cast onto clean quartz slides and dried under a gentle Ar flow. The material was layered until the desired optical density was achieved.

Absorption spectroscopy was performed using a Model 8453 Agilent spectrometer. Circular dichroism (CD) spectra were measured using an Olis DSM 17 CD spectrometer with an integration time of 3 s and a bandwidth of 1 nm. Toluene was used as the background for all measurements.

1H-NMR

For nuclear magentic resonance measurements NPLs were centrifuged into a pellet, then dried in a vacuum desiccator for 1 hour. The dry pellet was redispered in toluene-d8 or dissolved in DMSO-d6, depending on the experiment. Spectra were taken on a Bruker Avance 400 spectrometer at 400 MHz with chemical shifts reported in parts per million (ppm) on the delta (δ) scale. Solvent peaks were used as a reference value at 2.50 ppm and 2.30 ppm for DMSO-d6 and toluene-d8 respectively.

Appendix C.1.3 Computational Methods

We modeled the wave functions and CD spectrum of perovskite NPLs using an infinite 3D particle-in-box model.[1] This model was successfully used to study chiral imprinting on gold cluster. In this model, the electron and hole wavefunctions are treated separately with their own effective mass, m_e^*=0.24, m_h^*=0.17.

We assume that surface ligand induced NPL chirality arises from the electrostatic perturbation of the surface ligand to the wave function of the NPL. We approximate the surface ligand as a set of point charges arranged according to the stereochemistry. The partial charge of R-PEA is modeled from the ground state DFT calculation using Gaussian[2] with b3lyp[3] functional and 6-31g** basis set. All hydrogen except from one bonded to the chiral center are absorbed in heavy atoms. Only the four atoms (2 C, 1 N and 1 H) connected to the chiral center and the chiral center itself were used to perturb the box wavefunction. The charge perturbation is

$$\hat{V}_{charge} = \sum_i \frac{q_i q_j}{\sqrt{(x-x_i)^2 + (y-y_i)^2 + (z-z_i)^2}}$$ **Equation C. 1**

where q_i is the point charge for the adsorbates, q_j is 1 or -1 for hole and electron, (x_i, y_i, z_i) is the cartesian coordinate of the point charge.

The perturbation matrix element is $V_{mn} = \langle \phi_m | \hat{V}_{charge} | \phi_n \rangle$ where ϕ_m and ϕ_n are the unperturbed wavefunctions of the electron or hole state. The perturbed wavefunctions ψ' are obtained by diagonalizing the Hamiltonian $H = H_0 + V$, where H_0 is the unperturbed Hamiltonian with eigen energy on its diagonal.

We chose the (nx,ny,bz)=(0, 0, 0) state to represent the valance band and the double degenerate states (1, 0, 0) and (0, 1, 0) for conduction band to compute the optical properties. The transition dipole moment and magnetic dipole moment were computed between the valance band and conduction band

$$\mu = \iiint \psi'_{val} \hat{\mu} \psi'_{con} \, dxdydz$$ **Equation C.2**

$$m = \iiint \psi'_{val} \widehat{m} \psi'_{con} \, dxdydz$$ **Equation C.3**

where $\hat{\mu} = e(\hat{x} + \hat{y} + \hat{z})$ and $\widehat{m} = \hat{r} \times \hat{p}$.

The oscillator strength f and rotatory strength R are

$$f = \frac{2}{3} \Delta E \, \mu \cdot \mu$$ **Equation C.4**

$$R = Im(\mu \cdot m)$$ **Equation C.5**

The NPL is modelled by a N-by-N grid where each grid point is a unit cell. We assume the exciton size is much smaller than the size of NPL, and the chiral adsorbates outside of exciton have no contribution to the CD signal. The rotatory strength is computed between hole ground state (1,1,1) and electron second and third excited states (1,2,1) and (2,1,1). The computed rotatory strength shows mirror image for $\phi_{h,(1,1,1)} \rightarrow \phi_{e,(2,1,1)}$ and $\phi_{h,(1,1,1)} \rightarrow \phi_{e,(1,2,1)}$, which is consistent with the bisignate CD signals for chiral imprinted perovskite. We explored different exciton sizes, from 3 by 3 to 5 by 5 unit cell, i.e. 1.8 nm to 3 nm. We assume the PEA ligands have very little interaction between themselves and thus all have same binding mode. The rotatory strength is sensitive to the configuration of chiral PEA on the surface, as predicted by TD-DFT calculations. For m PEA on an n-by-n grid exciton, there are $\binom{n^2}{m} = \frac{n^2!}{m!(n^2-m)!}$ unique configurations. The rotatory strength of certain number of PEA m on the exciton rot_m is averaged over all configurations. For PEA:OA ratio x, there are $\frac{x}{1+x}N^2$ PEA on a NPL of N^2 grid, thus the probability of m PEA on the exciton is $p_m(x) = \binom{n^2}{m}\binom{N^2 - n^2}{x/(1+x)N^2 - m} / \binom{N^2}{x/(1+x)N^2}$. The overall rotatory strength is the sum over all possible number of PEA on the exciton $rot(x) = \sum_{m=0}^{n^2} rot_m p_m(x)$. When the NPL size N is much larger than the exciton size, increasing the NPL size N has no influence on the averaged rotatory strength. We take N=100, i.e. 60 nm for our calculations.

TD-DFT Calculations on Perovskite cluster

The halide terminated $3 \times 2 \times 1$ unit cell $(2.4nm \times 1.7nm \times 1.2nm)$ $CsPbBr_3$ perovskite clusters are built from the optimized unit cell. The perovskite clusters have halide terminated surface and contain unit cells. Hydrogen atoms are used to cap surface halide. We used the simplified Tamm-Dancoff approximated (sTDA)[4] to compute the absorption and CD spectra. The ground state wavefunctions were obtained from the Gaussian package with CAM-b3lyp[5] density functional and def2-SVP[6] basis set. The sTDA method is tested and compared with TD-DFT method on a $2 \times 1 \times 1$ cluster with chiral ligands. The computed results show that TDDFT computed absorption spectrum and rotatory strength can be well reproduced by the sTDA method.

DFT Calculations on bulk perovskite

We build MAPbBr3 unit cell with lattice parameter a=5.9Å.[7-9] We performed density functional theory (DFT) calculation using the Vienna ab initio simulation package (VASP)[10] to investigate the geometry, band structure, and the density of states of bulk perovskite and nanoplatelets. We used the linearized augmented-plane-wave (LPAW) method[11, 12] with the Perdew-Burke-Ernzerhof revised for solids (PBEsol)[13] exchange-correlation functional. The plane-waves were expanded with kinetic energy cut-off of 300 eV. A k-point mesh of 11×11×11 was used for the sampling of the Brillouin zones.

Appendix C.2 Supplemental Data

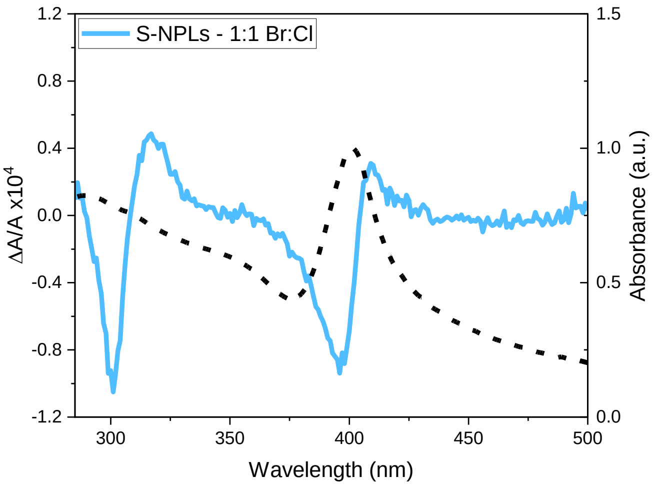

Figure C.1 Absorbance (dashed line) and CD (solid line) of S-PEA-capped perovskite NPLs synthesized with a 1:1 ratio of Br an Cl anions.

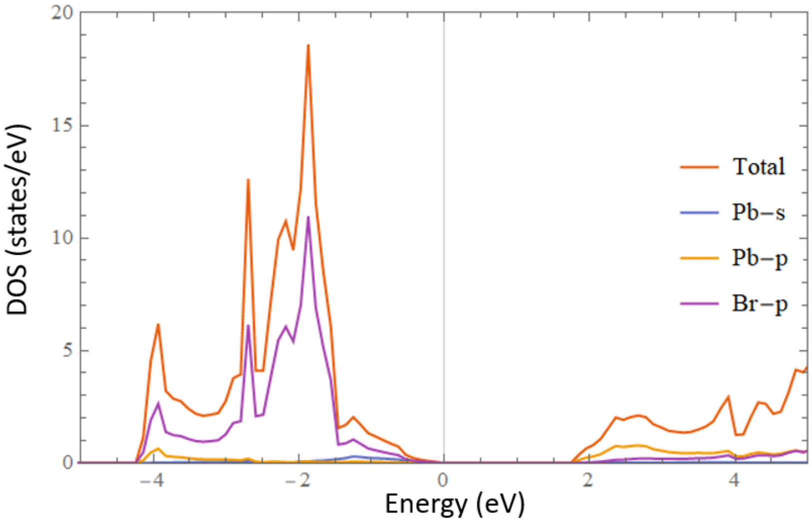

Figure C.2 Total density of states (TDOS) and Partial density of states (PDOS) of bulk MAPbBr3.

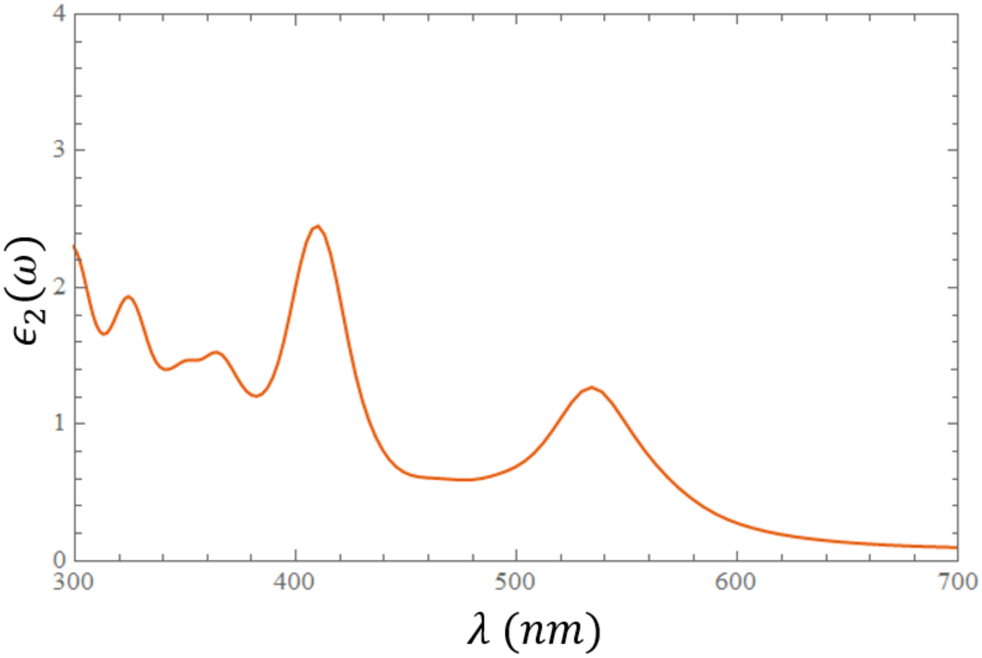

Figure C.3 Imaginary ϵ2 (ω) for MAPbB3 NPL in vacuum.

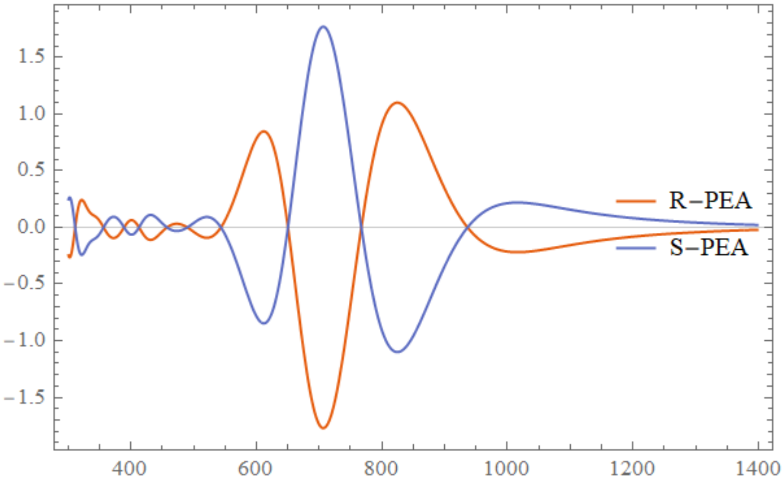

Figure C.4 Simulated CD spectra using a cluster model for single R- and S- adsorbate imprinting.

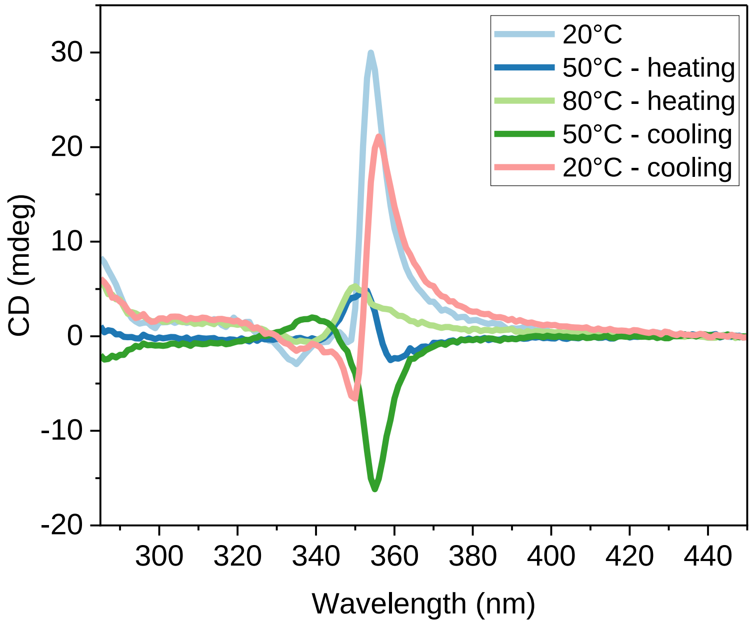

Figure C.5 Temperature-dependent CD spectra of X=Cl NPLs with S-PEA ligands.

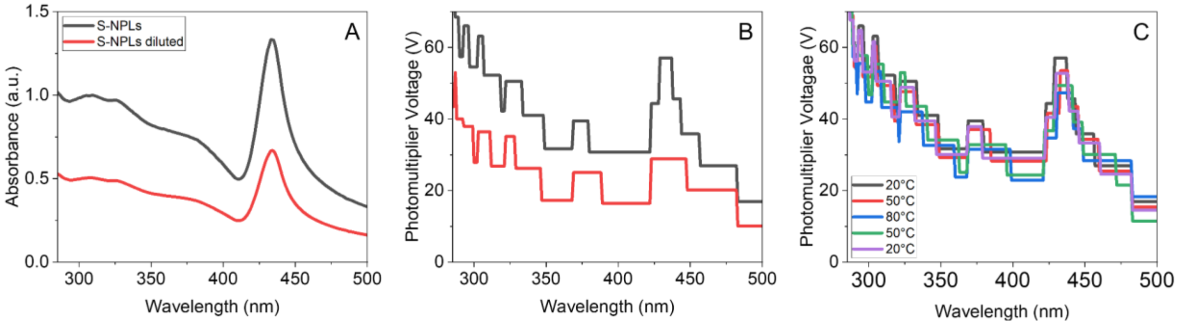

Figure C.6 (A) Absorbance spectra of S-PEA capped X=Br NPLs with different concentrations. (B) Photomultiplier (PMT) voltage measurements for the same samples as panel A measured in a CD spectrometer. (C) PMT voltages for a heated S-PEA capped X=Br NPLs.

PMT voltages measured by the CD instrument can be used as an approximation for changes in the sample's absorbance intensity. Figures S8 A and B show a method validation experiment, where absorbance for a NPL sample was decreased by 50%, resulting in a a 50% decrease in the PMT voltage. Plane C shows the PMT voltage measured during temperature-dependent CD experiments and only reveals a modest voltage variation at different sample temperatures. Therefore, it is concluded that temperature variation does not have a significant effect on the absorbance intensity of NPL samples.

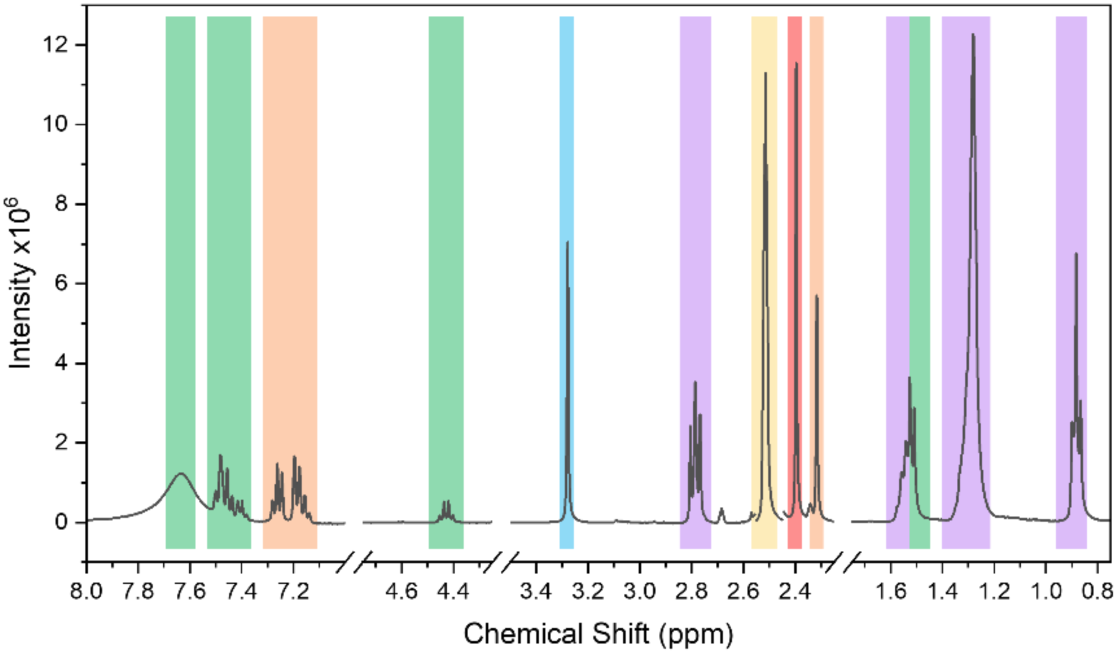

Species	Peak position	Assignment	
Octylamine	0.88	*a*	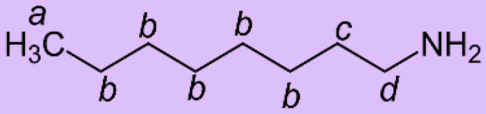
Octylamine	1.28	*b*	
Octylamine	1.54	*c*	
Octylamine	2.78	*d*	
S-PEABr	1.52	*a*	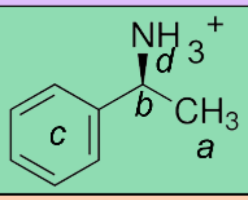
S-PEABr	4.43	*b*	
S-PEABr	7.46	*C*	
S-PEABr	7.64	*d*	
Toluene	2.32	*a*	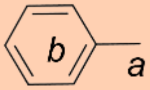
Toluene	7.22	*b*	
DMSO-d6	2.50		
MABr	2.40		
Water	3.28		

Figure C.7 NMR peak assignments.

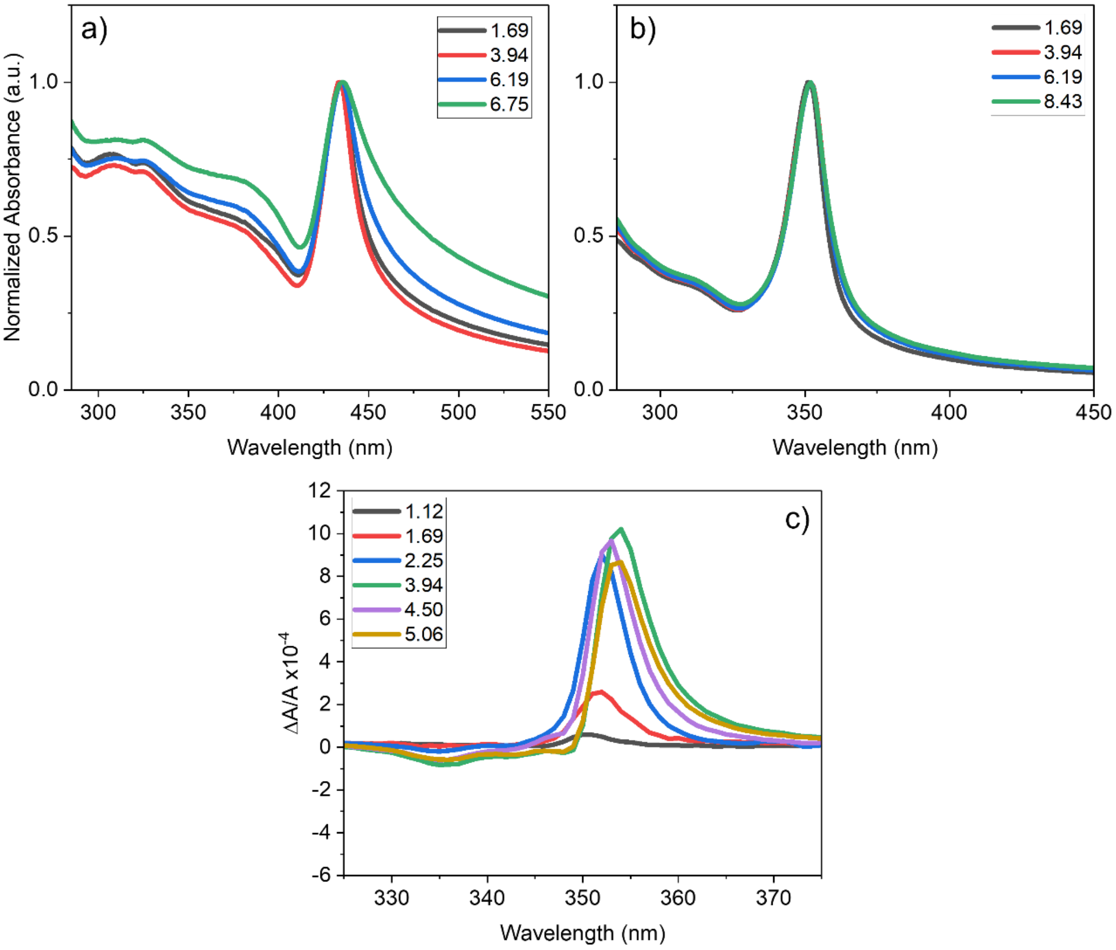

Figure C.8 Absorbance of Br (a) and Cl (b) samples with high PEA content. CD of Cl PEA:OA variation experiment (c). Legends indicate the synthetic PEA:OA ratio.

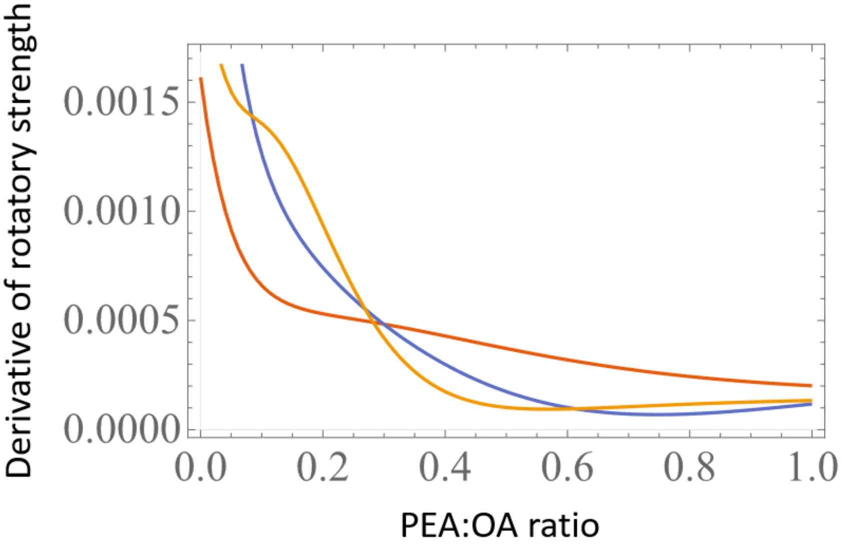

Figure C.9 The derivative of rotatory strength as the function of PEA:OA ratio for 3 exciton size: 3 by 3 (orange), 4 by 4 (blue) and 5 by 5 (yellow).

Appendix C.3 References

1. Goldsmith, M.-R.; George, C. B.; Zuber, G.; Naaman, R.; Waldeck, D. H.; Wipf, P.; Beratan, D. N., The chiroptical signature of achiral metal clusters induced by dissymmetric adsorbates. *PCCP* **2006,** *8* (1), 63-67.

2. Frisch, M. J.; Trucks, G. W.; Schlegel, H. B.; Scuseria, G. E.; Robb, M. A.; Cheeseman, J. R.; Scalmani, G.; Barone, V.; Petersson, G. A.; Nakatsuji, H.; Li, X.; Caricato, M.; Marenich, A. V.; Bloino, J.; Janesko, B. G.; Gomperts, R.; Mennucci, B.; Hratchian, H. P.; Ortiz, J. V.; Izmaylov, A. F.; Sonnenberg, J. L.; Williams; Ding, F.; Lipparini, F.; Egidi, F.; Goings, J.; Peng, B.; Petrone, A.; Henderson, T.; Ranasinghe, D.; Zakrzewski, V. G.; Gao, J.; Rega, N.; Zheng, G.; Liang, W.; Hada, M.; Ehara, M.; Toyota, K.; Fukuda, R.; Hasegawa, J.; Ishida, M.; Nakajima, T.; Honda, Y.; Kitao, O.; Nakai, H.; Vreven, T.; Throssell, K.; Montgomery Jr., J. A.; Peralta, J. E.; Ogliaro, F.; Bearpark, M. J.; Heyd, J. J.; Brothers, E. N.; Kudin, K. N.; Staroverov, V. N.; Keith, T. A.; Kobayashi, R.; Normand, J.; Raghavachari, K.; Rendell, A. P.; Burant, J. C.; Iyengar, S. S.; Tomasi, J.; Cossi, M.; Millam, J. M.; Klene, M.; Adamo, C.; Cammi, R.; Ochterski, J. W.; Martin, R. L.; Morokuma, K.; Farkas, O.; Foresman, J. B.; Fox, D. J. *Gaussian 16 Rev. A.03*, Wallingford, CT, **2016**.

3. Lee, C.; Yang, W.; Parr, R. G., Development of the Colle-Salvetti correlation-energy formula into a functional of the electron density. *Phys. Rev. B* **1988,** *37* (2), 785-789.

4. Grimme, S., A simplified Tamm-Dancoff density functional approach for the electronic excitation spectra of very large molecules. *J. Chem Phys.* **2013,** *138 24*, 244104.

5. Yanai, T.; Tew, D. P.; Handy, N. C., A new hybrid exchange–correlation functional using the Coulomb-attenuating method (CAM-B3LYP). *Chem. Phys. Lett.* **2004,** *393*, 51-57.

6. Weigend, F.; Ahlrichs, R., Balanced basis sets of split valence, triple zeta valence and quadruple zeta valence quality for H to Rn: Design and assessment of accuracy. *PCCP* **2005,** *7* (18), 3297-3305.

7. Mannino, G.; Deretzis, I.; Smecca, E.; La Magna, A.; Alberti, A.; Ceratti, D.; Cahen, D., Temperature-Dependent Optical Band Gap in CsPbBr3, MAPbBr3, and FAPbBr3 Single Crystals. *The Journal of Physical Chemistry Letters* **2020,** *11* (7), 2490-2496.

8. Jishi, R. A.; Ta, O. B.; Sharif, A. A., Modeling of Lead Halide Perovskites for Photovoltaic Applications. *J. Phys. Chem. C* **2014,** *118* (49), 28344-28349.

9. Choi, J. I. J.; Khan, M. E.; Hawash, Z.; Kim, K. J.; Lee, H.; Ono, L. K.; Qi, Y.; Kim, Y.-H.; Park, J. Y., Atomic-scale view of stability and degradation of single-crystal MAPbBr3 surfaces. *J. Mater. Chem. A* **2019,** *7* (36), 20760-20766.

10. Kresse, G.; Hafner, J., Ab initio molecular dynamics for liquid metals. *Phys. Rev. B* **1993,** *47* (1), 558-561.

11. Blöchl, P. E., Projector augmented-wave method. *Phys. Rev. B* **1994,** *50* (24), 17953-17979.

12. Kresse, G.; Joubert, D., From ultrasoft pseudopotentials to the projector augmented-wave method. *Phys. Rev. B* **1999,** *59* (3), 1758-1775.

13. Perdew, J. P.; Ruzsinszky, A.; Csonka, G. I.; Vydrov, O. A.; Scuseria, G. E.; Constantin, L. A.; Zhou, X.; Burke, K., Restoring the Density-Gradient Expansion for Exchange in Solids and Surfaces. *Phys. Rev. Lett.* **2008,** *100* (13), 136406.

Appendix D

Appendix D.1 Chiral Perovskites with Mixed Halide Compositions

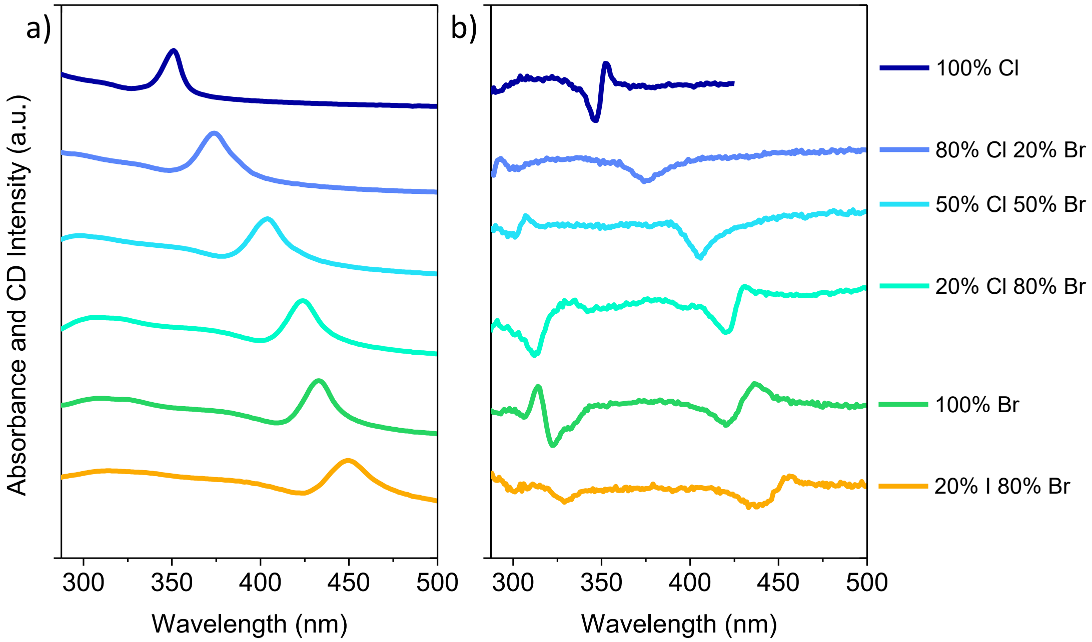

Figure D.1 Absorbance (a) and CD spectra (b) of S-chiral perovskite NPLs with different halide compositions in toluene. The percentages in the legend on the right indicate the fraction of chloride, bromide, or iodide used in the syntheis. The data are offset for clarity.

The well-known optical tuning of the perovskite's first excitonic transition energy with the halide composition[1-3] also manifests in their CD spectra. Figure D.1 shows absorbance (a) and CD spectra (b) of chiral NPL solutions with different halide compositions. The legend for Figure C.1 indicates the relative amounts of each halide added into the precursor mixture during the NPL synthesis. The mixed-halide samples exhibit two prominent bisignate CD transitions, much like those found for the pure halide NPLs. The energy shifts of the first exciton transitions observed in the absorbance spectra (Figure D.1a) correspond to the same energy shifts observed in the CD spectra (Figure D.1b) for each halide composition. The higher energy bisignate transitions for the samples containing large percentages of chloride ions occur beyond the spectral window of the solvent but can be observed in NPL films drop-cast onto a quartz substrate (shown in Figure 3.2). While the peak positions shift predictably and in good agreement with the absorbance spectra, the CD peak shapes differ significantly between pure halide NPLs (100% Br and 100% Chloride) and NPLs with mixed halide compositions.

The bisignate shape of the first excitonic transition is diminished in mixed halide samples compared to the same feature in NPLs with a pure halide composition and some samples appear almost inverted in sign; for example, see spectra with a 1:1 Br:Cl ratio. For the NPLs, the chiral ligand interacts directly with the lead halide octahedra on the NPL surface. The packing arrangement of the lead halide octahedra could be influenced by the identity of both the halide and the capping ligand.[4] In mixed halide samples, two lead sources are used in the synthesis ($PbBr_2$ and $PbCl_2$); thus, we hypothesize that the inhomogeneity of the NPL surface in mixed halide systems results in disordered packing of the octahedra, and thus in a decreased ability of the ligand to pack uniformly on the NPL surface. Mechanistic studies of the formation of hybrid perovskites have suggested that PbX_2 does not dissociate during synthesis, but is rather solubilized via complex formation in the presence of trace amounts of water, or exfoliated into 1D sheets that transform into the perovskite structure when combined with the methylammonium cation.[5, 6] If so, the PbX_2 source can play an important role in the composition and chemistry of the NPL surface. We hypothesize that the mixture of PbX_2 sources results in inhomogeneity of the NPL surface in mixed halide systems leading to more disordered packing of the lead octahedra, and thus in a decreased ability of the ligand to pack uniformly on the NPL surface. This disruption in ligand packing can lead to inhomogeneous dipole orientations and a disruption of the CD features. A similar effect has been reported for chiral CdSe nanoparticles, where different nanoparticle crystal structures led to an inversion of the Cotton effects.[7]

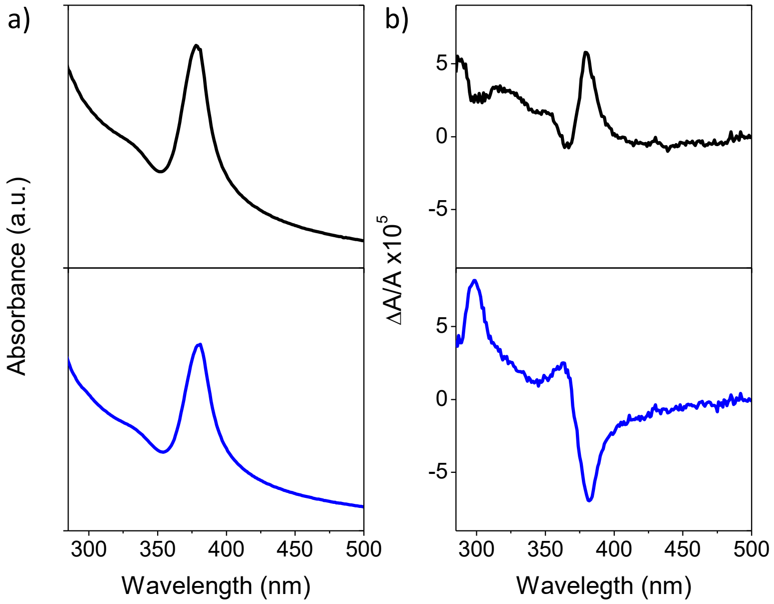

Figure D 2 Absorbance (a) and CD spectra (b) of R-chiral NPLs containing 71% chloride and 29% bromide ions. The black spectra are for NPL synthesized by mixing pure bromide and chloride precursor solutions with the desired proportions, and the blue spectra represent NPLs synthesized with lead (II) bromide, methylammonium chloride and phenylethylammonium chloride, yielding a 71:29 Cl:Br ratio.

To test this hypothesis, NPLs synthesized in the same manner as those in Figure D.1 were compared to NPLs with the same overall halide composition, but with a single source of lead and, presumably, a more homogeneous NPL surface. NPLs were synthesized with a single source of lead, $PbBr_2$, while keeping all other reagents in their chloride variants. This mixture of compounds yields a 71:29 Cl:Br composition; that same ratio was replicated via mixing of pure halide precursor solutions, which contain both $PbCl_2$ and $PbBr_2$ precursors. Figure D.2 shows the results from this study, where the samples with a single Pb precursor are shown in blue, and the NPL formed via mixing two pure halide solutions are shown in black. The absorbance spectra in panel (a) show similar band gap energies for the two samples; however, the CD spectra in panel (b) differ significantly. A complete inversion of the peak sign is observed when the NPLs are synthesized from a mixture of lead sources, similarly to the effect observed in Figure D.1. The NPLs with a single lead source ($PbBr_2$) maintain the same bisignate shape and sign that is observed in 100% Br and Cl samples.

Appendix D.2 Davydov Splitting

Another notable change between NPLs of varying halide compositions is found in the energy difference between the two halves of the bisignate peak for the lowest energy transition, which decreases as the band gap increases. The energy difference between the peak and trough of the bisignate (Figure C.3 inset) is known as the Davydov splitting and its magnitude is determined by the interaction of the two chromophores in a coupled oscillator according to equation C.12):[8]:

$$V_{ij} = \frac{\mu_i \mu_i}{r_{ij}^3} \left[\overrightarrow{e_\imath} \cdot \overrightarrow{e_\jmath} - 3\left(\overrightarrow{e_\imath} \cdot \overrightarrow{e_{\imath\jmath}}\right)\left(\overrightarrow{e_\jmath} \cdot \overrightarrow{e_{\imath\jmath}}\right) \right] \qquad \textbf{Equation D. 1}$$

where V_{ij} denotes the energy shift from the center point of the transition to the peak of each lobe (thus the Davydov splitting is $2V_{ij}$); μ_i and μ_j are the transition dipole moments of the two oscillators; r_{ij} is the distance between the dipoles, and $\overrightarrow{e_\imath}$ and $\overrightarrow{e_\jmath}$ are the corresponding unit vectors.

Because the distance between the coupled chromophores (i.e. the NPL and the chiral ligand) depends on the halide identity, the Davydov splitting should scale with the lattice properties of the perovskite.

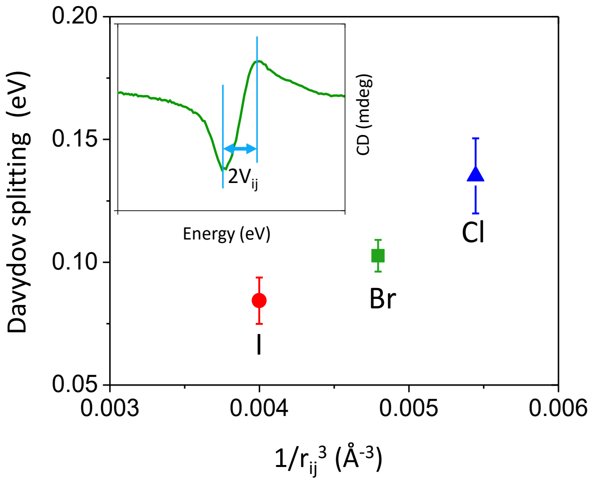

Figure D. 3 Davydov splitting ($2V_{ij}$) as a function of $1/r_{ij}^{3}$, where r_{ij} is the lattice constant a for each pure halide composition. The data points represent the average splitting values for samples with pure iodide (red), bromide (green), and chloride (blue) halide compositions. The inset shows a representative determination of $2V_{ij}$.

Figure D.3 shows the experimentally determined Davydov splitting, $2V_{ij}$, plotted as a function of the lattice constant a, representative of the term r_{ij}, for the pure halide compositions. Lattice constants for methylammonium lead chloride, bromide, and iodide perovskites were obtained from the literature.[9, 10] The error bars are representative of the distribution of Davydov splitting energies across multiple experiments, and V_{ij} is plotted as a function the inverse cube of a. As the size of the anion decreases from iodide to bromide, to chloride, so does a; we thus expect the energy of the Davydov splitting to be inversely proportional to the size of the halide ions in the perovskite structure. The increased splitting differences in the spectra are consistent with the change in distance between the ligand and the Pb^{2+} ion and thus further corroborate a coupled oscillator model for chiral imprinting in the NPL system, as suggested in chapters 2.0 and 3.0.

Appendix D.3 Experimental Details

Synthesis of precursor salts

Chiral phenylethylammonium halide salts were synthesized by mixing equimolar amounts of the desired chiral amine and HBr, HCl or HI in 15 mL of absolute ethanol. The reaction was stirred in an ice bath for 2 hours, then the solvent was removed via rotary evaporation until crystals were formed. The crystals were collected, recrystallized with chlorobenzene, and then vacuum filtered and washed several times with toluene. The product was kept in a desiccator overnight, then transferred into an Ar glove box.

NPL synthesis

NPL synthesis was performed in an Ar glove box at room temperature. Solutions of each precursor (except for octylamine) were prepared in anhydrous DMF. The concentrations were chosen to reflect the desired ratio of reagents in the overall synthesis, for example 0.08M $PbCl_2$, 0.04M MACl, 0.36M S- or R-PEACl. Equal amounts of each solution were added into a glass vial and mixed well. Octylamine was added such that the amount was equal to the number of moles of PbX_2 added into the precursor mixture. In some cases, for example with pure iodide NPLs, the amount of chiral and achiral ligands was increased slightly to inhibit thickness polydispersity. For a single batch, 20 μL of the precursor mixture were injected into 10 mL of anhydrous toluene while agitating with a vortex stirrer for 30 seconds. The NPLs were purified *via* centrifugation and resuspended in fresh anhydrous toluene to an optical density of approximately one.

Spectral measurements

The spectral data were collected in a 1-cm quartz cuvette, which was pretreated with dimethyldichlorosilane in order to prevent adsorption of the perovskites onto the walls of the cuvette. To study optical transitions occurring beyond the spectral window of toluene, NPL suspensions in toluene were drop-cast onto clean quartz slides and dried under a gentle Ar flow. The material was layered until the desired optical density was achieved.

Absorption spectroscopy was performed using a Model 8453 Agilent spectrometer. Circular dichroism (CD) spectra were measured using an Olis DSM 17 CD spectrometer with an integration time of 3 s and a bandwidth of 1 nm (chloride and bromide samples) or a JASCO 715 (iodide samples). Toluene was used as the background for all measurements.

Appendix D.4 References

1. Tyagi, P.; Arveson, S. M.; Tisdale, W. A., Colloidal Organohalide Perovskite Nanoplatelets Exhibiting Quantum Confinement. *J. Phys. Chem Lett.* **2015,** *6* (10), 1911-1916.
2. Weidman, M. C.; Goodman, A. J.; Tisdale, W. A., Colloidal Halide Perovskite Nanoplatelets: An Exciting New Class of Semiconductor Nanomaterials. *Chem. Mater.* **2017,** *29* (12), 5019-5030.
3. Weidman, M. C.; Seitz, M.; Stranks, S. D.; Tisdale, W. A., Highly Tunable Colloidal Perovskite Nanoplatelets through Variable Cation, Metal, and Halide Composition. *ACS Nano* **2016,** *10* (8), 7830-7839.
4. Billing, D. G.; Lemmerer, A., Synthesis and crystal structures of inorganic–organic hybrids incorporating an aromatic amine with a chiral functional group. *Cryst. Eng. Comm.* **2006,** *8* (9), 686-695.
5. Liu, K.; Jiang, Y.; Jiang, Y.; Guo, Y.; Liu, Y.; Nakamura, E., Chemical Formation and Multiple Applications of Organic–Inorganic Hybrid Perovskite Materials. *J. Am. Chem. Soc.* **2019,** *141* (4), 1406-1414.

6. Yang, S.; Zheng, Y. C.; Hou, Y.; Chen, X.; Chen, Y.; Wang, Y.; Zhao, H.; Yang, H. G., Formation Mechanism of Freestanding CH3NH3PbI3 Functional Crystals: In Situ Transformation vs Dissolution–Crystallization. *Chem. Mater.* **2014,** *26* (23), 6705-6710.

7. Tohgha, U.; Deol, K. K.; Porter, A. G.; Bartko, S. G.; Choi, J. K.; Leonard, B. M.; Varga, K.; Kubelka, J.; Muller, G.; Balaz, M., Ligand Induced Circular Dichroism and Circularly Polarized Luminescence in CdSe Quantum Dots. *ACS Nano* **2013,** *7* (12), 11094-11102.

8. Berova, N.; Bari, L. D.; Pescitelli, G., Application of electronic circular dichroism in configurational and conformational analysis of organic compounds. *Chem. Soc. Rev.* **2007,** *36* (6), 914-931.

9. Baikie, T.; Barrow, N. S.; Fang, Y.; Keenan, P. J.; Slater, P. R.; Piltz, R. O.; Gutmann, M.; Mhaisalkar, S. G.; White, T. J., A combined single crystal neutron/X-ray diffraction and solid-state nuclear magnetic resonance study of the hybrid perovskites CH3NH3PbX3 (X = I, Br and Cl). *J. Mater. Chem. A* **2015,** *3* (17), 9298-9307.

10. Baikie, T.; Fang, Y.; Kadro, J. M.; Schreyer, M.; Wei, F.; Mhaisalkar, S. G.; Graetzel, M.; White, T. J., Synthesis and crystal chemistry of the hybrid perovskite (CH3NH3)PbI3 for solid-state sensitised solar cell applications. *J. Mater. Chem. A* **2013,** *1* (18), 5628-5641.

Appendix E

Appendix E.1 Supplemental Data

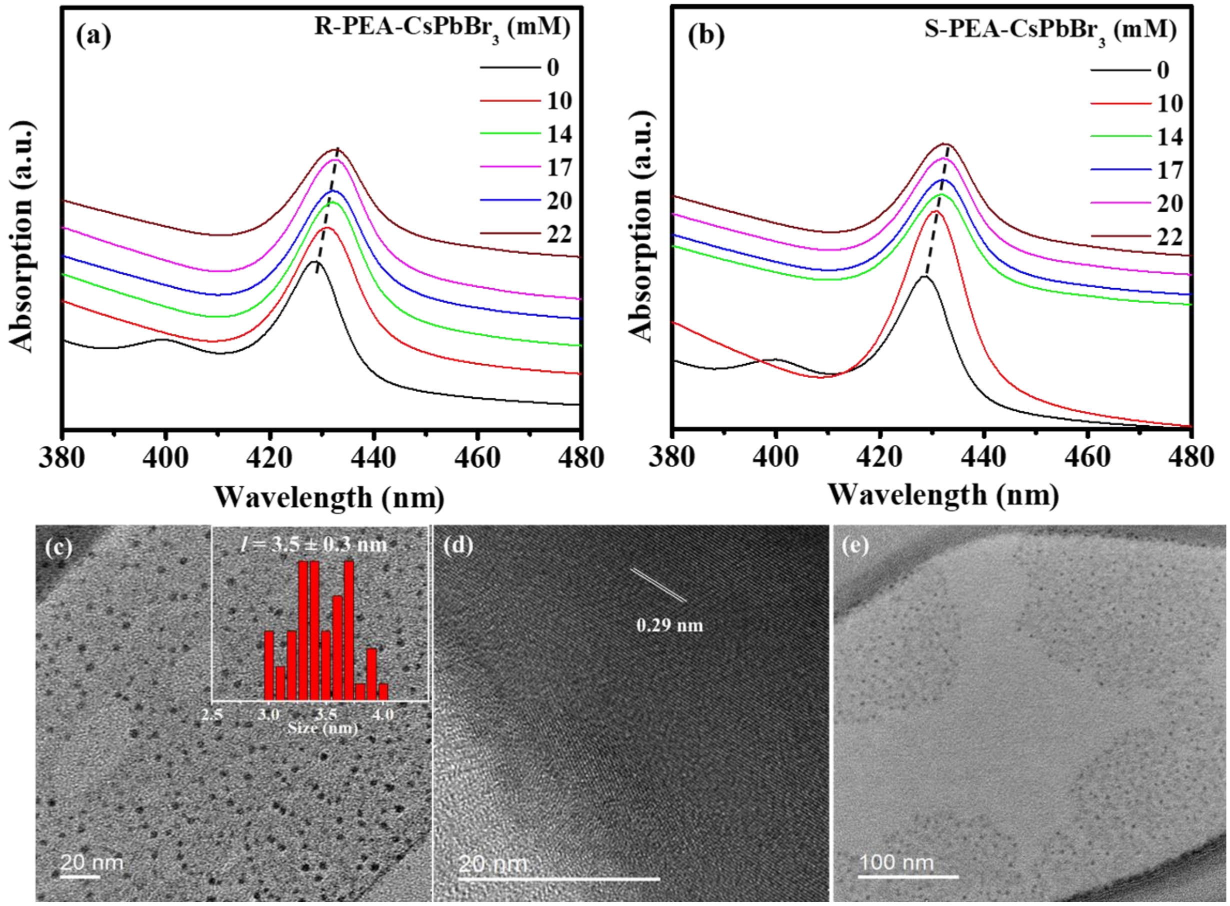

Figure E.1 (a,b) UV-Vis absorption spectra of R- and S-PEA-CsPbBr$_3$ NPs with increasing PEA concentration is shown. The NPs were dispersed in toluene and are offset for clarity. (c-e) TEM images of R- PEA-CsPbBr$_3$ NPs with [PEA] = 20 mM in the NP dispersion.

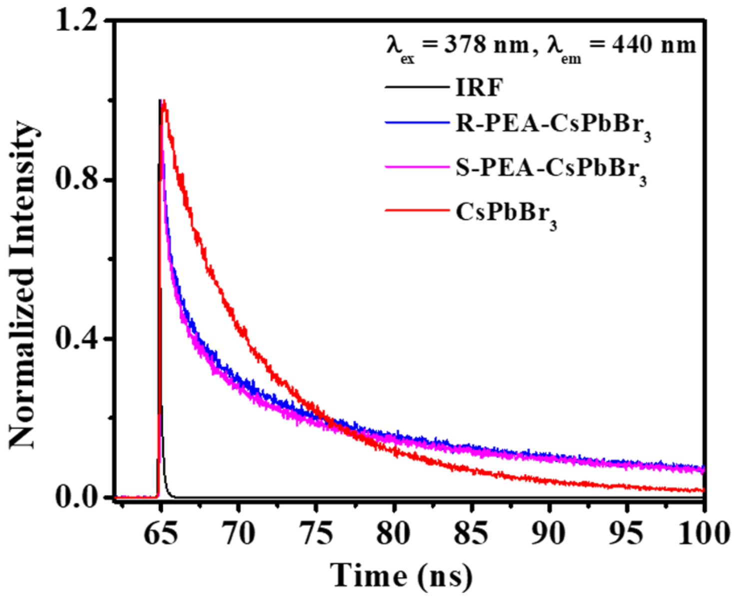

Figure E.2 Emission decay profiles (dotted lines) and fits (solid lines) of CsPbBr3 and R- and S-CsPbBr3 NPs in toluene are shown. The PEA concentration was maintained at 10 mM in the NP dispersion.

Table A.1 Lifetime parameters of the different nanoparticle (NP) systems studied.

System (NP)	a_1	τ_1 (ns)	a_2	τ_2 (ns)	a_3	τ_3 (ns)	$<\tau>$ (ns)^2
CsPbBr$_3$	0.35 ± 0.04	2.20 ± 0.20	0.58 ± 0.03	6.70 ± 0.10	0.07 ± 0.01	17.10 ± 0.20	5.85 ± 0.23
R-/S-PEA-CsPbBr$_3$	0.85 ± 0.08	0.78 ± 0.03	0.10 ± 0.01	5.9 ± 0.07	0.06 ± 0.007	30.0 ± 0.30	3.00 ± 0.30

The decays are fitted to a multiexponential model using the equation $I(t) = \Sigma a_i \exp(-t/\tau)$, where $\Sigma a_i = 1$.

$^2 <\tau> = a_1\tau_1 + a_2\tau_2 + a_3\tau_3$ with τ_1, τ_2, and τ_3 being the three lifetime components having relative amplitudes a_1, a_2, and a_3 respectively. $\chi^2 \leq 1.26$.

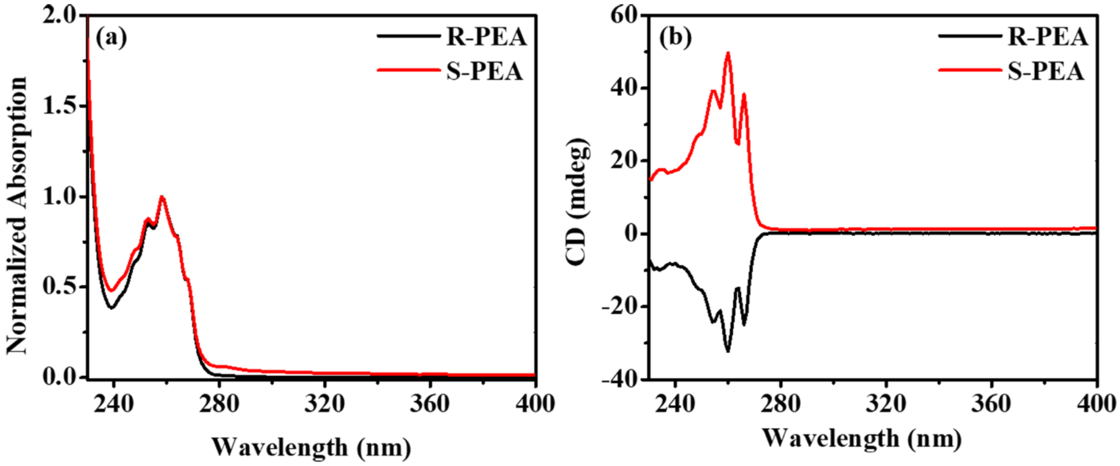

Figure E.3 (a) UV-vis absorption and (b) CD spectra of R-(black) and S-PEA (red) in methylcyclohexane.

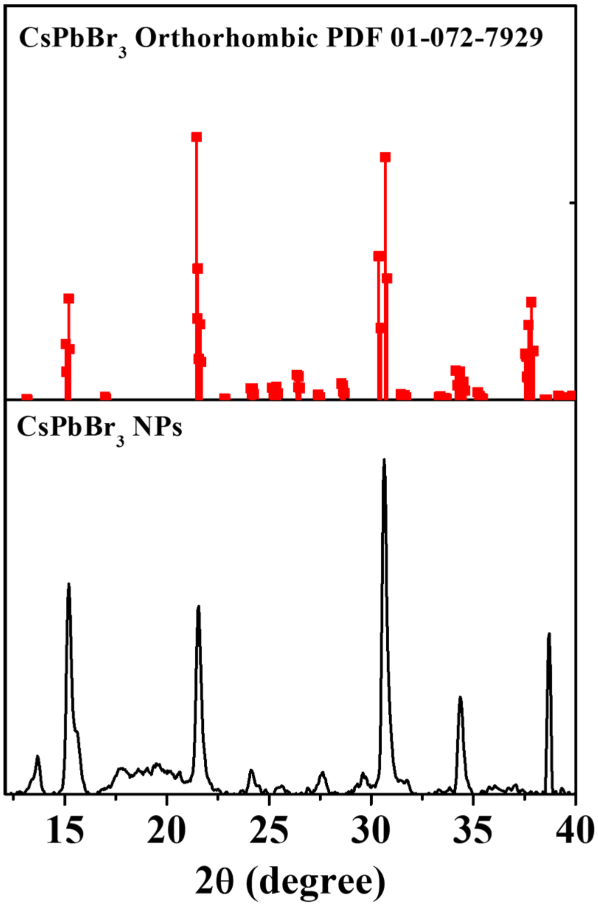

Figure E.4 Powder XRD patterns of CsPbBr3 NPs (black) in agreement with an orthorhombic crystal structure (red).

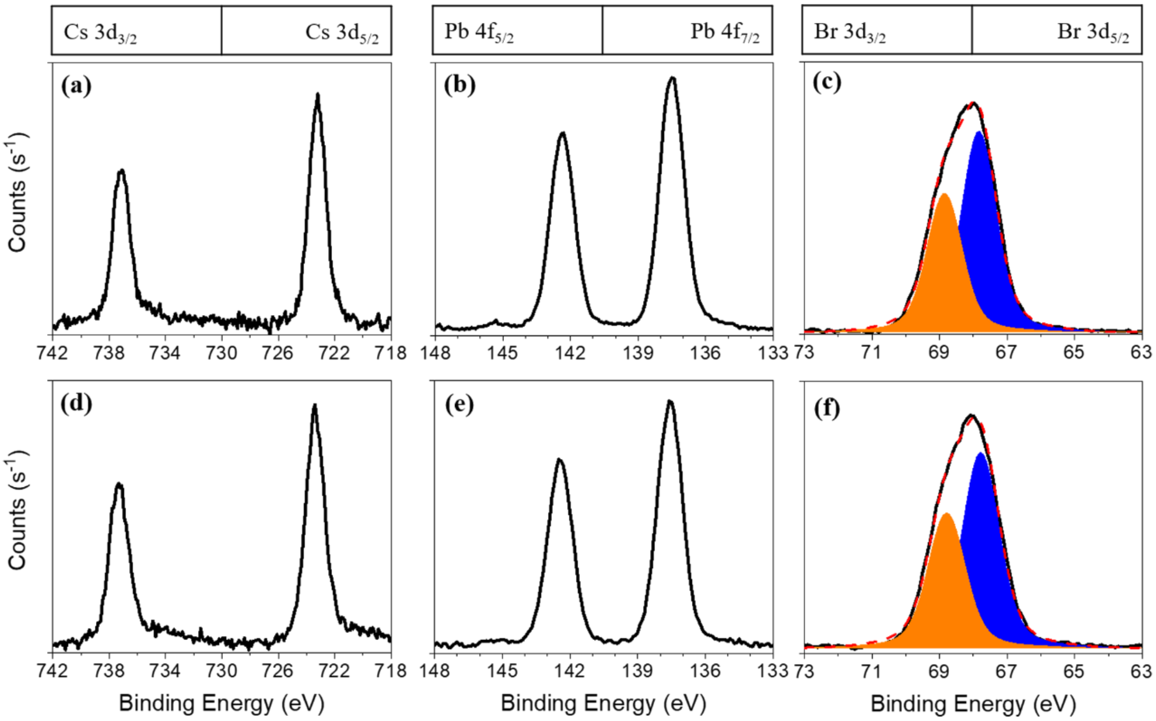

Figure E.5 (a) Cs 3d, (b) Pb 4f, (c) Br 3d X-ray photoelectron spectra of the CsPbBr3 NPs along with the corresponding spectra for the R-PEA-CsPbBr3 NPs (d-f) are shown.

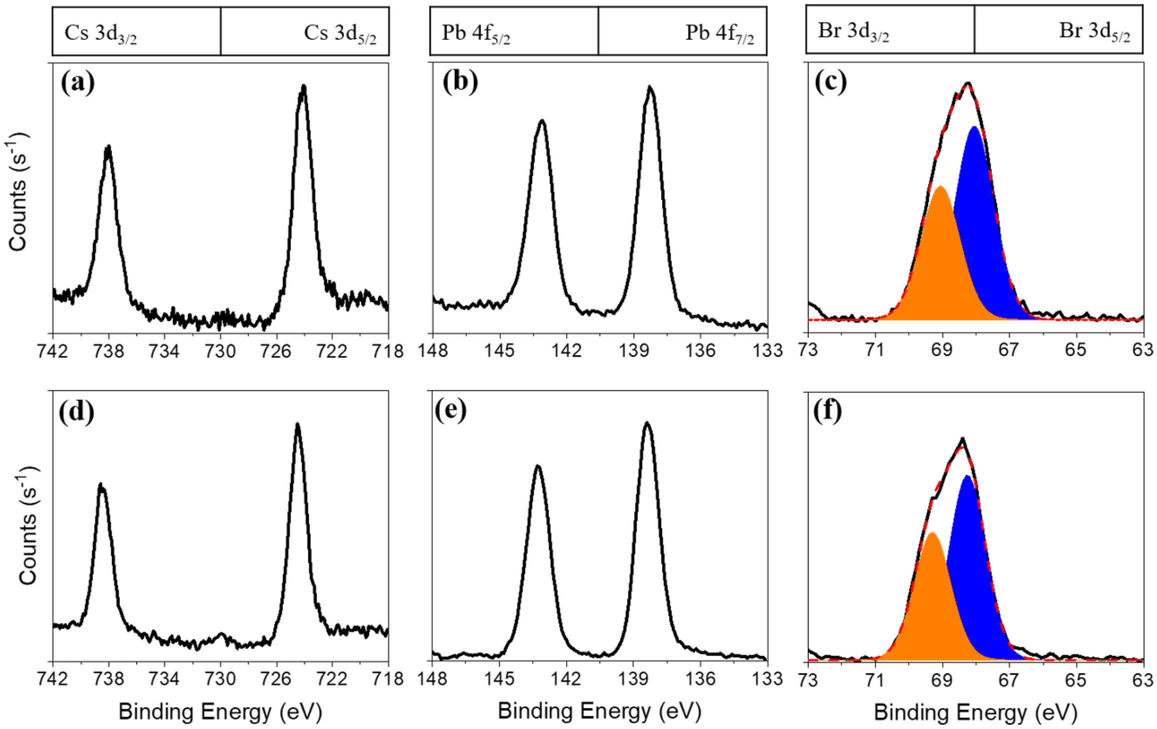

Figure E.6 (a) Cs 3d, (b) Pb 4f, (c) Br 3d X-ray photoelectron spectra of R- NEA-CsPbBr3 NPs and (d) Cs 3d, (e) Pb 4f, (f) Br 3d X-ray photoelectron spectra of R-OcAm-CsPbBr3 NPs are shown.

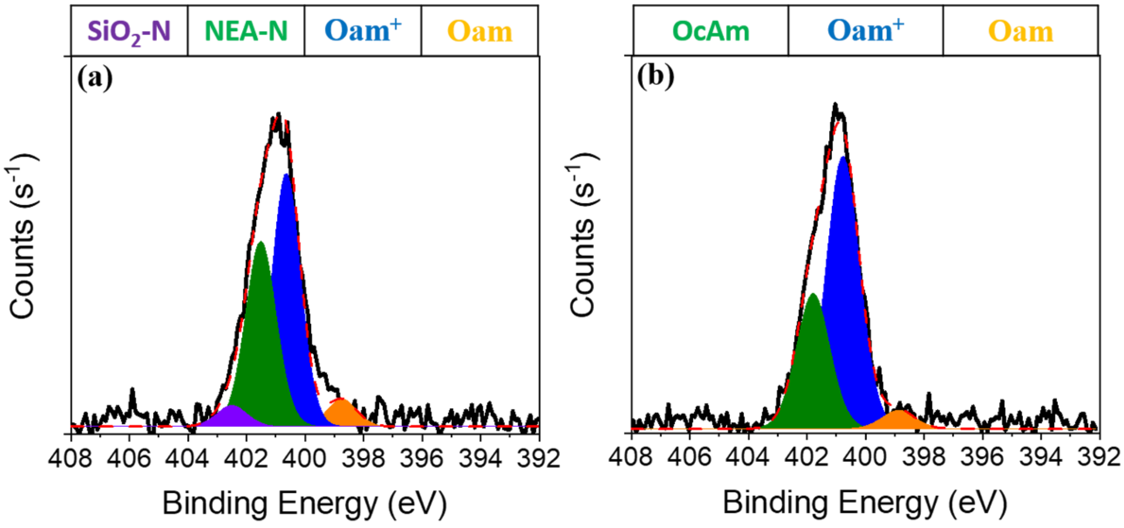

Figure E.7 N 1s X-ray photoelectron spectra of (a) R-NEA-CsPbBr3 NPs and (b) R-OcAm-CsPbBr3 NPs are shown. The signal at SiO2-NEA signal arises from excess ligand interacting with the substrate.

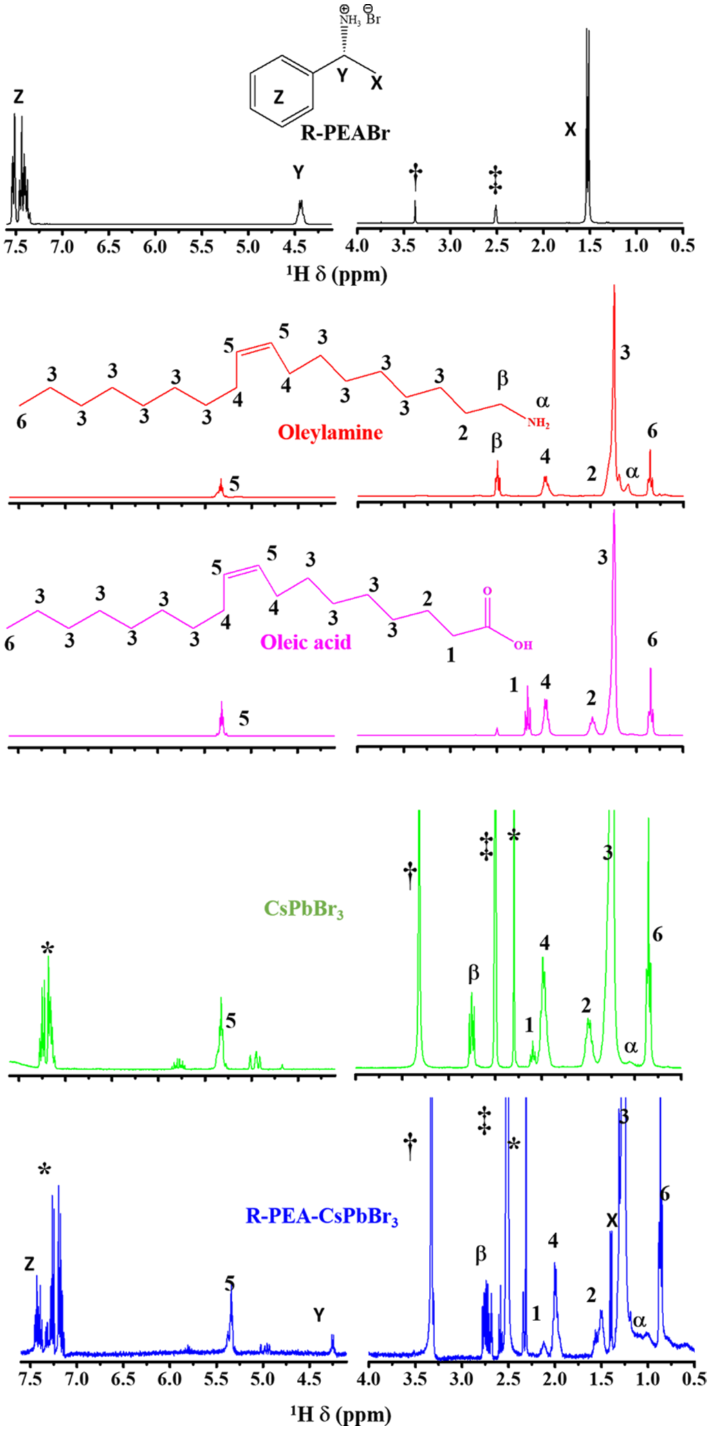

Figure E.8 ^{1}H NMR spectra of R-PEABr (black), oleylamine (red), oleic acid (pink), $CsPbBr_3$ (green) and R-PEA-$CsPbBr_3$ (blue) NPs. Residual solvent resonances are marked as *, † and ‡ for toluene, H_2O and DMSO respectively. The inset shows the molecular structure and the corresponding resonance identification of the ligands.

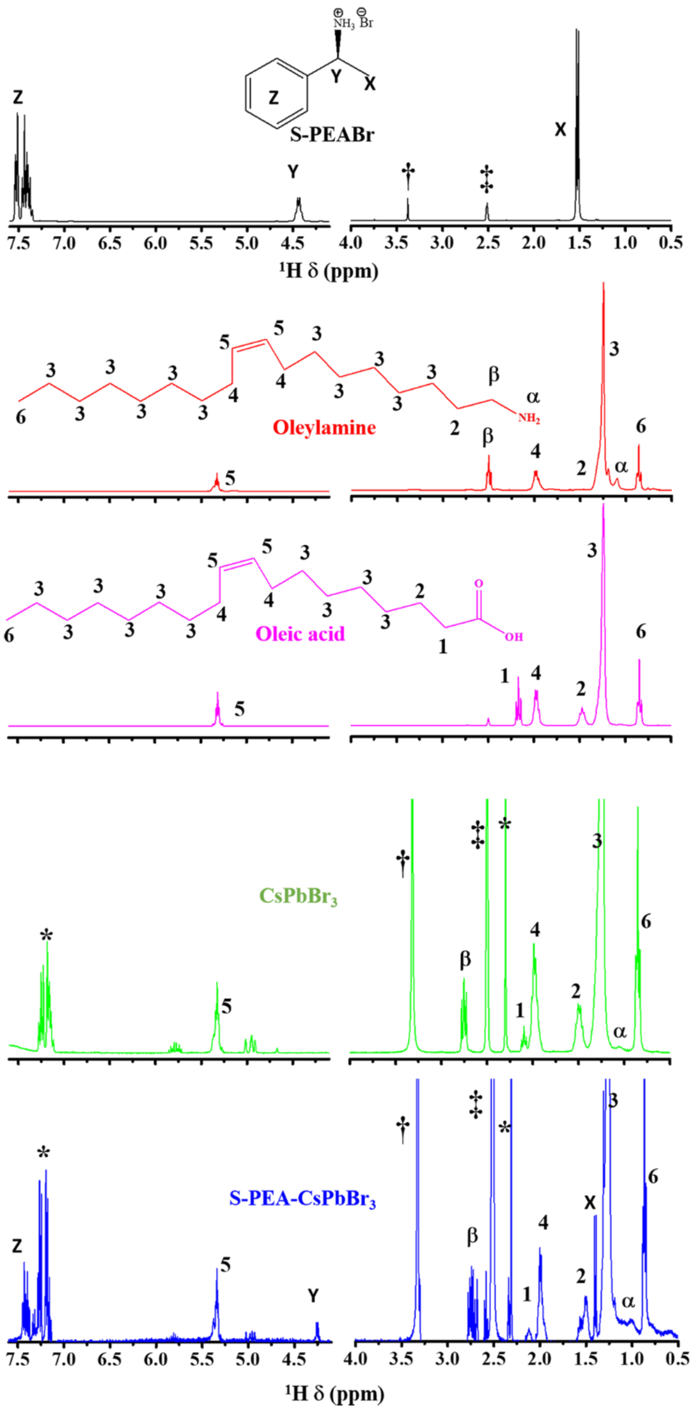

Figure E.9 ^{1}H NMR spectra of S-PEABr (black), oleylamine (red), oleic acid (pink), $CsPbBr_3$ (green) and S-PEA-$CsPbBr_3$ (blue) NPs. Residual solvent resonances are marked as *, † and ‡ for toluene, H_2O and DMSO respectively. The inset shows the molecular structure and the corresponding resonance identification of the ligands.

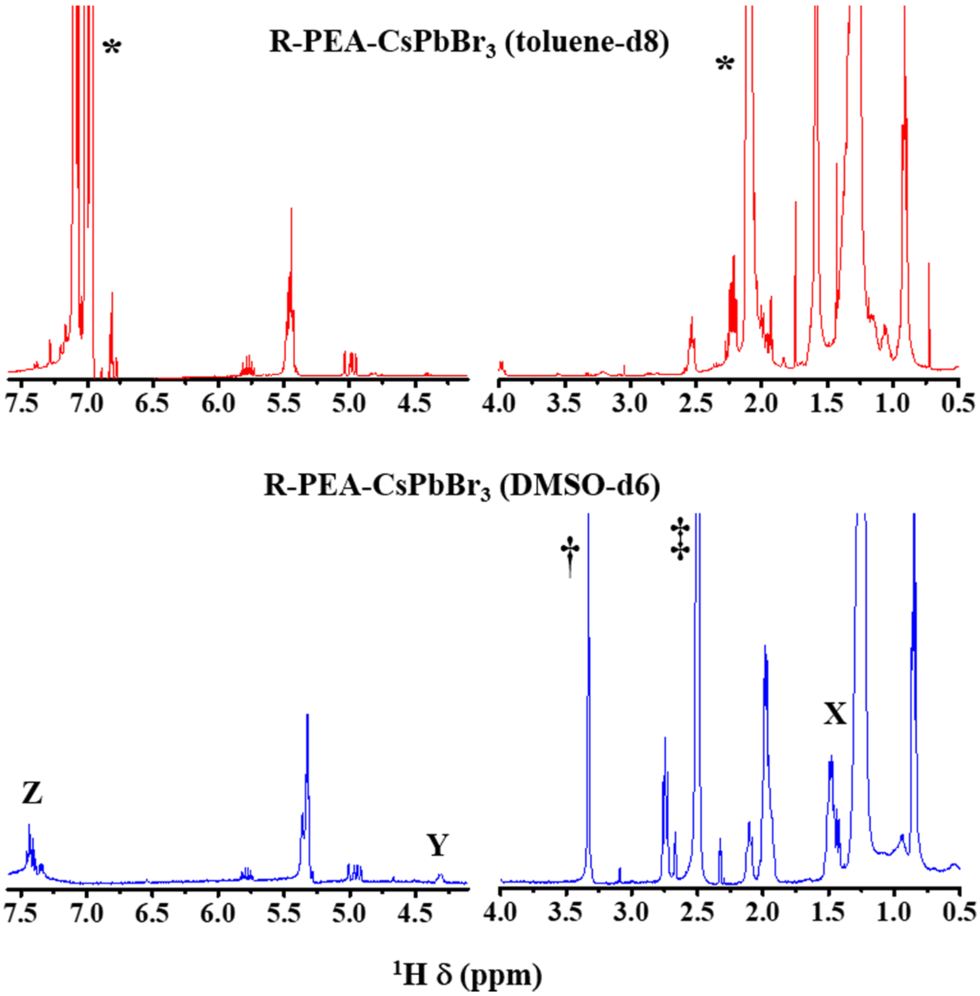

Figure E.10 ^{1}H NMR spectra of R-PEA-CsPbBr$_3$ NPs in toluene-d8 (red) and DMSO-d6 (blue) are shown. Residual solvent resonances are marked as *, † and ‡. Contributions from PEA are marked according to the nomenclature in Figure E.8.

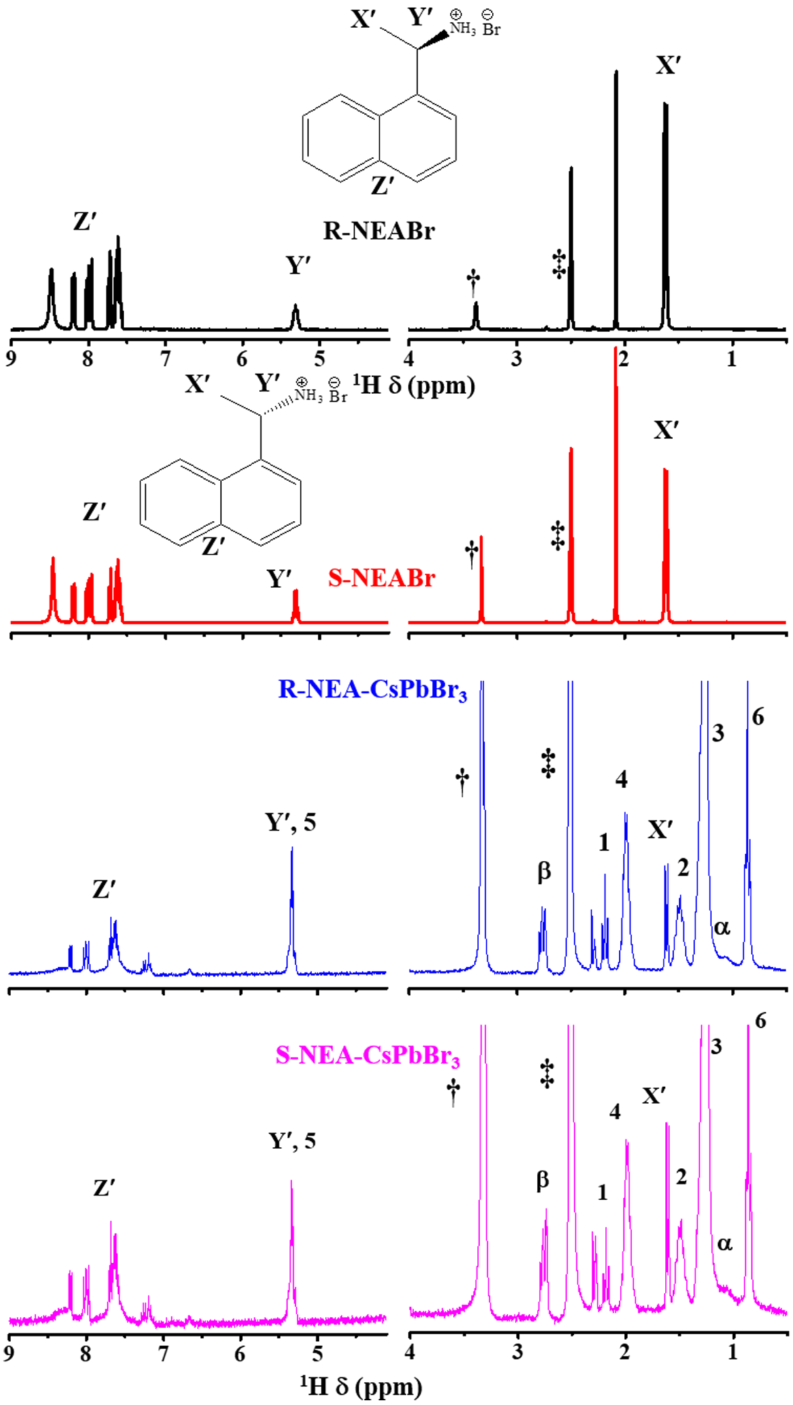

Figure E.11 ^{1}H NMR spectra of R- (black) and S-NEABr (red) and R- (blue) and S-NEA-CsPbBr$_3$ (pink) NPs are shown. Contributions from oleic acid and oleylamine are marked according to the nomenclature in Figure *C.8*. Residual solvent resonances are marked as † and ‡.

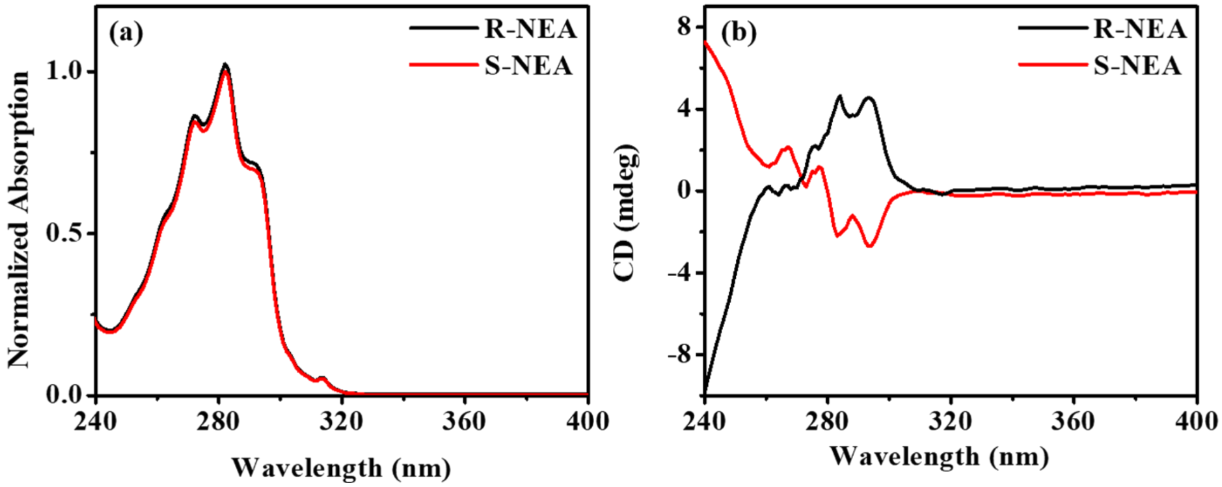

Figure E.12 (a) UV-vis absorption and CD spectra of R- (black) and S-NEA (red) in methylcyclohexane.

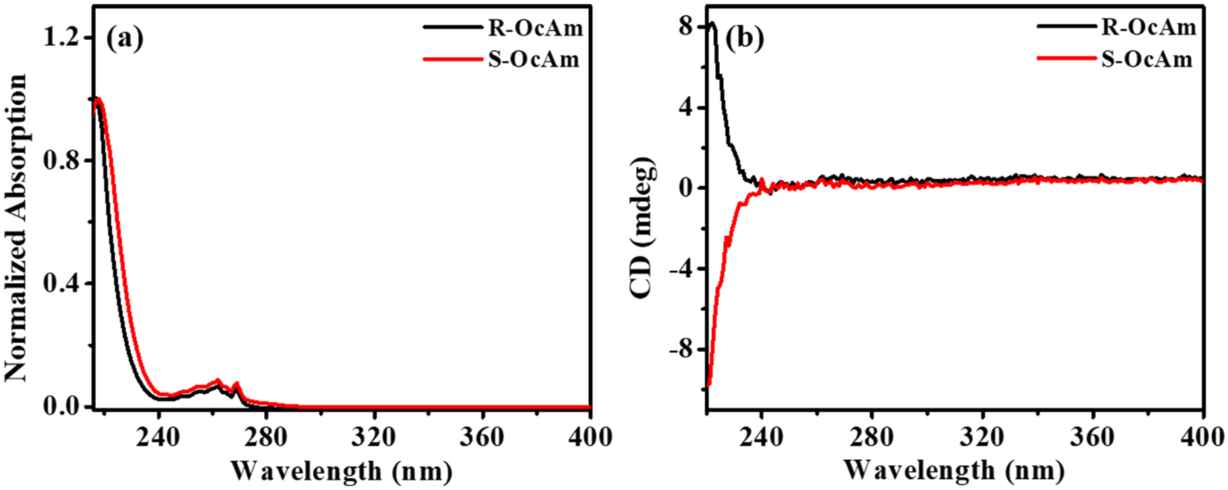

Figure E.13 (a) UV-vis absorption and CD spectra of R-(black) and S-OcAm (red) in methylcyclohexane.

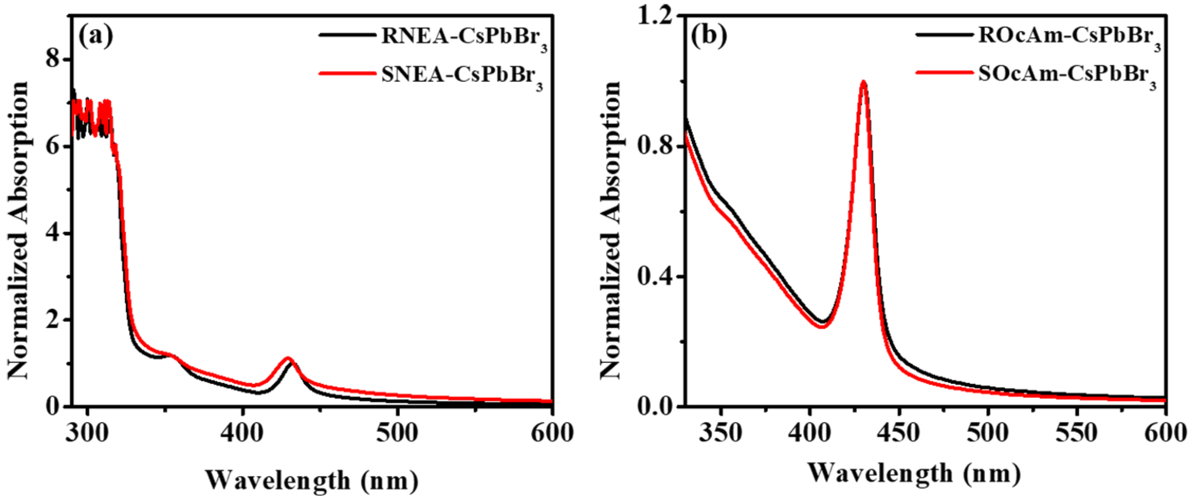

Figure E.14 Normalized absorption spectra of (a) R- and S- NEA-CsPbBr$_3$ NPs ([NEA = 30 mM in NP dispersion). The NEA based absorption transition is centered at 300 nm and (b) R- and S-OcAm-CsPbBr$_3$ NPs ([OcAm] = 11 mM in NP dispersion).

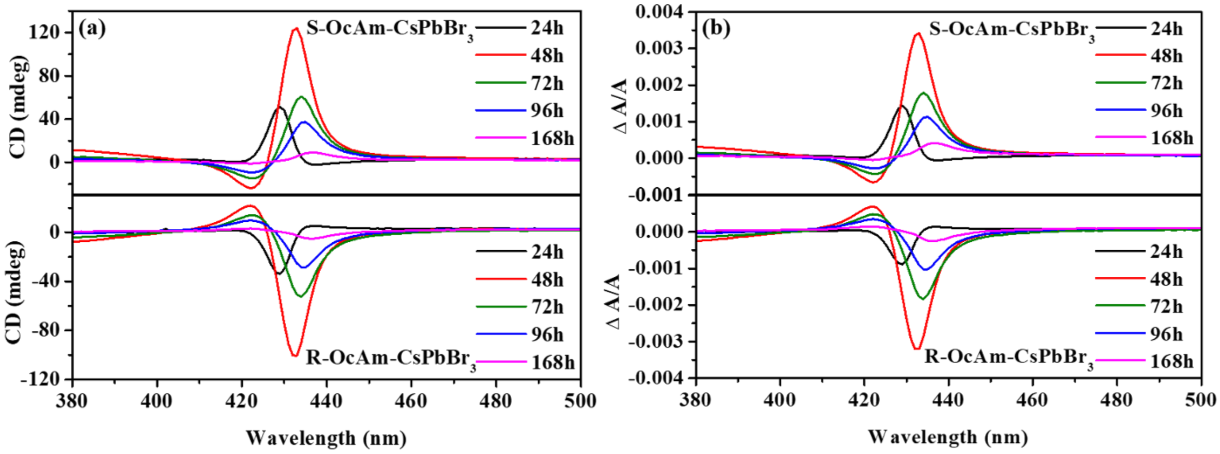

Figure E.15 (a) Progression of the CD signals as a function of ligand incubation time and (b) their corresponding representation in terms of ΔA/A are shown for R- and S-OcAm-CsPbBr$_3$ NPs.

Note that the R- and S-OcAm have positive and negative CD signals respectively, as shown in Fig. E.13 but show a flip in sign for the R- and S-OcAm-CsPbBr$_3$ NPs. This is not unusual and can be explained based on the differences on the coordination geometry of ligands as they interact with the NP surface and has been previously shown to be operative for chiral II-VI semiconductor NPs as well (Nano Lett., 2016, **16**, 4583-4589).

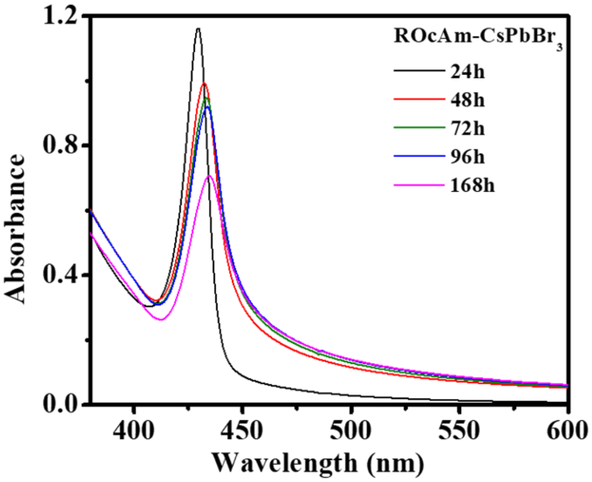

Figure E.16 UV-vis absorption spectra of R-OcAm-CsPbBr3 NPs as a function of ligand incubation time.

Appendix F

Appendix F.1 Supplemental Data

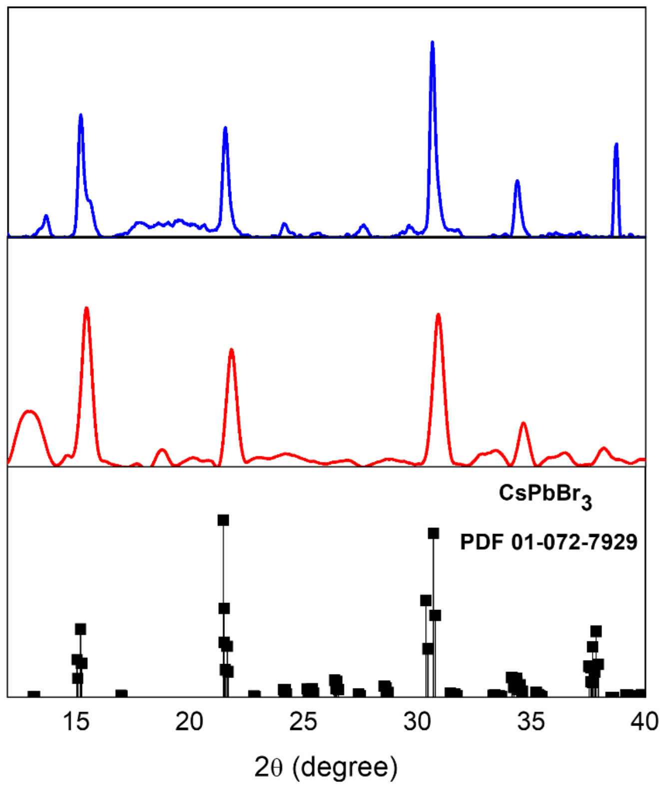

Figure F.1 XRD patterns of achiral (blue) and chiral (red) 2 nm NPs. A reference pattern for CsPbBr$_3$ is shown in the bottom panel. Chiral NPs are formed via ligand exchange with S-MPEABr..

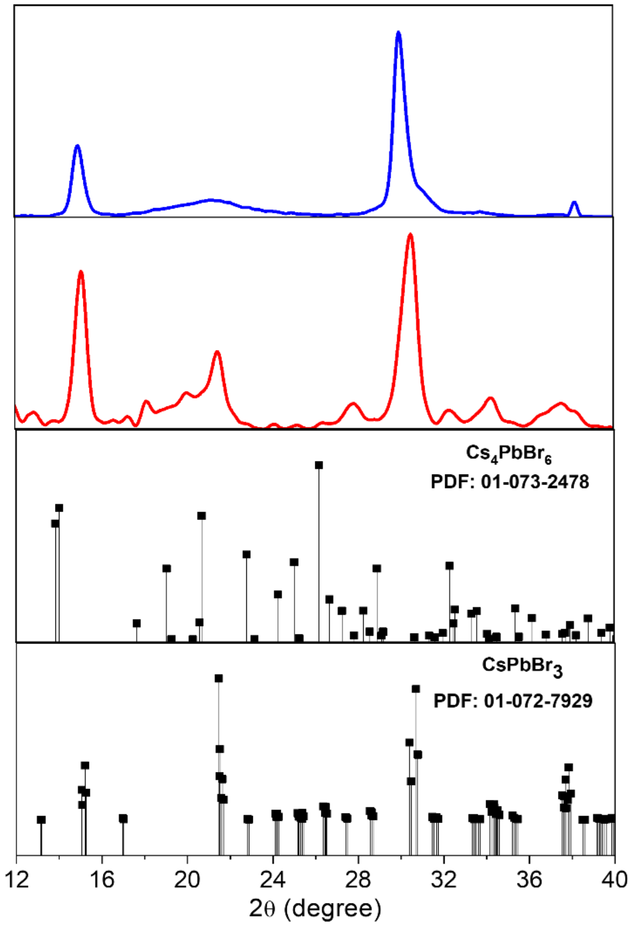

Figure F.2 XRD patterns of achiral (blue) and chiral (red) 4 nm NPs. Reference patterns for CsPbBr$_3$ and Cs$_4$PbBr$_6$ are shown in the bottom panels. Chiral NPs are formed via ligand exchange with S-MPEABr.

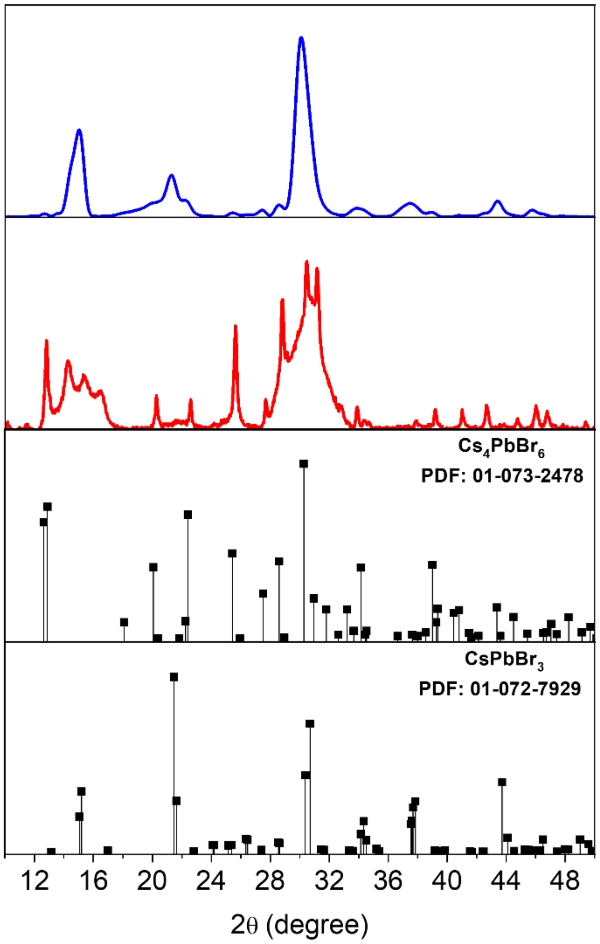

Figure F.3 XRD patterns of achiral (blue) and chiral (red) 6 nm NPs. Reference patterns for $CsPbBr_3$ and Cs_4PbBr_6 are shown in the bottom panels. Chiral NPs are formed via ligand exchange with S-MPEABr.

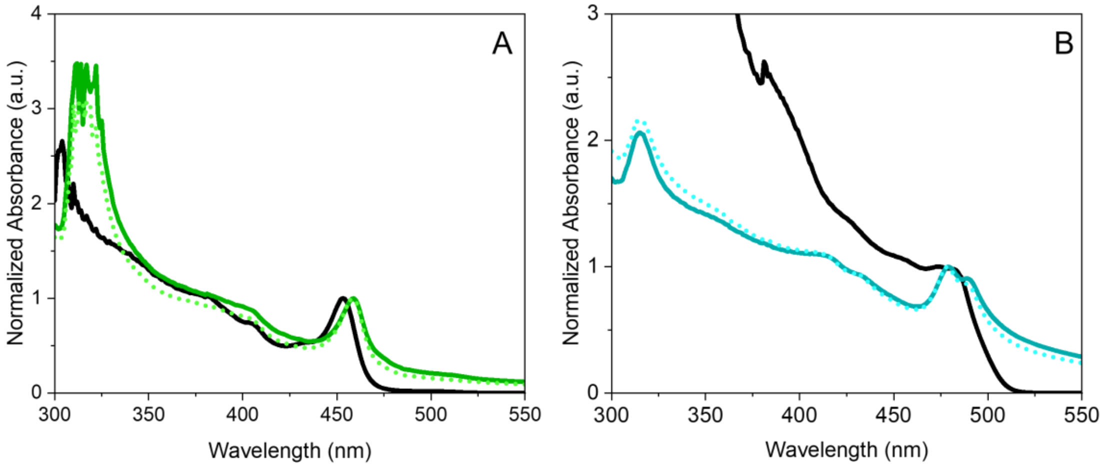

Figure F.4 Absorbance spectra for 4 nm (A) and 6 nm (B) NPs. Black spectra signify achiral NPs, R-NPs are shownn with solid colored lines and S-NPs are shown with dotten colored lines. Both sizes exhibit peaks at 315 nm after ligand exchange, attributed to Cs_4PbBr_6.

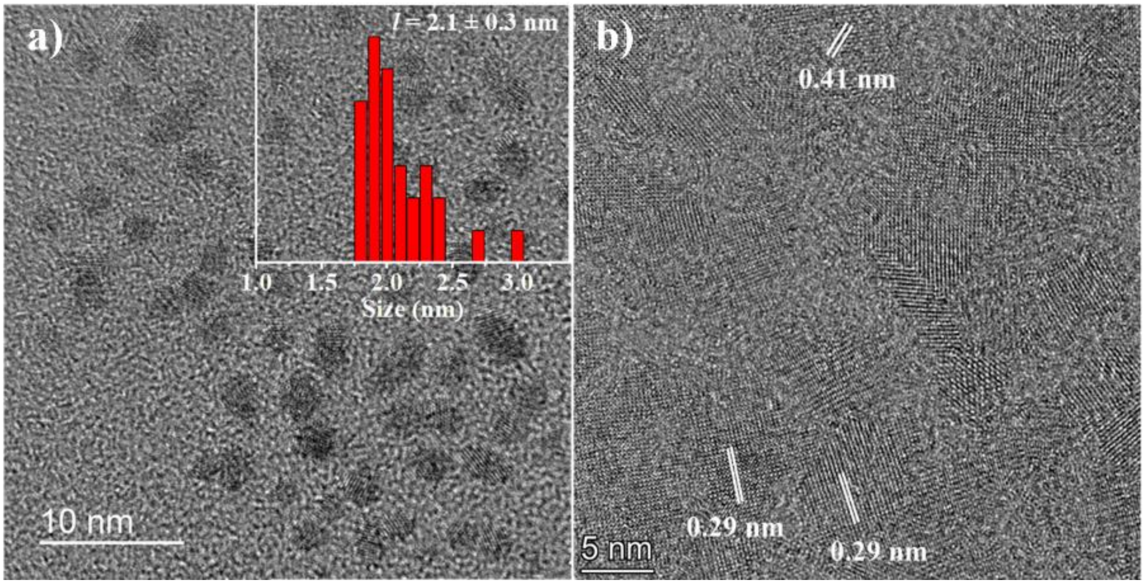

Figure F.5 (A) TEM image and histogram for achiral NPs in the 2 nm size regime. (B) HR-TEM image of NPs in the 2 nm size regime. Lattice spacings of 0.41 and 0.29 nm are marked and correspond to the (020) and (220) planes of orthorhombic $CsPbBr_3$.

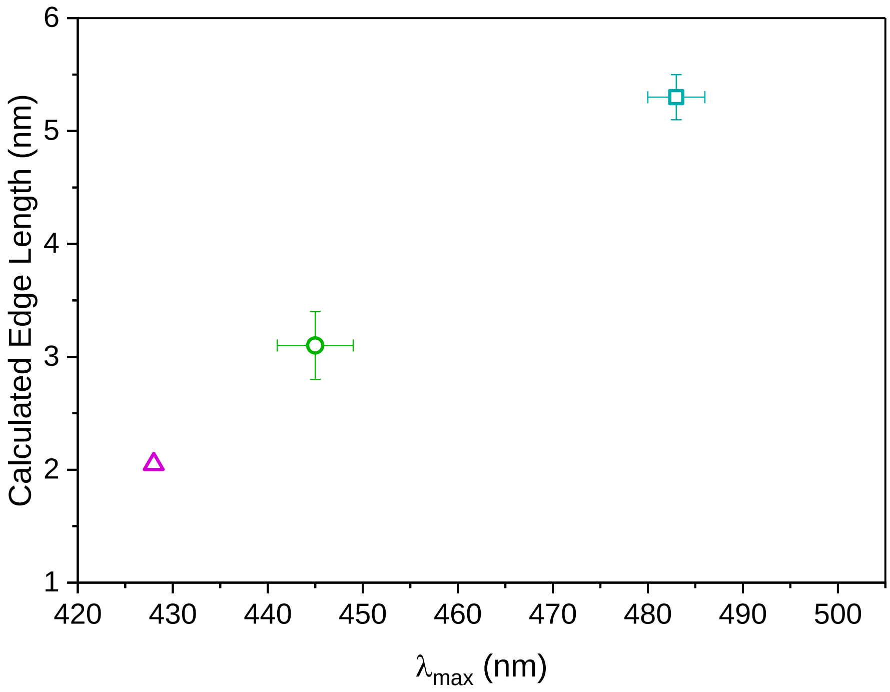

Figure F. 6 Edge lengths for achiral NPs derived from the experimental λ_{max} via Equation 5.1.

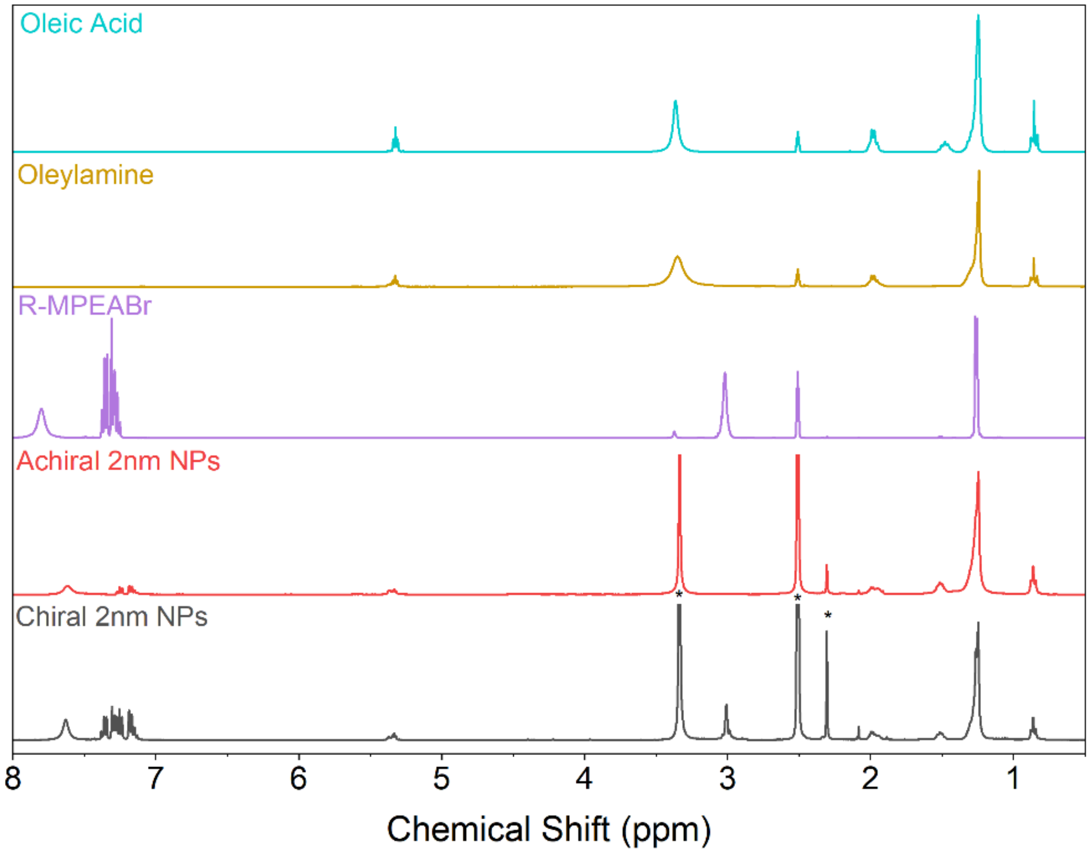

Figure F.7 Proton NMR spectra of chiral (black) and achiral (red) digested perovskite NPs and pure ligands (OA – aqua, OAm – yellow, R-MPEABr – purple). Solvent and impurity peaks are marked with stars and originate from trace amounts of water (3.3 ppm), DMSO (2.5 ppm), and toluene (2.3 ppm).

Appendix G

Appendix G.1 Supplemental Data

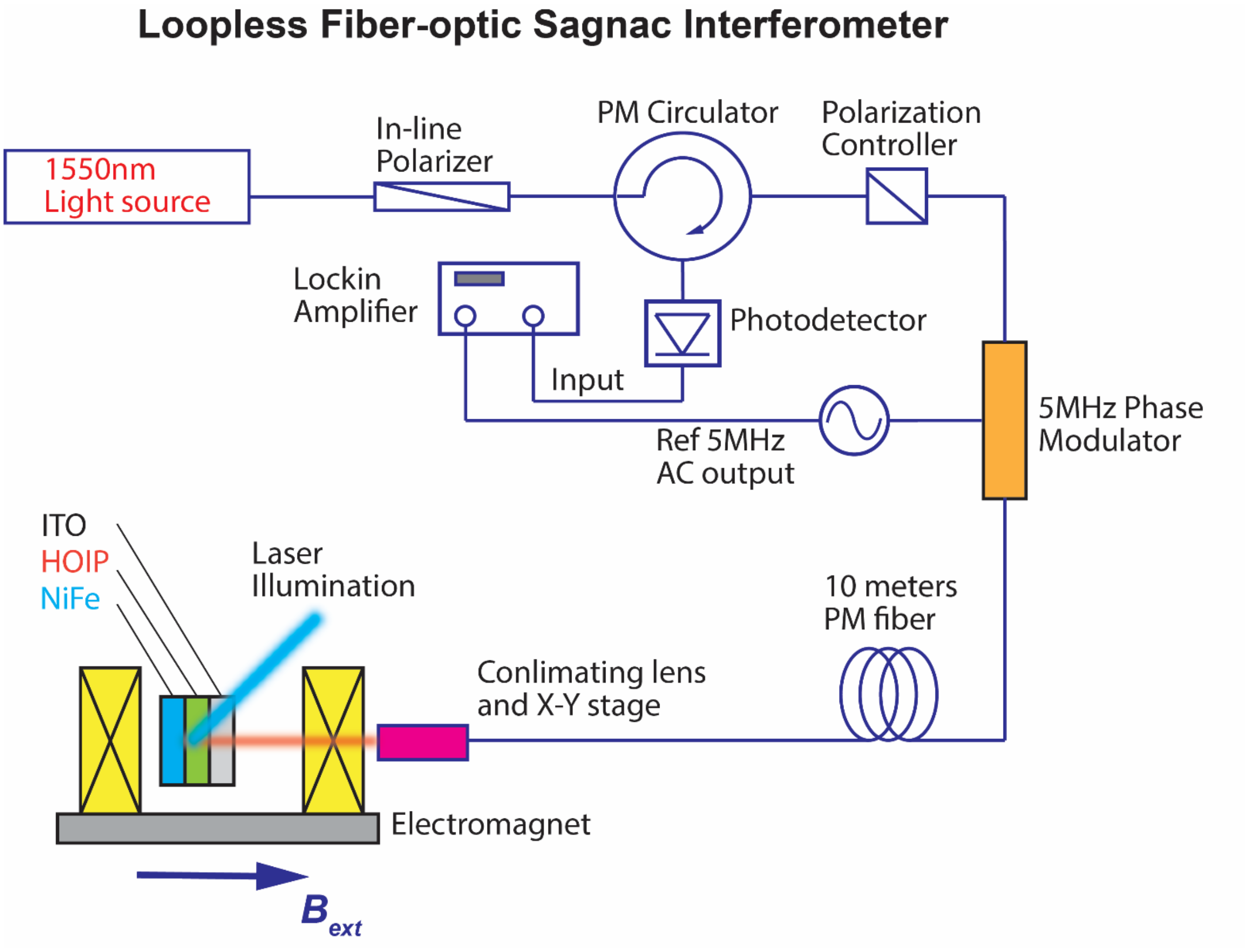

Figure G.1 Ultrasensitive fiber-based loopless Sagnac set up for probing the photoinduced Kerr signals in the Chiral-HOPI/NiFe heterostructure. The chiral-HOIP sample was illuminated by a laser diode through the transparent ITO substrate. The change of Kerr signal at the HOIP/NiFe interface is detected by the collimated Sagnac beam in the Faraday configuration which has the highest sensitivity for the photogenerated magnetization along the out-of-plane direction.

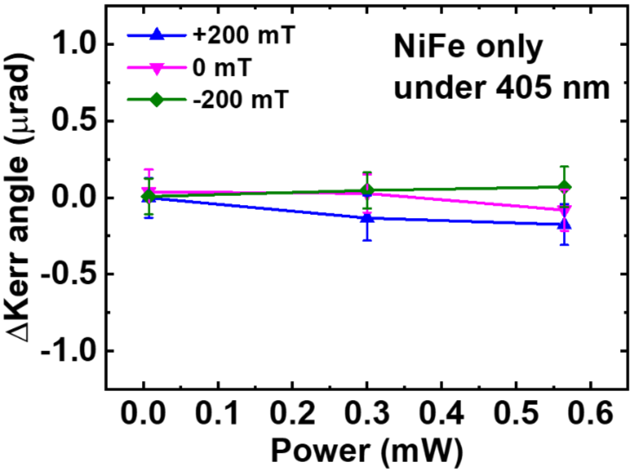

Figure G.2 Control experiment #1: Laser power dependence of the ΔKerr angle in the NiFe only sample without HOIP layers under same 405 nm illumination. Figure shows the power dependence for the NiFe only sample under +210 mT (Blue), 0 mT (Pink), and -200mT (Olive) external magnetic field, respectively. The absence of substantial change of Kerr angle in the NiFe only sample (<0.2 μrad) confirms that photoinduced Kerr responses of these chiral HOIP assemblies shown in Figure 4 require both the chiral HOIP and the ferromagnetic layer.

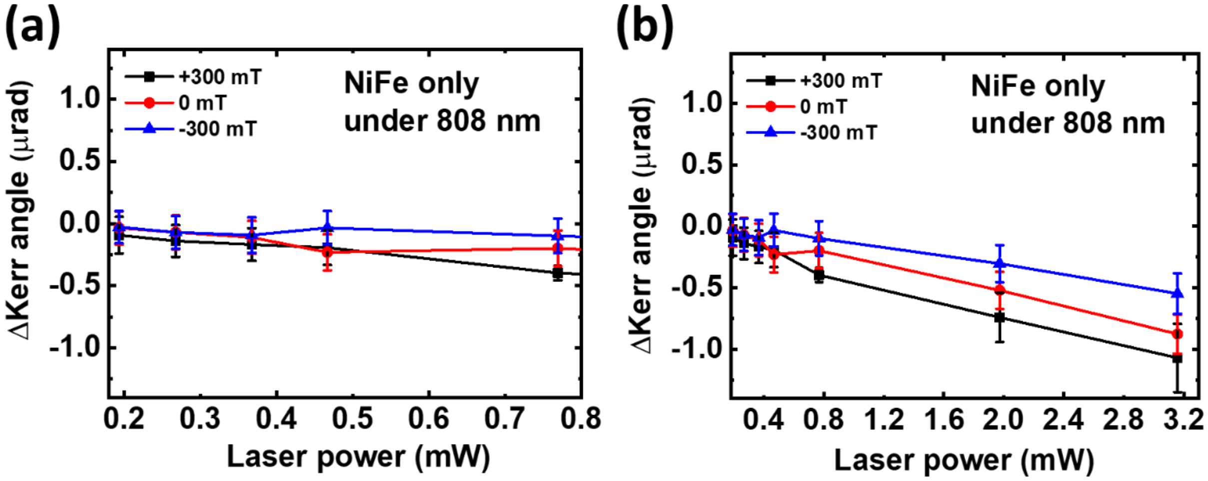

Figure G.3 Control experiment #2: Laser power dependence studies of the ΔKerr angle in the NiFe only sample without HOIP layers under 808 nm illumination. Panel (a) shows the power dependence for a NiFe only sample under +300 mT (Black, squares), 0mT (Red circles), 300mT (Blue, triangles) external magnetic field under the same laser intensity that used for the chiral-HOIP samples. Panel (b) shows the power dependence of photoinduced Kerr signals under a high laser illumination up to 3.0 mW. The reduction of Kerr signals is attributed to the combination of laser-induced heating effect and longitudinal spin Seebeck effect upon out-of-plane temperature gradient.

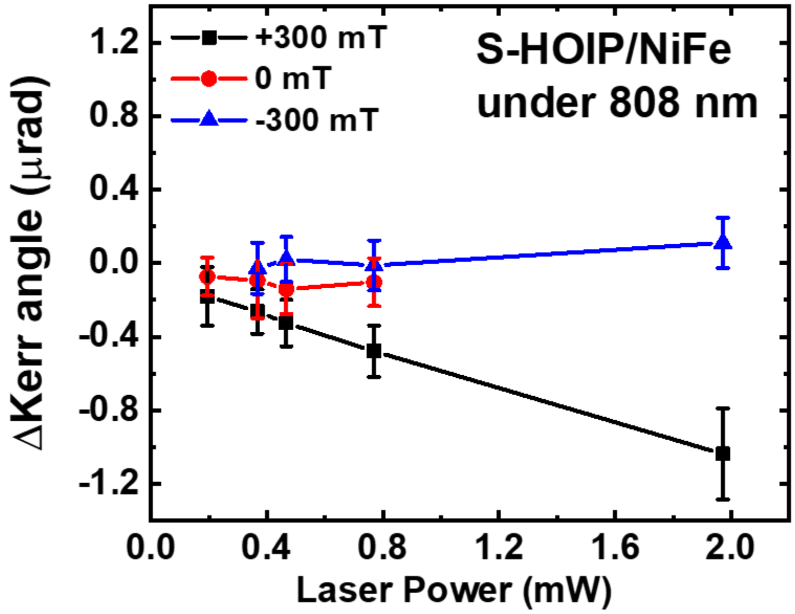

Figure G.4 Control experiment #3: Laser power dependence studies of the ΔKerr angle in S-HOIP/NiFe sample under 808 nm excitation for which the absorbance of chiral-HOIPs is negligible. No change of Kerr angles is observed unless the sample is illuminated at the high laser power caused by the laser heating (> 1 mW).

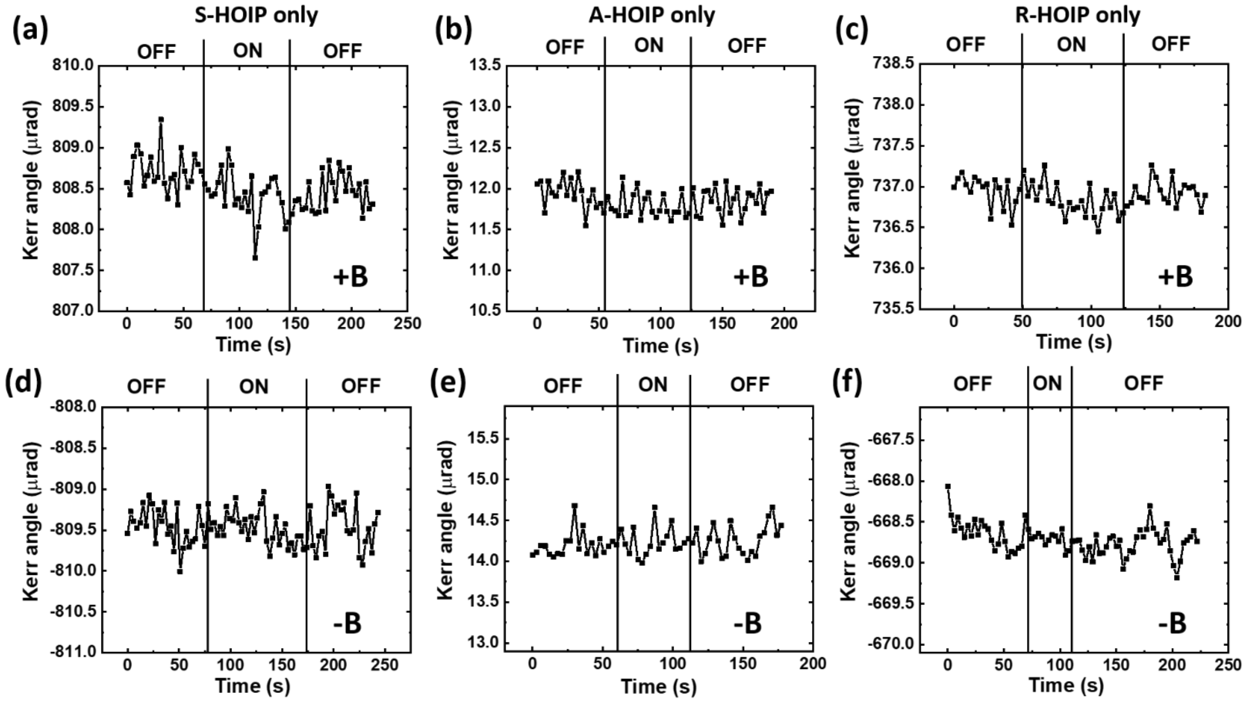

Figure G.5 Control experiment #4: Absence of photoinduced Kerr signal in the R/S and A-HOIP thin film under 405 nm illumination. Figure shows the absence of change in Kerr signals upon 405 nm illumination for *S*-HOIPs, A-HOIPs, and *R*-HOIPs thin film without ferromagnetic NiFe layer under positive (top, (a)-(c)) and negative (bottom, (d)-(f)) out-of-plane field, respectively.

Appendix G.2 Discussion and DFT Calculations

Previous measurements on quantum dot (QD)-chiral SAM - ferromagnetic substrates showed that optical excitation of the QD coincides with the emergence of a magnetic field normal to the substrates surface.[1] The origin of the effect was associated with a spin-transfer torque process and the sign of the magnetization was determined by the sense of the chiral molecules' spin-filtering (up versus down spins). A change of light polarization only changed the magnitude of the resulting field; *i.e.*, the direction of the photoinduced magnetization was controlled by the chirality of the linker molecule. Assuming a similar process for the chiral-HOIP/ferromagnetic films studied here, the photoexcitation of the chiral-HOIP will drive a spin-polarized current between the HOIP and the ferromagnetic substrate and generate a magnetization, ΔM_{light}. The sign (direction) of the spin current, hence ΔM_{light}, is determined by the spin filtering property of the chiral HOIPs.

Second, the electronic density of states formed between the chiral-HOIP and the ferromagnetic substrate will depend on the substrates' magnetization, its spin-dependent interaction with the chiral-HOIP and the spinterface. That is, the orbital interactions (hybridization) between the HOIP and the 3d orbitals in the ferromagnet are enantiospecific and dependent on the sign of the magnetization. This dependence was recently shown using AC Kelvin probe force microscopy measurements on chiral-SAM /ferromagnetic architectures, for which the experimental contact potential difference displays a dependence on the handedness of the chiral SAM and the magnetization direction of the ferromagnetic substrate.[2] For instance, an *S*-chiral SAM shows a positive (negative) shift in the contact potential difference when measured under negative (positive) magnetization, as compared to an achiral SAM film; and the reverse was found for *R*-chiral SAMs. If a similar principle operates for the HOIP/ferromagnet interfaces, then the voltage drop across the interface will depend on the direction of the magnetization of the ferromagnet and the HOIP chirality.

It is noteworthy that 2D chiral-HOIPs have recently been shown to display ferroelectric properties,[3, 4] and we posit that the chiral-HOIP/NiFe interface is similar.[5] The magnitude of ferroelectric effects on poled samples can be quite large[6] and reversing the poling potential can be used to create a switchable photodiode.[5] Ferroelectric HOIPs have been shown to exhibit domain wall formation, or localized dipolar fields.[7] According to the CISS effect the spin preference for the transmission of electrons should flip if the direction of the electric field is flipped.[8] Thus we infer that the chiral-HOIP/ NiFe interface forms a helicity-dependent magnetic spinterface with a local electric field that changes sign as the magnetization of the NiFe layer changes sign under the external magnetic field, so that, the photoresponse (or extra magnetic response) depends on both the HOIP chirality and the external magnetization.

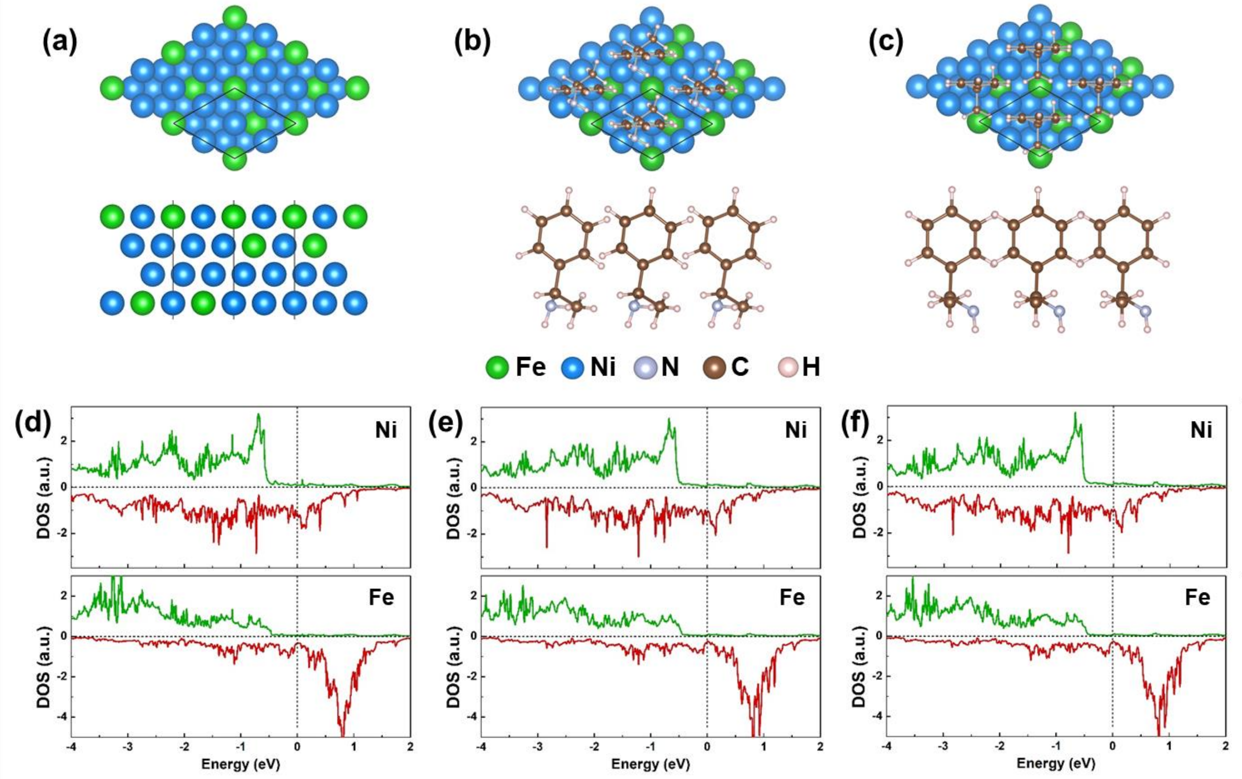

Figure G.6 Top and side views of the structures of (a) NiFe, (b) *R*-PEA/NiFe, and (c) *S*-PEA/NiFe. The black rhombus indicates the unit cell. The substrate NiFe is not shown in the side views of (b) and (c) to clearly represent the molecules of *R*-PEA and *S*-PEA. Density of states of (d) NiFe, (e) *R*-PEA/NiFe, and (f) *S*-PEA/NiFe. The green and red colors represent the spin-up and -down states, respectively.

We calculated the electrical dipole moment of *R(S)*-PEA to be ~1.575 Debye, as indicated by the molecular electronic potential distribution in Fig. G.7, which provides one factor contributing to the spin-selective molecular adsorption [circular dichroism (CD)]. However, the HOMO-LUMO gaps of *R*- and *S*-PEA are 6.12 and 5.85 eV (Fig. F.8), respectively, which is much bigger than the laser energy used (405 nm). Therefore, the magnetic dipole moment that can only arise upon photoexcitation is absent, such that no CD effect is expected from the chiral molecules alone, nor the net contribution *via* the CISS effect. Thus, we hypothesize that the inorganic perovskite framework in combination with the chiral molecules is necessary to account for the observed photoinduced magnetism *via* the CISS effect.

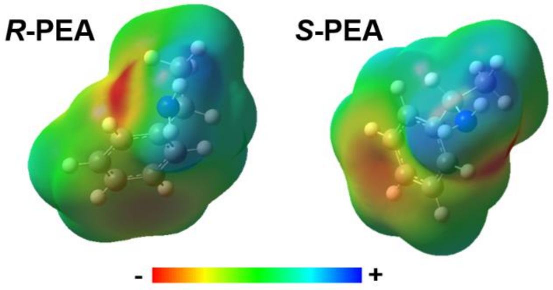

Figure G.7 The molecular electronic potential distribution of *R*(*S*)-PEA. The blue and red colors represent positive and negative.

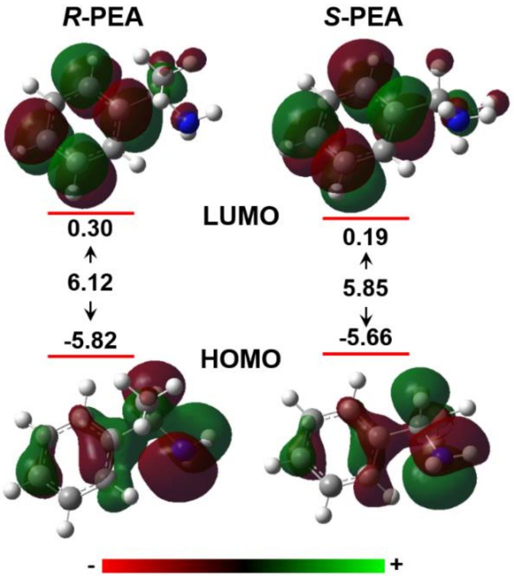

Figure G.8 HOMO and LUMO of *R*(*S*)-PEA. The green and red colors represent positive and negative. The numbers are in the unit of eV.

Appendix G.3 References

1. Ben Dor, O.; Morali, N.; Yochelis, S.; Baczewski, L. T.; Paltiel, Y., Local Light-Induced Magnetization Using Nanodots and Chiral Molecules. *Nano Lett.* **2014,** *14* (11), 6042-6049.

2. Ghosh, S.; Mishra, S.; Avigad, E.; Bloom, B. P.; Baczewski, L. T.; Yochelis, S.; Paltiel, Y.; Naaman, R.; Waldeck, D. H., Effect of Chiral Molecules on the Electron's Spin Wavefunction at Interfaces. *J. Phys. Chem. Lett.* **2020,** *11* (4), 1550-1557.

3. Gao, J.-X.; Zhang, W.-Y.; Wu, Z.-G.; Zheng, Y.-X.; Fu, D.-W., Enantiomorphic Perovskite Ferroelectrics with Circularly Polarized Luminescence. *J. Am. Chem. Soc.* **2020,** *142* (10), 4756-4761.

4. Hu, Y.; Florio, F.; Chen, Z.; Phelan, W. A.; Siegler Maxime, A.; Zhou, Z.; Guo, Y.; Hawks, R.; Jiang, J.; Feng, J.; Zhang, L.; Wang, B.; Wang, Y.; Gall, D.; Palermo Edmund, F.; Lu, Z.; Sun, X.; Lu, T.-M.; Zhou, H.; Ren, Y.; Wertz, E.; Sundararaman, R.; Shi, J., A chiral switchable photovoltaic ferroelectric 1D perovskite. *Sci Adv 6* (9), eaay4213.

5. Spaldin, N. A.; Ramesh, R., Advances in magnetoelectric multiferroics. *Nat. Mater.* **2019,** *18* (3), 203-212.

6. Garten Lauren, M.; Moore David, T.; Nanayakkara Sanjini, U.; Dwaraknath, S.; Schulz, P.; Wands, J.; Rockett, A.; Newell, B.; Persson Kristin, A.; Trolier-McKinstry, S.; Ginley David, S., The existence and impact of persistent ferroelectric domains in MAPbI3. *Sci Adv 5* (1), eaas9311.

7. Liu, S.; Zheng, F.; Koocher, N. Z.; Takenaka, H.; Wang, F.; Rappe, A. M., Ferroelectric Domain Wall Induced Band Gap Reduction and Charge Separation in Organometal Halide Perovskites. *J. Phys. Chem. Lett.* **2015,** *6* (4), 693-699.

8. Kumar, A.; Capua, E.; Kesharwani Manoj, K.; Martin Jan, M. L.; Sitbon, E.; Waldeck David, H.; Naaman, R., Chirality-induced spin polarization places symmetry constraints on biomolecular interactions. *Proc. Natl. Acad. Sci.* **2017,** *114* (10), 2474-2478.